

# Applications on Ground-based Tropospheric Measurements using Multi-Axis Differential Optical Absorption Spectroscopy



Ossama Ibrahim



Dissertation  
submitted to the  
Combined Faculties for the Natural Sciences and for Mathematics  
of the Ruperto-Carola University of Heidelberg, Germany  
for the degree of  
Doctor of Natural Sciences

presented by: Ossama Ibrahim  
born in: Cairo

oral examination: 27.01.2009



**Applications on Ground-based Tropospheric  
Measurements using Multi-Axis Differential  
Optical Absorption Spectroscopy**

Referees: Prof. Dr. Ulrich Platt  
Prof. Dr. Thomas Wagner



## Zusammenfassung

In dieser Doktorarbeit werden die MAX-DOAS Meßergebnisse von zwei wichtigen atmosphärischen Spurengasen, BrO und NO<sub>2</sub>, vorgestellt. Dabei wurden die MAX-DOAS Messungen von unterschiedlichen Plattformen (auf einem Schiff, auf dem Dach eines Autos oder an einem festen Ort installiert) und unter verschiedenen atmosphärischen Bedingungen durchgeführt. Die Messung von BrO sind wichtig zur Untersuchung des Einflusses von Halogenverbindungen in der marinen Grenzschicht. Die NO<sub>2</sub>-Messungen dienen der Quantifizierung von Quellen der Luftverschmutzung sowie zur Validierung von Satelliteninstrumenten.

BrO-Ergebnisse, die mit der MAX-DOAS Methode vom Oktober-November 2003 an Bord des Forschungsschiffes Polarstern ueber dem Atlantik gemessen wurden, regaben BrO Mischungsverhaeltnis zwischen 3 und 18 ppt im Gebiet zwischen 10 und 30 Grad noerdlicher Breite. Mithilfe von Strahlungstransportrechnungen konnte zudem Information ueber die Hoehenverteilung abgeleitet werden. Die Beziehungen zwischen erhoehtem troposphärischem BrO und verschiedenen biologischen und chemischen Parametern im Ozean und der Atmosphaere wurden im Detail untersucht. Hierdurch konnte wichtige Information ueber moegliche Quellen und Vorlaeufersubstanzen der aktivierten Halogenverbindungen gefunden werden.

NO<sub>2</sub>-Messungen wurden mithilfe eines MAX-DOAS Instruments, das auf ein Autodach montiert war, durchgeführt. Mit diesem Aufbau konnten an mehreren Tagen Messungen entlang einer Route um die Staedte Mannheim und Ludwigshafen durchgeführt werden. Die Entwicklung einer neuen Auswertungsmethode erlaubte die Bestimmung absoluter troposphärischer Spurenstoffsaekulendichten, von denen die NO<sub>2</sub> Fluesse in und aus der umkreisten Flaechе abgeleitet werden konnten. Die Ergebnisse der Auto-Messungen wurden auch mit Satellitendaten verglichen und es zeigte sich gute uebereinstimmung. MAX-DOAS-Messungen von NO<sub>2</sub> wurden auch waehrend der internationalen Meßkampagne (DANDELIONS) in Cabauw, Niederlande, im Mai-Juni 2005 durchgeführt. Dabei wurde eine gute uebereinstimmung mit den Ergebnissen der anderen Gruppen und mit Satellitenmessungen erzielt.

## Abstract

In this thesis, results of MAX-DOAS measurements of two important atmospheric trace gases, NO<sub>2</sub> and BrO, are presented. The MAX-DOAS technique was applied from different platforms (ship-borne, on top of a car or fixed at one measurement site) and for different conditions. The BrO observations are important for the correct understanding of tropospheric chemistry in the marine boundary layer. The NO<sub>2</sub> observations are used for the quantification of pollution sources and for the validation of satellite observations.

BrO Results from measurements over the Atlantic ocean aboard the Research Vessel Polarstern during October-November 2003 are presented and discussed. BrO Mixing ratios were estimated to be between 3 and 18 ppt in the area between 10 and 30 degrees latitude. Also information on the altitude distribution could be obtained using radiative transfer modelling. The relation of enhanced tropospheric BrO concentrations to several biological, chemical parameters in the ocean and atmosphere were studied in detail. Interesting information on potential sources and precursors of activated bromine compounds could be retrieved.

NO<sub>2</sub> observations were carried out using a MAXDOAS instrument on a car top around the cities of Mannheim and Ludwigshafen. The development of a new retrieval technique enabled the determination of the absolute values of tropospheric vertical trace gas column densities, from which the NO<sub>2</sub> fluxes into and outside this area were quantified. Results from the Auto-MAX-DOAS were compared to satellite measurements whenever possible and good agreement was found. MAX-DOAS observations of NO<sub>2</sub> were also carried out during the international measurements campaign

---

(DANDELIONS) in Cabauw (The Netherlands) in May-June 2005. Good agreement was found with data sets from the other groups and with satellites measurements.

# Contents

<b>1</b>	<b>Introduction</b>	<b>3</b>
<b>2</b>	<b>Chemistry in the Troposphere</b>	<b>5</b>
2.1	Nitrogen Dioxide . . . . .	5
2.2	Atmospheric Ozone Chemistry . . . . .	9
2.2.1	Ozone in the Stratosphere . . . . .	9
2.2.2	Ozone in the Troposphere . . . . .	12
2.3	Tropospheric Halogen Chemistry . . . . .	14
2.3.1	The Mechanism of Ozone Depletion . . . . .	14
2.3.2	Sources and Reaction Cycles of Reactive Halogen Species . . .	15
<b>3</b>	<b>Differential Optical Absorption Spectroscopy</b>	<b>19</b>
3.1	DOAS Overview . . . . .	19
3.2	The Lambert-Beer Law . . . . .	21
3.3	The Measurement Procedure . . . . .	23
3.4	The Spectral Analysis . . . . .	26
3.4.1	The Analysis Procedure . . . . .	26
3.4.2	Validity Consideration . . . . .	30
3.5	Passive DOAS Characteristics . . . . .	32
3.5.1	Fraunhofer Lines . . . . .	32
3.5.2	The Ring Effect . . . . .	33
3.5.3	The Solar $I_0$ Effect . . . . .	35
3.6	Multi-Axis-DOAS . . . . .	36
<b>4</b>	<b>Radiative Transfer in the Atmosphere</b>	<b>41</b>
4.1	Parameters of the Radiative Transfer . . . . .	41
4.2	Scattering Processes . . . . .	42
4.2.1	Rayleigh Scattering . . . . .	42
4.2.2	Raman Scattering . . . . .	43
4.2.3	Mie Scattering . . . . .	44
4.3	Visibility . . . . .	46
4.4	The Air Mass Factor Concept . . . . .	47
4.5	Radiative Transfer Modeling . . . . .	51
4.5.1	Introduction . . . . .	51
4.5.2	The Radiative Transfer Model Tracy . . . . .	52
4.5.3	The Radiative Transfer Model Tracy-II/McArtim . . . . .	53

---

4.6	Profile Retrieval . . . . .	55
4.6.1	Direct Comparison Approach . . . . .	55
<b>5</b>	<b>Instrumentation</b>	<b>63</b>
5.1	The Mini-MAX-DOAS Instrument and Set-up . . . . .	63
5.2	The Polarstern Instrument and Set-up . . . . .	69
5.3	Corrections on the Spectra . . . . .	75
5.3.1	Electronic Offset . . . . .	75
5.3.2	Dark Current . . . . .	75
5.3.3	Spectrograph Stray Light . . . . .	76
<b>6</b>	<b>Results from Polarstern Measurements</b>	<b>79</b>
6.1	Polarstern Overview . . . . .	79
6.2	The cruise ANT-XXI . . . . .	81
6.3	BrO Results . . . . .	86
6.4	Radiative Transfer calculations . . . . .	86
6.4.1	Calculation and comparison of Ratios . . . . .	93
6.5	BrO-Correlations Studies . . . . .	97
6.5.1	BrO-Chlorophyll Correlations . . . . .	98
6.5.2	BrO-Aerosol Correlations . . . . .	118
<b>7</b>	<b>Results from Auto-MAX-DOAS measurements</b>	<b>129</b>
7.1	Introduction . . . . .	129
7.2	Results from measurements along the roads . . . . .	130
7.2.1	Brussels-Heidelberg measurements . . . . .	130
7.2.2	Vertical Column Densities Calculation Method . . . . .	133
7.2.3	Comparison with Satellites . . . . .	138
7.2.4	Hemel Hempstead Fire . . . . .	141
7.3	Results from encircling pollution sources . . . . .	162
7.3.1	Results From Encircling Mannheim-Ludwegshaven Area . . . . .	162
7.3.2	General Considerations for encircling measurements . . . . .	173
<b>8</b>	<b>Results from DANDELIONS campaign</b>	<b>177</b>
8.1	DANDELIONS campaign overview . . . . .	177
8.2	MAX-DOAS measurements in Cabauw . . . . .	178
8.3	MAX-DOAS NO <sub>2</sub> results . . . . .	178
8.4	Investigation of the spatial homogeneity . . . . .	180
8.5	MAX-DOAS ground-based results comparisons . . . . .	184
8.6	Comparisons with Satellite results . . . . .	186
<b>9</b>	<b>Summary and Outlook</b>	<b>187</b>
9.1	Summary . . . . .	187
9.1.1	The Polarstern campaign: . . . . .	187

---

9.1.2	Auto-MAX DOAS measurements . . . . .	189
9.1.3	DANDELIONS campaign . . . . .	190
9.2	Outlook . . . . .	191
<b>Appendix A</b>		<b>193</b>
	BrO dSCDs time series from the MAX-DOAS on board of the Polarstern RV . . . . .	193
<b>Appendix B</b>		<b>201</b>
	NO <sub>2</sub> VCDs Comparisons between MAX-DOAS Instruments . . . . .	201
<b>List of Figures</b>		<b>265</b>
<b>List of Tables</b>		<b>270</b>
<b>Bibliography</b>		<b>273</b>
<b>Acknowledgements</b>		<b>283</b>



# 1 Introduction

Human activities contribute to climate change by causing changes in Earth's atmosphere in the amounts of greenhouse gases, aerosols (small particles), and cloudiness. The largest known contribution comes from the burning of fossil fuels, which releases carbon dioxide gas to the atmosphere.

Greenhouse gases and aerosols affect climate by altering incoming solar radiation and outgoing infrared (thermal) radiation that are part of Earth's energy balance. Changing the atmospheric abundance or properties of these gases and particles can lead to a warming or cooling of the climate system.

Since the start of the industrial era (about 1750), the overall effect of human activities on climate has been a warming influence. The human impact on climate during this era greatly exceeds that due to known changes in natural processes, such as solar changes and volcanic eruptions. (IPCC Fourth Assessment report).

Bromine monoxide is a very important atmospheric trace gas, because it destroys ozone very effectively. Since ozone is needed for the formation of  $HO_x$ , the most important oxidizing substance in the troposphere, BrO has a large influence on the oxidation capacity of the atmosphere. Furthermore, in the stratosphere BrO contributes to the formation of the stratospheric ozone hole. In addition to the bromine catalyzed ozone destruction, bromine monoxide is also involved in other important aspects of atmospheric chemistry: Bromine radicals lead to a decrease in Cloud Condensation Nuclei (CCNs), especially in remote marine regions, via the reduction of atmospheric sulphur dioxide. The decline of CCNs has an important consequence for the climate, because it implies a reduction of atmospheric albedo. In polar regions bromine radicals are responsible for the oxidation of gaseous elemental mercury, enabling the uptake of toxic mercury by biological organisms [Hollwedel, 2005].

Within the frame of this work, measurements of  $NO_2$  at industrial-urban areas and also measurements of BrO at the MBL were carried out. The importance of these two trace gases comes from their wide influence in the atmospheric chemistry. Both gases exist in the stratosphere and play important roles in ozone destruction. They also exist in the troposphere and play some role also in tropospheric ozone depletion. Detecting and quantifying  $NO_2$  and BrO in the troposphere was one of the main tasks in this work. Further analysis, modeling and calculations were done to shed some light on the spatial extent in which both trace gases exist in the troposphere, since their existence in the stratosphere is obvious. In this work, measurements, studies and calculations are done for this purpose.

This work consists of three parts. In the first part, results are represented from BrO

measurements on board of Polarstern Research Vessel during October-November 2003° n the cruise between Bremerhaven (Germany) and Cape Town (South Africa). In the second part, Auto-MAX DOAS (Car DOAS) measurements were carried out at Mannheim- Ludwigshafen Industrial / urban area and on the road between Brussels (Belgium) and Heidelberg (Germany) and also on the north coast of France during a big fire event near from London (UK). NO<sub>2</sub> was detected during these measurements with the car DOAS. In third and last part, we participated in a large international measurement campaign where we carried out long time series NO<sub>2</sub> measurements (about two months) at the Cabauw experimental site for Atmospheric Research.

# 2 Chemistry in the Troposphere

## 2.1 Nitrogen Dioxide

Nitrogen dioxide ( $\text{NO}_2$ ) forms part of a family of gases which are often expressed by  $\text{NO}_x$  ( $=\text{NO}_2+\text{NO}$ ) since  $\text{NO}_2$  and  $\text{NO}$  rapidly convert into each other in the atmosphere.  $\text{NO}_x$  is of large importance for chemical processes in the atmosphere: They have a strong impact on the oxidative capacity of the atmosphere because they influence the abundance and partitioning of  $\text{HO}_x$  radicals ( $\text{HO}_x=\text{OH}+\text{HO}_2$ ). Furthermore, they act as a catalysator in the formation of ozone ( $\text{O}_3$ ) in the troposphere. However in the stratosphere,  $\text{NO}_x$  enhance the degradation of the ozone layer.  $\text{NO}_x$  is mostly removed from the atmosphere in form of nitric acid ( $\text{HNO}_3$ ) which is, besides sulfuric acid ( $\text{H}_2\text{SO}_4$ ), an important component of acid rain.

The effective lifetime of  $\text{NO}_2$  depends on the solar radiation, and ranges between 33 hours in winter times and 12 hours in summer times [Beirle et al., 2003]. There are many sources for nitrogen oxides: The largest source is the anthropogenic fossil fuel combustion in industrial activities and traffic. Thus, the  $\text{NO}_x$  values are much higher in urban areas than in rural regions. Also air traffic whose exhaust gases are emitted mostly in the upper troposphere must not be ignored as  $\text{NO}_x$  source. Furthermore  $\text{NO}_x$  is generated by the burning of biomass e.g. during forest fires as well as clearings of forest by fire. Moreover, emissions from soil owing to fertilizer and microbiological processes, like e.g. putrefaction, contribute to the  $\text{NO}_x$  budget. Also thunderstorms are an important source in the production of  $\text{NO}_x$  because air which is exposed to lightnings is strongly heated up. Finally,  $\text{NO}_x$  diffuses from the stratosphere into the troposphere. Table 2.1 lists the most important  $\text{NO}_x$  sources as well as their amounts of emission and uncertainties [Lee et al., 1997].

The relatively high uncertainties in Table 2.1 show, that the understanding of the processes which generates  $\text{NO}_x$  is still in progress [Leue et al., 2001; Beirle et al., 2003]. Yet, it can easily be seen that more as the half of the emissions have anthropogenic origin. Such sources are concentrated on small spots. Thus, in especially high polluted areas, mixing ratios in the order of magnitude of 100 ppb<sup>1</sup> can occur. In contrast, natural  $\text{NO}_x$  sources are distributed more equally over the Earth. Figure 2.1 shows the tropospheric mean repartition of  $\text{NO}_2$  retrieved from satellite measurements during 18 months. Large cities can easily be recognized by significant larger  $\text{NO}_2$  column densities.

---

<sup>1</sup>1 ppb = 1 part per billion =  $10^{-9}$  mixing ratio

Table 2.1:  $NO_x$  emissions sorted by sources [Lee et al., 1997].

Emission source	Emission [mt]	Uncertainty [mt]
Industry and traffic	22	13-31
Biomass burning	7,9	3-15
Soil emissions	7	4-12
Thunderstorms	5	2-20
Air traffic	0,8	0,6-1
Stratospheric diffusion	0,6	0,4-1

Nitrogen oxides are produced in the atmosphere whenever air is heated to temperatures higher than 2000 K, e.g. in combustion processes. In this case, the thermal energy is high enough to dissociate  $O_2$  into atomic oxygen which reacts with molecular nitrogen to form NO:



Another byproduct is  $N_2O$  can be generated. In the troposphere,  $N_2O$  is inert (lifetime of about 120 years) and thus, does not play a chemical role. However in the stratosphere, the strong UV radiation can dissociate  $N_2O$  (at  $\lambda < 298$  nm) yielding atomic oxygen for further reactions.

NO, as it is produced in reaction 2.1, is rapidly oxidized by ozone to  $NO_2$ :



$NO_2$  mostly yielded from reaction (2.2) can be photolyzed by UV radiation of the sun below 420 nm generating ozone (see reaction (2.3)). Under direct sun exposure at noon, this happens fast and the mean lifetime of  $NO_2$  only accounts to several minutes.



where  $O(^3P)$  reacts rapidly with  $O_2$  to ozone:



with M as required collision partner (e.g.  $N_2$  or  $O_2$ ) due to conservation of energy and spin momentum. Since other reactions with  $O(^3P)$  can be neglected, each  $NO_2$  molecule leads to the generation of an ozone and NO molecule. However, according to reaction (2.2), NO and  $O_3$  form  $NO_2$  again. Finally, a photostationary state arises between  $NO_2$  and NO which is referred to as the Leighton ratio [Leighton, 1961]:

$$\frac{[NO]}{[NO_2]} = \frac{j_{NO_2}}{k_{NO} \cdot [O_3]} \quad (2.5)$$

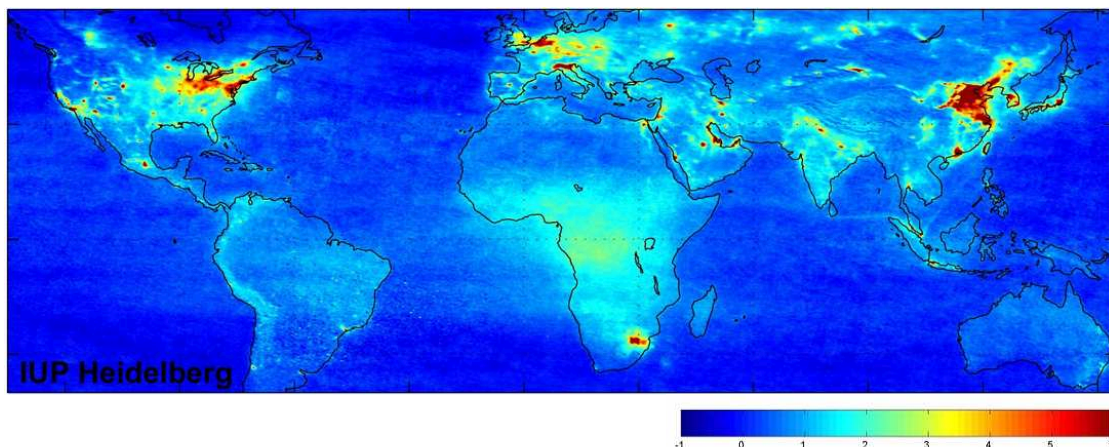


Figure 2.1: Mean repartition of tropospheric  $\text{NO}_2$  in  $10^{15}$  molecules/ $\text{cm}^2$  retrieved by the satellite instrument SCIAMACHY during 18 months. Large cities can easily be recognized by significant larger  $\text{NO}_2$  column densities. Adapted from [Beirle and Wagner, 2004].

with  $j_{\text{NO}_2}$  as photolysis frequency of  $\text{NO}_2$  and  $k_{\text{NO}}$  as rate constant of the reaction of ozone with  $\text{NO}$  (reaction (2.2)). The photolysis frequency  $j_{\text{NO}_2}$  depends on the solar radiation and thus change over the day. Yet, the rate constant  $k_{\text{NO}}$  is temperature dependent and accounts to  $1.8 \times 10^{-14} \text{ cm}^3 \text{ molecule}^{-1} \text{ s}^{-1}$  at 298 K [Atkinson et al., 2004]. Typically, the Leighton ratio in the lower troposphere is between 0.5 and 1 depending on the ozone concentration and the photolysis frequency. With increasing height the ratio increases due to higher photolysis frequency of  $\text{NO}_2$ .

In the photostationary state, on average ozone neither is formed nor destroyed. Net ozone production is observed if  $\text{NO}_x$  is sufficiently abundant to react with peroxy radicals,  $\text{HO}_2$  and  $\text{RO}_2$ . In this case, the following reaction can occur:



whereby the peroxy radicals are generated from oxidation of volatile organic compounds (VOCs), which are abundant in urban areas. To a very small amount ( $\approx 0.1\%$ ), it is assumed that also other products, such as  $\text{HNO}_3$ , can be produced in this reaction.

Thus, ozone is produced by reaction (2.3) and (2.4), but not degraded by  $\text{NO}$  in the same extent. This can lead to the so-called photosmog with large amounts of ozone, oxidized VOCs and organic aerosols. However, peroxy radicals also can react with ozone to molecular oxygen and  $\text{OH}$ . But this only plays a role if the concentrations of  $\text{NO}_x$  are very low:



Thus, it depends on the different abundances of  $\text{NO}_x$  and VOCs if more ozone is produced by reactions (2.3) and (2.4) or destroyed by reaction (2.7). This is illustrated in Figure 2.2 where ozone mixing ratio isopleths are plotted.

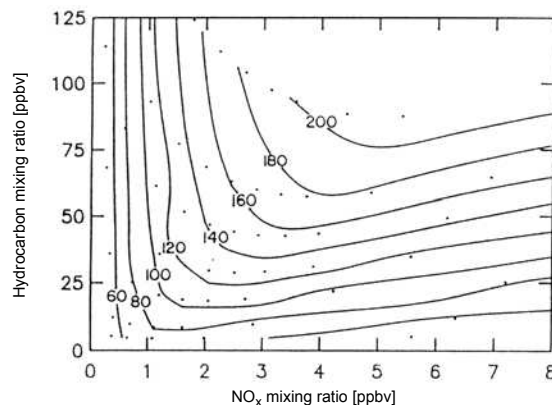


Figure 2.2: Ozone mixing ratio isopleths (in ppb) derived from simulations [Sillman et al., 1990]. In the top left of the diagram the ozone production is limited by the mixing ratio of  $\text{NO}_x$ , in the bottom right by the mixing ratio of VOCs.

The decomposition product of  $\text{NO}_2$  is mostly nitric acid ( $\text{HNO}_3$ ) which is generated by the reaction with OH:



Hence, this reaction is not only a sink for  $\text{NO}_2$ , but also for OH. Thus,  $\text{NO}_2$  contributes to the degradation of the concentration of the hydroxyl radical.

$\text{NO}_2$  can also be further oxidized to  $\text{NO}_3$ :



However during daylight,  $\text{NO}_3$  is degraded by photolysis within several seconds in two ways:



and furthermore, by the rapid reaction with NO:



At day, the photolysis and the NO concentrations prevent a significant level of  $\text{NO}_3$  concentration. Yet by night, when no photolysis occurs so that also NO concentrations are low,  $\text{NO}_3$  can accumulate in the atmosphere.

Additionally,  $\text{NO}_3$  can react with  $\text{NO}_2$  yielding  $\text{N}_2\text{O}_5$ :



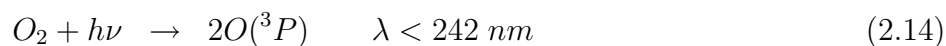
$\text{NO}_3$ ,  $\text{NO}_2$  and  $\text{N}_2\text{O}_5$  are in a thermodynamic equilibrium which depends strongly on temperature [Finlayson-Pitts and Pitts jr., 2000].  $\text{N}_2\text{O}_5$  is degraded mainly by reaction on water (droplet) surfaces [Mentel et al., 1996], and is an important process of  $\text{NO}_x$  on local and global scales.

## 2.2 Atmospheric Ozone Chemistry

The presence of ozone in the atmosphere was first proposed by [Schönbein, 1840]. The existence of ozone in the troposphere, which is the lowermost part of the atmosphere, was discovered by [Houzeau, 1858]. In the late 19th century, spectroscopic studies showed that ozone is present at a higher mixing ratio in the stratosphere than near the ground ([Hartley, 1881]). This presence of ozone in the stratosphere with a maximum concentration at 15-30 km altitude is commonly referred to as "*the ozone layer*" and extremely important for life on earth because it shields plants, animals, and humans from harmful solar UV radiation. The discovery of "*the Antarctic ozone hole*" in the 1980s by [Farman et al., 1985] strongly enhanced the interest in stratospheric ozone chemistry. Although ozone in the troposphere only makes up about 10% of the total ozone column, it plays an important role in tropospheric chemistry because it is a precursor of the hydroxyl radical ( $\text{OH}$ ) and therefore significantly influences the oxidation efficiency of the lower atmosphere (e.g. [Crutzen and Zimmermann, 1991]). Furthermore, elevated levels of tropospheric ozone can be harmful to health.

### 2.2.1 Ozone in the Stratosphere

In 1930, [Chapman, 1930] introduced the first photochemical theory of stratospheric ozone. The ozone production is started by the photolysis of an oxygen molecule by ultraviolet radiation with wavelength  $\lambda < 242 \text{ nm}$  (reaction 2.14). Then ozone is formed via reaction 2.15, M being a collision partner necessary for energy and momentum conservation.



The destruction of ozone in the stratosphere can be explained by photolytic de-

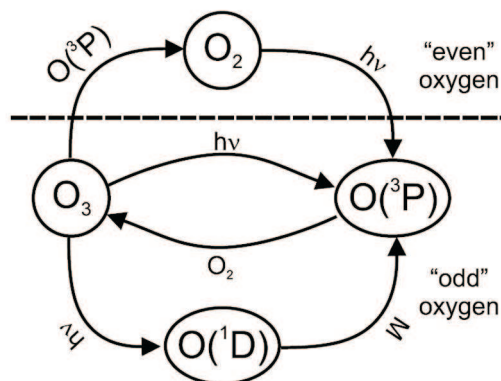


Figure 2.3: The Chapman cycle. Adapted from [Hönninger, 2002].

composition:



Via reactions 2.15, 2.16, and 2.18  $O$  and  $O_3$  are rapidly transformed into one another. The two compounds  $O$  and  $O_3$  are collectively referred to as  $O_x$  or "odd oxygen". Odd oxygen is a chemical family, which is a group of molecules that interconvert at a more rapid rate than either is converted to species not in the family. In the case of stratospheric ozone,  $O_x$  cycles on a fast timescale, much faster than it is converted back to even oxygen. Thus the only process in the Chapman cycle (for reaction scheme see Figure 2.3), in which *odd oxygen* (i.e.  $O$  and  $O_3$ ) is removed, is the reaction of ozone and atomic oxygen producing molecular oxygen (reaction 2.19).

Today we know that the observed ozone concentration profiles cannot be solely explained by the Chapman cycle. These reactions overestimate the amount of ozone in the stratosphere by about a factor of two. Other mechanisms involving additional losses caused by hydrogen oxides, chlorine, and combined chlorine and bromine chemistry have to be included to bring model calculations and measurements into agreement.

For example,  $OH$  radicals formed from stratospheric water vapor influence the ozone budget of the stratosphere via catalytic ozone destruction. Fortunately, the stratosphere is very dry, limiting this loss pathway. This dehydration is due to the fact that the up-mixing of water vapor from the troposphere is strongly constrained by the tropopause, which acts as a cold trap. The oxidation of methane is also an

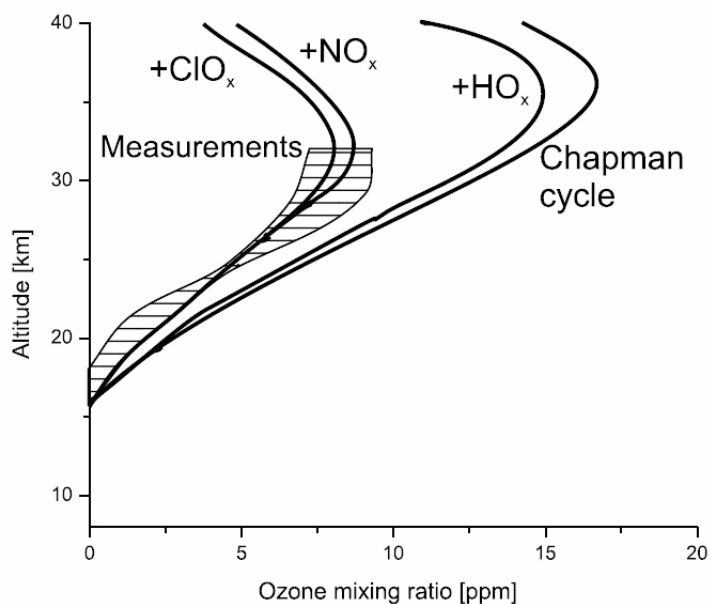
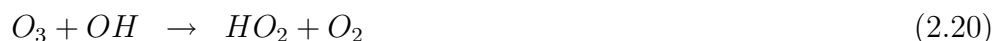


Figure 2.4: Comparison between observed and modelled stratospheric ozone mixing ratio, if only the Chapman cycle is taken into account and by taking  $HO_x$ ,  $NO_x$ , and  $ClO_x$  chemistry into account. The measurements can be explained best, if  $HO_x$ ,  $NO_x$ , and  $ClO_x$  chemistry is included in the models. (Adapted from [Röth, 1994])

important source of stratospheric water vapor. In 1950, [Bates and Nicolet, 1950] presented the following catalytic reaction cycle involving the hydrogen oxide radical:



The hydrogen compounds  $OH$  and  $HO_2$  are grouped as the  $HO_x$  family and this so called " $HO_x$  - cycle" is an efficient sink for ozone because the reactions involved are very fast. In the early 1970s, similar reaction cycles involving  $NO$  and  $NO_2$  ( $NO + NO_2 \equiv NO_x$ ) were discovered. The  $NO_x$  - cycle as proposed by [Crutzen, 1970] and [Johnston, 1971]:



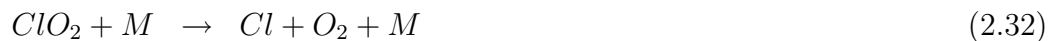


The most important source of stratospheric  $NO$  is biogenic  $N_2O$ , which is released from soils or the oceans. The lifetime of  $N_2O$  is long enough for it to be transported into the stratosphere, where the reaction with atomic oxygen produces nitric oxide.

Some years after the discovery of the  $NO_x$  - cycle, another important mechanism of catalytic ozone destruction was found. Starting from the question if chlorofluorocarbons (CFCs) can affect the ozone layer, [Molina and Rowland, 1974] discovered the chlorine cycle:



A source of chlorine is the photolysis of biogenous  $CClH_3$  and anthropogenic CFCs in the stratosphere by ultraviolet radiation. Both substances are released in the troposphere and transported into the stratosphere because their lifetime is longer than typical troposphere to stratosphere transport times. Finally, also a combined bromine-chlorine cycle accounts for the abundance of ozone in the upper atmosphere ([McElroy et al., 1986]):

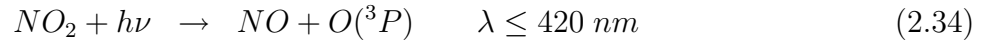


The consideration of all cycles leads to an ozone budget in the stratosphere that matches the measurements (see Figure 2.4 adapted from [Röth, 1994]).

### 2.2.2 Ozone in the Troposphere

In the troposphere, ozone cannot be produced by the photolysis of molecular oxygen (see equation 2.14) because the high energy UV radiation needed for this process is almost completely absorbed in the higher atmosphere by  $O_2$  and  $O_3$ . So except for areas with urban pollution it was commonly thought that ozone in the troposphere originates from the stratosphere and is mixed downwards through the

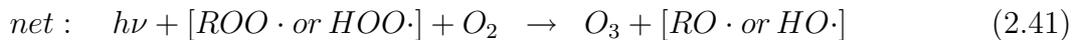
tropopause with the earth's surface being the dominant sink. This opinion changed when [Fishman and Crutzen, 1978] compared the known sink and source mechanisms for tropospheric ozone in the northern and southern hemispheres and concluded that there must be a significant tropospheric source of ozone. It turned out that only about 15% of the tropospheric ozone is mixed downwards through the tropopause and that the main tropospheric source of ozone is the anthropogenic production via  $NO_x$  chemistry.  $NO_x$  and ozone are related in the following cycle:



The sum of this cycle simply absorbs UV and deposits heat, leaving ozone unchanged. However, if other reactions can compete with the odd-oxygen production (reaction 2.34) or ozone destruction (reaction 2.36), the cycle becomes imbalanced and may produce ozone. Oxidation products of  $CO$ , methane, and higher hydrocarbons include peroxy radicals and hydro peroxy radicals. These compounds have the general form  $ROO\cdot$ , where R is an organic molecule or  $HOO\cdot$  in the case of hydro peroxy. These peroxy radicals compete with reaction 2.36:



When this reaction substitutes for reaction 2.36, the net reaction produces ozone:



Thus we see that tropospheric ozone is produced by reactions of  $CO$ , methane, and higher hydrocarbons catalyzed by  $NO_x$  and sunlight. In remote areas (e.g. the arctic boundary layer) the  $NO_x$  levels in general are low. For methane, the net reaction cycle can be summarized as follows:



where typically  $y=2.5$  ozone molecules are formed per methane molecule ([Hönninger, 2002]).

The picture of ozone chemistry in the troposphere however is not complete. In recent years it has been discovered that the ozone budget of the lower atmosphere in polar regions is strongly influenced by halogen chemistry ([Barrie et al., 1988], [Tuckermann et al., 1997], [Hönninger et al., 2004]). The following chapter on halogen chemistry presents a detailed discussion of these processes.

## 2.3 Tropospheric Halogen Chemistry

The 5 halogens fluorine, chlorine, bromine, iodine and astatine are elements with seven electrons in the valence shell. One more electron is sufficient for them to reach the very stable inert gas configuration and that is the reason why they are very reactive chemicals. Halogen chemistry was first found to be important in the stratosphere when in 1974 [Molina and Rowland, 1974] discovered that anthropogenically emitted halogen compounds cause ozone depletion in the stratosphere. The discovery of the stratospheric ozone hole over Antarctica during springtime by [Farman et al., 1985] further enhanced the interest on atmospheric halogen chemistry because it turned out that heterogeneous reactions on polar stratospheric clouds (PSC) leading to chlorine activation play an important role ([Solomon et al., 1986]).

The first evidence for important tropospheric reactions involving halogens arose, when [Barrie et al., 1988] related sudden reduction of tropospheric ozone levels in the polar planetary boundary layer during polar sunrise to elevated concentrations of filterable bromine. Further field campaigns, for instance at Alert, Canada ([Hausmann and Platt, 1994b]), Spitsbergen ([Tuckermann et al., 1997]) and the Canadian Hudson Bay ([Hönninger et al., 2004]) confirmed that polar ozone depletion events (ODEs) are a common phenomenon during Arctic springtime and are caused by halogen chemistry. Today we know that halogens in the lower atmosphere do not only occur in polar regions. Measurements of halogens have been reported e.g. in volcanic plumes ([Bobrowski et al., 2003]), at salt lakes ([Hönninger et al., 2004]), the dead sea basin ([Hebestreit et al., 1999]), and in the marine boundary layer at mid latitudes. The role of halogen compounds in the earth's atmosphere is still object of research and not completely understood.

### 2.3.1 The Mechanism of Ozone Depletion

The ozone destruction during polar ozone depletion events is caused by reactive halogens (e.g. *Br*, *Cl*). The basic reactions that destroy ozone are:



where the lifetime of a halogen atom against the reaction with ozone is very short in the troposphere ( $\tau = 0.08s$  for  $Cl$  and  $\tau = 0.8s$  for  $Br$  at  $\approx 40$  ppb<sup>2</sup> of  $O_3$  according to [Hönninger, 2002]). One halogen molecule can destroy a large number of  $O_3$  molecules, since  $BrO$  and  $ClO$  are converted back to reactive  $Br$  and reactive  $Cl$  in three main reaction cycles which are discussed below. These reactions are significantly slower than reactions 2.43 and 2.44 and thus are the rate limiting steps in the ozone destruction cycles.

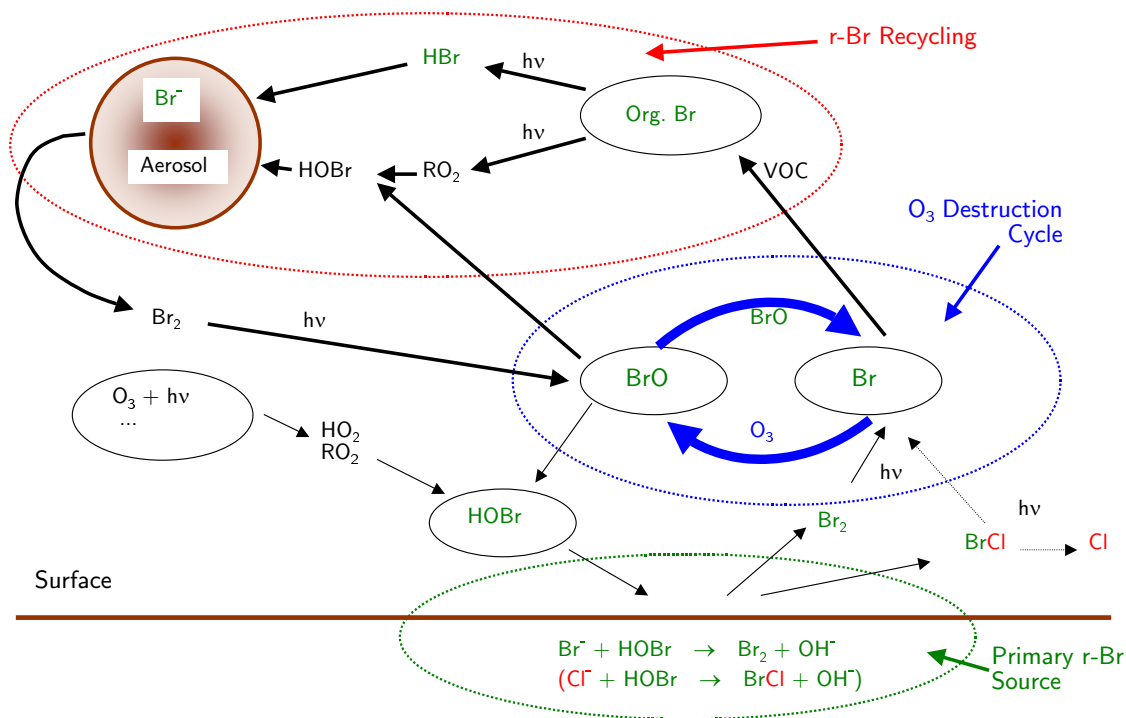


Figure 2.5: An overview of tropospheric bromine chemistry during polar sunrise including the bromine explosion and excluding chlorine chemistry (Adapted from [Hönninger, 2002]).

### 2.3.2 Sources and Reaction Cycles of Reactive Halogen Species

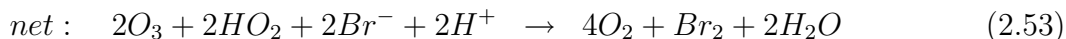
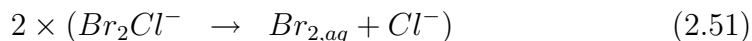
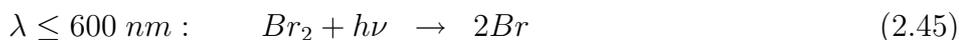
Under conditions occurring during Arctic springtime, there are two possible sources of Reactive Halogen Species (RHS) as discussed by e.g. [Barrie et al., 1988], [Tuckermann et al., 1997] and [von Glasow et al., 2004]:

The liberation from sea salt in the aerosol or on the surface of the Arctic ocean ice.

<sup>2</sup>ppb = parts per billion

The degradation of organohalogen compounds (e.g.  $CH_3Br$ ,  $CHBr_3$ ) originating from anthropogenic or natural emissions.

The photolysis lifetime of the most important organo-halogen compounds under conditions typical for springtime in polar regions is quite long. Thus this source is unlikely to be important in the Arctic. However, in recent years strong indications arose that reactive halogen species in the gas phase (e.g.  $Br_2$  or  $BrCl$ ) are released into the atmosphere by autocatalytic liberation of reactive bromine from sea salt reservoirs. The following autocatalytic reaction cycle converts  $Br^-$  to  $Br_2$  ([Fan and Jacob, 1992], [Vogt et al., 1996]):



where "aq" denotes the liquid phase. Reaction 2.50 is very fast. Thus the concentration of  $BrCl$  in the liquid phase remains small and only little  $BrCl$  is directly released into the gas phase. If  $BrCl$  is released into the gas phase, it subsequently photolyzes forming one  $Cl$  and one  $Br$  atom. In this case, only one reactive bromine atom is released via the uptake of one  $HOBr$  molecule. However, a second reactive halogen atom in form of  $Cl$  is produced. This  $Cl$  atom can either destroy ozone and produce  $ClO$  or react with hydrocarbons forming  $HCl$ . As mentioned before, the lifetime of bromine against hydrocarbon loss is more than two orders of magnitude longer than the respective lifetime of chlorine. This difference emphasizes the dominant role of bromine chemistry in ozone depletion.

An overview of the reactions presented above is given in Figure 2.5. For every  $Br$  atom taken up by the sea salt surface in the form of  $HOBr$ , two halogen atoms are released into the gas phase in the form of  $BrCl$  or  $Br_2$ . If the amount of  $Br^-$  that is available is sufficient and the gas phase bromine loss is low enough, these cycles lead to an exponential increase of the released bromine and therefore are referred to as "the bromine explosion" ([Platt et al., 1997a]). In reaction 2.47 one  $HO_2$  molecule is destroyed converting  $BrO$  to  $HOBr$ , thus besides the presence

of  $O_3$  the production of  $HO_2$  is important for the autocatalytic cycles to proceed. Finally, acidity and a preferred release of  $Br_2$  compared to the release of  $BrCl$  as for instance reported by [Fickert et al., 1999] are prerequisites for the bromine explosion. To determine whether sea salt aerosol or the sea ice surface is the dominant source for halogen activation, [Lehrer et al., 2004] presented model calculations. They concluded that sea salt aerosol is a minor source compared the source strength of the sea ice surface and that halogen activation from the sea ice surface alone leads to an exponential increase of RHS. Furthermore they stated that in order to keep enough bromine in the active reservoir, halogen recycling on aerosol surfaces is essential (They calculated that a bromine atom is recycled about 30 times before participating in the primary activation process again).



# 3 Differential Optical Absorption Spectroscopy

## 3.1 DOAS Overview

The Differential Optical Absorption Spectroscopy (DOAS) is a very sensitive and widely used measurement technique to detect trace gases in the atmosphere [Perner and Platt, 1979; Platt, 1994]. It was introduced by Platt et al. [1979] measuring atmospheric trace gases with an artificial light source. Since then, DOAS has been applied to measure concentrations of many trace gas for the first time, e.g. OH by Perner et al. [1976], HONO by Perner and Platt [1979] and Platt and Perner [1980], NO<sub>3</sub> by Platt et al. [1980], BrO in the stratosphere by Sanders et al. [1988] and in the troposphere by Hausmann and Platt [1994a], IO by Alicke et al. [1999], and CHOCHO by Volkamer et al. [2005]. A variety of other trace gases absorbing in the UV and the visible wavelength region can be detected as well [Platt, 1994], e.g. NO<sub>2</sub>, ClO, O<sub>3</sub>, SO<sub>2</sub>, CS<sub>2</sub>, HCHO, OClO, H<sub>2</sub>O, and NH<sub>3</sub>. Most recently, CH<sub>4</sub> could be measured in the near IR wavelength region from satellite [Frankenberg et al., 2005] and from a ground-based device [Woyde, 2007].

DOAS is based on the absorption of light traversing a gas volume and being attenuated characteristically for each trace gas in this volume. From the spectral position of these absorbing lines and their strengths, the trace gases can be identified and quantified. Because DOAS is capable of measuring the composition of ambient air in the open atmosphere without interaction caused by the measurement process, it can also detect highly reactive species, such as the free radicals OH, NO<sub>3</sub>, halogen oxides and NO<sub>2</sub>. Furthermore, DOAS is able to measure several trace gases simultaneously, which reduces measurement time and allows to analyse the different chemical components in the observed air mass.

Generally, DOAS can be performed actively, using artificial light sources, as well as passively with natural, extraterrestrial light sources, which is most commonly the sun owing to its high intensity in comparison, for instance, to the moon. Passive DOAS can be divided into scattered light measurements pointing somewhere to the sky and direct light measurements, which point directly onto the sun or the moon. Active setups often use high pressure Xe-arc lamps, but most recently also light emitting diodes (LEDs) were introduced [Kern et al., 2006; Sihler, 2007], which need far less power, have a much longer life time, are easier to handle and have less spectral structures than the traditional Xe-arc lamps; however, their wavelength

range is much more limited. The following list gives an overview on the most common DOAS applications:

**Multi-Axis(MAX)- and Zenith-Sky-DOAS** measure scattered sunlight mostly from the ground and provide information on the concentration of trace gases in the atmosphere integrated along the light path. Zenith-Sky-DOAS instruments only point to the zenith and are suitable to investigate stratospheric absorbers. In contrast, MAX-DOAS measurements, on which this work is based, vary the viewing direction, are sensitive for trace gases in the troposphere and can deliver information on the altitude profile of trace gases (see chapter 3.6). MAX-DOAS devices are easy to maintain and also suit to conduct long-term measurements.

Since recently, these devices have been installed on different platforms, such as airplanes (AMAX-DOAS), vessels (SMAX-DOAS) and cars (Auto-MAX-DOAS). This gives the possibility to observe atmospheric gases along the respective tracks.

**Long path DOAS** uses artificial light sources. Typically, light is sent out by a Newton telescope and is reflected by a retro reflector array usually in a distance of several kilometers, before it is received again. Thus, the measurement is constrained to the lowermost atmosphere. But in contrast to scattered light instruments, the derivation of concentrations and mixing ratios is easy and measurements by night are possible. It is adverse that the operation of long path DOAS devices requires a relatively large effort. By using several long path instruments together, tomography measurements can provide information on spatial distributions of trace gases. Multiple reflection cells (White cells) convolve the light path many times and, therefore, can measure trace gases of a small air mass parcel. The very young method Cavity Enhanced Absorption Spectroscopy uses this principle.

**Satellite borne DOAS** enables to receive a global picture of the spatial distribution of atmospheric trace gases. Instruments such as Global Ozone Monitoring Instrument (GOME) onboard the satellite ERS-2, the SCanning Imaging Absorbtion SpectroMeter for Atmospheric CHartographY (SCIAMACHY) onboard Envisat, the Ozone Monitoring Instrument (OMI) onboard NASA/EOS AURA and finally GOME2 onboard METOP measure reflected and in the Earth's atmosphere scattered sunlight (Nadir mode) and direct sunlight traversed the Earth's atmosphere (Limb mode), respectively.

**Imaging DOAS** enables to retrieve two-dimensional images of the distribution of trace gases. It has been applied to exhaust-gas plumes of power plants and volcanic plumes.

**Balloon borne DOAS** measurements use either scattered or direct sunlight which the latter requires a good alignment to the sun even in atmospheric turbulence. They are able to provide altitude profiles of atmospheric trace gases up to the stratosphere.

## 3.2 The Lambert-Beer Law

The Lambert-Beer law (see equation (3.1)), on which absorption spectroscopy is based, describes how light is absorbed by matter. Three parameters determine the attenuation of light: the concentration  $c$  of the the absorbing material, its cross section  $\sigma$  (i.e. the probability of absorption) and the length  $L$  of the light path through the absorbing material:

$$I(\lambda, L) = I_0(\lambda) \cdot e^{-c \cdot \sigma \cdot L} \quad (3.1)$$

In this work, the light source consists of the sun and the matter of the Earth s atmosphere. The sunlight traversing the atmosphere is both absorbed by the different trace gases  $i$  in the atmosphere and scattered. Scattering processes can be the Mie and Rayleigh scattering, which are described in detail in section 4.2. A part of the incident light reaches finally the Earth s surface with the intensity  $I(\lambda, L)$ :

$$I(\lambda, L) = I_0(\lambda) \cdot e^{-\int_0^L [\sum_j \sigma_j(\lambda, T, p) \cdot c_j(l) + \epsilon_M(\lambda, l) + \epsilon_R(\lambda, l)] dl} \quad (3.2)$$

where  $I(\lambda, L)$  and  $I_0(\lambda)$  denote the wavelength dependent intensities after and before, respectively, passing the atmosphere;  $I(\lambda, L)$  is also dependent on the length of the light path assuming that more absorbing and scattering processes take place when the light path through the atmosphere is longer.  $\sigma_j(\lambda, T, p)$  are the cross sections of the different trace gases, which are dependent on the wavelength  $\lambda$ , the temperature  $T$  and to a minor degree the pressure  $p$ .  $c_j(l)$  are the concentrations of the different trace gases  $j$  along the light path.  $\epsilon_M(\lambda, l)$  and  $\epsilon_R(\lambda, l)$  stand for the extinction coefficients of the Mie and Rayleigh Scattering, respectively, which both are also wavelength dependent.

The logarithm of the ratio of the initial and attenuated intensity is defined as the optical density  $\tau(\lambda)$ :

$$\tau(\lambda) := \ln \left( \frac{I_0(\lambda)}{I(\lambda, L)} \right) \quad (3.3)$$

However, the calculation of  $\tau$  needs the knowledge of  $I(\lambda, L)$  and  $I_0(\lambda)$ . While  $I(\lambda, L)$  can be determined easily at the Earth s surface, in most cases,  $I_0(\lambda)$  is not known and would have to be measured simultaneously from space. Furthermore, the scattering processes metioned above are overlaid to the absorption structure of

the trace gases and would disturb the retrieval of the absorption structures. Both restrictions can be overcome by separating the absorption cross section  $\sigma(\lambda, T, p)$  in a narrow and a broad band part,  $\sigma'(\lambda, T, p)$  and  $\sigma^B(\lambda, T, p)$ , respectively:

$$\sigma_{abs}(\lambda, T, p) := \sigma'(\lambda, T, p) + \sigma^B(\lambda, T, p) \quad (3.4)$$

Figure 3.1 illustrates the extraction of the narrow band (differential) part from the absolute cross section of ozone. With equation (3.4) the Lambert-Beer law for  $n$  trace gases can now be written as:

$$\begin{aligned} I(\lambda, L) &= I_0(\lambda) \cdot e^{-\int_0^L [\sum_{j=0}^n (\sigma'_j(\lambda, T, p) + \sigma_j^B(\lambda, T, p)) \cdot c_j(l) + \epsilon_M(\lambda, l) + \epsilon_R(\lambda, l)] dl} \\ &= I'_0(\lambda) \cdot e^{-\int_0^L [\sum_{j=0}^n (\sigma'_j(\lambda, T, p)) \cdot c_j(l)] dl} \end{aligned} \quad (3.5)$$

where  $I'_0(\lambda)$  contains the initial intensity as well as the broad band absorption part of the trace gases and the Mie and Rayleigh scattering, which are both broad banded, too.  $I'_0(\lambda)$  can be computed from the measured spectrum  $I(\lambda, L)$  by applying a low pass filter. Mathematically, the differential absorption cross sections  $\sigma'_j(\lambda, T, p)$  can be yielded by applying a high pass filter to the absorption cross sections  $\sigma_j(\lambda, T, p)$ .

Similarly, from (3.3) and (3.5) follows the differential optical density  $\tau'(\lambda)$ , which is sketched in Figure 3.2:

$$\tau'(\lambda) = \ln \left( \frac{I'_0(\lambda)}{I(\lambda, L)} \right) \quad (3.6)$$

Since DOAS uses only differential cross sections, no absolute calibration of  $I_0(\lambda)$  is necessary. The trace gas can be measured by merely observing differential values.

The primary quantity of a DOAS measurement is the slant column density (SCD)  $S$  which is the integrated concentration along the light path and is given in the unit molecules per  $\text{cm}^2$ :

$$S = \int_0^L c \, dl \quad (3.7)$$

Comparing equation (3.6) with equation (3.7) and taking into account equation (3.3), it follows for the slant column density:

$$S = \frac{\tau'(\lambda)}{\sigma'(\lambda, T, p)} \quad (3.8)$$

Since for scattered light measurements the DOAS analysis is applied to the ratio of the measured spectrum  $I(\lambda)$  and the reference spectrum  $I_0(\lambda)$  which also contains a certain amount of trace gas absorption, the actual quantity of the DOAS measurement is the differential slant column density (dSCD), i.e. the difference between the actual SCD and the SCD of the reference spectrum.

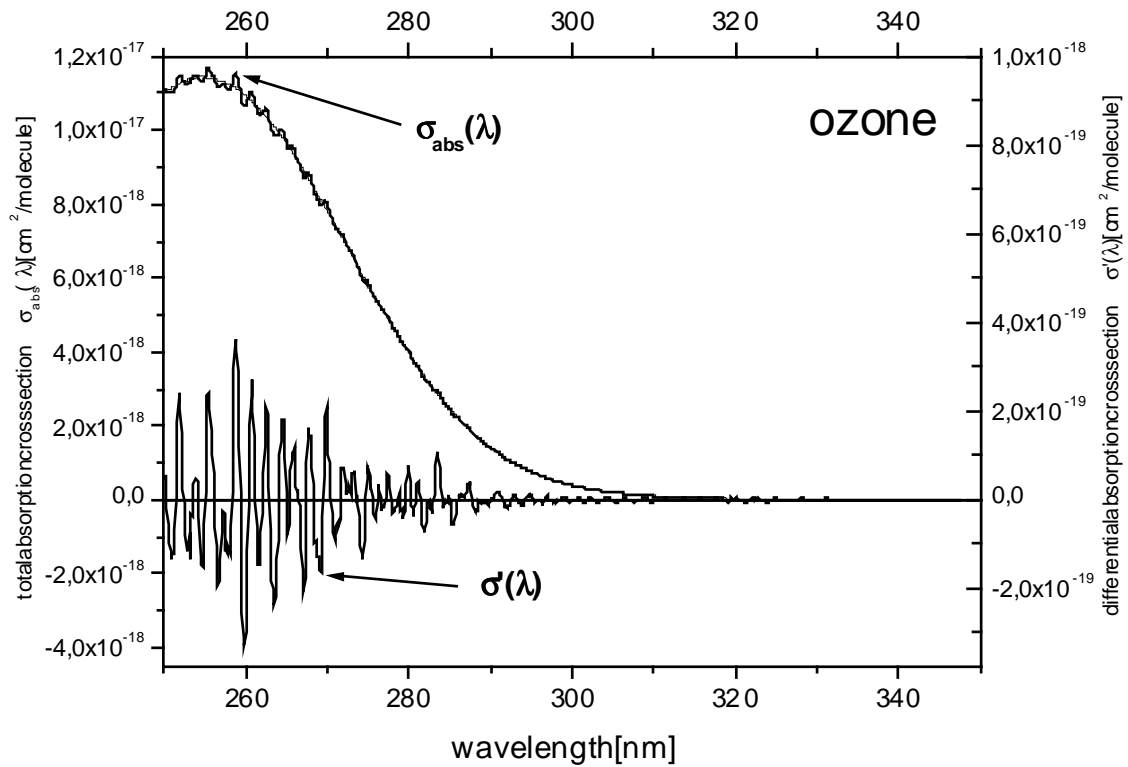


Figure 3.1: Absolute cross section  $\sigma_{abs}(\lambda)$  and narrow band (differential) cross section  $\sigma'(\lambda)$  of ozone as instance.  $\sigma'(\lambda)$  can be extracted by subtracting the broad band part of the cross section from  $\sigma_{abs}(\lambda)$  which is mathematically the application of a high pass filter.

### 3.3 The Measurement Procedure

In Figure 3.3 the measurement procedure of a simplified DOAS setup is illustrated. Light with the initial intensity  $I_0(\lambda)$  traverses the observing air mass (atmosphere). Along the light path  $L$ , it is affected by extinction owing to absorption as well as scattering processes by molecules and aerosol particles before  $I(\lambda, L)$  is collected by a telescope (see Figure 3.3a). In this example, only one absorber, namely formaldehyde, is considered. The telescope focusses the light to an entrance slit of a grating spectrograph with a detector which records the spectrum of the dispersed light. Owing to the limited resolution of the spectrograph (determined by the entrance slit and the grating properties), the spectral resolution of spectrum  $I(\lambda, L)$  is degraded (see Figure 3.3b). The mathematical description of this process is a convolution with the instrument function  $H$  yielding  $I^*(\lambda, L)$  as it is projected by the spectrograph on the detector:

$$I^*(\lambda, L) = H * I(\lambda, L) = \int I(\lambda') \cdot H(\lambda - \lambda') d\lambda' \quad (3.9)$$

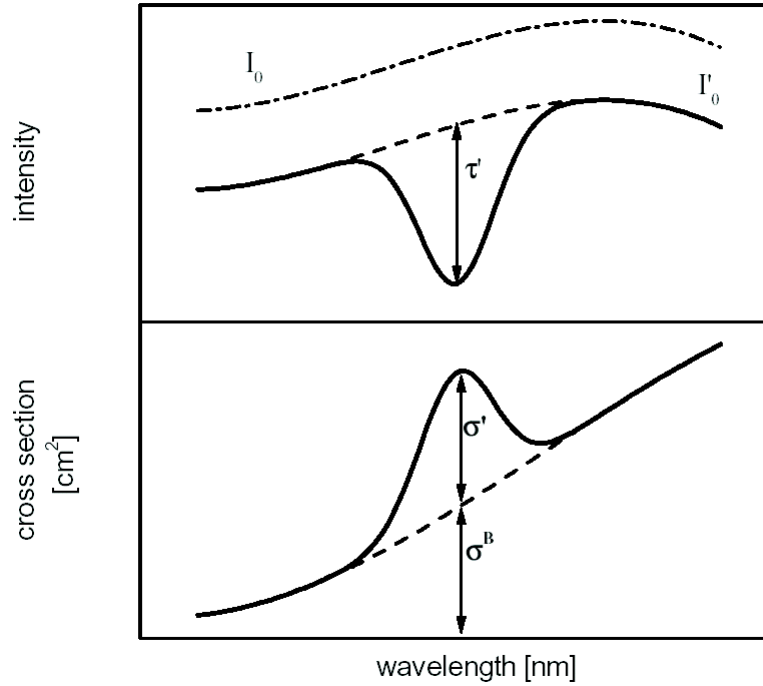


Figure 3.2: Above: The differential optical density  $\tau'$  which is derived from  $I'_0$ . Below: Dispartment of the absolute cross section  $\sigma_{abs}$  into a broad band part  $\sigma^B$  and a narrow band part  $\sigma'$ .

By the multi channel detector the wavelength range is mapped into  $n$  discrete pixels, numbered  $i$ , each integrating the light in a small wavelength range between  $\lambda_i$  and  $\lambda_{i+1}$  (see Figure 3.3c):

$$I'(i) = \int_{\lambda_i}^{\lambda_{i+1}} I^*(\lambda', L) d\lambda' \quad (3.10)$$

These channels are read out and the spectra are stored and logarithmized yielding  $J(i)$  by a connected PC. The correlation between wavelengths and channels of the spectrograph can usually be approximated by a polynomial:

$$\lambda(i) = \sum_{k=0}^q \gamma_k \cdot i^k \quad (3.11)$$

where the mapping of the pixel  $i$  to the wavelength  $\lambda(i)$  is given by  $\gamma_k$  and is referred to as wavelength-pixel-mapping or wavelength calibration.  $\gamma_0$  denotes a spectral shift of the spectrum while  $\gamma_1$  stands for a spectral squeeze or stretch of the whole spectrum. A parameter  $\gamma_k$  with  $k \geq 2$  indicates a distortion of the spectrum

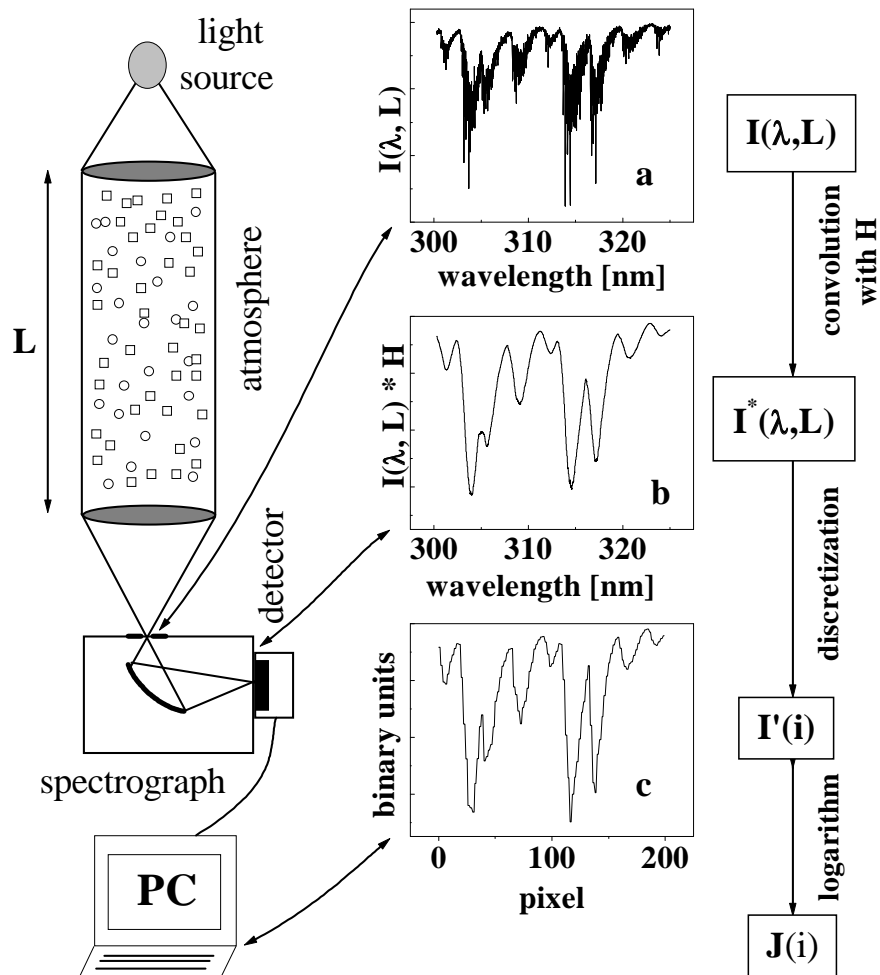


Figure 3.3: *The components of a simplified DOAS setup. Light traverses an air mass and is attenuated by an absorber, characteristically for the trace gas in the atmosphere (in this example formaldehyde). (a) shows the respective spectrum with the absorption structure of formaldehyde. In (b) the light was convolved by the spectrograph and (c) shows the mapping by the detector. Afterwards the spectrum consisting of discrete pixels is stored in a connected PC [Stutz and Platt, 1996].*

and an unequal spectral pixel width. In contrast, a linear wavelength-pixel-mapping yields a constant spectral pixel width. The parameter vector  $(\gamma_k)$  changes easily if the measurement conditions are not stable. For instance, a varying temperature of the spectrograph usually leads to a shift in the wavelength calibration. This has to be either avoided or later corrected accordingly.

After having derived the suitable wavelength calibration it has also to be applied to the differential trace gas cross sections  $\sigma'_j(\lambda, T, p)$  so that the wavelength-pixel-mapping of the measured spectrum and the cross sections are the same. Furthermore,  $\sigma'_j(\lambda, T, p)$  have to be converted to the same resolution as the spectrograph. If the cross sections are measured with the same spectrograph, both restrictions are already inherently fulfilled. However, often cross sections are used which are measured in the laboratory with a different measurement device and which have a much higher resolution. Thus, subsequently they have to be convolved with the instrument function  $H$ :

$$\sigma^*(\lambda, T, p) = H * \sigma(\lambda, T, p) = \int \sigma(\lambda', T, p) \cdot H(\lambda - \lambda') d\lambda' \quad (3.12)$$

In Figure 3.4 the high resolution cross sections which are used in this work are shown between 290 and 460 nm. In the spectral analysis, which is a numerical process and which is described in the following section, up to ten trace gases can be identified simultaneously in one single spectrum [Platt, 1994].

## 3.4 The Spectral Analysis

### 3.4.1 The Analysis Procedure

The aim of the spectral analysis is the retrieval of the slant column densities of trace gases in the observed air mass. For that, the Lambert-Beer Law from equation (3.5) is taken and logarithmized:

$$\ln(I(\lambda, L)) = \ln(I_0(\lambda)) - \int_0^L \left( \sum_{j=0}^n (\sigma'_j(\lambda, T, p) + \sigma_j^B(\lambda, T, p)) \cdot c_j(l) + \epsilon_M(\lambda, l) + \epsilon_R(\lambda, l) \right) dl \quad (3.13)$$

Mathematically, the separation of the narrow and broad band part can be achieved by merging all broad banded spectral components, namely the broad band part of the trace gas absorption cross sections  $\sigma_j^B(\lambda, T, p)$ , the Mie scattering  $\epsilon_M(\lambda, l)$  and the Rayleigh scattering  $\epsilon_R(\lambda, l)$ , to one polynomial [Platt et al., 1979]. Consequently, the differential trace gas cross sections  $\sigma'_j(\lambda, T, p)$  remain:

$$\ln(I(\lambda, L)) = \ln(I_0(\lambda)) - \int_0^L \left( \sum_{j=0}^n \sigma'_j(\lambda, T, p) \cdot c_j(l) dl + \sum_{m=0}^p \alpha_m \cdot \lambda^m \right) dl \quad (3.14)$$

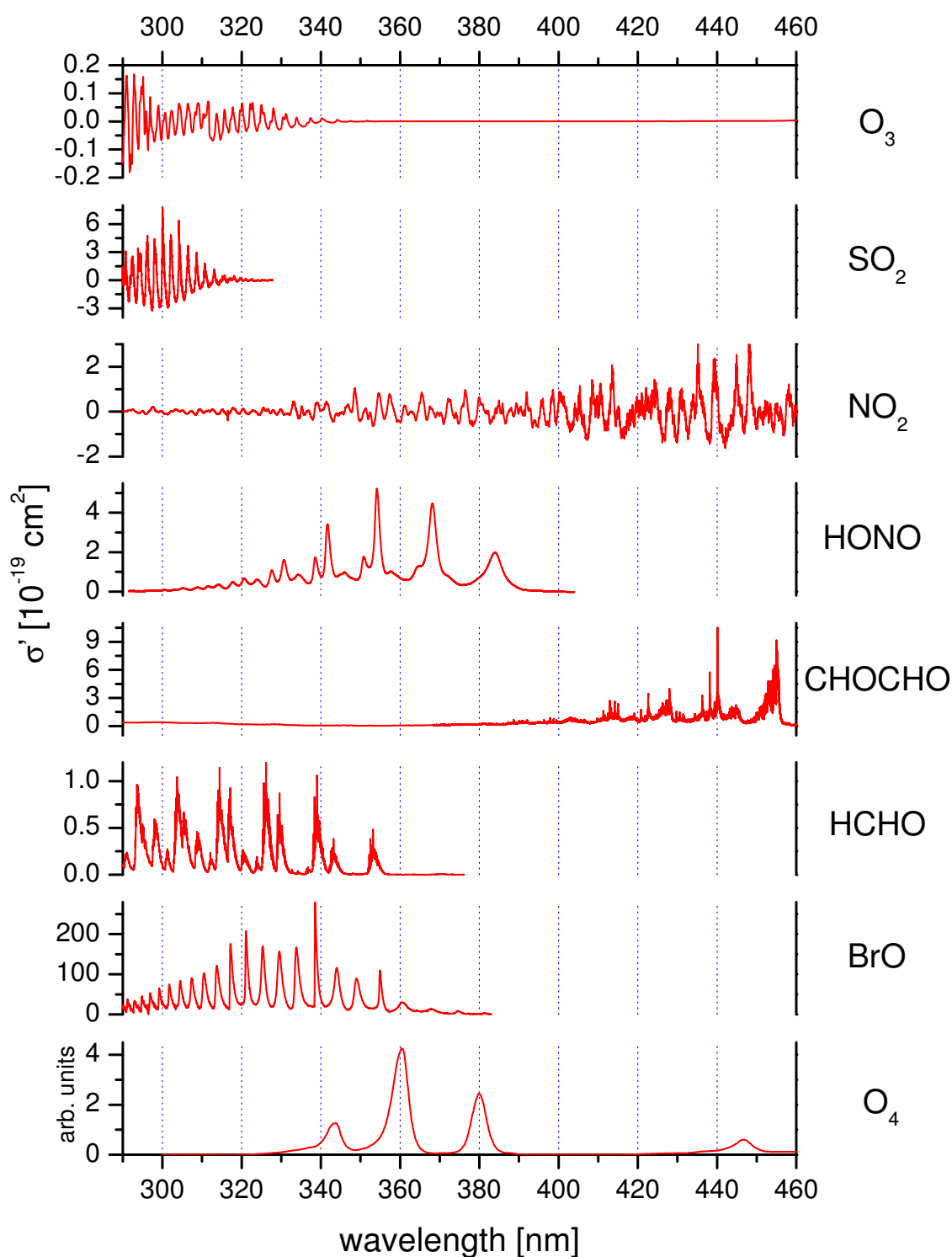


Figure 3.4: High resolution cross sections from literature in the wavelength range from 290 to 460 nm. From top to down:  $O_3$  [Bogumil et al., 2003],  $SO_2$  [Vandaele et al., 1994],  $NO_2$  [Vandaele et al., 1998],  $HONO$  [Stutz et al., 2000],  $CHOCHO$  [Volkamer et al., 2005],  $HCHO$  [Meller and Moortgat, 2000] as well as  $BrO$  [Wilmouth et al., 1999] in  $10^{-19} \text{ cm}^2$  and  $O_4$  [Greenblatt et al., 1990] in arbitrary units.

with the polynomial  $\sum_{m=0}^p \alpha_m \cdot \lambda^m$  of the degree  $p$ , which has to be chosen accordingly to the broad banded shape. A higher polynomial degree than required could affect the retrieval of the differential structures.

Since the differential trace gas cross sections  $\sigma'_j(\lambda, T, p)$  and the polynomial do not depend on the light path through the observed air mass they can be excluded from the integral (regarding  $T$  and  $p$  to be constant in the investigated air mass):

$$\ln(I(\lambda, L)) = \ln(I_0(\lambda)) - \left( \sum_{j=0}^n \sigma'_j(\lambda, T, p) \cdot \int_0^L c_j(l) dl + \sum_{m=0}^p \alpha_m \cdot \lambda^m \right) \quad (3.15)$$

With equation (3.7), it can also be written as:

$$\ln(I(\lambda, L)) = \ln(I_0(\lambda)) - \left( \sum_{j=0}^n \sigma'_j(\lambda, T, p) \cdot S_j + \sum_{m=0}^p \alpha_m \cdot \lambda^m \right) \quad (3.16)$$

The solution of equation (3.16) delivers the values for  $S_j$  and can be retrieved by a least squares fit [Gomer et al., 1993; Stutz and Platt, 1996]. Thereby, a combination of a linear least squares fit [Albritton et al., 1976; Bevington, 1969] and the non-linear Levenberg-Marquardt method [Levenberg, 1944; Marquardt, 1963] is applied. The latter is an iterative procedure starting with the linear solution of the least squares fit.

The linear least squares fit procedure simulates numerically  $\ln(I(\lambda, L))$  as exact as possible by means of the slant column densities  $S_j$  and the polynomial so that the difference  $\chi^2$  between  $\ln(I(\lambda, L))$  and the fit (i.e. the right side of equation (3.16)) becomes minimal. Thereby,  $\sigma'_j(\lambda, T, p)$ ,  $n$  and  $p$  are fixed parameters:

$$\chi^2 := \int_{\lambda_1}^{\lambda_2} \left( \ln(I(\lambda, L)) - \ln(I_0(\lambda)) + \sum_{j=0}^n \sigma'_j(\lambda, T, p) \cdot S_j + \sum_{m=0}^p \alpha_m \cdot \lambda^m \right)^2 d\lambda \stackrel{!}{\rightarrow} \min \quad (3.17)$$

where  $\lambda_1$  and  $\lambda_2$  determine the limits of the wavelength range in which the analysis should be performed. The wavelength range should suitably include strong differential absorption features of the trace gas of interest. Since the output of the measurement is not a continuous spectrum, but discrete pixel the integral over the wavelength can be replaced by a sum:

$$\chi^2 := \sum_{k=k_{\lambda_1}}^{k_{\lambda_2}} \left( \ln(I(k, L)) - \ln(I_0(k)) + \sum_{j=0}^n \sigma'_j(k, T, p) \cdot S_j + \sum_{m=0}^p \alpha_m \cdot k^m \right)^2 \stackrel{!}{\rightarrow} \min \quad (3.18)$$

with  $k_{\lambda_1}$  and  $k_{\lambda_2}$  as the pixel numbers of the start and the end wavelength, respectively, of the investigated wavelength range. For condition (3.18), the analytical solution can be derived by performing the partial derivations of  $\chi^2$  with respect to the free parameters  $S_j$  and  $\alpha_m$ .

In practice, this condition can not be totally fulfilled in that way that the minimum becomes zero. This is due to inevitable noise during the measurement procedure. The most important noise source is that, even with constant intensity of the light source, the number of detected photons varies around a mean value. Beside this photon noise, also instrument noise occurs. That means that in the electronics statistical variations are superimposed to the measured signal. Thus, a residual  $R$  remains which is the difference between  $\ln(I(k, L))$  and the fitted logarithm of the intensity:

$$R_k = \ln(I(k, L)) - \ln(I_0(k)) + \sum_{j=0}^n \sigma'_j(k, T, p) \cdot S_j + \sum_{m=0}^p \alpha_m \cdot k^m \quad (3.19)$$

The root mean square (RMS)  $\chi$  of the residual is a measure for the quality of a trace gas retrieval. The lower the RMS the better the spectral analysis can be considered. An ideal spectral analysis leads to an unstructured and only noisy residual. However, a misalignment of the wavelength calibration, an inclusion of inaccurate cross sections or not considered absorbers could easily cause systematic structures in the residual.

The described linear fitting procedure inherently cannot include non linear effects, e.g. a change in the wavelength calibration. The spectral analysis is very sensitive on changes in the wavelength calibration, especially for absorbers with small optical densities. Even wavelength shifts of only a few percent of a pixel can lead to strong systematic structures in the residual. Allowing a shift and a squeeze/stretch, respectively, of a spectrum can compensate for the changing of the wavelength calibration of a spectrum. This can be done by adding a polynomial to the original wavelength grid with  $\lambda_k$  creating a new wavelength grid with  $\lambda'_k$ :

$$I(\lambda_k) \rightarrow I(\lambda'_k) \quad \text{with} \quad \lambda'_k = \lambda_k + s_0 + s_1(\lambda_k - \lambda_c) + s_2(\lambda_k - \lambda_c)^2 \quad (3.20)$$

where  $\lambda_c$  denotes the centre wavelength of the investigating wavelength range (see equation (3.18)),  $s_0$  the shift parameter and  $s_1$  and  $s_2$  the squeeze/stretch parameters.

Furthermore, an artificial signal can be overlaid to the spectra s intensities. This can be due to stray light in the housing of the spectrograph, a nonlinearity between the signal of the detector and the light intensity or unstable detector electronics. Normally these additional signals vary only slowly with wavelength so that an polynomial which is added to the intensity is able to compensate for them:

$$I(\lambda) \rightarrow I(\lambda') = I(\lambda) - P_{add} \quad (3.21)$$

$P_{add}$  is referred to as additive or prelogarithmic polynomial and is not related to the polynomial introduced in equation (3.14), which, in turn, accounts for the broad banded part of the measured sunlight.

These non-linear effects are solved with the Levenberg-Marquardt algorithm, which varies the wavelength calibration and the additive polynomial numerically to achieve the best fit of the slant column densities in the measured spectrum.

### 3.4.2 Validity Consideration

The linear least squares fit in the spectral analysis provides the best results and accounts most for errors if the following assumption are valid:

*The errors of the pixels must have a finite variance* [Albritton et al., 1976]. Since the dominant noise source is normally photon noise, for which the error distribution accord with the Poisson statistics, this assumption is fulfilled.

The least squares fit normally presumes that *the intensity errors of the individual pixels are independent* [Albritton et al., 1976; Bevington, 1969]. However, the instrument function of the measurement instrument ranges over at least several pixels. Thus, the adjacent pixels cannot be regarded as strictly independent so that the presumption is not strictly valid.

This can lead, despite high diligence, to statistical structures in the residual which are not caused by noise. In most cases these structures occur randomly and vary continuously. In a pure noise residual the width of any structure would be only one pixel, hence indicating independent pixel intensities. But here, groups of adjacent pixel intensities seem to change simultaneously in the residuals in a random way. In order to quantify the statistical effect of residual structures on the DOAS retrieval error an approach based on simple Monte Carlo methods [Hausmann et al., 1997, 1999] can be applied or the fit errors can be multiplied with the appropriate factor for the respective spectral analysis [Stutz and Platt, 1996]. In any case, such structures have to be evaluated carefully in terms of spectral fit quality and uncertainty estimation.

In contrast, stable residual structures cannot be described by statistical methods and are caused by systematic errors in the analysis, such as a not considered additional absorber or neglected special features of the instrument.

*The systematic error of the pixel is zero* [Albritton et al., 1976]. It depends on the measurement instrument if this is given. The different pixels of some detectors do not have the same sensibility so that systematic pixel-to-pixel variabilities can occur. For correction, these can be measured by a broad-banded light source with smooth wavelength dependency.

*The slant column density of the trace gas of interest is constant within the wavelength range of the spectral analysis.* For weak absorbers, it usually can

be assumed that this is satisfied even if the strongly wavelength dependent Rayleigh scattering has an impact on the slant column density. However, in case of a strong absorber, the wavelength dependency of the absorption cross section has a non-negligible effect because they can influence the light path distribution through the atmosphere. Thus, the SCD is affected by the strong absorption from the trace gas itself. For instance, ozone in the UV range absorbs strongly to shorter wavelengths (see Figure 3.1) and, thus, influences the SCD itself there, too. Furthermore, this makes a strong impact on slant column densities of other trace gases in the same wavelength range. However, corrections derived from radiative transfer modeling can account for this effect.

*The finite spectral resolution of the measurement instrument has a negligible effect on the spectral analysis.* In practice, the typical spectral resolution of a DOAS instrument is in the order of tenths to several nanometers in the UV-Vis range. This is much larger than the natural band width of atmospheric absorptions. In the spectral analysis, this mismatch is overcome by convolving the absorption cross sections  $\sigma(\lambda, T, p)$ , hence by calculating  $H * \sigma(\lambda, T, p)$  with the instrument function  $H$  (see equation (3.12)) yielding  $\sigma^*(\lambda, T, p)$ .

However, as already described in section 3.3, in the measurement process, the lower resolution is already originated in the spectrograph (determined by the entrance slit and the grating) and therefore affects actually the intensity (see equation (3.9)):

$$I^*(\lambda, L) = H * I(\lambda, L) = H * (I_0(\lambda) \cdot e^{-\sigma(\lambda, T, p) \cdot S}) \quad (3.22)$$

for the simplified case of only one absorber and no broad band features. From equation (3.22),  $\tau(\lambda)$  can be written as:

$$\tau(\lambda) = \ln \left( \frac{H * I_0(\lambda)}{H * (I_0(\lambda) \cdot e^{-\sigma(\lambda, T, p) \cdot S})} \right) \quad (3.23)$$

For weak absorbers ( $\tau(\lambda) \ll 1$ ), the logarithm can be approximated by the first two terms of the Taylor expansion so that the convolution and the logarithm function can be exchanged:

$$\begin{aligned} \tau(\lambda) &\approx H * \ln \left( \frac{I_0(\lambda)}{I_0(\lambda) \cdot e^{-\sigma(\lambda, T, p) \cdot S}} \right) = H * \sigma(\lambda, T, p) \cdot S \\ &= \sigma^*(\lambda, T, p) \cdot S \end{aligned} \quad (3.24)$$

which complies with the mathematical operation mentioned above. However, for optically thick absorbers the convolution and the logarithm cannot be exchanged even by approximation. In this case, the slant column densities can not be retrieved directly, but iterative methods, such as in Frankenberg et al.

[2005], have to be applied.

Therefore, the finite spectral resolution of the instrument can have an effect on the spectral analysis. But for most cases as well as in this work, the optical densities are so small that the presumption above is valid. However, it should be alluded to the  $I_0$ -Effect (section 3.5.3) which arises when the light source features fine structures (compared to the resolution of the instrument). In this case, additional corrections have to be applied.

## 3.5 Passive DOAS Characteristics

### 3.5.1 Fraunhofer Lines

For passive DOAS measurements commonly the Sun is the light source. The shape of the solar spectrum at the top of the atmosphere is given by the individual physical processes on the sun. As first approximation the solar spectrum can be considered as an emission spectrum of a black body with a surface temperature of about 5800 K. This continuous spectrum is overlaid by many strong absorption lines which arise by discrete absorption and re-emission of radiation in the Sun's photosphere (see Figure 3.5a). The respective absorption structure is referred to as Fraunhofer lines (first discovered by Josef Fraunhofer, 1787 - 1826) and produces strong variations of the intensity of the solar spectrum. The Fraunhofer lines are not constant in shape and strength. They rather vary slightly over time and change depending on the observation of different regions of the solar disc. This plays an important role in direct sun observations, in scattered light measurements, however, this can be neglected and averages out, respectively.

In the UV-Vis wavelength range, the optical densities of the Fraunhofer lines are typically in the order of two to three magnitudes higher than the optical densities of the trace gases in the Earth's atmosphere. Accordingly, the Fraunhofer lines can easily distort the measurement values if they are not removed thoroughly in the spectral analysis. Thus, a Fraunhofer reference spectrum (FRS) has to be included, which also serves as  $I_0$  spectrum. Therefore, the FRS would have to be measured from space not being influenced by absorptions in the Earth's atmosphere. However, on the one hand the effort can be considered as too large to send a measurement device into the space (only) for measurements of the FRS, on the other hand the averaging of the Fraunhofer lines (over the solar disc) would have to be performed. Consequently, in practice, the FRS is acquired from the measurement site at times and at measurement geometries at which the absorptions in the Earth's atmosphere are assumed to be lowest. This procedure accepts that retrieved absorption signal of the trace gases is reduced by a small amount which is included in the FRS itself. Although the Langley plot (see section 4.22) is sometimes able to quantify this amount the FRS has to be chosen carefully from the measured spectra.

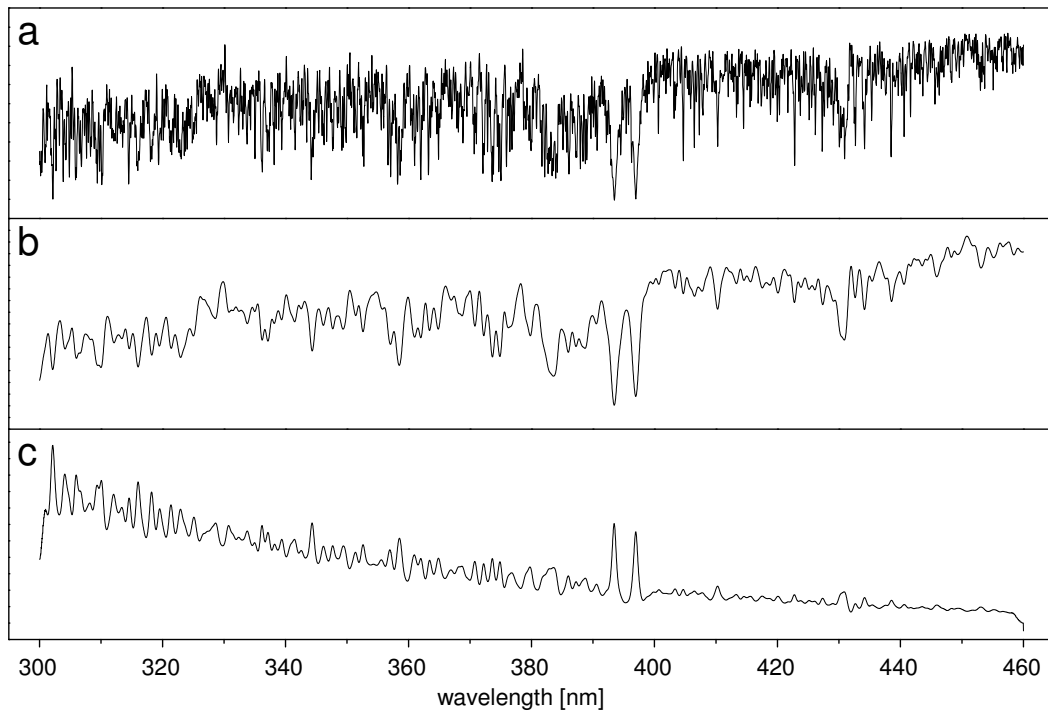


Figure 3.5: (a): High resolution solar spectrum in the wavelength range from 300 to 460 nm. The continuous spectrum is overlaid by Fraunhofer lines. (b): The same as in (a), but convolved with a Gaussian instrument function with 0.7 nm full width at half maximum, which is a typical resolution for DOAS measurements. (c): Ring spectrum modelled from (b). When the solar spectrum has dips, the Ring spectrum features peaks and vice versa, which illustrates the Filling-in process.

### 3.5.2 The Ring Effect

The Ring effect - named after Grainger and Ring [1962] - leads to a reduction of the observed optical densities of the Fraunhofer lines and is based on inelastic rotational Raman scattering (see section 4.2.2) of photons with air molecules [Bussemer, 1993; Fish and Jones, 1995; Burrows et al., 1996]. Such scattering processes cause a change of the photon's wavelength due to the interaction between a rotating molecule and an oscillating electric field [Brinkmann, 1968]. As a result of the low light intensity in the wavelength ranges of Fraunhofer lines compared to the adjacent wavelengths, there is a larger probability of photon scattering into the wavelength range of a Fraunhofer line from the outside than vice versa. This is why the depth (i.e. intensity) of solar Fraunhofer lines in scattered light is less than in extraterrestrial observations. Therefore, the Ring effect is also called "Filling-in".

This effect has to be corrected thoroughly when applying the DOAS method because the atmospheric absorptions can be as much as one to two orders of magnitude smaller than the Ring effect. The magnitude of the Ring effect increases with longer light paths and accordingly with higher solar zenith angles. Therefore, the Ring effect has to be accounted for accurately and a so called Ring reference spectrum (or briefly Ring spectrum) has to be included into the fitting process when scattered sunlight is measured (see Figure 3.5c).

The scattered sunlight intensity  $I_{meas}$  observed by DOAS measurements is composed by the elastic Rayleigh and Mie scattering processes,  $I_{Rayleigh}$  and  $I_{Mie}$ , as well as by Raman scattering  $I_{Raman}$ :

$$I_{meas} = I_{Rayleigh} + I_{Mie} + I_{Raman} = I_{elastic} + I_{Raman} \quad (3.25)$$

As described in section 3.2, the logarithm of the measured spectrum has to be taken for the DOAS analysis:

$$\begin{aligned} \ln(I_{meas}) &= \ln(I_{elastic} + I_{Raman}) \\ &= \ln(I_{elastic}) + \ln\left(1 + \frac{I_{Raman}}{I_{elastic}}\right) \\ &\approx \ln(I_{elastic}) + \frac{I_{Raman}}{I_{elastic}} \end{aligned} \quad (3.26)$$

whereby the Ring spectrum  $I_{Ring}$  can be found as:

$$I_{Ring} = \frac{I_{Raman}}{I_{elastic}} \quad (3.27)$$

There are two approaches to determine the Ring spectrum. Either it can be measured or modelled:

**Measured Ring spectrum:** The Ring spectrum can be measured by using the different properties of the scattering processes in terms of polarisation. While Rayleigh scattering on molecules polarizes light highly for scattering angles around 90 (see section 4.2.1) this occurs only weakly for rotational Raman scattering. By measuring spectra at different polarisation orientations, the Raman scattered intensity and hence a Ring spectrum can be measured [Solomon et al., 1987]. However, scattering on aerosols (Mie scattering) also has a weak wavelength dependence and contributes to the depolarized light fraction. Thus, the Ring spectrum also contains structures caused by Mie scattering, which actually do not belong to the Ring spectrum. Accordingly, the measurement would have to be conducted in the absence of aerosols to reach good accuracy, which is under normal conditions a quite unrealistic precondition. A further adverse effect is that the light path through the atmosphere depends on the polarisation direction. This can lead to trace gas absorption structures in the measured Ring spectrum [Wagner, 1999].

**Modelled Ring spectrum:** The spectrum of inelastically scattered light can be modelled by using the known rotational states of oxygen and nitrogen [Bussemer, 1993; Fish and Jones, 1995; Chance and Spurr, 1997], which are the two main constituents of the atmosphere. The modeling of the Ring spectrum can overcome the shortcomings of the measurement and show very good agreement with highly resolved atmospheric observations [Aben et al., 2001]. It can be performed either on basis of a measured solar spectrum from the data set to be analysed or on basis of a high resolution solar spectrum [Kurucz et al., 1984], which still has to be convolved with the instrument function  $H$  to match the spectral resolution.

In this work, the Ring spectra were modelled for the spectral analysis. Thereby, it turned out that the modeling from measured spectra provided better results with smaller and less structured residuals than from a high resolution solar spectrum. The calculation of the Ring spectra was performed by the software DOASIS [Kraus, 2004].

### 3.5.3 The Solar $I_0$ Effect

The denotation solar  $I_0$  effect is derived from the highly structured solar  $I_0$  spectrum whose strong variation in the intensity caused by the Fraunhofer lines (see section 3.5.1) affects the DOAS analysis [Platt et al., 1997b; Richter, 1997; Van Roozendaal et al., 1999]. Since the typical spectral resolution of a DOAS instrument is in the order of tenths to several nanometers in the UV-Vis range, the Fraunhofer lines cannot be resolved (see Figure 3.5a and b). Therefore, discrepancies between the absorption structures of a trace gas when observing scattered sunlight and its (convolved) absorption cross section can occur, which usually was generated in the lab with an unstructured light source. Hence, errors in the spectral analysis can arise.

In order to account for the solar  $I_0$  effect the absorption cross sections have to be calculated under consideration of these effects, yielding  $I_0$  corrected absorption cross sections  $\sigma_{I_0}^*(\lambda, T, p)$  [Johnston, 1996]:

$$\sigma_{I_0}^*(\lambda, T, p, S) = -\ln \left( \frac{I^*(\lambda)}{I_0^*(\lambda)} \right) \cdot \frac{1}{S} \quad (3.28)$$

Thereby,  $S$  denotes the slant column density of the respective trace gas and should be in the order of magnitude which is typically expected in the measurement.  $I_0^*(\lambda)$  is a high resolution solar spectrum  $I_0(\lambda)$ , e.g. from Kurucz et al. [1984], convolved with the instrument function  $H$ . And  $I^*(\lambda)$  is a convolved synthetic absorption spectrum calculated from the high resolution solar spectrum  $I_0(\lambda)$  and the absorption of the trace gas in the magnitude according to  $S$ :

$$I^*(\lambda) = H * I(\lambda) = H * (I_0(\lambda) \cdot e^{-\sigma(\lambda, T, p) \cdot S}) \quad (3.29)$$

whereby  $\sigma(\lambda, T, p)$  is the respective high resolved absorption cross section.

The  $I_0$  corrected absorption cross section  $\sigma_{I_0}^*(\lambda, T, p)$  only matches perfectly the absorptions in the measured spectrum if the assumed SCD accord to the measured SCD. However, slight deviations from it do not have a significant effect.

Generally, the solar  $I_0$  effect is strongest for strong absorbers, such as ozone. In this case, the retrieved SCD of weak absorbers can be affected significantly if it is not corrected. But for trace gases which are weak absorbers and do not exhibit high resolution spectral features the solar  $I_0$  effect is very small and can be neglected. In this work, the absorption cross sections of  $\text{NO}_2$  and  $\text{O}_3$  were  $I_0$  corrected with typical slant column densities of  $2,5 \cdot 10^{16}$  and  $1 \cdot 10^{20}$ , respectively. All other cross sections were convolved conventionally as described in section 3.3.

### 3.6 Multi-Axis-DOAS

”Traditional” setups point only to the zenith and are mostly sensitive to trace gases located in the stratosphere. In order to increase the sensitivity to trace gases close to the surface, the Multi-Axis-DOAS (MAX-DOAS) technique has been developed recently. MAX-DOAS instruments observe scattered sunlight from different viewing directions. In particular for observation directions pointing slightly above the horizon, high sensitivity for gases close to the ground is obtained since the longer light path through these gas layers yields significantly higher slant column densities [Hönninger and Platt, 2002; Leser et al., 2003; van Roozendaal et al., 2003; Wittrock et al., 2004; Hönninger et al., 2004; Wagner et al., 2004; Heckel et al., 2005; von Friedeburg et al., 2005; Frieß et al., 2006; Sinreich et al., 2007].

Figure 3.6 illustrates this on a simplified MAX-DOAS measurement sketch. The sunlight encounters the Earth’s atmosphere in a given angle, which is referred to as the solar zenith angle  $\vartheta$  (SZA) and is defined as the angle from the direction of the sun to the zenith. The sunlight is scattered (red points) in the line of sight of the different elevation angles  $\alpha$ , which are defined as the angles between the horizon and the pointing directions of the measurement device. In the Figure, the single scattering case is assumed. But in reality, also multiple scattering can occur. Finally, the scattered light is collected by the telescope of the measurement device. The green areas signify atmospheric absorbers in the stratosphere and troposphere, respectively. It can easily be seen that, in the troposphere, higher slant column densities are yielded when the elevation angle is lower.

The sensitivity difference between the troposphere and the stratosphere can be explained by the different measurement approach of MAX-DOAS. In section 3.2 the differential slant column density dSCD was introduced as the difference between the actual SCD and the SCD of the reference spectrum. On the one hand, the reference spectrum can be chosen with respect to the solar zenith angle  $\vartheta$

$$dS(\vartheta, \alpha) = S(\vartheta, \alpha) - S(\vartheta_{Ref}, \alpha) \quad (3.30)$$

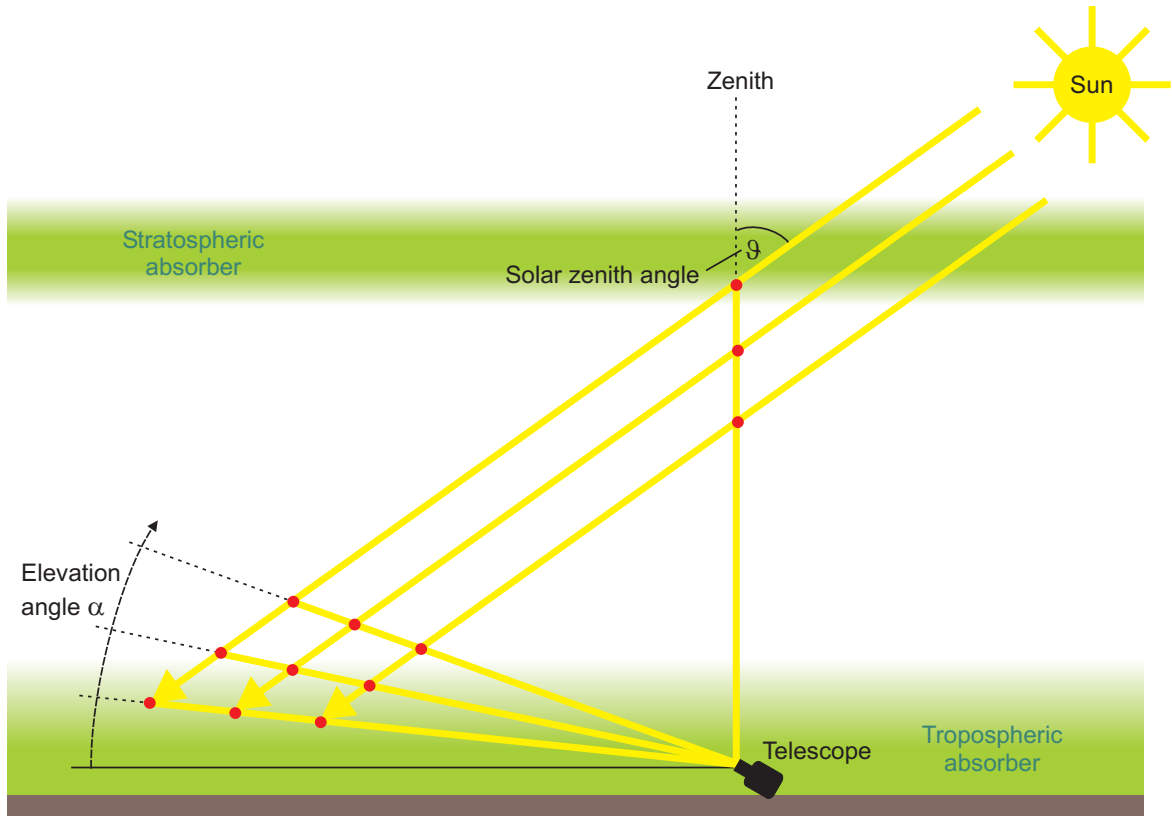


Figure 3.6: Sketch of a MAX-DOAS measurement in the single scattering case. The telescope points to different elevation angles including the zenith in order to collect scattered light. The red points indicate scattering events along the line of sight of the elevation angles.

where  $\vartheta_{Ref}$  should be chosen to be lowest so that the absorption in the reference is correspondingly low. In this case, the stratospheric absorption contributes to the yielded slant column density. On the other hand, the reference can be chosen with respect to the elevation angle  $\alpha$  - like in the MAX-DOAS technique - yielding  $\Delta S$ :

$$\Delta S(\vartheta, \alpha) = S(\vartheta, \alpha) - S(\vartheta, 90^\circ) \quad (3.31)$$

where the reference points to zenith and is measured at the same solar zenith angle  $\vartheta$  as the measurement at the elevation angle  $\alpha$ . The slant column density can be separated into a tropospheric part  $S_{trop}$  and a stratospheric part  $S_{strat}$  so that equation (3.31) can be written as:

$$\Delta S(\vartheta, \alpha) = (S_{trop}(\vartheta, \alpha) + S_{strat}(\vartheta, \alpha)) - (S_{trop}(\vartheta, 90^\circ) + S_{strat}(\vartheta, 90^\circ)) \quad (3.32)$$

Since the scattering objects, i.e. molecules and aerosols (see section 4.2), are located predominantly in the lower atmosphere, also the scattering events occur mostly

there. Thus, at a fixed solar zenith angle, the light path through the stratosphere is almost the same independently of the viewing direction so that the following approximation can be made:

$$\Delta S(\vartheta, \alpha) \approx S_{trop}(\vartheta, \alpha) - S_{trop}(\vartheta, 90^\circ) \quad (3.33)$$

Thus, there is a sensitivity mainly for tropospheric absorbers when changing the elevation angle  $\alpha$ . In practice, the instrument points often sequentially to the elevation angles including the zenith so that the presumption of the same solar zenith angle is not accurately fulfilled. Normally, this can be neglected since one measurement sequence does not take usually so long that the slightly changed SZA makes a significant effect. However, in the morning and evening when the SZA changes rapidly with time and in the UV wavelength range where ozone absorbs strongly it can influence the  $\Delta$ SCD sensibly.

Since the slant column density is defined as the concentration along the light path and, in a first approach, the randomly occurring scattering events normally cannot be retraced, quantitative conclusion cannot be made from the slant column density. Thus, the vertical slant column density (VCD)  $V$  is introduced and is the integrated concentration  $c(z)$  along the height  $z$ :

$$V = \int c(z) dz \quad (3.34)$$

The VCD does not depend on the wavelength, the light path or the observation geometry so that it can be used for comparison of measurements. From Figure 3.6, the VCD can be derived: For a trace gas located near to the ground the following geometrical approximation can be made:

$$V \approx \sin(\alpha) \cdot S(\alpha) \quad (3.35)$$

In contrast, the geometrical approximation alters considering the trace gas in the stratosphere:

$$V \approx \cos(\vartheta) \cdot S(\vartheta) \quad (3.36)$$

Combining both approximations, the connection between  $S(\vartheta, \alpha)$  and  $V$  can be written as [Hönninger, 2002]:

$$S(\vartheta, \alpha) \approx \left( a \cdot \frac{1}{\sin(\alpha)} + (1 - a) \cdot \frac{1}{\cos(\vartheta)} \right) \cdot V \quad (3.37)$$

with  $a$  as the fraction of the total vertical trace gas column located below the scattering altitude. It should be noted that this approximation is only valid for elevation angles  $\alpha$  larger than around 20 and solar zenith angles  $\vartheta$  smaller than around 70. Otherwise, the single scattering assumption is normally not even approximately

fulfilled because multi scattering events dominate. In this case, radiative transfer calculations lead to more accurate conversions between  $S(\vartheta, \alpha)$  and  $V$  (see section 4.5).

Because of its simple setup, MAX-DOAS has many properties of the desired uncomplicated tropospheric monitoring instrument. However, its adverse effect is the need for precise knowledge of the atmospheric radiative transport (see chapter 4), which, in turn, is largely determined by the aerosol load. Since recently, inverse models based on radiative transport models have been developed which allow to infer some degree of vertical resolution from MAX-DOAS measurements. In particular, when assuming a well mixed tropospheric trace gas layer (e.g. within the planetary boundary layer), its vertical extent can be determined with good accuracy (e.g. [Hönninger, 2002; Wittrock et al., 2004; Sinreich et al., 2005; Heckel et al., 2005; Frieß et al., 2006; Sinreich et al., 2007], see section 4.6) which is generally not possible with Zenith-Sky-DOAS or active DOAS measurements.



# 4 Radiative Transfer in the Atmosphere

## 4.1 Parameters of the Radiative Transfer

The radiative transfer in the atmosphere is a very complex interaction of many factors. It depends on several parameters which represent the current atmospheric conditions:

**The vertical temperature profile** is required because the absorption cross sections of the trace gases present in the atmosphere are temperature dependent.

**The vertical pressure profile** has to be known since the Rayleigh scattering events (see section 4.2.1) increase with pressure. The air pressure amounts to around 1 bar at sea level and decreases approximately exponentially with height.

**The vertical profile of ozone.** Owing to the Chappuis and the Huggins absorption bands, ozone is a strong absorber in the UV and has a large impact on the radiative transfer in this wavelength range. The maximum of the ozone concentration is located in the stratosphere at a height between 20 and 25 km.

**The aerosol extinction profile** affects significantly the light path in the atmosphere due to scattering (see section 4.2.3) and absorption. Aerosols are small particles or droplets in the atmosphere with diameters from about 0.01 to 10 micrometers. They can be originated from natural sources being sea salt particles, mineral dust or particles emitted from volcanos and bush fires. Aerosols from anthropogenic sources are fine dust, nitrates, sulfates and soot. Furthermore, aerosols can grow if they hit together, accumulate non volatile compounds or serve as condensation nuclei. It is distinguished between primary aerosols which are emitted directly into the atmosphere (e.g. sea salt particles) and secondary aerosols which are formed owing to physical or chemical processes of gases (e.g. sulfates or nitrates).

The aerosol extinction depends on the kind and the amount of the aerosols present in the atmosphere. It is the most crucial parameter because it can generally vary far more than the other three parameters, which, in turn, are known approximately. Since direct aerosol extinction measurements are not performed usually together with MAX-DOAS measurements, the uncertainties

in the vertical profile can lead to large errors. However, the aerosol extinction profile can be estimated by combining the MAX-DOAS measurements with radiative transfer modeling (see sections 4.5 and 4.6).

## 4.2 Scattering Processes

### 4.2.1 Rayleigh Scattering

Elastic scattering of electromagnetic radiation by matter when the wavelength of the incident light is much larger than the dimension of the particles is called Rayleigh scattering. In the scattering process, physically, an oscillating dipole is induced by electromagnetic radiation in a polarisable particle, e.g. air molecules [e.g. Van de Hulst, 1981].

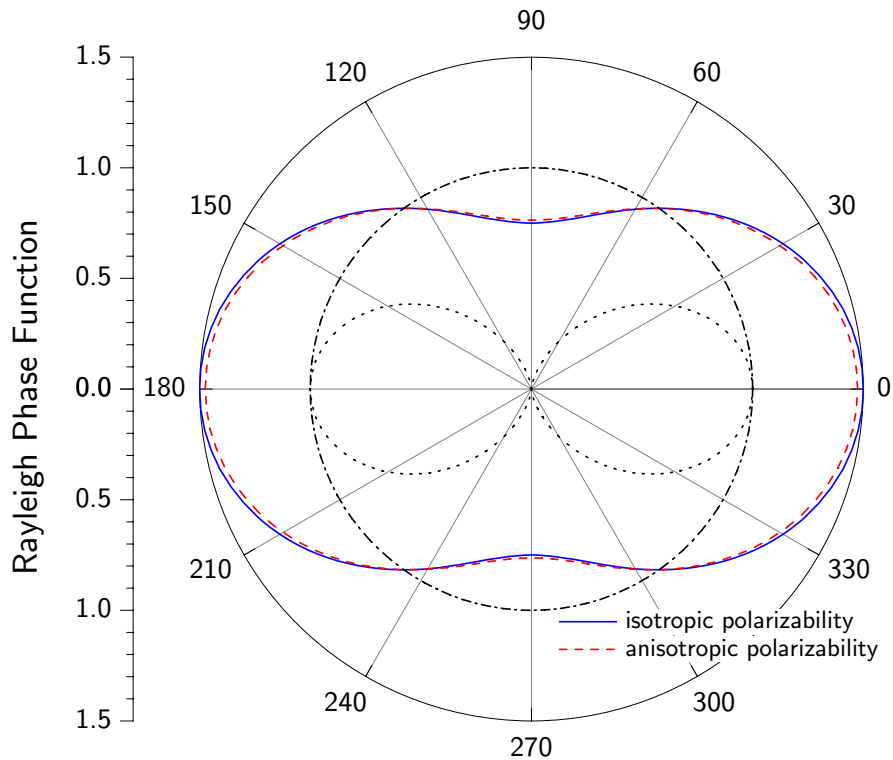


Figure 4.1: *Rayleigh scattering phase function  $\Phi_R(\theta)$  and its contributions (see text). Adapted from Hönninger [2002].*

The Rayleigh scattering phase function  $\Phi_R(\theta)$  shown in Figure 4.1 describes the relative intensity of the scattered light. Thereby,  $\theta$  is the scattering angle between the incident propagation direction and the direction after the scattering event. The

dotted black line is the contribution of light polarised parallel to the scattering plane which indicates the  $\sim \sin^2\theta'$  dependence of a Hertz dipole (where  $\theta' = \frac{\pi}{2} - \theta$  is the angle between dipole axis and Poynting vector of the incident light). In contrast, the dash dotted line shows the contribution of light polarised perpendicular to the scattering plane which does not feature a dependence on  $\theta$ . Finally, the blue line indicates the Rayleigh scattering phase function - the superimposition of both contributions - for unpolarised incident light which is given by:

$$\Phi_R(\cos(\theta)) = \frac{3}{4} \cdot (1 + \cos^2(\theta)) \quad (4.1)$$

If the anisotropy of the polarizability is taken into account (red dashed line, see Penndorf [1957]), equation (4.1) changes slightly to:

$$\Phi_R(\cos(\theta)) = 0.7629 \cdot (1 + 0.9324 \cdot \cos^2(\theta)) \quad (4.2)$$

An important feature of the Rayleigh scattering is its strong wavelength dependency which is approximately:

$$\sigma_R \propto \frac{1}{\lambda^4} \quad (4.3)$$

where  $\sigma_R$  as the Rayleigh cross section. The exact value for  $\sigma_R$  is calculated with [Penndorf, 1957]:

$$\sigma_R = \frac{3.9993 \cdot 10^{-32} \cdot x^4}{1 - 1.069 \cdot 10^{-2} \cdot x^2 - 6.681 \cdot 10^{-5} \cdot x^4} \cdot m^2 \quad (4.4)$$

where  $x = \frac{10^{-6}m}{\lambda}$ . For blue light the scattering probability is one order of magnitude larger than for red light. This explains the "blue" sky over the day when the sun stands high and the red light in the dawn and dusk when the light path through the atmosphere is extraordinarily long. However, over the day, the maximum of the scattered light spectrum is located in the UV wavelength range which is not visible for the human eye.

### 4.2.2 Raman Scattering

Raman scattering denotes inelastic scattering on air molecules. With respect to Rayleigh scattering, Raman scattering accounts to a few per cent depending on the wavelength [haug1996]. It can be described as light interacting with an air molecule that changes its excitation state during the scattering process. The photon either transfers part of its energy to the molecule (Stokes lines,  $\Delta J = +2$ , S-branch) or takes over part of the molecule's excitation energy (Anti-Stokes,  $\Delta J = -2$ , O-branch). If only the rotational excitation is affected ( $\Delta\nu = 0$ ) it is called rotational Raman scattering (RRS). If also the vibrational state changes the term rotational-vibrational Raman scattering (RVRS) is used ( $\Delta\nu = \pm 1$ ). Only discrete amounts

of energy given by the difference between the discrete excitation levels can be transferred between the photon and the molecule. For air molecules (mainly oxygen and nitrogen) RRS frequency shifts of up to  $\pm 200 \text{ cm}^{-1}$  occur, which corresponds to several nanometers in the UV/Vis wavelength range. In case of RVRS a vibrational shift of  $\pm 2331 \text{ cm}^{-1}$  for nitrogen and  $\pm 1555 \text{ cm}^{-1}$  for oxygen has to be added [Burrows et al., 1996; Haug, 1996; Sioris and Evans, 1999]. Since the RRS is one order of magnitude stronger than the RVRS, it dominates the Raman scattering and the RVRS can be neglected for the calculation of the Ring spectrum (see section 3.5.2).

While in terms of the Ring spectrum the consideration of Raman scattering is indispensable, the specific attributes of Raman scattering do not play an important role in the radiative transfer. Thus, they are not taken into account in the calculation of air mass factors (see section 4.4) and the modeling of the radiative transfer.

### 4.2.3 Mie Scattering

Mie scattering occurs if light is scattered on aerosols whose dimensions are similar or larger than the wavelength of the incident light (for a short description of aerosols see section 4.1). During the scattering process, the components of the aerosol are excited coherently and radiate themselves. The scattered light features interference properties owing to comparable dimensions with the incident light and minima as well as maxima in the intensity of the scattered light depending on the scattering angle  $\theta$  occur (see Figure 4.2 left column). Furthermore, Mie scattering generally prefers the forward scattering direction. Actually, Mie scattering only refers to spherical aerosols and there are other theories for non-spherical particles. However, also the non-spherical cases can mostly be well approximated by the spherical description of the Mie scattering.

Aerosols differ naturally strongly in shape and size so that the determination of the Mie scattering cross section can be very complex. This problem is addressed by the Mie theory, which includes a variety of numerical models to calculate scattering phase functions and extinction coefficients for given aerosol types and particle size distributions [Van de Hulst, 1981; Wiscombe, 1980]. The scattering phase function, which determines the direction and the strength of the scattered light, depends on the aerosol size parameter  $x$ :

$$x = \frac{2 \cdot \pi \cdot r}{\lambda} \quad (4.5)$$

with  $r$  being the radius of the aerosol and  $\lambda$  being the wavelength of the light. In Figure 4.2 Mie scattering phase functions  $\Phi_M(\theta)$  at 550 nm wavelength for water droplets with size parameters  $x = 1$ ,  $x = 3$  and  $x = 10$  are shown [Sanghavi, 2003]. Obviously, the larger the particle size, the more dominant is the forward scattering direction.

Aerosols with different aerosol size parameters exhibit different wavelength dependencies. The wavelength dependence is expressed by the Ångström coefficient

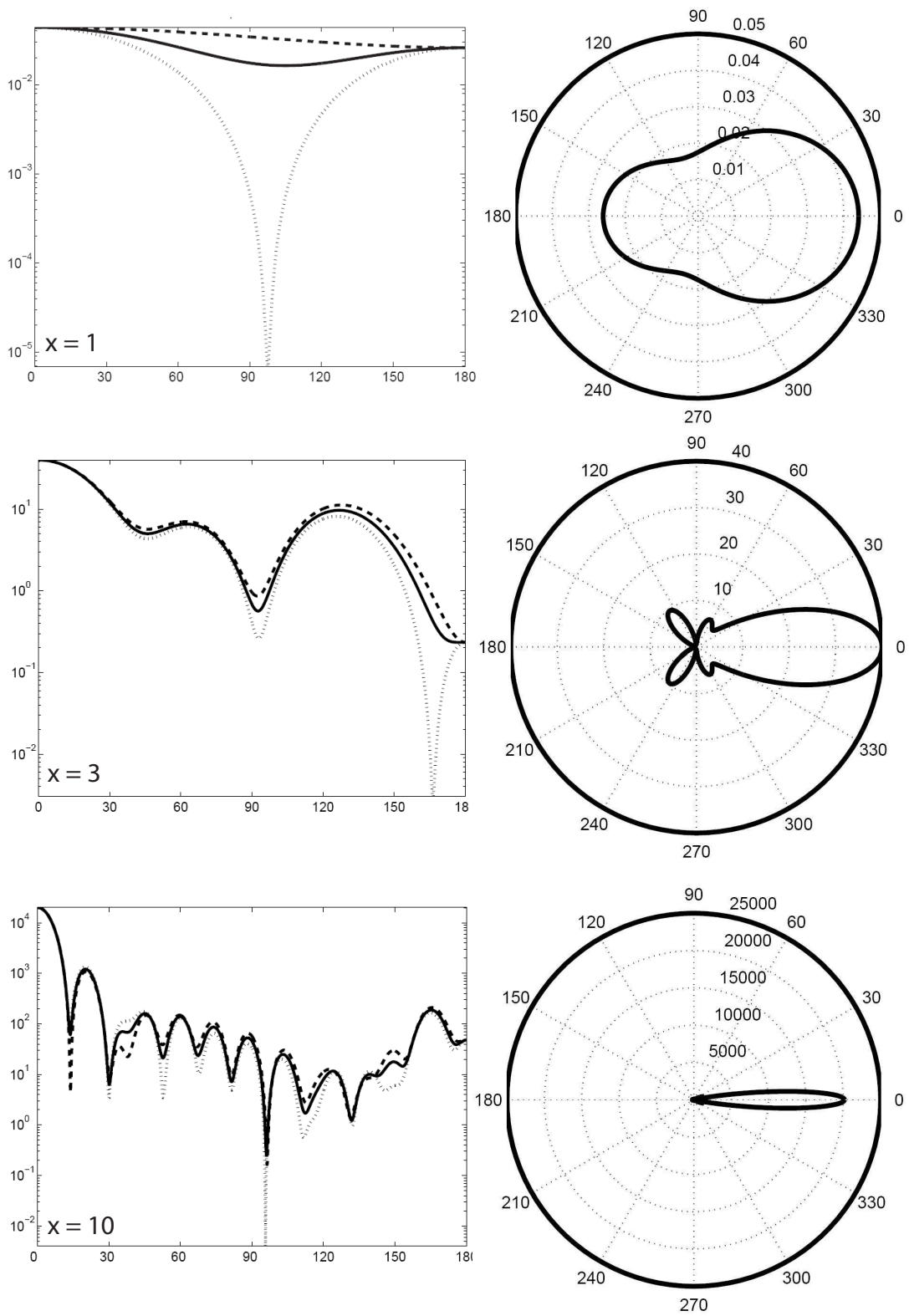


Figure 4.2: Mie scattering phase functions at 550 nm wavelength for water droplets with size parameters  $x = 1$  (top),  $x = 3$  (middle) and  $x = 10$  (bottom) [Sanghavi, 2003] on logarithmic scale (left) and linear scale (right).

$\alpha$ . For the Mie scattering cross section  $\sigma_M$  follows:

$$\sigma_M \approx \frac{1}{\lambda^\alpha} \quad (4.6)$$

whereby  $\alpha$  is larger for smaller aerosol size parameters. Rayleigh scattering can be regarded as a special case of Mie scattering reaching  $\alpha = 4$  (for  $x \rightarrow 0$ ). For typical atmospheric aerosols the Ångström coefficient is around 1.3 which indicates a small wavelength dependence.

In reality, aerosols of different size and chemical composition are present simultaneously in the atmosphere. By integrating the individual scattering properties of aerosols over their whole size distribution and considering the different chemical types, bulk scattering properties can be derived. In doing so, an asymmetry coefficient  $g$  is often introduced describing the averaged cosine of the scattering angle  $\theta$ . The asymmetry coefficient is a measure for the degree of forward-peakedness and parameterizes the rate of discrepancy to the Rayleigh scattering behaviour whereby the value 0 indicates a totally isotropic scattering behaviour and the value 1 scattering events solely in forward direction. In urban regions, the asymmetry coefficient ranges typically around 0.7. Very common is the Henyey-Greenstein phase function approximation [Henyey and Greenstein, 1941] utilizing the asymmetry coefficient  $g$ :

$$\Phi_{HG}(\theta) = \frac{1 - g^2}{\sqrt{(1 + g^2 - 2g \cos(\theta))^3}} \quad (4.7)$$

with  $\theta$  being the scattering angle. The Henyey-Greenstein approximation underestimates slightly the backward scattering, but its advantage is the easy calculation.

Aerosols not only scatter but also absorb light depending on the surface of the aerosol. This is described by the single scattering albedo (SSA)  $\omega$  (as well as by the imaginary part of the complex refractive index) which is the scattering fraction of the aerosol extinction  $\epsilon_M$ .

$$\omega = \frac{\epsilon_{M_{scatt}}}{\epsilon_M} = \frac{\epsilon_{M_{scatt}}}{\epsilon_{M_{scatt}} + \epsilon_{M_{abs}}} \quad (4.8)$$

where  $\epsilon_{M_{scatt}}$  and  $\epsilon_{M_{abs}}$  are the scattering and absorbing fractions of  $\epsilon_M$ , respectively.  $\omega = 0$  means that only absorption and no scattering occurs when light hitting an aerosol which can be assumed from soot.  $\omega = 1$  stands for the contrary case where only scattering and no absorption takes place as it is approximately for e.g. sea salt. While in the visible wavelength range, the SSA for urban aerosols amounts to nearly 1, in the UV range, it can decrease significantly.

### 4.3 Visibility

The visibility is determined by the radiative transfer in the atmosphere and is connected with the extinction of light. Extinction, hence scattering and absorption, can

happen by both molecules and aerosols. However, in reality the molecule extinction is that weak that, in presence of aerosols, the aerosol extinction dominates. Thus, the visibility can be utilized as a first approximation of the aerosol extinction. It can be determined from the contrast  $C$  between a laminar object and its background if there is no limitation due to the resolution of the human s eye:

$$C = \left| \frac{H - H_0}{H_0} \right| \quad (4.9)$$

where  $H$  and  $H_0$  are the brightness of the object and the background felt by the human s eye, respectively. Without glare, a contrast of about 2 % is normally sufficient to distinguish between the object and the background.

Applying the Lambert-Beer law,  $H$  can be expressed by the extinction coefficient  $K$  of the atmosphere:

$$H = H_0 \cdot (1 - e^{-K \cdot d}), \quad (4.10)$$

with  $d$  as the distance between the human s eye and the object. Combining the equations (4.9) and (4.10) yields

$$C = e^{-K \cdot d} \quad (4.11)$$

If  $d$  corresponds to the maximum visibility  $R$  the contrast  $C$  has to amount to 0.02 as explained above. Thus, equation (4.11) can be written as

$$R = \frac{3,9}{K} \quad (4.12)$$

This relation is just a rough approximation, but under normal conditions without glare the extinction coefficient derived from the maximum visibility can be retrieved in good accuracy [Roedel, 2000].

## 4.4 The Air Mass Factor Concept

As introduced in chapter ??, the primary quantity of a DOAS measurement analysis is the slant column density  $S$ , which is the integrated concentration along the light (see equation 3.7). The slant column density depends on several parameters. These are the wavelength  $\lambda$ , the solar zenith angle  $\vartheta$ , the elevation angel  $\alpha$  and the relative azimuth angle  $\phi$  which is the horizontal angle between the telescope direction and the sun. Thus, the slant column density is generally hard to evaluate. In contrast, the vertical column density  $V$  is the integrated concentration along the height (see equation 3.34) and is independent of the wavelength of the measurement geometry.  $V$  is fully determined by the trace gas profile. The Air Mass Factor (AMF)  $A$

connects both quantities and is defined as [Noxon et al., 1979; Solomon et al., 1987; Marquard et al., 2000]:

$$A(\lambda, \theta, \alpha, \phi) := \frac{S(\lambda, \theta, \alpha, \phi)}{V} \quad (4.13)$$

Like the slant column density, the air mass factor  $A$  depends on the wavelength  $\lambda$ , the solar zenith angle  $\vartheta$ , the elevation angle  $\alpha$  and the relative azimuth angle  $\phi$ . It is determined by the radiative transfer in the atmosphere and, hence, by its parameters. Since the air mass factor expresses the light path ratio between the slant and the vertical path through the atmosphere, it is a measure for the length of the light path in the atmosphere depending on the state of the atmosphere.

The relation between the SCD and the VCD can also be expressed by the optical density  $\tau$  when sunlight passes through a concentration field  $c(\vec{x})$  under the assumption that the temperature and the pressure dependency of the absorption cross section  $\sigma$  is small:

$$\tau(\lambda) = -\ln\left(\frac{I(\lambda)}{I_0(\lambda)}\right) = \sigma(\lambda) \cdot \int_0^L c(\mathbf{x}) dl = \sigma(\lambda) \cdot S(\lambda) \quad (4.14)$$

Taking equation (4.13) into account, equation (4.14) can be written as under the assumption of a well defined light path through the atmosphere:

$$A(\lambda) = \frac{\tau(\lambda)}{\sigma(\lambda) \cdot V} \quad (4.15)$$

In section 3.6, the slant column densities for absorbers close to the ground and in the stratosphere  $S_{trop}(\alpha)$  and  $S_{strat}(\vartheta)$ , respectively, were approximated (see equations (??) and (??)). These can be applied to the respective air mass factors  $A_{trop}(\alpha)$  and  $A_{strat}(\vartheta)$  so that it follows:

$$A_{trop}(\alpha) = \frac{S_{trop}(\alpha)}{V} \approx \frac{S_{trop}(\alpha)}{S_{trop}(\alpha) \cdot \sin(\alpha)} = \frac{1}{\sin(\alpha)} \quad (4.16)$$

and neglecting refraction on the atmosphere

$$A_{strat}(\vartheta) = \frac{S_{strat}(\vartheta)}{V} \approx \frac{S_{strat}(\vartheta)}{S_{strat}(\vartheta) \cdot \cos(\vartheta)} = \frac{1}{\cos(\vartheta)} \quad (4.17)$$

As already mentioned in section 3.6 the approximations in equations (4.16) and (4.17) can normally only be made for elevation angles larger than around 20° and solar zenith angles smaller than around 70°. For this, it has to be assumed that light is scattered only once in the line of sight of the elevation angle. Or more precisely, in case of the tropospheric absorber the last scattering event should be above the absorber layer and, in case of the stratospheric absorber, the first scattering event

should be below the absorber layer, and the photons should not be scattered back into the respective absorber layer.

In the measurement process, the observed intensity is not caused by scattered photons which all took the same light path. It is rather a sum of scattered photons which passed through the atmosphere on many different light paths which makes the description more complicated. So, a probability density function  $p(k, \lambda)$  can be introduced where  $k$  describes the set of possible light paths [Marquard et al., 2000].  $p(k, \lambda)$  is regarded as the probability that a photon with wavelength  $\lambda$  traverses the atmosphere on a given light path  $\mathbf{x}_k(l)$  from the sun to the telescope. Hence, the observed intensity is the integrated intensity over all possible light paths to the telescope, weighted with the according probability. The optical density  $\tau$  can now be written as

$$\tau(\lambda) = -\ln\left(\frac{I(\lambda)}{I_0(\lambda)}\right) = \ln\left(\int p(k, \lambda) \cdot e^{-\sigma(\lambda) \cdot V \cdot \int \hat{c}(\mathbf{x}_k(l)) dl} dk\right) \quad (4.18)$$

under the assumption that  $\sigma(\lambda)$  is independent of temperature and pressure so that it can be placed outside the inner path integral. The trace gas profile  $c(\mathbf{l})$  is written as the product of the vertical column density and the 'relative' profile shape  $\hat{c}(\mathbf{l}) = \frac{c(\mathbf{l})}{V}$  which is independent of the trace gas amount.

Including equation (4.18) into equation (4.15), the air mass factor  $A$  for scattered light observations is

$$A(\lambda) = -\frac{1}{\sigma(\lambda) \cdot V} \cdot \ln\left(\int p(k, \lambda) \cdot e^{-\sigma(\lambda) \cdot V \cdot \int \hat{c}(\mathbf{x}_k(l)) dl} dk\right) \quad (4.19)$$

Equations (4.18) and (4.19) have several important implications for the interpretation of scattered light measurements:

Equation (4.18) implies that the observed optical density is not a linear superposition of the optical densities along the individual light paths  $\mathbf{x}_k$ . Thus, the Lambert Beer law is only strictly fulfilled if there exists a single well defined light path  $\mathbf{x}_0(l)$ , i.e. when observing direct light. Then, the probability density function is delta distributed,  $p(k, \lambda) = \delta(k)$ . In this case, equations (4.14) and (4.18) are equivalent.

The air mass factor for scattered light is not only a function of the relative profile shape  $\hat{c}(\mathbf{l})$ . Since the vertical column density cannot be divided out in equation (4.19) it also depends on the vertical column density:  $A(\lambda) = A(\lambda, V)$ . Therefore, the determination of the vertical column density is equivalent to the solution of the implicit relationship (see equation(4.13))

$$V = \frac{S(\lambda)}{A(\lambda, V)} \quad (4.20)$$

which can be generally solved iteratively [Marquard et al., 2000]. However, this method is very time consuming because the air mass factor has to be calculated for each iteration step.

The air mass factor does not only depend on wavelength  $\lambda$ , but also on the product of the absorption cross section  $\sigma(\lambda)$  and the slant column density  $S$ . The air mass factor, and therefore also the respective slant column density, is modulated with the wavelength dependency of the trace gas cross section:

$$\tau(\lambda) = \sigma(\lambda) \cdot S(\lambda) = \sigma(\lambda) \cdot V \cdot A(\lambda, \sigma(\lambda) \cdot S) \quad (4.21)$$

The spectral analysis can be affected strongly since it is performed over a finite wavelength range. For strong absorbers, such as ozone in the UV, the wavelength dependence of the air mass factors leads to a modulation of the absorption structure. It can be compensated for by using  $\sigma(\lambda) \cdot A(\lambda)$  instead of  $\sigma(\lambda)$  as the trace gas reference spectrum [Diebel et al., 1995; Richter, 1997]. Then the VCD is determined directly by the retrieval.

In case of a single absorber present in the atmosphere, the probability density function  $p(k, \lambda)$  is determined only by Rayleigh and Mie scattering and is expected to be a broad banded function of  $\lambda$ . However, if additional absorbers in the considered wavelength range are present in the atmosphere, it is also a function of the cross sections and concentration fields of the additional absorbers. This may have a significant impact on the radiative transfer.

The air mass factors can be calculated by radiative transfer models (see section 4.5). Thereby, single scattering radiative transfer models can use equation (4.19). This has the advantage to be fast and relatively easy to implement. However, this simplification can lead to significant errors. Therefore, multiple scattering radiative transfer models provide a more reliable air mass factor calculation, but need a much higher calculation effort.

Air mass factors calculated by radiative transfer modeling need to be retrieved thoroughly to fit to measured slant column densities. Since the measured slant column densities are retrieved with respect to a Fraunhofer reference spectrum, differential slant column densities  $dS(\vartheta, \alpha)$  are the output of the measurement (see equation (??)):

$$dS(\vartheta, \alpha) = S(\vartheta, \alpha) - S_{Ref} \quad (4.22)$$

The dependence of the air mass factor on the solar zenith angle  $\vartheta$  can be used to convert the differential slant column densities  $dS(\vartheta)$  into absolute slant column densities  $S(\vartheta)$ . With equation (4.13), equation (4.22) can be written as:

$$dS(\vartheta) = V \cdot A(\vartheta) - S_{Ref} \quad (4.23)$$

The differential slant column density  $dS(\vartheta)$  is a linear function of the air mass factor  $A(\vartheta)$  if the vertical column density  $V$  does not depend on the solar zenith angle  $\vartheta$ . This relationship, hence  $dS(\vartheta, \alpha)$  versus  $A(\vartheta, \alpha)$ , can be plotted in a diagram. The slant column density of the Fraunhofer reference spectrum,  $S_{Ref}$ , is given by the negative intercept of the ordinate and the vertical column density  $V$  by the slope of the linear fit. This method is called Langley plot.

In order to separate tropospheric from stratospheric absorbers, the  $\Delta$ SCD (see equation 3.31) can be plotted versus the tropospheric air mass factors  $\Delta A(\alpha)$ , with

$$\Delta A(\alpha) = A(\alpha) - A(90^\circ) \approx A(\alpha) - 1 \quad (4.24)$$

where  $A(90^\circ)$  can be calculated by radiative transfer modeling (see section 4.5) or approximated by the value 1. In this case, the slant column density of the Fraunhofer reference spectrum,  $S_{Ref}$  is eliminated so that the linear fit should pass the point of origin. The Langley plot equation can now be written as:

$$\Delta S(\alpha) = V \cdot \Delta A(\alpha) \quad (4.25)$$

again with the vertical column density  $V$  as the slope of the straight line. As described in section ??, the Langley plot can be potentially used to estimate the height and concentration of a well-mixed absorber layer.

The Langley plot implies that the vertical column density is constant over the measurement period and that the air mass factors must be recalculated in case of changes in any input parameter (especially changes in the vertical profile of the absorber itself are crucial). Furthermore, the air mass factors has to be independent of the vertical column density (see equation 4.19). The Langley plot is a simplified, but efficient way to retrieve the vertical column density and the slant column density of the FRS, in case the air mass factors are calculated thoroughly.

## 4.5 Radiative Transfer Modeling

### 4.5.1 Introduction

The radiative transfer in the atmosphere is determined by interactions of radiation with the compounds of the atmosphere and with Earth's surface. These interactions are absorption, scattering, refraction, thermal emission (only relevant in the infrared wavelength range) and reflection (determined by the albedo). The Radiative Transfer Equation (RTE) describes their influences on the radiance  $L$ . The radiance  $L$  which is also denoted simplified as intensity is the radiant flux  $\Phi$  per solid angle  $\Omega$  and projected radiation source area  $A_s$ :

$$L = \frac{\Phi}{\Omega \cdot A_s} \quad (4.26)$$

with the radiant flux being the radiant energy  $E$  per unit time  $t$ :

$$\Phi = \frac{dE}{dt} \quad (4.27)$$

In contrast, the irradiance  $B$  is defined as the radiant flux  $\Phi$  which is received by a projected illuminated area  $A_t$ :

$$B = \frac{\Phi}{A_t} \quad (4.28)$$

The radiance and the irradiance are given by the units  $[\frac{W}{sr \cdot m^2}]$  and  $[\frac{W}{m^2}]$ , respectively.

Radiative transfer models are aimed at solving the radiative transfer equation in order to calculate the radiance acquired by a specific instrument and for a defined atmospheric scenario. For instance, a DOAS device is such an instrument which measures at a given time and location. From the radiances, the air mass factors can be calculated. However, it is not possible to analytically solve the RTE without introducing simplifications. Thus, a numerical approach usually is used which can be applied in two different ways: The RTE is either solved analytically by calculating the radiant field of a given atmospheric state or by a statistical approach, where individual photon paths are simulated for a given atmospheric scenario. The radiant field can then be derived from the photon density. Due to simplifications, e.g. concerning the sphericity of the Earth, the analytical calculation is normally faster than the simulation of the statistical approach. However, analytical solutions sometimes are difficult or even impossible to find, while the statistical approach provides reasonable results owing to many individual simulations. But generally, the results converge with each other, if both an analytical solution could be found and the statistics in the simulation is good enough.

In the following sections, the different radiative transfer models are described which were used in this work. While Tracy and Tracy-II/McArtim apply the statistical approach, Sciatran analytically calculates the radiant field.

### 4.5.2 The Radiative Transfer Model Tracy

Tracy (Trace gas RAdiative monte Carlo Ymplementation) is a three dimensional radiative transfer model and was developed by the Institute of Environmental Physics of the University of Heidelberg [von Friedeburg, 2003]. It is based on the backward Monte Carlo method: a photon virtually emerges from a detector in an arbitrary line of sight direction and is followed through the atmosphere along its path until it leaves the top of the atmosphere. (In a forward model instead, a multitude of photons would need to be simulated before even one photon hits the detector, which would be very time consuming.) The various possible scattering or absorption events along the path are defined by suitable probability distributions. When, for example, a photon hits an air molecule, a random number is drawn - just like a game

of chance e.g. in Monte Carlo. If the number lies in a certain interval depending on the process' probability, this process occurs and the photon is e.g. scattered to a different direction of propagation. After the last scattering event and before leaving the atmosphere, the probability is calculated that the direction of the photon after this event points at the sun. Then, the probability of absorption of the photon from the location of the last scattering event to the top of the atmosphere is determined. Finally, the complete photon path weighted with all probabilities is included in the calculation of the intensity. For the modeling, the atmosphere is discretized vertically and horizontally into so-called voxels with homogeneous atmospheric properties. Therefore, a fine discretisation is necessary if parameters change strongly. Profiles of pressure, temperature, ozone, aerosols and several trace gases as well as the wavelength have to be included for the modeling, yielding air mass factors for every trace gas specified.

In Tracy, the modeling of the total air mass factor is based on calculations for optically thin absorbers, i.e. weak absorbers [Solomon et al., 1987; Perliski and Solomon, 1993; Eskes and Boersma, 2003], applying the following equation:

$$A = \frac{\ln\left(\frac{I_0}{I}\right)}{\sigma(\lambda) \cdot V} \quad (4.29)$$

which is a combination of equations (4.14) and (4.15). Here  $I_0(\lambda)$  denotes the measured intensity without the absorber of interest, but with the absorption of all other present absorbers, while  $I(\lambda)$  is the detected intensity considering all absorbers. This formula works well as long as the impact of the absorption of the trace gas of interest on the light path distribution can be neglected. When this is not the case, e.g. for ozone in the UV, then the light paths contributing to  $I(\lambda)$  are influenced by the absorption of the trace gas of interest itself and thus they differ from the light paths contributing to  $I_0(\lambda)$  (see also section 4.4). In this work, this does not lead to errors because all trace gases of interest are weak absorbers.

### 4.5.3 The Radiative Transfer Model Tracy-II/McArtim

Tracy-II and McArtim which both are developed by Deutschmann and Wagner [2006] are almost identical, complete recompositions of Tracy with new features and improvements. Both also apply the backward Monte Carlo method at a given wavelength. However, the calculation of the photon path probability has been improved: The various possible scattering or absorption events along the path are still described by suitable probability distributions. However, here the generation of the photon paths is independent of the position of the sun. Instead at each scattering event the probability that the photon is scattered into the sun is calculated. When enough light paths are modeled, the contribution of each light path to the intensity measured at the detector is calculated by weighting the sum of the probabilities of all scattering events along the path (local estimation method [Marchuk et al.,

1980]). When setting the Sun's position to a specific solar zenith angle, then a forward run of the model calculates the corresponding air mass factors and intensities, using the paths and probabilities generated in the backward run. Furthermore, Tracy-II/McArtim uses a different approach for the air mass factor calculation and calculates so-called box-AMFs  $A_{box}$  instead. When the atmosphere is divided along its vertical axis into several layers of height  $h$ , also called boxes, then  $A_{box_i}$  is the air mass factor for box  $i$  under the assumption of a horizontally homogeneous trace gas distribution in the box. The box-AMF is then defined by [Eskes and Boersma, 2003]:

$$A_{box_i} = \frac{d [\ln (\frac{I_0}{I})]}{d [\sigma(\lambda) \cdot V_i]} \quad (4.30)$$

According to equation (4.13) this can also be written as:

$$A_{box_i} = \frac{dS}{dV_i} \quad (4.31)$$

The box-AMF describes how strongly the measured SCD changes with an alteration of  $V_i$ . This expresses the sensitivity of the measurement towards changes of the vertical column density within the box  $i$ . box-AMFs (normalized to 1) are identical with weighting functions [Rodgers, 1976, 2000] which are the weights for the sensitivity of the measurement towards specific atmospheric layers. Thus, they provide information in which boxes the measurement of an absorber is most sensitive. From that, the most suitable measurement geometries can be derived when investigating an absorber with a known vertical profile.

Total AMF is calculated from the Box-AMFs  $A_{box_i}$  for each box  $i$  and the respective trace gas profile. It is the sum of the box-AMFs from the surface to the top of the atmosphere (TOA) and the corresponding partial trace gas vertical columns  $V_i$  divided by the VCD:

$$A = \frac{1}{V} \cdot \sum_i A_{box_i} \cdot V_i \quad (4.32)$$

For weak absorbers the box-AMFs are independent from the profile. Then, arbitrary trace gas profiles can be used with the same set of box-AMFs in order to derive total AMFs for different scenarios. In contrast, for strong absorbers the same height profile as used for the calculation of the respective box-AMFs must be used for the calculation of the total AMF.

Tracy-II/McArtim can also calculate the so-called normalized radiance  $L_n$ . It can be derived by modeling the radiance  $L$ , which is received by the measurement device, and the solar irradiance  $B$ :

$$L_n = \frac{L}{\pi \cdot B} \quad (4.33)$$

The normalized radiance describes which fraction of the sunlight can be detected by the measurement device. It is suited to check model runs with respect to potential errors in the settings as well as the consistency of models themselves [Wagner et al., 2007]. Furthermore, Tracy-II/McArtim can provide optical densities as well as photon path length distributions and photon scattering distances.

In Tracy-II/McArtim, the radiative transfer is modeled in a fully spherical and three-dimensional atmosphere. Three-dimensional profiles of trace gases and aerosols are considered in the calculation as well. A specific relief can be included so that significant valleys or mountains which can influence the radiative transfer are taken into account. However, refraction is not fully developed until now but is planned to be done soon. Yet, in this work, refraction has a very weak impact because this work focusses on absorbers in the troposphere.

Tracy-II and McArtim are identical except for a detail in the generation of the path through the atmosphere. In Tracy-II, paths are determined without consideration of absorption. Therefore, absorption is taken into account later in the weighting of the intensity by an additional factor. In contrast, McArtim considers absorption already in the generation of the paths. Thus, in case of strong absorptions, the path through the atmosphere can be simulated more realistically. Furthermore, the omitting of an additional weighting factor in the intensity calculation makes McArtim one order of magnitude faster in radiative transfer modeling than Tracy-II.

## 4.6 Profile Retrieval

### 4.6.1 Direct Comparison Approach

The direct comparison approach is based on the comparison of measured and modeled values. It is a relatively simple algorithm, which converts a set of slant column density MAX-DOAS measurements of the oxygen dimer ( $O_4$ ) and of a trace gas of interest, e.g.  $NO_2$ ,  $CHOCHO$  and  $HCHO$  (see sections ?? and ??), into atmospheric aerosol extinction and the absolute concentration and mixing ratio of the trace gas of interest within the atmospheric boundary layer [Sinreich et al., 2005]. In addition the height of the atmospheric boundary layer usually can be derived. The algorithm is based on radiative transfer modeling, taking into account the current aerosol scenario as determined from the  $O_4$  measurements. Since the concentration of the oxygen dimer  $O_4$  is proportional to the square of the  $O_2$  concentration, the majority of  $O_4$  is located close to the surface, and its vertical profile decreases exponentially with a scale height of approximately 4 km. The variation of the  $O_4$  dSCD with elevation can therefore be used to quantify the aerosol extinction in the lower troposphere. Variations in the  $O_4$  dSCDs are generally not caused by changes in concentration, but in aerosol scattering [Wagner et al., 2004; Frieß et al., 2006].

The profile retrieval is split into two steps. Firstly, sets of  $O_4$  AMFs for a variety of aerosol scenarios are calculated and then compared with  $O_4$  AMFs measured

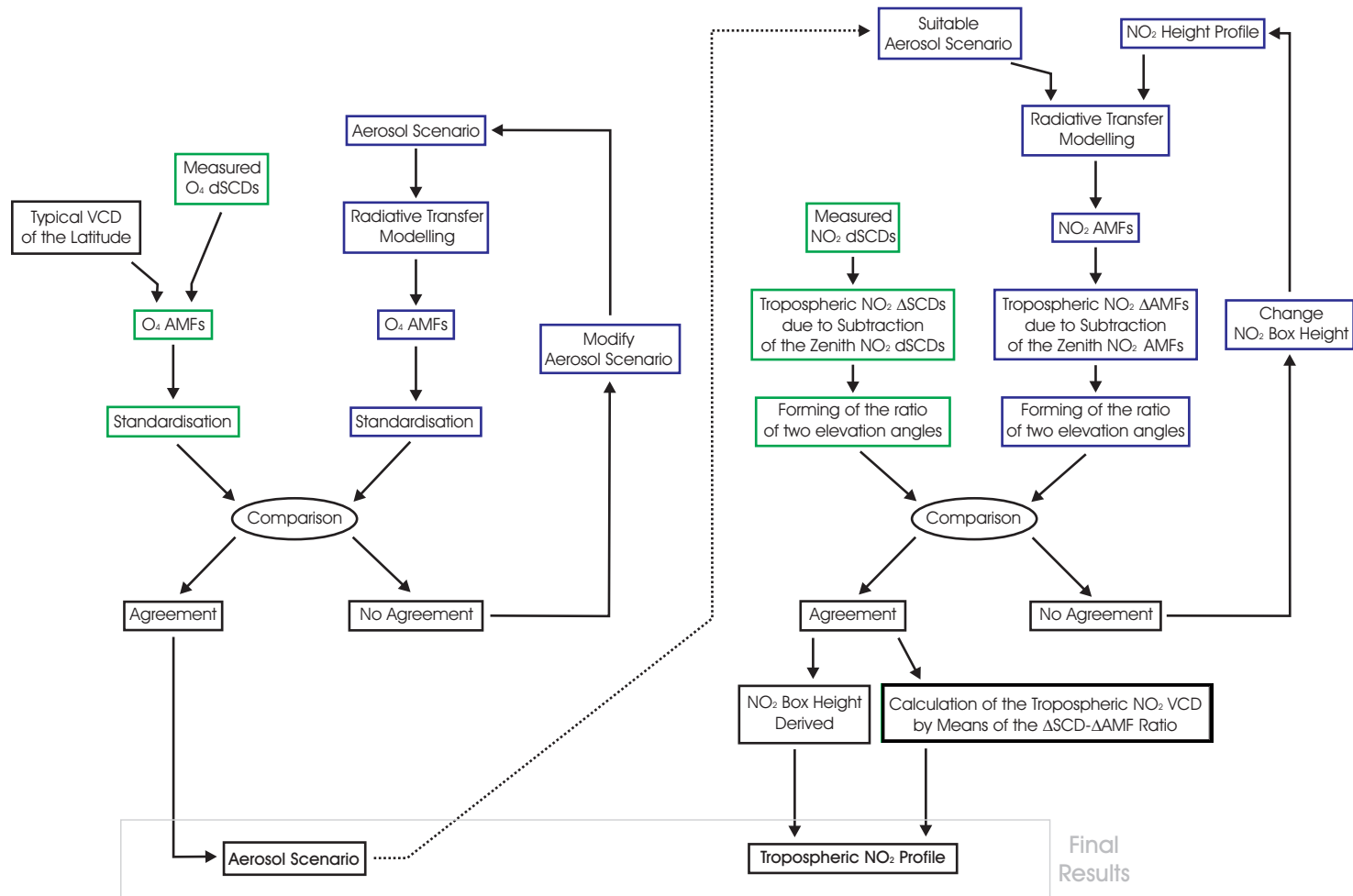


Figure 4.3: Sketch of the retrieval process. Left: the retrieval of the aerosol scenario, right: the derivation of the tropospheric trace gas profile (here  $NO_2$ ) is shown for which the aerosol profile must be known (dotted line). Green boxes are measurement-based, blue boxes are based on radiative transfer and preparation steps of radiative transfer modelling, respectively.

for a series of elevation angles in order to determine the adequate aerosol scenario. Secondly, this best-matching aerosol scenario is taken as input for AMF calculations of the trace gas of interest to derive its height profile. The details of this method are sketched in Figure 4.3 for  $\text{NO}_2$  as the trace gas of interest.

For the retrieval of the aerosol height profile,  $\text{O}_4$  air mass factors for several aerosol scenarios have to be calculated. Since the bulk of the aerosol is expected to be present in the lower atmosphere (in particular, in the boundary layer), box profiles (i.e. profiles with constant aerosol properties from the surface up to a certain altitude and zero extinction above) can be assumed. Aerosol profiles of this type are likely to occur in well mixed boundary layers. Yet also exponentially decreasing profiles of the aerosol extinction with altitude can be taken into account. A selection of aerosol scenarios are listed in Table 4.1, for which  $\text{O}_4$  air mass factors were calculated with Tracy. In Figure 4.4, the air mass factors are plotted as a function of the logarithm of the elevation angle for 70° solar zenith angle. The highest  $\text{O}_4$  air mass factors occur when no aerosols are included, and the AMF generally decreases with increasing aerosol load, except for the zenith direction. Furthermore, the  $\text{O}_4$  AMFs of the exponentially decreasing scenarios vary less strongly with aerosol extinction than the AMFs for the box profiles with equal aerosol extinction.

Table 4.1: *Applied aerosol profiles for the calculation of  $\text{O}_4$  air mass factors.*

	Type	Aerosol extinction [ $\text{km}^{-1}$ ]	Height [km]
Scenario 1	(no aerosols)	0	0
Scenario 2	box	0.025	2
Scenario 3	box	0.025	3
Scenario 4	box	0.035	2
Scenario 5	box	0.05	2
Scenario 6	box	0.1	1
Scenario 7	box	0.25	2
Scenario 8	box	0.5	1
Scenario 9	exp. decrease	0.05 (at surface)	2.7 (scale height)
Scenario 10	exp. decrease	0.1 (at surface)	2.7 (scale height)

In the following, the measured  $\text{O}_4$  SCDs must be converted into AMFs using a vertical column density calculated from a typical mid-latitude air density profile. Both measured and modelled AMFs were converted to dAMFs by subtracting the respective zenith sky AMF at noon (which is referred to as standardisation in Figure 4.3). This procedure must be applied to all scenarios listed in Table 4.1. Afterwards, the measured dAMFs are compared with the calculated dAMFs of the different scenarios. The best matching scenario can be taken in the further calculation of

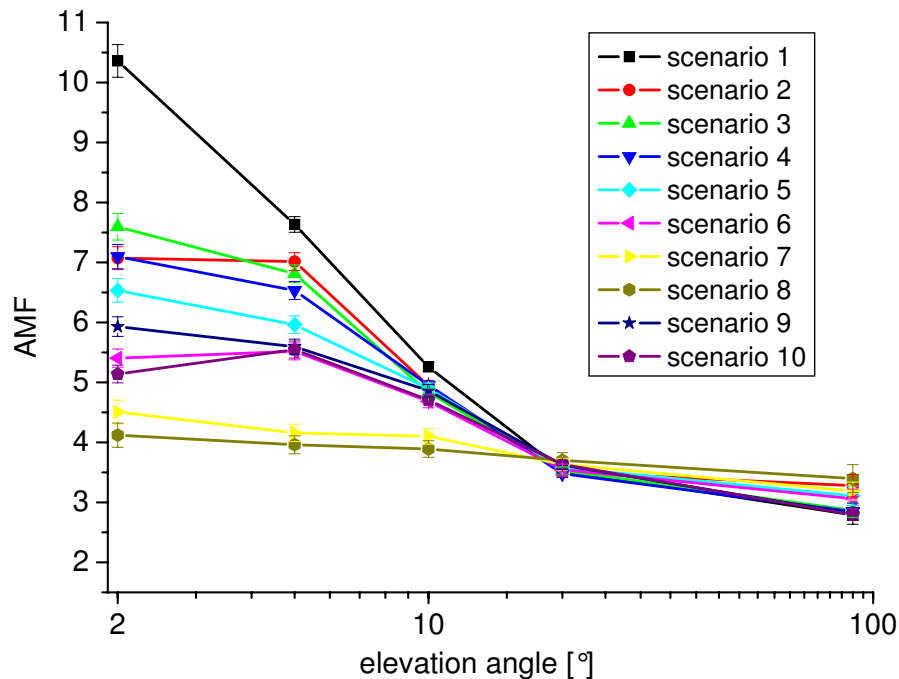


Figure 4.4: Calculated  $O_4$  air mass factors as a function of the logarithm of the elevation angle for  $70^\circ$  solar zenith angle,  $440\text{ nm}$  and a Henyey-Greenstein phase function with an asymmetry coefficient of  $0.65$  [Sinreich et al., 2005]. The  $O_4$  AMFs decrease with higher elevation angle and higher aerosol extinction.

the trace gas profile. Thereby, some deviations in the agreement might have to be accepted owing to the simplified aerosol profile shape or possibly other factors, e.g. an incorrect scattering phase function.

To illustrate the potential of MAX-DOAS  $O_4$  measurements to retrieve information on the aerosol extinction profile, the ratio of  $2^\circ$  and  $90^\circ$  elevation angles of calculated  $O_4$  AMFs as a function of aerosol extinction coefficient for a box profile with  $2\text{ km}$  height is shown in Figure 4.5. This plot also demonstrates the strong sensitivity of  $O_4$  AMFs to aerosols, in particular in the presence of low aerosol extinction. As shown in Figure 4.5, the MAX-DOAS measurements in this instance are sensitive to visibilities above  $16\text{ km}$  (the visibility corresponds to approximately  $3.9$  times the aerosol extinction length), corresponding to aerosol extinctions lower than about  $0.25\text{ km}^{-1}$ . This result was obtained from the ratio of AMFs at different elevations, without consideration of the information gained from the absolute values which would enhance the sensitivity even further, in particular for higher aerosol loads.

The retrieval of the trace gas profile information uses a similar approach as for the retrieval of the aerosol profile described above. Trace gas  $\Delta$ AMFs (hence AMFs

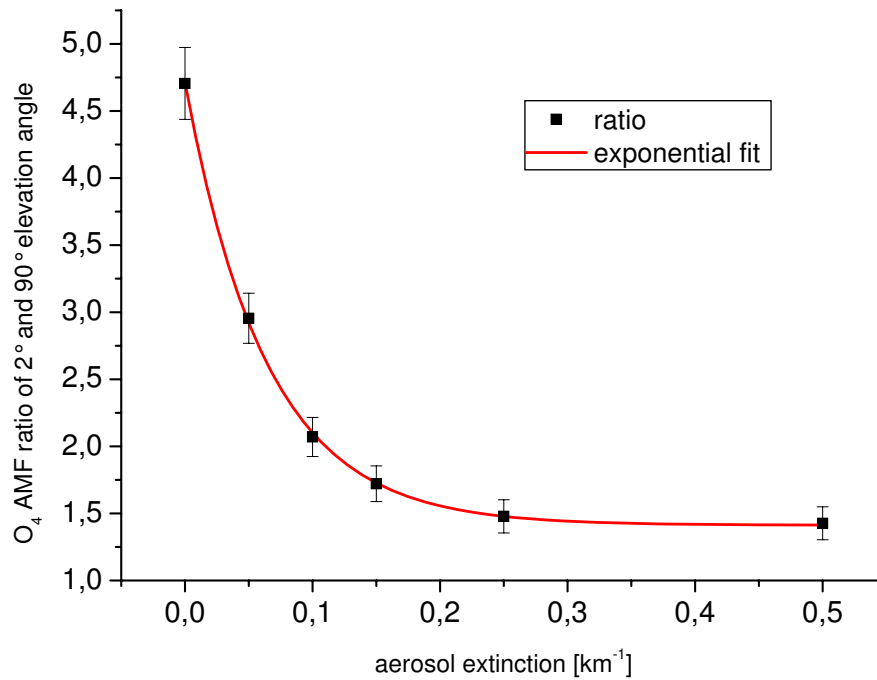


Figure 4.5: Ratio of  $O_4$  air mass factors calculated for 2 and 90 elevation angles versus the aerosol extinction coefficient assumed for a box profile with 2 km height. The sensitivity is remarkable up to  $0.25 \text{ km}^{-1}$  aerosol extinction (corresponding to a visibility of about 16 km).

with respect to the AMF in zenith direction) are calculated using the retrieved aerosol extinction profile and are compared to the observed MAX-DOAS  $\Delta$ SCDs. The tropospheric trace gas distribution can also be represented by a box profile, and the height of the box is varied now in the course of the calculation. For a weak absorber, it is not necessary to vary the concentration in the model since, in contrast to the sensitivity of the  $O_4$  AMF on the absolute aerosol extinction, the trace gas AMF depends only on the shape of the vertical profile and not on the absolute concentration. Therefore, the ratio of the  $\Delta$ AMFs obtained from the measurements at two elevation angles provide sufficient information to derive the height of the tropospheric trace gas box. This requires that the measured ratio matches with the calculated ratio of a specific box height.

An example is shown in Figure 4.6 where the ratios of modeled  $\text{NO}_2$   $\Delta$ AMFs at 2 and 20 elevation angle as a function of the  $\text{NO}_2$  box height are plotted (see Sinreich et al. [2005]). An exponential fit was applied to the data. The corresponding average ratio of the measured  $\text{NO}_2$  slant column density ( $\text{NO}_2$   $\Delta$ SCD ratio) is  $6.0 (\pm 0.3)$  (bold error bar in Figure 4.6). A comparison of this ratio to the modelled ratio leads to an  $\text{NO}_2$  box height of  $1500 (\pm 300)$  m. Finally, the tropospheric trace gas

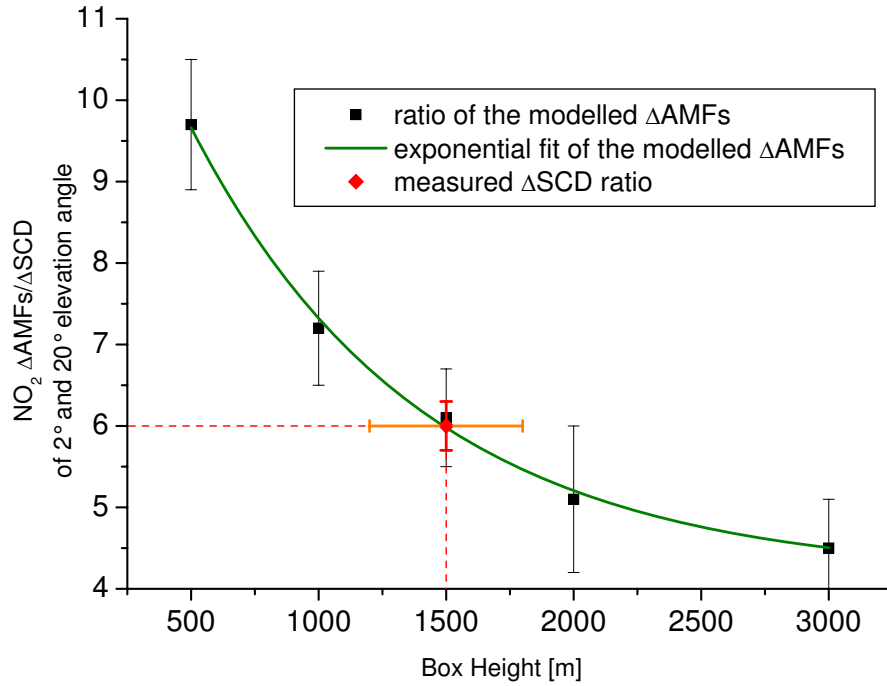


Figure 4.6: Ratios of the modelled  $NO_2$   $\Delta AMFs$  (black) and the measured  $NO_2$   $\Delta SCD$  (red) of 2 and 20 elevation angle. To the modelled ratios an exponential fit (green) was applied. The orange horizontal error bar shows the inaccuracy calculated from both the modelling and the measurement error.

concentration  $c_{trop}$  is retrieved from the calculated  $\Delta AMFs$   $\Delta A_{calc}$  (at the matching height) and the measured  $\Delta SCDs$   $\Delta S_{meas}$  at the two elevation angles  $\alpha_1$  and  $\alpha_2$  divided by the height  $h$  of the box:

$$c_{trop} = \frac{1}{h} \cdot \frac{\Delta S_{meas}(\alpha_1) - \Delta S_{meas}(\alpha_2)}{\Delta A_{calc}(\alpha_1) - \Delta A_{calc}(\alpha_2)} \quad (4.34)$$

This relatively simple approach implies some uncertainties:

1. fitting error of the (differential) SCDs of  $O_4$  and trace gases,
2. errors in the radiation transfer calculation (e.g., statistical errors of the Monte-Carlo approach or due to simplifications in the Mie scattering),
3. possible oversimplification of the assumed aerosol scenario (see Table 4.1) as well as the trace gas distribution,
4. temporal variations during recording the elevation sequence, and
5. effects of clouds.

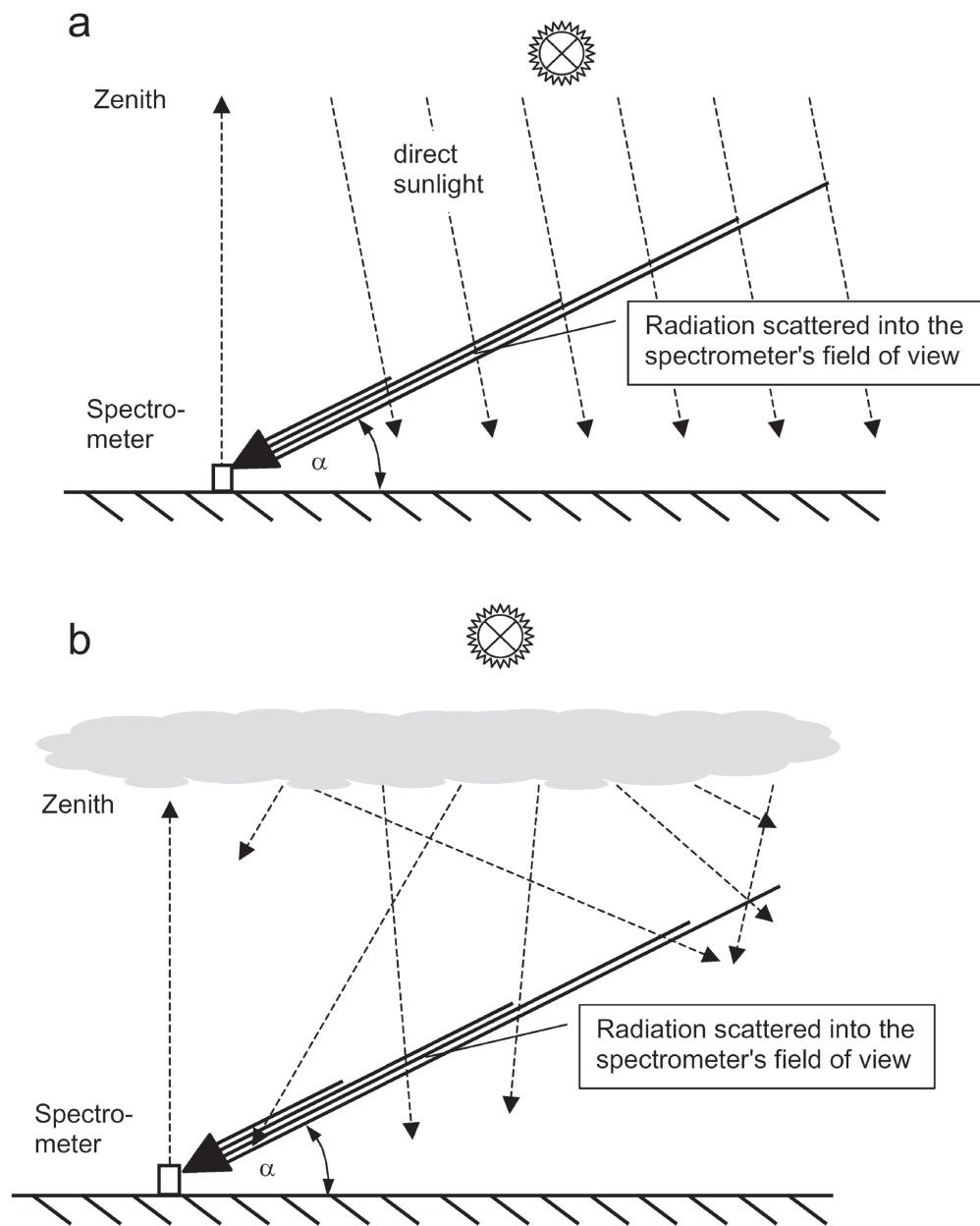


Figure 4.7: (a) Sketch of MAX-DOAS measurement geometry under the clear sky single scattering assumption. (b) MAX-DOAS measurements under cloudy conditions. Photons from sunlight entering the lower atmosphere are successively scattered towards the instrument within the field of view of the telescope.

Error sources (1) and (2) are probably minor (in the order of 10 % or below), compared to the potential influence of the latter two sources of uncertainty.

Concerning uncertainty (3) the aerosol and trace gas scenarios used here are – admittedly – quite coarse in that they only assume a single homogeneous layer with fixed combinations of height and extinction or concentration. More flexible representations of the atmospheric conditions, consisting of e.g., two layers with variable height and extinction or concentration including horizontal inhomogeneities, should considerably reduce uncertainty (3). The dimension of error source (4) depends on the circumstances (e.g. time of day, changing winds in the proximity of strong aerosol or trace gas sources). Thus, temporal variations must be thoroughly considered in the evaluation of the retrieval.

In terms of error source (5), the radiative transfer under clear sky is quite well understood at present, cloudy conditions were not systematically analyzed to date. In the measurement process, photons from sunlight entering the lower atmosphere are successively scattered towards the instrument within the field of view of the telescope. While under clear sky conditions, the single scattering case can be assumed (see Figure 4.7a), under cloudy conditions (assuming the cloud layer being located above the aerosol layer(s)) diffuse light originating from the lower cloud boundary is now scattered towards the instrument (see Figure 4.7b). Clearly, this is likely to change the relative lengths of the light paths at high (i.e. zenith) and low observation elevation angles. Also the (constant) additional light path inside the cloud has to be considered. However, the general dependence of the  $O_4$  slant column density as a function of elevation angle is likely to remain the same. Yet, the influence of clouds can be avoided by selecting cloud free periods when applying this comparison approach.

# 5 Instrumentation

## 5.1 The Mini-MAX-DOAS Instrument and Set-up

A miniaturized Multi AXis Differential Optical Absorption Spectroscopy (Mini-MAX-DOAS) instrument was used for the Auto-MAX-DOAS measurements. The Mini-MAX-DOAS device consists mainly of the following components:

**Entrance optics** : Quartz lens,  $f = 40$  mm,  $d = 20$  mm, field of view  $\sim 0.6^\circ$  coupled to a quartz fiber bundle.

**A commercial miniature spectrometer** : crossed Czerny-Turner spectrograph-detector unit called USB2000 (from Ocean Optics Inc.) and it is placed inside a metal housing. The spectrograph has a spectral resolution of 0.7 nm.

**Electronics** : which control the operation of the device.

The Mini-MAX-DOAS device can be mounted on a tripod or on a metal substrate on the top of a car or any other platform and it can operate during motion or while being stable. Figure 5.1 shows two photographs of the Mini-MAX-DOAS instrument. Left: Opened housing with the main constituents of the Mini-MAX-DOAS. Right: the Mini-MAX-DOAS during operation on a tripod. Figure 5.2 shows a scheme of the parts of Ocean Optics USB2000 spectrograph-detector unit. In this figure, ADC refers to an Analog-to-Digital Converter.

**Operation of the Mini-MAX-DOAS device:** The light is collected via the entrance optics and led by the quartz fiber to the Ocean Optics USB2000 spectrograph-detector system. The light is spectrally dispersed by the grating and then led to the CCD detector by collimating mirrors. See Figure 5.2. The collected signals are converted to digital format by the ADC converter and then saved on a computer hard disk for subsequent spectral evaluation. The spectrograph-detector unit can be cooled by a Peltier cooler to a stable temperature of up to  $30^\circ$  below ambient temperature in order to minimize changes in the optical properties of the spectrograph and to reduce the detector dark current (see section 5.3.2).

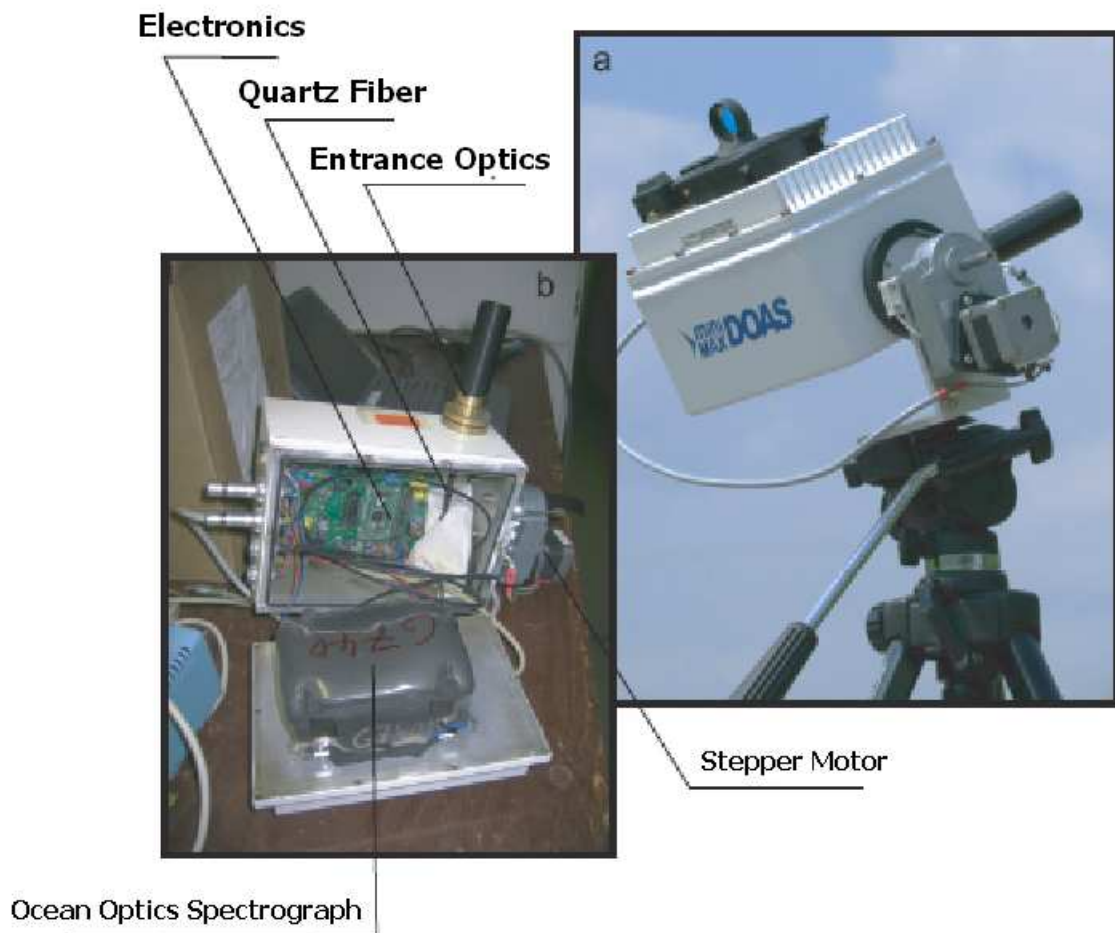


Figure 5.1: *Mini-MAX-DOAS instrument. Left: Opened housing with the main constituents of the Mini-MAX-DOAS. Right: the Mini-MAX-DOAS during operation on a tripod.*

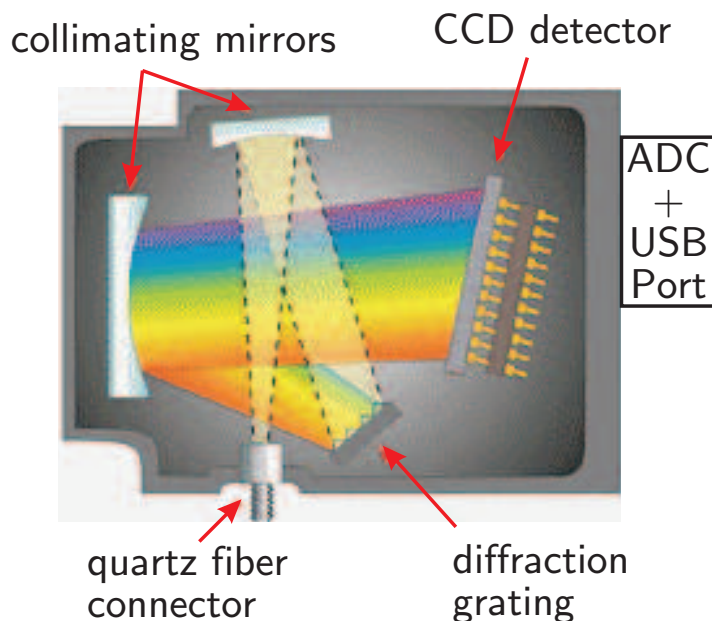


Figure 5.2: A scheme of the parts of Ocean Optics USB2000 spectrograph-detector unit.

In this work, the detector temperature was kept at  $0^{\circ}\text{C}$ . In order to keep the interior of the housing dry and to avoid condensation of water vapor on the grating or mirrors, the Mini-MAX-DOAS housing was sealed and a drying agent (silica gel) was placed inside the housing.

To prevent direct sun light from being scattered into the fiber and also as a protection against rain, a tubular black sun shield (22 mm diameter, 80 mm length) is attached in front of the entrance optics. This sun shield is shown also in Figure 5.1. The entrance optics and the sun shield together will be called the telescope for simplicity. Also a filter (UG5) of thickness 1 mm is used in front of the lens to block the visible light of wavelengths  $<400$  nm to reduce stray light in the spectrometer (see section 5.3.3). Figure 5.3 shows the transmittance of a UG5 filter of 1 mm thickness between wavelengths 220 nm and 800 nm. The transmittance between 400 nm and 650 nm is extremely low in order to block the visible light in this range.

To prepare the Mini-MAX-DOAS device for actual measurements, positioning the device is the initial step. The device is adjusted to direct the telescope to look horizontally as an initial position. This position is called the zero elevation angle, where the elevation angle is defined as the angle between the horizontal and the viewing direction of the telescope. Thus looking up to the zenith direction means elevation angle of  $90^{\circ}$ . The Mini-MAX-DOAS device can be aligned to horizontal level by a water-balance. A stepper motor and gear box with a reed-end switch

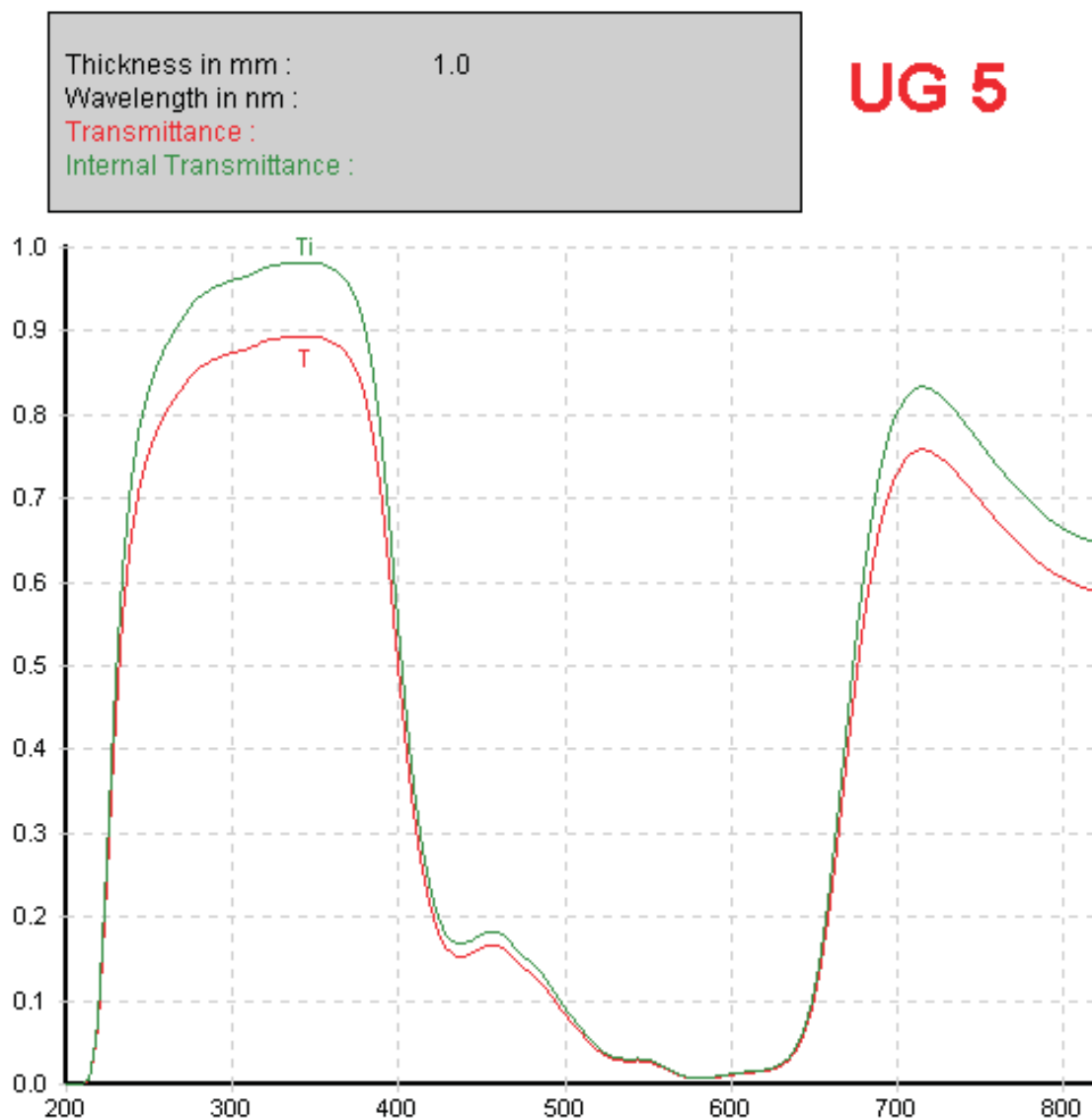


Figure 5.3: *Transmittance of UG5 filter of 1 mm thickness between wavelengths 220 nm and 800 nm.*

have been used for turning the device to point along different elevation angles. This allows the telescope to collect light from different slant directions in the atmosphere. The whole device is moving as one unit to different elevation angles and not only the telescope unit. In other MAX-DOAS set-up configurations, the telescope unit only is moved to different elevation angles (such as as the Polarstern MAX-DOAS instrument) as will be indicated in the next section.

Measurements, stepper motor motion, cooling and electronics are controlled by the software DOASIS (DOAS Intelligent System) [Kraus, 2004] on a laptop computer (also possible with a hand-held pocket computer). The software package DOASIS allows to execute JScript routines which enable a fully automated measurement procedure.

Usually measurements are taken at different elevation angles in repeated sequences of different elevation angles (at least zenith direction and another elevation angle  $<90^\circ$ ). The spectra measured at an elevation of  $90^\circ$  (zenith) are used as Fraunhofer Reference Spectra (FRS) in the spectral retrieval. While the power of the spectrograph-detector unit is provided by the USB port, the cooling and stepper motor movement need a 12 V power supply with 4 A peak current at maximum cooling. In this work, a commercial car battery of 12 V was used during measurements.

Using a car as a mobile platform for the Mini-MAX-DOAS enables more possibilities for measurement strategies and enables easier access to remote areas with interesting measurements sites (such as industrial areas, heavily polluted urban areas, mixed urban-industrial areas and megacities). The Mini-MAX-DOAS instrument was installed on the roof of a car (in this work: The VW bus of the IUP Heidelberg and another private rented car).

The instrument was attached to a metal plate (100 cm  $\times$  80 cm) fixed with screws on the luggage carrier on the car roof. The USB cable and power cable of length of about 2 m were connecting the Mini-MAX-DOAS instrument to the indoor set-up: the laptop computer and the battery. All measurements, stepper motor motion and the detector temperature were continuously controlled by the measurement script (see above).

Figure 5.4 shows an overview of the complete set-up of the Mini-MAX-DOAS instrument on an automobile platform (Auto-MAX-DOAS).

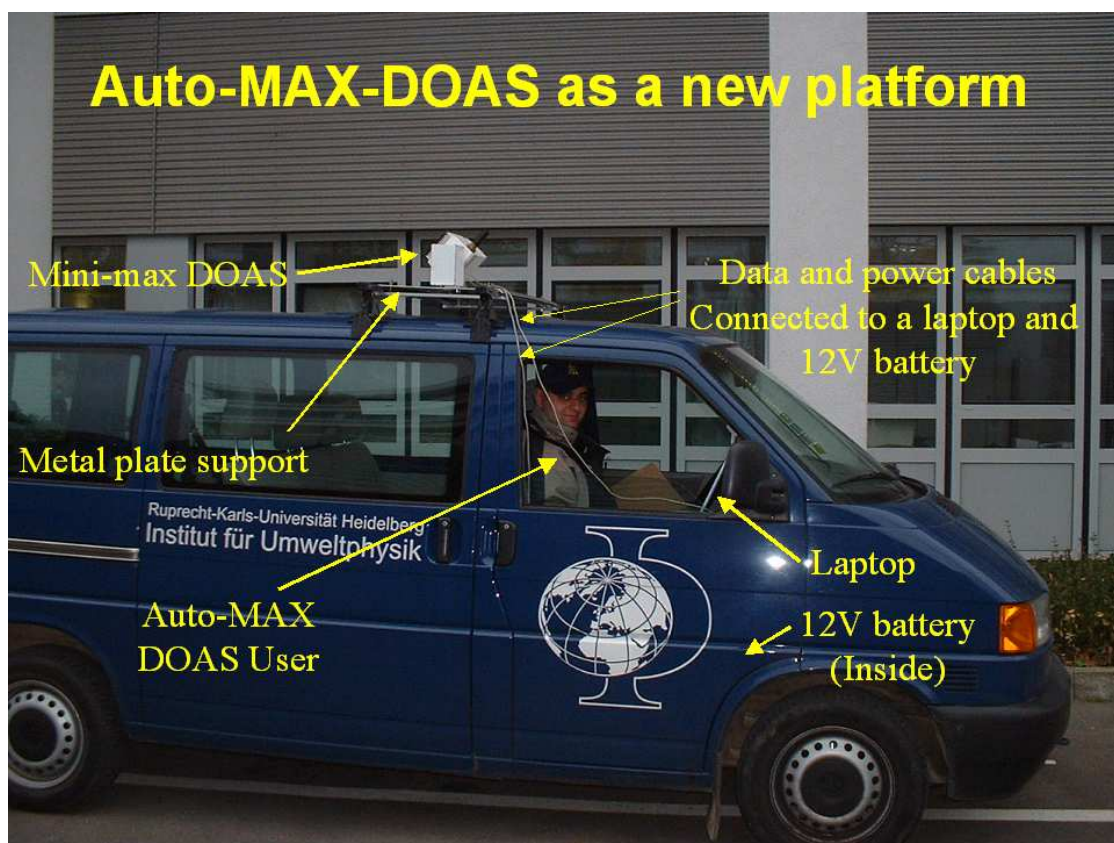


Figure 5.4: Overview of the complete set-up of the Mini-MAX-DOAS instrument on an automobile platform (Auto-MAX-DOAS).

## 5.2 The Polarstern Instrument and Set-up

The other instrument type used for MAX-DOAS measurements in this work was the Polarstern Instrument. It earned this name from its frequent use on board the Research Vessel Polarstern (RV Polarstern), both, in this work and during previous measurement campaigns. This instrument was also used in this work during the DANDELIONS campaign in the Netherlands. During use on board RV Polarstern, the Polarstern Instrument is specially adapted in order to allow for its smooth operation on the moving ship as will be explained further in this section.

The constituents and operation of the Polarstern Instrument are more sophisticated than those of the Mini-MAX-DOAS instruments. The main constituents of the Polarstern Instrument can be divided into : **outdoor set-up** and **indoor set-up** and the **connecting cables** between them.

Here, the structure and operation of each of the above constituents will be explained:

(A) **The outdoor set-up**: Consists of **four telescope units** which are arranged in parallel to each other and **a cardanic suspension system** for stabilizing the telescope units and compensating for the rolling and pitching movements of the ship during motion in the sea. Figure 5.5 shows the whole cardanic suspension system (left picture) and the four telescopes units in their grey housings (right picture).

The **cardanic suspension system** consists of a 30 kg lead weight which is suspended along a vertical metal rod supporting the four telescope units. The vertical rod is attached to a rigid frame fixed with respect to the ship, such that the rod is free to oscillate in any vertical plane. A nail board is attached at the bottom of the weight so that it hangs with its nails immersed into the bristles of a conventional brush fixed with respect to the ship. The weight ensures a constant vertical positioning of the supporting rod even as the ship pitches and rolls, while the nail board-conventional brush system provides enough friction to damp any oscillation of the suspension as it moves to regain its vertical alignment.

The **four telescope units** in their grey housings contain several components. These components can be classified according to their function into three groups:

1. **Components for measurements** (during daylight):
  - a) **A quartz lens** with a focal length of 20 mm which focusses the light (scattered sunlight during daytime measurements) received by the viewing cone of the telescope on a separate quartz fiber bundle
  - b) Each of the **quartz fiber bundles** consists of seven fibers (with 150  $\mu\text{m}$  diameter each) and they are arranged vertically on top of each other. These fiber bundles lead the light from the outdoor telescopes to the the

indoor spectrometer. The field of view is determined to be  $1.1^\circ$ . The accuracy is estimated to be  $0.5^\circ$ .

- c) In each telescope unit, a **stepper motor** with a reed-end switch used to adjust it individually to any elevation angle between horizon ( $0^\circ$ ) and zenith ( $90^\circ$ ). Unfortunately, due to the failure of the stepper motors, it was chosen to fix each telescope at a certain elevation angle and keep it measuring at that angle. The elevation angles were chosen to be  $3^\circ$ ,  $10^\circ$  and  $90^\circ$ .

## 2. Components for calibration (during night):

- a) **A halogen lamp:** its spectrum is taken at night during calibrations and this spectrum delivers information on the pixel-to-pixel variability of the detector.
- b) **Mercury-neon lamp:** its spectrum is taken also at night for calibration. The line spectrum is used for the determination of instrumental line shape as well as for spectral calibration.

## 3. Components for protection purposes and to maintain the quality of measurements:

- a) **A shutter at the entrance of each telescope:** to prevent direct sunlight from entering the telescope and damaging the detector when the telescope is looking directly at the sun. The light intensity at the front of the telescope's unit is detected by a photo diode and when the telescope is pointing at the sun, the shutter is automatically closed. Also shutters are closed at night so calibration measurements can be performed without being affected by external light sources (e.g. moon, stars or artificial lights).
- b) **A heating coil:** placed adjacent to the internal wall of each telescope's unit housing. This heating coil ensures that the temperature of the telescope unit keeps above the freezing point so that ice or hoarfrost could not form on the telescope. This heating also ensures that there is no water vapor condensation on the lens.

One telescope was not included in measurements because in the original design of the instrument it was supposed to be connected to a spectrograph operate at wavelengths between 400 nm and 700 nm (in the visible range) which was not used

in this work.

The other three telescopes were connected to a commercial instrument operating in the range between 320 nm and 460 nm (see below).

Figure 5.6 shows the connecting cables between the outdoor set-up and the indoor set-up on board of the RV Polarstern. Cables include power cables and the fiber bundles. The left Picture shows the connecting cables emerging from the telescopes and entering the fiber-optics inlet. The right picture shows the inlet from inside.

**The indoor set-up** consists of a **PC**, **spectrometer**, **CCD camera** and **Isel controllers** (for lamps, stepper motor and shutters). Figure 5.7 shows the indoor set-up on board of the RV Polarstern.

The **spectrograph** is a commercial instrument with 300 mm focal length (Acton model 300). It covers the wavelength range from approximately 320 nm to 460 nm and had a resolution of 0.7 nm FWHM. As illustrated in Figure 5.8, the incoming light from the three telescopes is led to a grating via mirrors where it is spectrally dispersed. A second mirror focusses the light onto a two-dimensional imaging CCD detector (Andor model DV420-OE) with 1024 horizontal and 256 vertical pixels (see Figure 5.8).

Figure 5.9 shows an example of a measurement. Three areas with measurement signal which are separated from each other by blue background correspond to the light of the three telescopes. Each of the three light bands consists of seven smaller light bands. These seven bands correspond to the seven fibers which constitute the bundle. Since the entrance slit consists of the three fiber bundles on top of each other separated by some distance (see Figure 5.8), the light bands fall on the CCD detector as shown in Figure 5.9. Each of the three light bands in Figure 5.9 corresponds to the light coming from one fiber bundle but after being dispersed by the grating and directed onto the CCD detector by mirrors (see Figure 5.8). The light intensity is color coded. Red means highest intensity. Then come the yellow, the green and finally the blue with the lowest intensity. The blue areas represent the background (CCD detector surface not illuminated by light from telescopes). For the retrieval of trace gases, the two-dimensional image of the CCD detector (Figure 5.9) was converted into three one-dimensional spectra, corresponding to the three areas with measurement signal. The lines of each area with measurement signal were added and saved in the binary MFC-format which is suitable for retrieval [Gomer et al., 1995].

While the spectrograph was heated to a stable temperature above +30°C in order to minimize changes in its optical properties, the CCD detector was cooled to -30°C in order to reduce detector dark current. The signal of the CCD detector was transferred to a PC via a specialized Andor PCI-board.

A special USB-operated control unit enabled to individually switch on and off the different lamps of the telescopes as well as to open and close the different shutters. This was also possible via commands from the PC.



Figure 5.5: *The outdoor part of the Polarstern instrument. Left: the whole outdoor part including the telescopes housing, cardanic system and the stabilizing nail board with conventional brush. Right: the four telescopes in their grey housings pointing to different elevation angles during measurements.*



Figure 5.6: *On board of the RV Polarstern: Cables include power cables and the fiber bundles cables. Left: the cables from telescopes going down to the indoor set-up in the (A) Deck of RV Polarstern. Right: the inlet of the cables to the indoor set-up.*

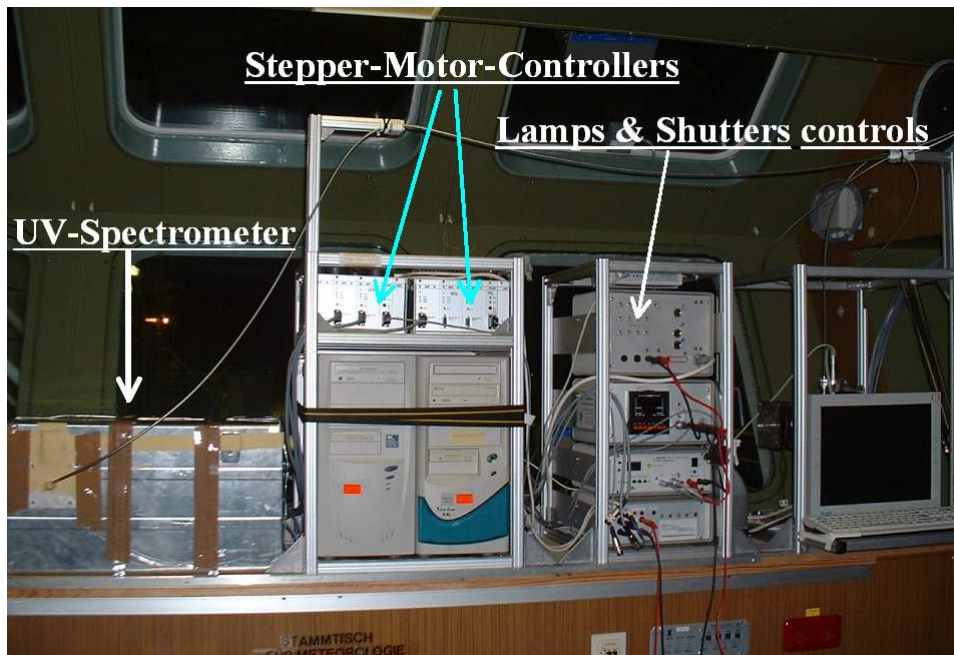


Figure 5.7: *Indoor set-up on board of the RV Polarstern. It consists of a PC, spectrometer, CCD camera and Isel controllers for lamps, stepper motor and shutters.*

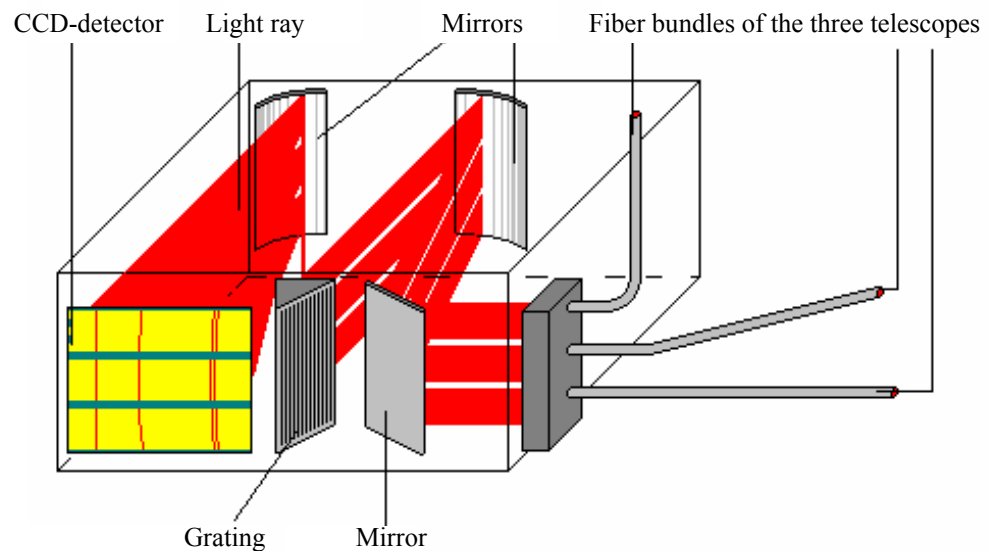


Figure 5.8: *Illustration of the light paths from the fiber bundles of the three telescopes to the two-dimensional CCD detector of the Polarstern instrument.*

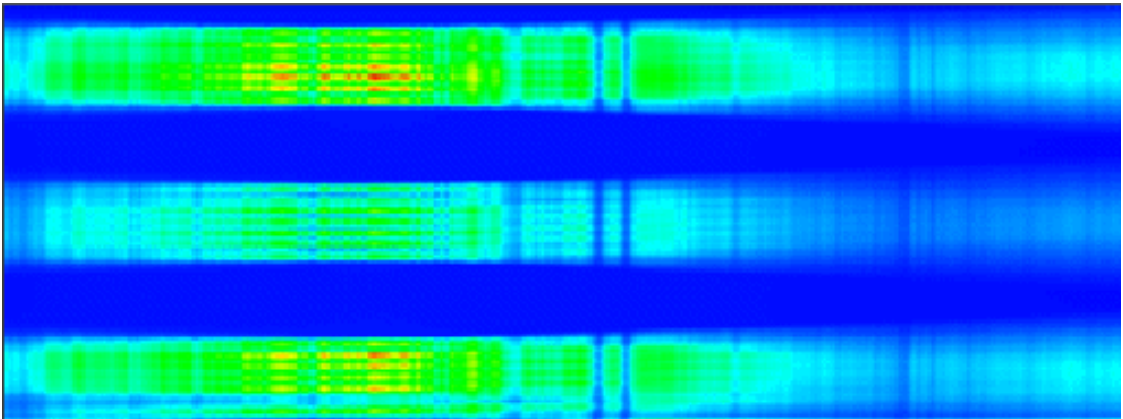


Figure 5.9: *Example of an image of the CCD chip with 256 horizontal lines and 1024 pixels. The light intensity is color coded. Red means highest intensity then come the yellow, green and blue.*

The Polarstern instrument was operated by a specialized measurement program [Frieß, 2001]. The measurement routine was set to acquire measurement spectra for solar zenith angles (SZA) below  $97^\circ$ .

At solar zenith angles above  $97^\circ$ , the shutters closed automatically. This was done periodically in order to acquire spectra of dark current and offset (see section 5.3) as well as mercury-neon and halogen lamp spectra. The SZA was also calculated by the measurement program using universal time provided by the computer clock and the geographical position. The geographical position was updated manually several times per day during the cruise on the RV Polarstern.

## 5.3 Corrections on the Spectra

The measured raw spectra need to be corrected for background signals prior to the DOAS analysis. This includes electronic offset, dark current and spectrograph stray light.

### 5.3.1 Electronic Offset

The electronic offset is an artificial electronic signal which is added to the measurement signal to avoid negative signals caused by electronic noise at low intensity level. Negative signals cannot be handled by the analog-digital converter.

Since the offset signal can disturb the retrieval of trace gases it has to be subtracted from each scan. For correction, the offset spectrum can be acquired when the detector is not exposed to light. The integration time has to be chosen as short as possible to avoid any other signal than the electronic offset.

For statistical reasons, the electronic offset is usually measured by adding many scans. It is assumed that, except for detector noise, it does not change by time so that it can be subtracted from each spectrum. Thereby, the ratio of the number of scans of the measurement spectrum and of the offset spectrum have to be multiplied with the offset spectrum in order to match the offset signal in the measurement spectrum.

It is noteworthy that the intensity of the electronic offset may change if the temperature varies.

### 5.3.2 Dark Current

Another signal which is overlaid to the measured spectra is the dark current. It arises due to self discharge of the CCD detector. Thermally excited electrons contribute to the charge of the measurement signal so that the dark current spectrum is superimposed to the measurement signal. The dark current is proportional to the Boltzmann factor  $e^{-\Delta E/kT}$ . Since it increases exponentially with temperature it can be significantly reduced by cooling the detector.

The dark current is acquired also in the absence of light. A single scan with an integration time as long as possible is taken and corrected for the offset signal.

It is assumed that the dark current signal is proportional to the integration time of the measurement. Hence, the dark current signal can easily be corrected by subtracting the dark current spectrum weighted with the ratio of the integration times of the measured spectrum and the dark current spectrum.

In reality, the proportionality is not fully correct because the dark current is slightly dependent on the saturation level of each CCD pixel [Stutz, 1991]. Nevertheless, the proportional correction accounts for the dark current approximately correct and

was applied in this work.

### 5.3.3 Spectrograph Stray Light

Stray light in the spectrometer is light which is generated from higher diffraction orders of the light diffracted by the grating. Nevertheless it may reach the detector and lead to an additional signal which can significantly disturb the original measurement signal.

Like the electronic offset and dark current, it has to be accounted for. However, the correction is much more difficult because the intensity of stray light depends on the light intensity, also of wavelengths which are not measured. The intensity of stray light cannot be directly estimated from the light spectrum. Yet in practice, to some extent, the stray light can be accounted for during the spectral analysis procedure by fitting an additional polynomial. It is of advantage to identify the stray light before analyzing the measurement spectra.

Figure 5.10 shows the stray light areas in the background areas on the CCD chip between the three measurements bands ( measurements area 1, measurements area 2, measurements area 3).

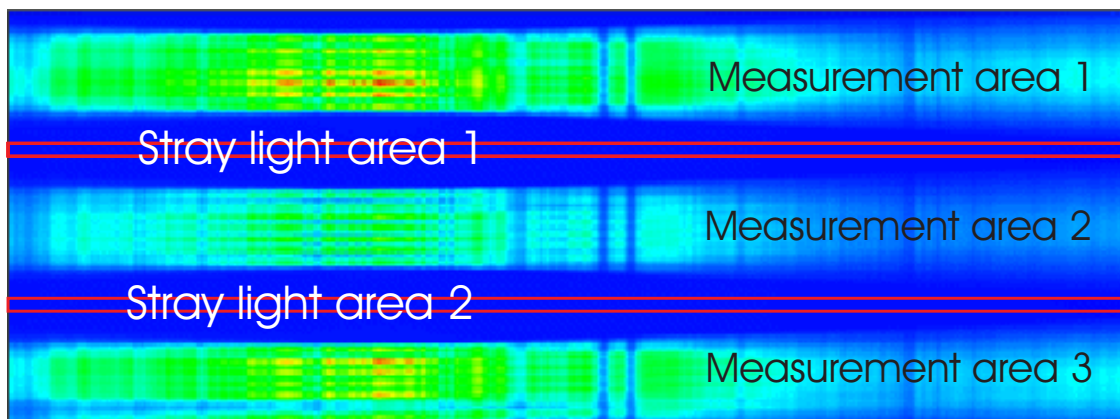


Figure 5.10: *The stray light areas in the background areas on the CCD chip between the three measurements bands (measurements area 1, measurements area 2, measurements area 3).*

There it turned out that spectrograph stray light only plays a minor role and does not require a special correction. However, the two-dimensional CCD-chip of the Polarstern instrument detects the light of three telescopes simultaneously. This holds the risk that light from one line of the CCD-chip reaches another line owing to e.g. reflections in the spectrograph.

This is apparent in the measured images, where elevated values occur also in the background areas (blue areas between the three measurements areas, see Figure 5.10). To further investigate the stray light, the minimum areas on the CCD-chip between the measurement areas were searched.

A minimum base of about ten lines was identified in which the intensity is relatively constant, each in the middle between the measurement areas (see Figure 5.10). Based on that, it was concluded that besides offset and dark current, only spectrograph stray light could be found there. It turned out that stray light could amount to up to 40 % of the measurement signal. Typical values were between 3 and 15 %. This allows to subtract the values of the stray light from the measurement areas, weighted with the number of lines each, which was done in this work.



# 6 Results from Polarstern Measurements

## 6.1 Polarstern Overview

The Polarstern research and supply vessel is the most important tool in Germany's polar research program. The vessel is owned by the German Government and is provided to the Alfred Wegener Institute (AWI) for Polar and Marine Research in the Helmholtz Association as a large scale facility by the Minister of Science and Education. Since it was first commissioned in 1982, the Polarstern has completed a total of 30 expeditions to the Arctic and Antarctic. She was specially designed for working in the polar seas and is currently the most sophisticated polar research vessel in the world. The Polarstern is a double hulled icebreaker, which would enable her to overwinter in the ice sheets of the polar seas. Polarstern can break through ice 1.5 meters thick at a speed of approx. 5 knots. Thicker ice must be broken by ramming. Figure 6.1 shows a picture of research vessel Polarstern (RV Polarstern). Table 6.1 shows some technical data about Polarstern.



Figure 6.1: *Research Vessel Polarstern*

Table 6.1: *Polarstern technical data.*

Icebreaker Design	Hamburgische Schiffbau-Versuchsanstalt
Overall Length	118 m
Height to Main Deck	13.6 m
Draught	max. 11.2 m
Maximum Displacement	17,300 t
Light Weight	11,820 t
Engine Power (4 engines)	approx. 14,000 kW (20,000 bhp)
Maximum Speed	16 kn

The Polarstern spends almost 320 days a year at sea. Between November and March it usually sails to and around the waters of the Antarctic, while the northern summer months are spent in Arctic waters.

The MAX-DOAS instrument (of the IUP, Heidelberg University) was mounted on board of Polarstern during the last few years (since 2000) in its cruises between Bremerhaven (Germany) and Antarctic taking continuous measurements.

### Ship weather station

The RV Polarstern has a meteorological observatory, which is run by the shipping department of the German weather service (DWD)<sup>1</sup> and maintained scientifically and technically by the AWI. The observatory provides weather forecasts as well as auxiliary weather information for the ship command, scientists and helicopter service as well as for the long-term recording and registration of meteorological parameters. The observatory is fitted with highly accurate and continuously recording sensors. The observatory has its own data acquisition system (2 PCs, based on LINUX) for local data acquisition as well as for the transfer of relevant data to the PODAS system. Other high-end technical equipment enables the reception of weather information and satellite images. The German weather service supplies the requested forecast data via e-mail. An hourly weather report is also automatically generated, and enhanced with visual observations and transmitted as above.

### Synoptic Observations

The observations are carried out every three hours. They include measurements and visual observations. All data are 10 minute averages or instantaneous observations at the given time in UTC. During night time when the weather observer is not on duty the 3 hourly meteorological observations are performed automatically.

<sup>1</sup>DWD: Deutsche Wetter Dienst / German Weather Service

Thus, no visual observations are available. All data are generally coded according the definitions of the World Meteorological Organization (WMO) (FM12/13) and transferred without delay into the Global Telecommunication System GTS were they contribute to the world wide weather forecasts.

### Upper Air Soundings

Upper air balloon soundings are carried out routinely. They include profile measurements of pressure, temperature, relative humidity and wind vector. Vertical ozone profiles are also occasionally measured. Usually, the soundings start from the heliport (10 m above sea level) and end between 15 and 37 km.

The computer system on board continuously captures and stores meteorological, oceanographic and other data as required. For the soundings VAISALA radiosondes, carried by helium-filled balloons (TOTEX 350 - 1500) are used. The data is coded (FM35-Temp) and transferred directly to the Global Telecommunication System (GTS) by a Data Collecting Platform (DCP) where they contribute to weather forecasting.

To obtain the ozone profiles an additional ozone sensor (VAISALA, ECC5A/6A) has been attached to the radiosonde. The wind vector is determined with the aid of the OMEGA/GPS navigation system. Data reception and evaluation were originally carried out by a MicroCora System (VAISALA), however in 1993 the MicroCora was replaced by the DigiCora (VAISALA).

## 6.2 The cruise ANT-XXI

Measurements were continuously carried out during the twenty first Antarctic cruise ANT-XXI during 2003/2004. Between 22.10.2003 and 02.06.2004, Polarstern completed five cruise legs taking the route :

Bremerhaven - Cape Town - Antarctic - Cape Town - Bremerhaven.

Table 6.2 shows the time periods of the five legs of the cruise ANT-XXI and their departure and arrival stations.

Figure 6.2 shows route of the first leg of the cruise (ANT-XXI/1). Also table 6.3 shows the latitudes reached by the RV Polarstern around noon time at each day during the first leg of the cruise.

During the first leg of the cruise, continuous trace gases measurements using the Polarstern MAX-DOAS Instrument of the IUP Heidelberg were carried out. Atmospheric trace gases like NO<sub>2</sub>, BrO, O<sub>3</sub> besides the oxygen dimer O<sub>4</sub> were detected using the DOAS retrieval.

Measurements were continuously carried out during the daylight from twilight to twilight. The measurements were supposed to be carried out at five different elevation

Table 6.2: *Time periods of the five legs of the cruise ANT-XXI and their departure and destination stations.*

Leg Number	From	To
Leg (1) ANT-XXI/1	Bremerhaven (22.10.2003)	Cape Town (15.11.2003)
Leg (2) ANT-XXI/2	Cape Town (17.11.2003)	Cape Town (18.01.2004)
Leg (3) ANT-XXI/3	Cape Town (21.01.2004)	Cape Town (25.03.2004)
Leg (4) ANT-XXI/4	Cape Town (27.03.2004)	Cape Town (06.05.2004)
Leg (5) ANT-XXI/5	Cape Town (07.05.2004)	Bremerhaven (02.06.2004)

angles for each telescope using the stepper motors to move them but unfortunately the stepper motor controllers had some problems so they did not work properly then each of the three telescopes had to be fixed at their positions at elevation angles  $3^\circ$ ,  $10^\circ$  and  $90^\circ$ .

The meteorological conditions during the campaign were obtained from the Polarstern Synoptic Observations and Upper Air Soundings. The meteorological conditions can affect important parameters for the measurements in direct or indirect ways. Such parameters could strongly affect the attempt to attribute the detected gases concentrations to their sources, predict the fate of the detected gases and also the ability to calculate the concentrations of detected gases themselves in terms of absolute units such as parts per trillions in volume pptv.

Such parameters -for example- are like:

Proxies for light path distributions (e.g. cloudiness and visibility), air masses transport (e.g. wind speed and direction), aerosol production (e.g. wind speed), height of Boundary Layer (BL) (e.g. vertical temperature profiles). Here we show some of the meteorological conditions during the first leg of the cruise (ANT-XXI/1).

Figures 6.3 and 6.4 show vertical temperature profiles during the first week and the second week of measurements (during the first leg of the cruise) where the Polarstern covered the distance between latitudes  $53^\circ$  N and  $5^\circ$  S. Temperature inversions are noticed on some days during these two weeks: 29.10.2003, 30.10.2003 (see Figure 6.3) and 31.10.2003 and also on 01.11.2003, 03.11.2003, 06.11.2003 and 07.11.2003 (see Figure 6.4).

These temperature inversions can be indicators of the height of the BL above the surface. Notice that for some days there are two lines in the graphs, this means the radio sond measurements were carried out twice at these days for their special importance for the meteorological measurements. Usually for these days, one sond measurement was done in the morning and the other is done in the afternoon so some slight differences in temperature profiles between morning and afternoon should be expected as it is visible in the graph.

Table 6.3: *Latitudes reached by the RV Polarstern around noon time at each day during the first leg of the cruise.*

Date	Time (UTC)	Latitude
22.10.2003	11:45	50
23.10.2003	12:25	48.25
24.10.2003	12:18	45.92
25.10.2003	12:23	45.23
26.10.2003	12:44	41.53
27.10.2003	12:51	36.80
28.10.2003	12:57	31.70
29.10.2003	13:02	28.10
30.10.2003	13:20	24.95
01.11.2003	13:21	19.44
02.11.2003	13:23	13.92
03.11.2003	13:16	8.90
04.11.2003	13:04	5.10
05.11.2003	12:54	2.14
06.11.2003	12:42	-1.38
07.11.2003	12:29	-5.42
08.11.2003	12:16	-9.15
09.11.2003	12:03	-12.96
10.11.2003	11:48	-16.32
11.11.2003	11:33	-19.87
12.11.2003	11:23	-22.83
13.11.2003	11:10	-26.85
14.11.2003	10:56	-31.22

Also comparing the two Figures, it is visible that temperatures during the second week are generally higher than those of the 1st week because Polarstern was moving from the mid latitude regions (first week) to equatorial regions (second week).

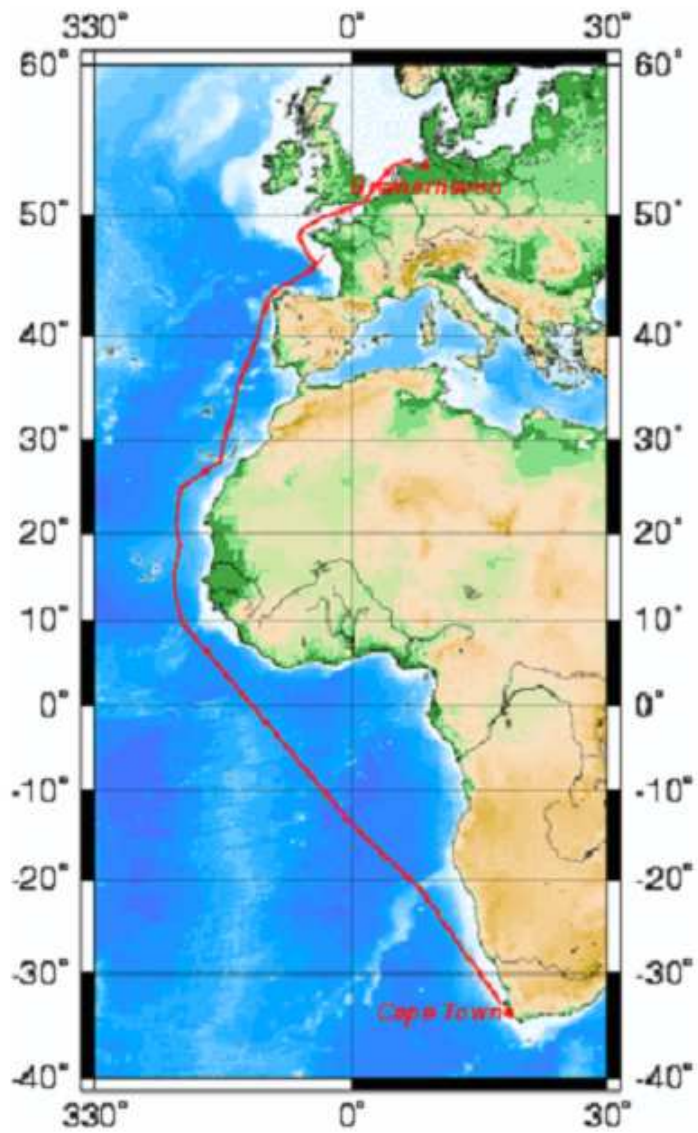


Figure 6.2: *The route of the first leg ANT-XXI/1 of the cruise (Bremerhaven to Cape Town).*

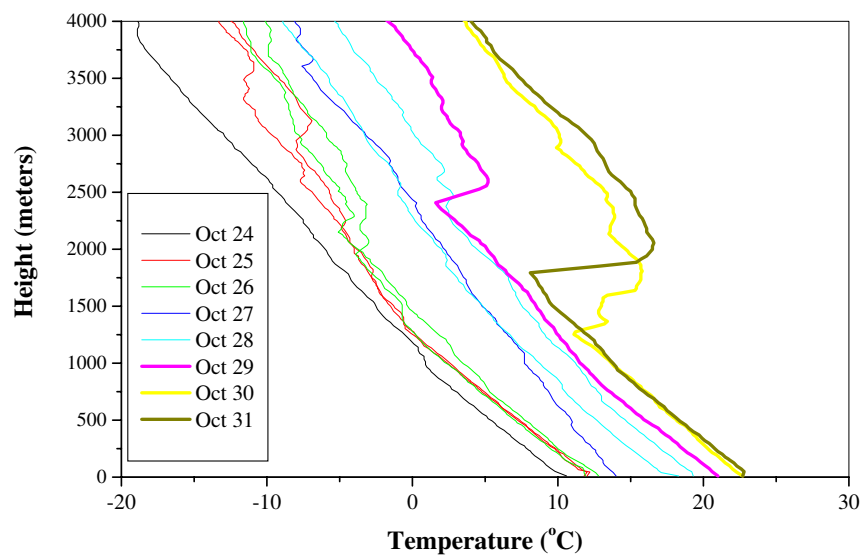


Figure 6.3: *Temperature vertical profiles of the first four kilometers of atmosphere during the first week of measurements of the cruise leg (ANT-XXI/1).*

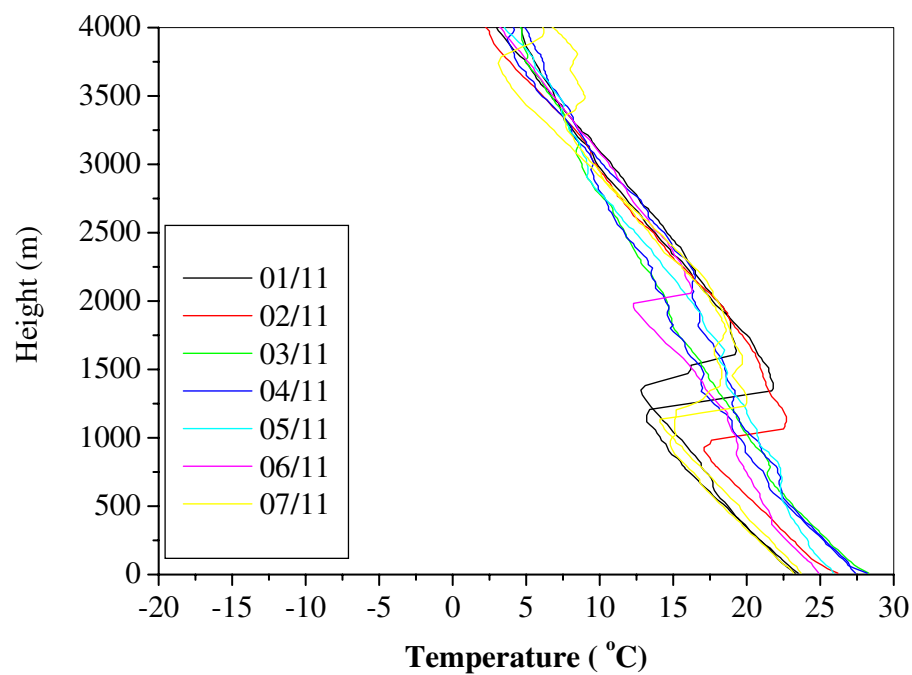


Figure 6.4: *Temperature vertical profiles of the first four kilometers of atmosphere during the second week of measurements of the cruise leg (ANT-XXI/1).* [Source: Upper Air Sounding Data of the Polarstern meteorological observatory (Available on line at: <http://www.awi.de/en/infrastructure/ships/polarstern/>)].

### 6.3 BrO Results

MAX-DOAS measurements were continuously carried out during the five legs of the cruise ANT-XXI. This section presents the results from the first leg of this cruise (ANT-XXI/1) (22.10.2003 - 14.11.2003). During some days, enhanced tropospheric BrO was successfully detected and quantified. The route started at Bremerhaven (Germany) and ended at Cape Town (South Africa). Since BrO exists in the stratosphere and can exist also in the troposphere, it is necessary to differentiate between both. In case of no tropospheric BrO, the dSCDs from the three different elevation angles of MAX-DOAS would not show any difference. While on the other hand, the existence of additional BrO in the troposphere would cause the dSCDs detected by telescopes looking at lower elevation angles  $3^\circ$  and  $10^\circ$  to be higher than that of  $90^\circ$  (zenith) looking telescope.

The dSCDs of BrO were retrieved using the Windoas software (see section ??).

Figures 6.5 and 6.6 show the enhanced tropospheric BrO dSCDs during some days as examples: 26.10.2003, 29.10.2003, 30.10.2003 and 31.10.2003. Appendix A shows the whole time series of BrO dSCDs between 23.10.2003 and 14.11.2003. Elevated tropospheric dSCDs could be seen during these days from the differences between the dSCDs values retrieved from telescopes at elevation angles of  $3^\circ$  and  $10^\circ$  and those retrieved from the telescope at  $90^\circ$  angle (zenith).

These differences indicate the presence of tropospheric concentrations of BrO.

The tropospheric dSCDs could be more clearly shown if they are expressed as the differences between dSCDs at different elevation angles and dSCDs at zenith ( $90^\circ$ ): (dSCDs  $3^\circ$  - dSCDs  $90^\circ$ ) and (dSCDs  $10^\circ$  - dSCDs  $90^\circ$ ). For Simplicity, these two quantities will be called: DSCD $3^\circ$  and DSCD $10^\circ$  respectively.

Figure 6.7 shows an example of the calculation method of both quantities (DSCD $3^\circ$ ) (top) and (DSCD $10^\circ$ ) (bottom) from the data. Figure 6.9 shows DSCD $3^\circ$  and DSCD $10^\circ$  respectively along the latitudes during the 1st leg of the cruise. Figure 6.8 shows the exact positions of the RV Polarstern during the three week of measurements. The diameters of the red dots indicate the relative values of the BrO (DSCDs  $3^\circ$ ), while the white dots indicate days when BrO (DSCDs) could not be detected or days of no measurements.

### 6.4 Radiative Transfer calculations

From the differences of the BrO dSCDs for the different elevation angles, information on the altitude range of the tropospheric BrO-layer can be derived. For that purpose we apply the method that is described in detail in [?].

For a detailed analysis using this method to estimate the altitude range, we selected two (half) days with mostly clear skies and also elevated BrO dSCDs for the telescopes at  $3^\circ$  and  $10^\circ$  elevation angles (29.10.2003 and 31.10.2003). Since cloudiness would cause perturbations in the observed  $O_4$  dSCDs which - in turn - would com-

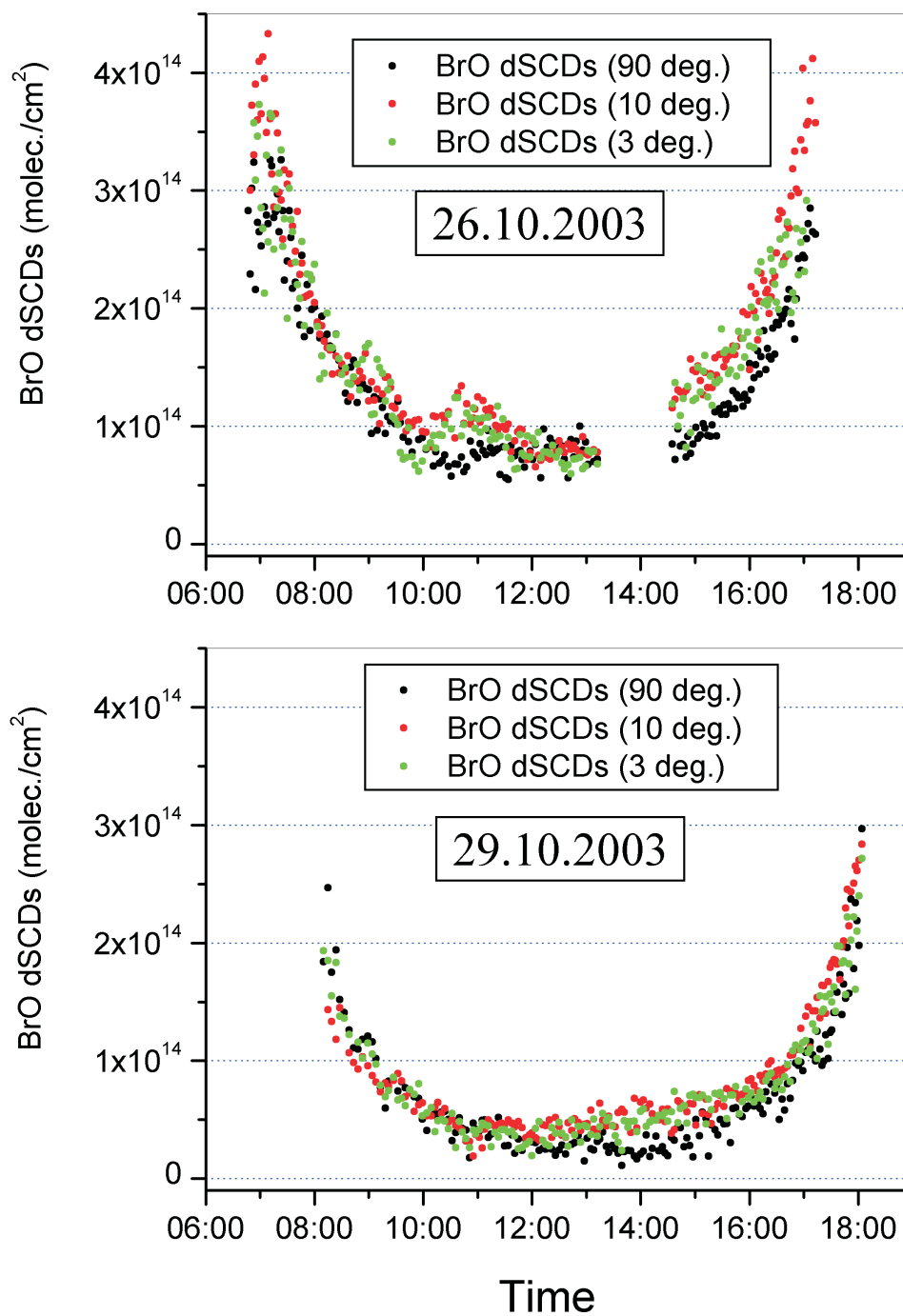


Figure 6.5: *Two days with enhanced tropospheric BrO dSCDs: 26.10.2003 and 29.10.2003.*

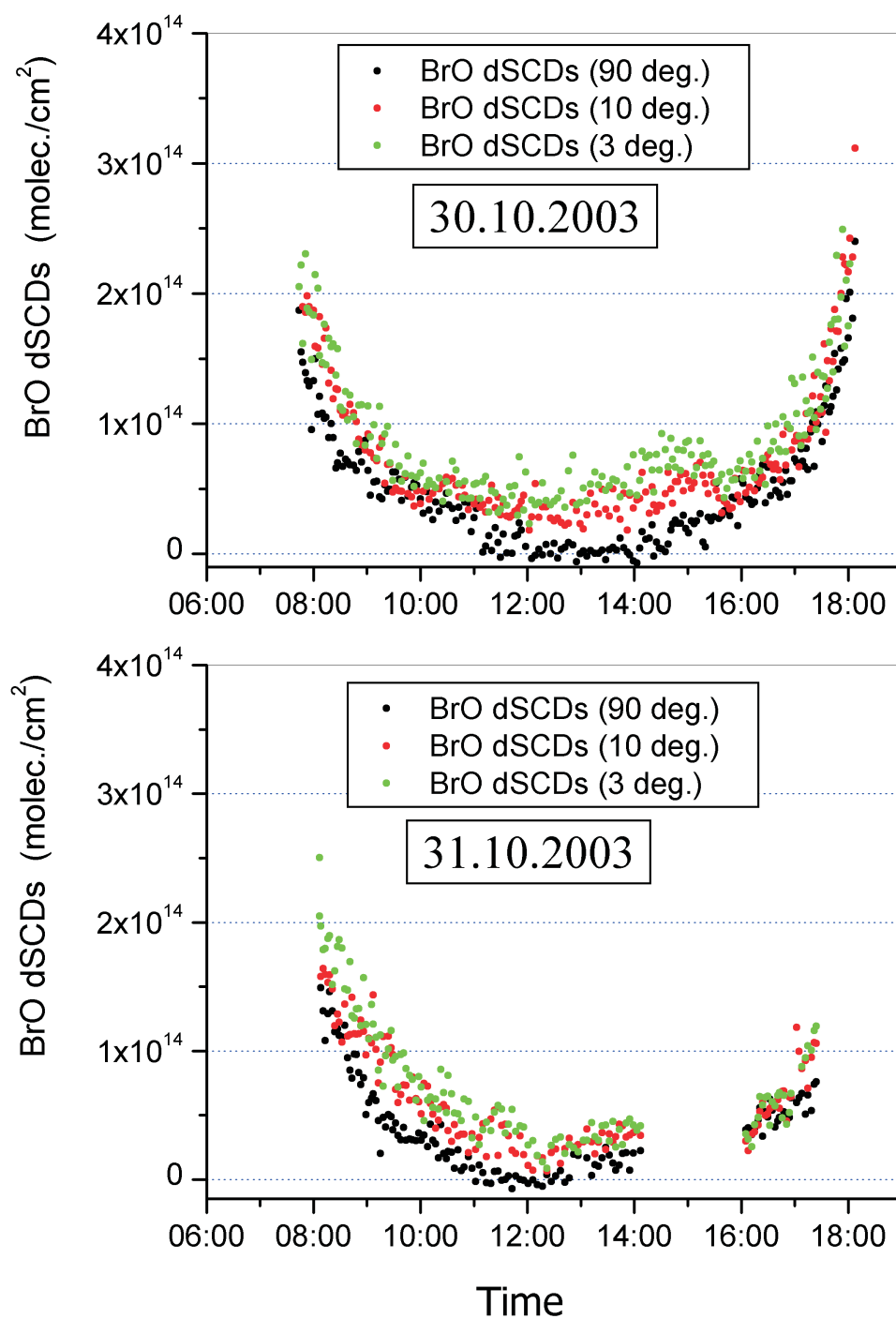


Figure 6.6: *Two days with enhanced tropospheric BrO dSCDs: 30.10.2003 and 31.10.2003.*

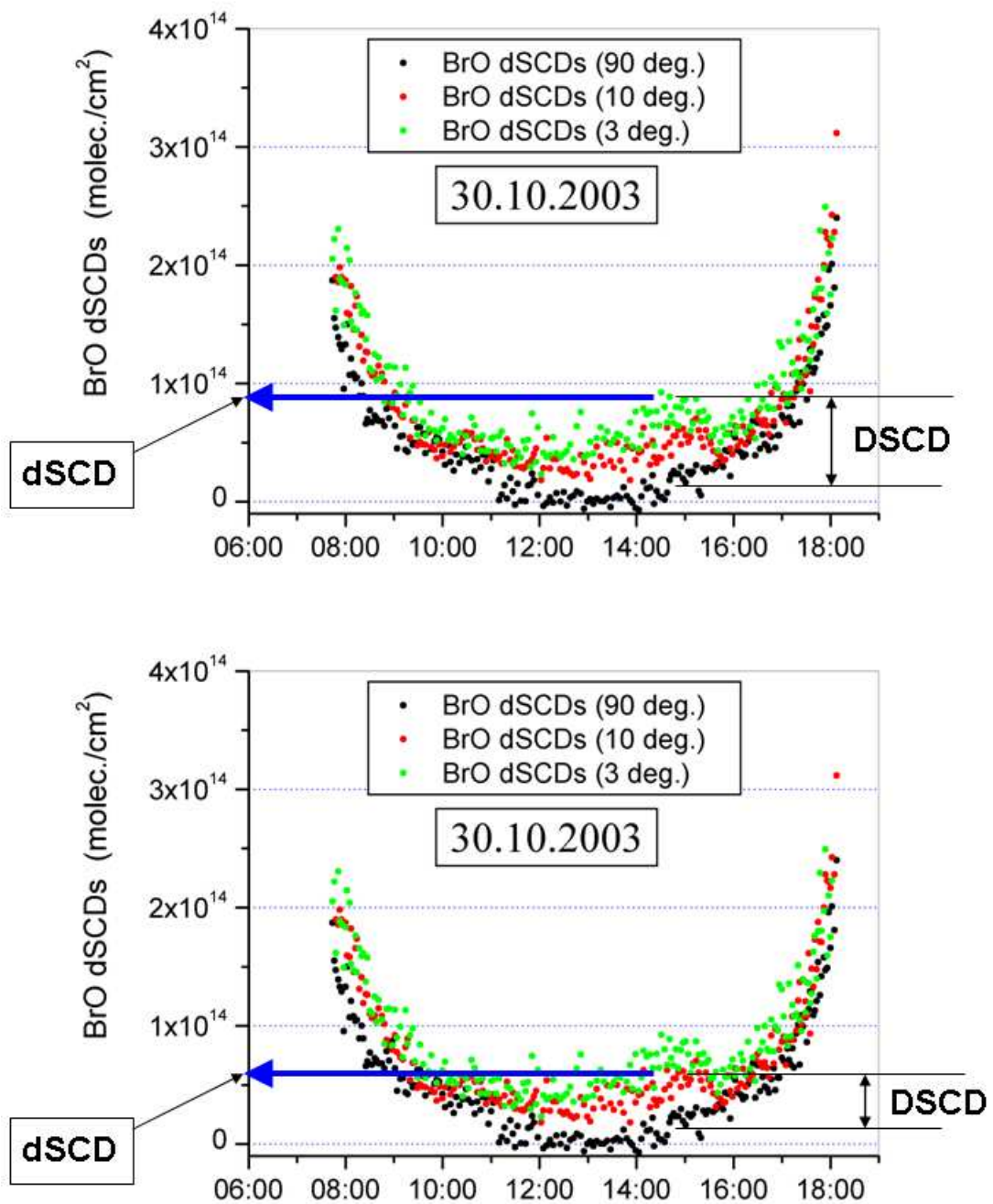


Figure 6.7: An Example shows the difference between *dSCDs* and *DSCDs*. The *dSCDs* of 3° and 10° are the differential slant column densities calculated from the spectral retrieval using one reference spectrum (*FRS*). The *DSCDs* are the differences between the *dSCDs* at elevation angles 3° or 10° and the *SCD*<sub>90°</sub>.

plicate the radiative transfer calculations, the analysis was restricted to clear sky conditions. The first step of this altitude retrieval method is: the estimation of the atmospheric aerosol load since the aerosol load strongly affects the radiation transfer of light collected by MAX-DOAS telescopes.

On 29.10.2003, the smooth diurnal variation of  $O_4$  dSCDs and BrO dSCDs in the second half of the day indicates a rather clear day. However, on this day, the expected order of the measured  $O_4$  and BrO absorption was reversed (the absorptions for  $10^\circ$  elevation are larger than for  $3^\circ$  elevation) (See Figure 6.10 middle panel (left) starting from 12:14 o'clock on the X-Axis: the reversed order of  $O_4$  optical depth is visible).

This reversed order of the  $O_4$  dSCDs (and optical depth) values between the  $3^\circ$  and the  $10^\circ$  elevations could be explained if the optical path of photons reaching the  $3^\circ$  telescope were shorter than those of the  $10^\circ$  telescope.

Possible reasons for this finding have been investigated by modeling the radiative transfer using different scenarios for clouds and aerosols of different optical depths and altitudes (sensitivity studies).

The following can be concluded from these sensitivity studies<sup>2</sup>:

The values of the measured  $O_4$  absorptions could be correctly modeled if a thin cloud layer (optical depth of about 0.5) is assumed at high altitude, while close to the ground a shallow aerosol layer (geometrical depth about 50m, optical depth of about 0.1) exists.

On 31.10.2003, the measured  $O_4$  absorptions (and consequently optical depths) during the first half of the day show also a relatively smooth variation. In contrast to the 29.10.2003, now the measured  $O_4$  and BrO absorptions are in the expected order for typical MAX-DOAS observations with the higher BrO dSCDs values were found at the lower elevation angle (i.e.  $3^\circ$  here). These observations could be correctly modeled for an assumed aerosol layer close to the ground (geometrical depth about 50 m, optical depth about 0.02).

---

<sup>2</sup>Modeling the radiative transfer was carried out using Tracy-II model (see chapter 4)



Figure 6.8: *The exact positions of the RV Polarstern during the three week of measurements. The diameters of the red dots indicate the relative values of the BrO (DSCDs  $\mathcal{P}$ ), while the white dots indicate days when BrO (DSCDs) could not be detected or days of no measurements.*

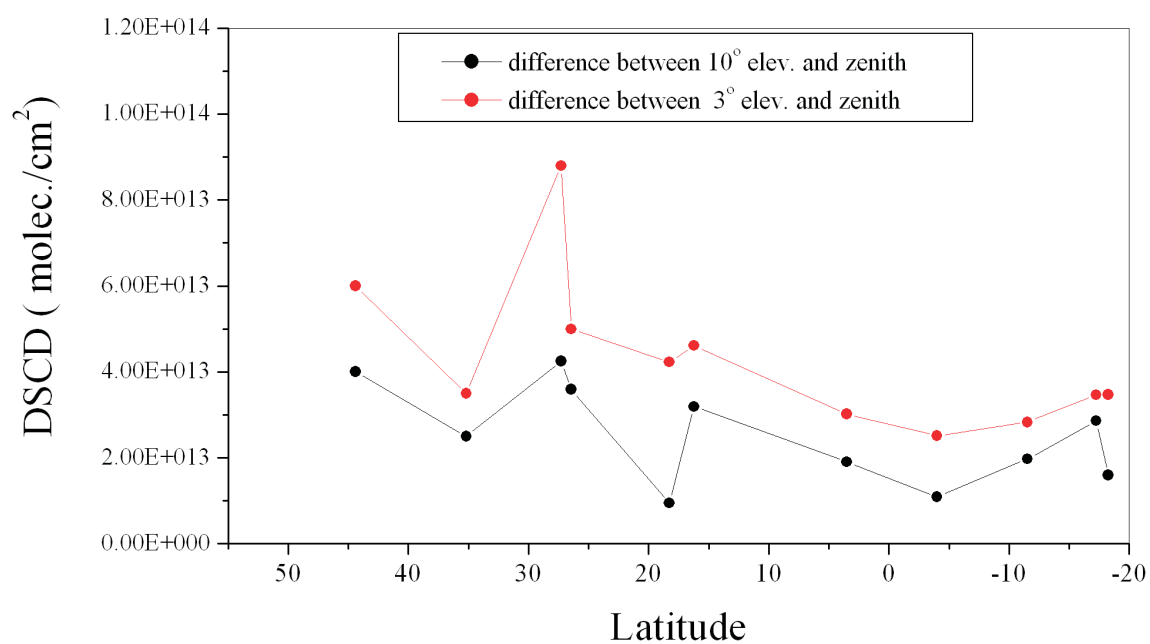


Figure 6.9: Tropospheric BrO DSCDs during the 1st leg of the cruise ANT-XXI/1.

### 6.4.1 Calculation and comparison of Ratios

Based on these estimated aerosol properties, it is possible to calculate AMF for various possible BrO height profiles.

From the BrO Air Mass Factors (AMF) for the different elevation angles the ratio of modeled Differential Air Mass Factors DAMF ( $R_{modeled}$ ) can be calculated as follows:

$$R_{modeled} = (AMF3^\circ - AMF90^\circ) / (AMF10^\circ - AMF90^\circ)$$

It can be compared to the ratio ( $R_{measured}$ ) of the corresponding measured BrO dSCDs:

$$R_{measured} = (dSCD3^\circ - SCD90^\circ) / (dSCD10^\circ - SCD90^\circ)$$

$$R_{measured} = DSCD3^\circ / DSCD10^\circ$$

It should be noted that  $R_{measured}$  is independent of the absolute value of the BrO concentration; thus the comparison between  $R_{measured}$  and  $R_{modeled}$  yields information on the relative BrO concentration profile independently from the values of BrO concentration themselves. Figure 6.10 shows the measured BrO dSCDs and  $O_4$  Optical Densities respectively for the two selected days (top), the relatively smooth variation of the BrO dSCDs and  $O_4$  Optical Densities (middle) and finally the ratio of the measured BrO dSCDs for  $3^\circ$  and  $10^\circ$  ( $R_{measured}$ ) for both selected days (bottom).

From this Figure, it is clear that: on 29.10.2003; the measured ( $R_{measured}$ ) is mostly between 0 and 1.5 and on 31.10.2003, ( $R_{measured}$ ) was between 0.75 and 2.2. See the bottom panel of Figure 6.10.

Three different assumptions for the BrO layer thickness were tested:

1. Layer thickness of 200 m (between ocean surface and 200 m above surface).
2. Layer thickness equal to that of the Boundary Layer (BL) for each of the two selected days (between ocean surface and the BL top).
3. Layer thickness equaling the whole troposphere (between the ground surface and the tropopause).

The assumed BL heights for both days 29.10.2003 and 31.10.2003 were deduced from the temperature inversion around these heights (see Figure 6.3) and it was about 2400 m for 29.10.2003 and about 1800 m for 31.10.2003.

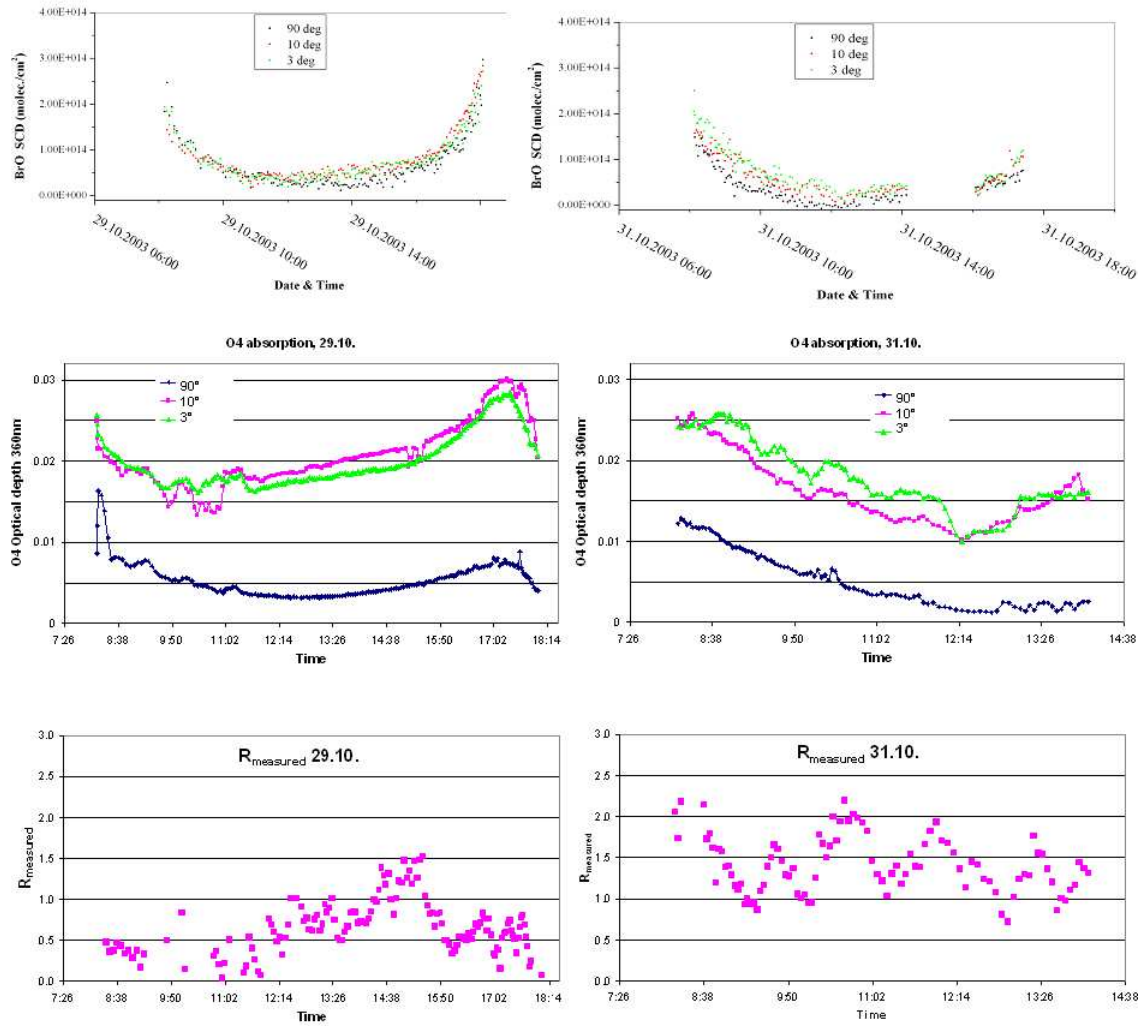


Figure 6.10: *Top and middle: Measured BrO dSCDs and O<sub>4</sub> Optical Densities respectively for the two selected days. Bottom: Ratio of the measured BrO DSCD for 3° and 10° for both selected days.*

For the retrieved aerosol scenario on the day 29.10.2003 (a thin cloud layer at high altitude of optical density about 0.5 and also a shallow aerosol layer of geometrical depth about 50m, optical depth of about 0.1) ,  $R_{modeled}$  was found from calculations to be about:

1.44 for an assumed layer between 0 and 200m of height.

0.83 for a layer between 0 and 2400 m of height (BL height).

0.62 for the whole troposphere of height.

For the retrieved aerosol scenario on the day 31.10.2003 (an aerosol layer of geometrical depth about 50 m, optical depth about 0.02),  $R_{modeled}$  was found from calculations to be about:

2.8 for an assumed layer between 0 and 200m of height.

1.77 for a layer between 0 and 1800 m of height (the estimated BL height for that day).

1.09 for the whole troposphere height.

For each of the two days, the aerosol scenario was assumed to be unchanged during the day in order to avoid complicating the radiative transfer calculations.

For both days, variations of the  $R_{measured}$  of BrO dSCDs are observed during the day (see Figure 6.10 bottom panel). These variations indicate substantial vertical gradients of the tropospheric BrO concentrations. Taking into account that the instruments were on board of a moving platform (vessel), the variations of the  $R_{measured}$  along the day indicate also variations of the BrO vertical profile.

By calculating the Differential Air Mass Factors (DAMFs) for the three different elevation angles ( $3^\circ$ ), ( $10^\circ$ ) and ( $90^\circ$ ) according to the different BrO layer-thickness scenarios, the conversion of the BrO dSCDs into tropospheric VCDs becomes possible and subsequently also into BrO mixing ratios.

Figure 6.11 shows a plot of DAMFs for the three different elevation angles ( $3^\circ$ ), ( $10^\circ$ ) and ( $90^\circ$ ) calculated according to the different BrO layer height scenarios. The expected dependence of the DAMFs values for the three different elevation angles ( $3^\circ$ ), ( $10^\circ$ ) and ( $90^\circ$ ) on the different BrO layer-thickness scenarios is visible in the graph.

The comparison between the values (range of values) of  $R_{measured}$  and the  $R_{modeled}$  values for different assumed BrO layer-thickness is the next step to be able to determine the most probable layer thickness of BrO. Figure 6.11 shows the values of the  $R_{measured}$  in comparison to those of  $R_{modeled}$ . It is clear from the graph that the

range of values of  $R_{measured}$  allows different possibilities.

From Figure 6.11 by investigating the above mentioned three relations, the following could be found:

1. It becomes obvious that the BrO DAMF strongly depend on the assumed layer height and also on the prevailing aerosol scenario of the selected days. Since the maximum observed BrO dSCDs of about  $5 \times 10^{13}$  (molec./ $cm^2$ ), see Figure 6.10, and depending on the aerosol scenario and the assumed layer height: the factors for the conversion of the measured DSCD  $3^\circ$  into the corresponding BrO concentration varies between  $1 \times 10^5$  and  $6 \times 10^5$ .

The respective factors for the conversion into mixing ratios range between  $2.7 \times 10^{24}$  and  $1.6 \times 10^{25}$ . The conversion factors between the BrO DSCD (expressed in  $1 \times 10^{13}$  molec./ $cm^2$ ) and the BrO mixing ratios (expressed in ppt) range between 0.6 and 3.7. These conversion factors would represent BrO mixing ratios between 3 and 18 ppt depending on the assumed layer height of BrO (minimum concentration for biggest layer thickness and vice versa).

Also it should be noted that for the day 29.10.2003: The calculated values of DAMFs for the elevation angle ( $3^\circ$ ) are less than those of ( $10^\circ$ ) which is compatible with the finding that BrO dSCDs from the former were less than those of the latter. But in case of the 200 m layer-height scenario: this is not the case. Since the BrO layer is concentrated in only 200 m layer, it is expected that the ( $3^\circ$ ) light-path length would be very enhanced so the ( $3^\circ$ ) DAMF in this case would be more than that of ( $10^\circ$ ) although of the mentioned above conditions.

2. For the comparison between the values of  $R_{measured}$  (actually the range of  $R_{measured}$  values) and  $R_{modeled}$  values:

It should be noted that the observed minima of  $R_{measured}$  would also be in agreement with the assumption of a BrO layer reaching up to higher altitudes, probably even filling the whole troposphere. This can be seen from the comparison of these minimum values with  $R_{modeled}$  values (see Figure 6.11).

Nevertheless, these low values of  $R_{measured}$  could also be explained with horizontal gradients of the BrO field. In contrast, the observed maxima of  $R_{measured}$  can only be explained if the BrO layer is confined close to the surface (see the higher limit (the right black line) of  $R_{measured}$  in Figure 6.11).

3. The systematic decrease of the  $R_{modeled}$  values with the increase of the assumed layer height, which is obviously expected.

The fact that there are only two elevation angles (besides zenith) limits the ability to estimate the layer-height more precisely. For sure having more elevation angles

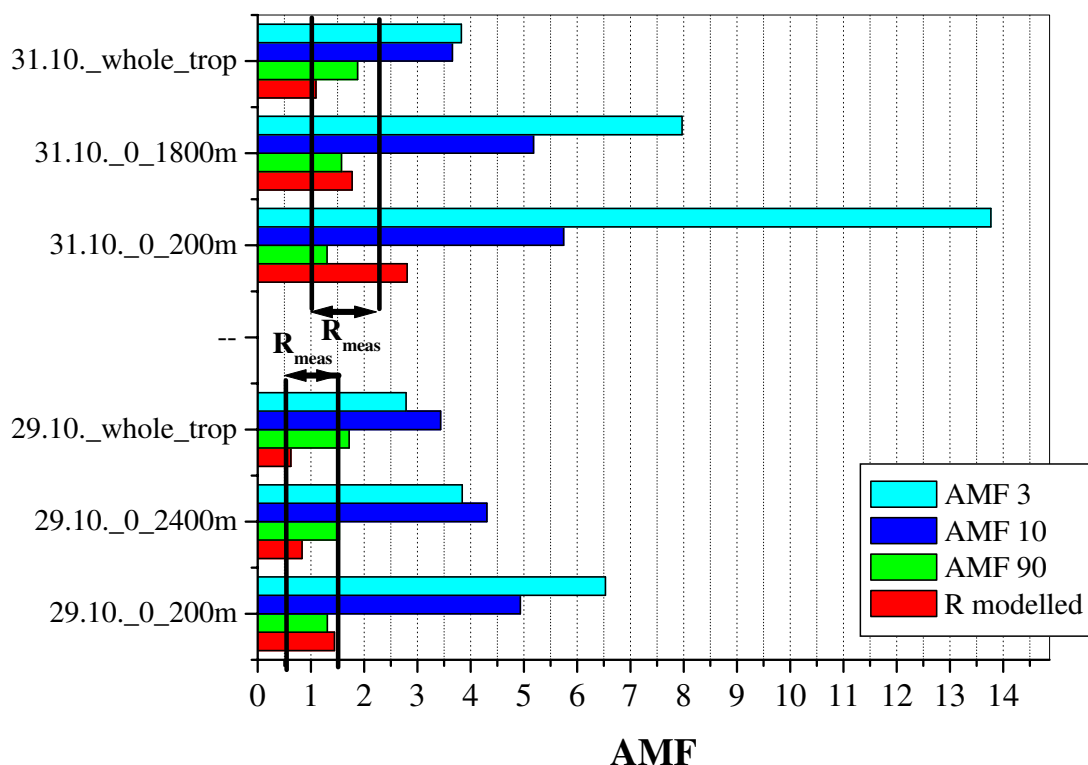


Figure 6.11: Calculated differential Air Mass Factors of BrO for three different elevation angles ( $9^\circ$ ), ( $10^\circ$ ) and ( $90^\circ$ ) calculated according to the different BrO layer height scenarios (200 m, BL height and whole troposphere) and also  $R_{modelled}$  and the ranges of  $R_{measured}$  for the two days 29.10.2003 and 31.10.2003.

(about five to six) would have enhanced this ability.

## 6.5 BrO-Correlations Studies

In this section, in order to explore the possible correlation of BrO tropospheric Differential Slant Column Densities [BrO (DSCDs)] with a set of various interesting parameters, the study of covariance of BrO (DSCDs) with these parameters is shown. The two major issues here are:

(1) To investigate the possible contribution of short-lived organo-halogens as precursors of BrO. In order to do that, the correlation between BrO (DSCDs) and biological activity in the sea / ocean waters is studied. The satellite Chlorophyll data are taken here as an indicator of biological activity (phytoplankton and algae).

(2) To study the possible contribution of auto-catalytic oxidation of marine aerosols in the process of BrO production in the Marine Boundary Layer (MBL). In order to do that, the correlations between BrO (DSCDs) and various marine aerosol parameters are studied. The possible correlation with dust aerosol optical depth (AOD) is also investigated.

### 6.5.1 BrO-Chlorophyll Correlations

Chlorophyll is important as an indicator of marine biological activity, e.g. due to algae and phytoplankton, which are sources of short-lived organo-halogens. Satellite maps of Chlorophyll concentrations (in  $mg/m^3$ ) were obtained from SeaWifs. Chlorophyll concentrations at specific locations along the cruise route were deduced from SeaWifs maps and correlations with BrO MAX-DOAS (DSCDs) were established.

Figure 6.12 show the following: The left panels show the positions of the RV Polarstern during each day of measurements at noon time. The right panels show the weekly average chlorophyll concentrations for the corresponding weeks of measurement (since daily values are not available). The diameters of the red dots in the left panels indicate the relative values of the BrO (DSCDs), while the white dots indicate days when BrO (DSCDs) could not be detected or days of no measurements. The first, second and third week of measurements are represented in top, middle and bottom panels respectively. The black gaps in the chlorophyll maps in Figure 6.12 indicate cloudiness. This sometimes leads to losing information about chlorophyll concentrations at these locations.

Figure 6.13 shows the correlation between the BrO (DSCDs) (in  $molec./cm^2$ ) and the local chlorophyll concentrations (in  $mg/m^3$ ) at the positions of the RV Polarstern on the corresponding days (positions at which the highest BrO (DSCDs) values were detected during the day). The graph shows a positive correlation between Chlorophyll concentrations and BrO (DSCDs) for both elevation angles  $3^\circ$  and  $10^\circ$  with correlation coefficients ( $R = 0.335$ ) and ( $R = 0.430$ ) respectively.

In addition to the local chlorophyll concentration, the detected BrO (DSCDs) might also be affected by two additional factors:

- (1) The chlorophyll concentrations upwind of the measurements positions.
- (2) The time period that the investigated air masses were in contact with the sea surface (i.e. contact with BrO precursors from algae and phytoplankton and also marine aerosols).

As such, it is interesting to study these two factors and their possible correlations with the BrO (DSCDs). In order to do that, back trajectories of air masses using the HYSPLIT model were studied in detail. Thus, it was possible to determine the length of time that air masses were in contact with the sea surface (in hours) for

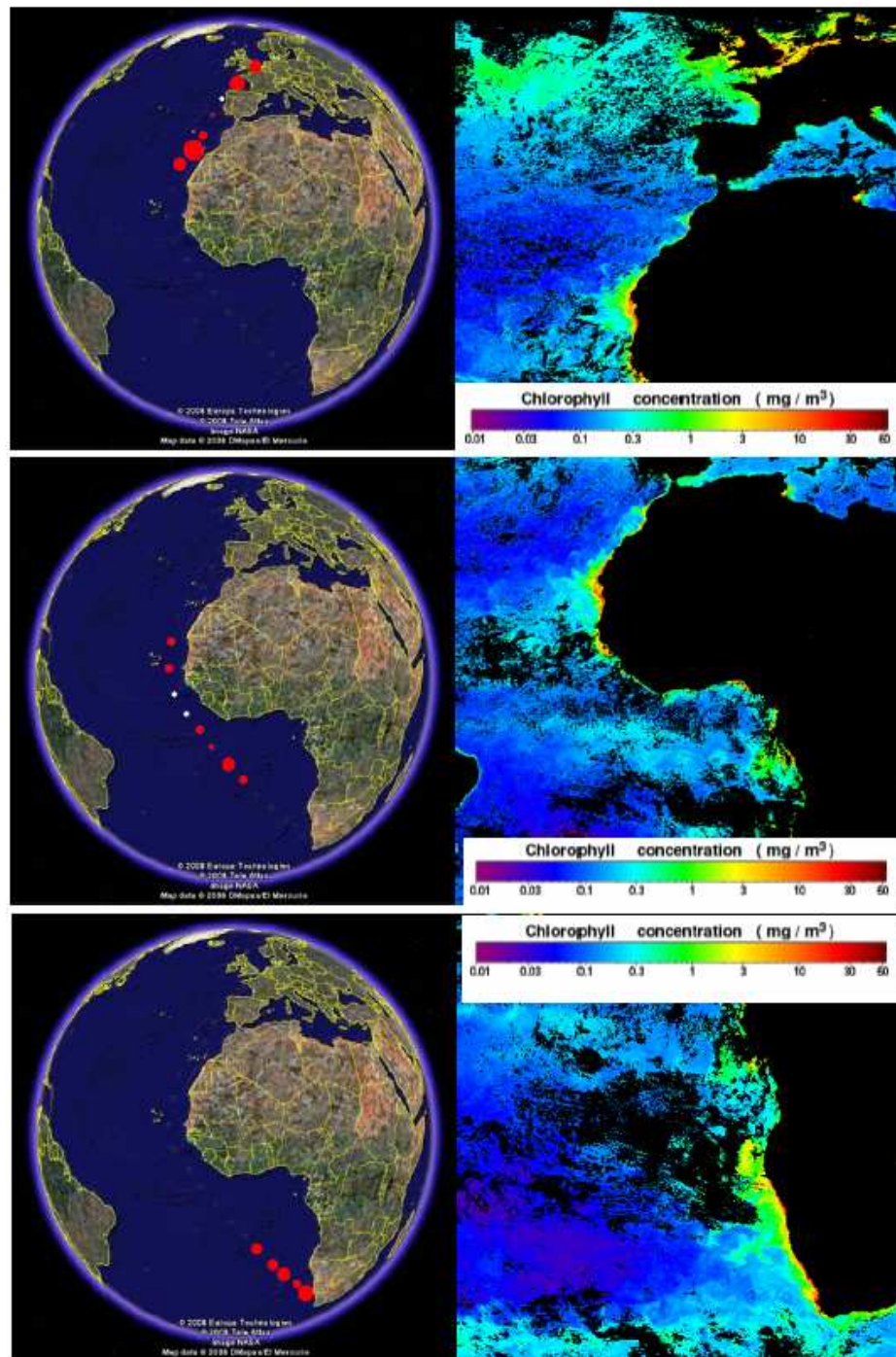


Figure 6.12: *The left panels show the positions of the RV Polarstern during each day of measurements at noon time. The right panels show the weekly average chlorophyll concentrations for the corresponding weeks of measurement*

each day, and to determine the average and maximum chlorophyll concentrations along the track of each back trajectory. Figure 6.14 shows two examples of calculated back trajectories with HYSPLIT model. Left and right panels show the back trajectories during the days 31.10.2003 and 09.11.2003 respectively.

The red, blue, and green lines represent the five days back trajectories of air masses ending up at heights of 20, 200, 500 m above sea level (a.s.l) respectively. On 31.10.2003, the air masses in general are coming from the North East direction and the air mass at 20 m above sea level (a.s.l) was in contact with the ocean surface for 72 hours (i.e. 3 days out of the last 5 days). On 29.10.2003, the air masses in general are coming from the South East. Also it shows that the air mass at the 20 m height (a.s.l) was in contact with the ocean surface for 56 hours (i.e. 2.33 days). It is noticed from both panels that the air masses at 200 m and 500 m were not in direct contact with the water surface during the previous five days immediately before the measurement day. Only the back trajectories ending at 20 meters a.s.l had contact with the water surface. By overlaying daily back trajectory graphs (e.g. Figure 6.14) over the satellite maps of chlorophyll weekly average concentrations (e.g. Figure 6.12, the average and maximum chlorophyll concentrations along the track of back trajectories could be deduced for each day within an error margin of 10% ( $0.02 - 2 \text{ mg}/m^3$ ). Obviously this is done for the back trajectories ending up at 20 m a.s.l because they are the only ones having contact to the sea water surface prior to measurements dates.

Then correlation plots were established. Obviously these correlations would be more precise using daily satellite maps of chlorophyll concentrations but unfortunately the daily satellite maps have many coverage gaps and cannot be practically used for this purpose. So instead, the maps of weekly chlorophyll concentration averages were used.

It is important to know how long the air masses were in contact with the water surface. So studying the back trajectories carefully, these time periods (contact time with water surface) in hours/days were determined from the HYSPLIT back trajectories. Figure 6.15 shows a series of time periods when back trajectories were in contact with sea surface (in days). The vertical lines indicate the duration when the (20m a.s.l) back trajectories were in contact with the water surface. Red vertical lines indicate days with measurements and the black vertical lines indicate days with no BrO data.

It is important to notice that the air masses were in contact with the water surface for several days (4-5 days) only a few times. Most of the back trajectories were in contact with the water surface for one to three days prior to the measurements. Only three trajectories had water surface contact longer than three days. See Figure 6.15.

Figure 6.16 shows the correlation of BrO (DSCDs) ( $\text{molec.}/cm^2$ ) with the average chlorophyll concentrations ( $\text{mg}/m^3$ ) along the tracks of back trajectories. The graph shows a positive correlation between the two quantities for both elevation angles ( $3^\circ$

and  $10^\circ$ ) with correlation coefficients ( $R = 0.321$ ) and ( $R = 0.314$ ) respectively.

Figure 6.17 shows the correlation of BrO (DSCDs) ( $\text{molec.}/\text{cm}^2$ ) with the Maximum Chlorophyll concentrations ( $\text{mg}/\text{m}^3$ ) along the tracks of back trajectories (during the time they were in contact with water surface). The graph shows a positive correlation between the two quantities for both elevation angles  $3^\circ$  and  $10^\circ$  with correlation coefficients of ( $R = 0.301$ ) and ( $R = 0.392$ ) respectively. Figure 6.18 shows the correlation plot of BrO (DSCDs) with the water surface contact time. The graph shows a positive correlation between the two quantities for both elevation angles  $3^\circ$  and  $10^\circ$  with correlation coefficients of ( $R = 0.286$ ) and ( $R = 0.120$ ) respectively.

In order to get some idea about the total (amount of exposure) of air masses to the BrO precursors emitted by algae and phytoplankton: There are two important factors: (1) The value of average and maximum chlorophyll concentrations along the tracks of back trajectories.

(2) The duration of contact between the investigated air masses and the water surface.

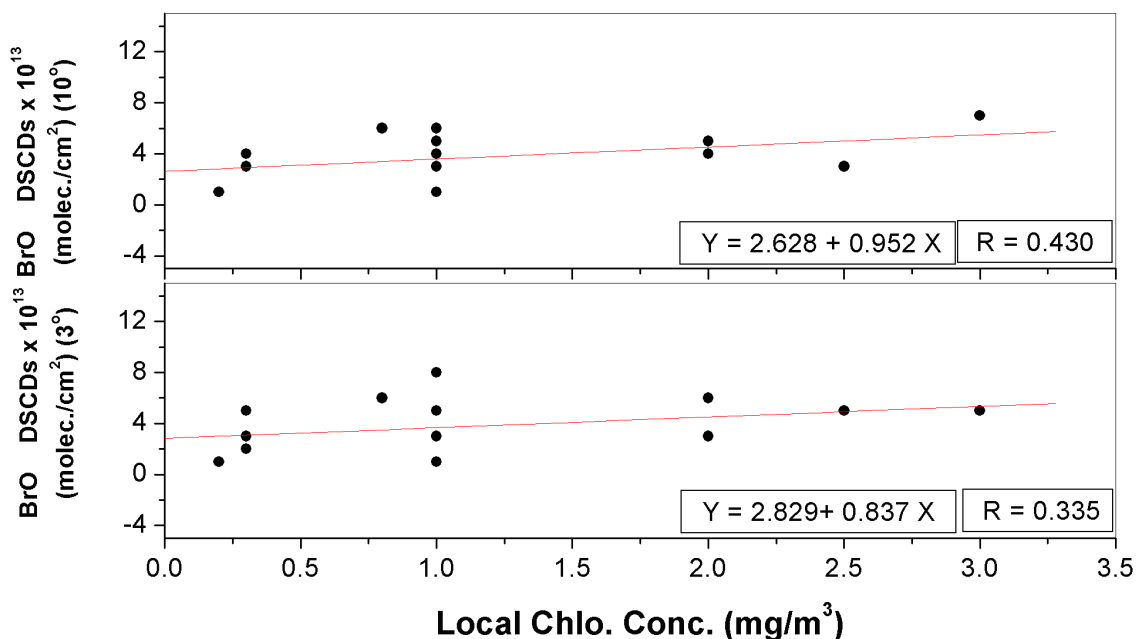


Figure 6.13: The correlation between the BrO (DSCDs) (in  $\text{molec.}/\text{cm}^2$ ) and the local chlorophyll concentrations (in  $\text{mg}/\text{m}^3$ ) at the positions of the RV Polarstern on the corresponding days (positions at which the highest BrO (DSCDs) values were detected during the day).

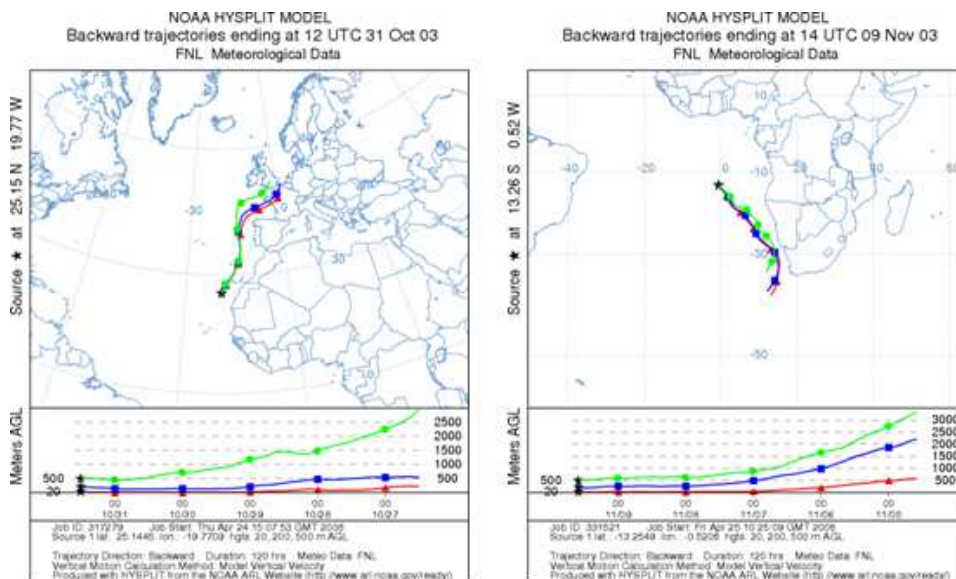


Figure 6.14: Two examples of calculated back trajectories with HYSPLIT model. Left and right panels show the back trajectories during the days 31.10.2003 and 09.11.2003 respectively.

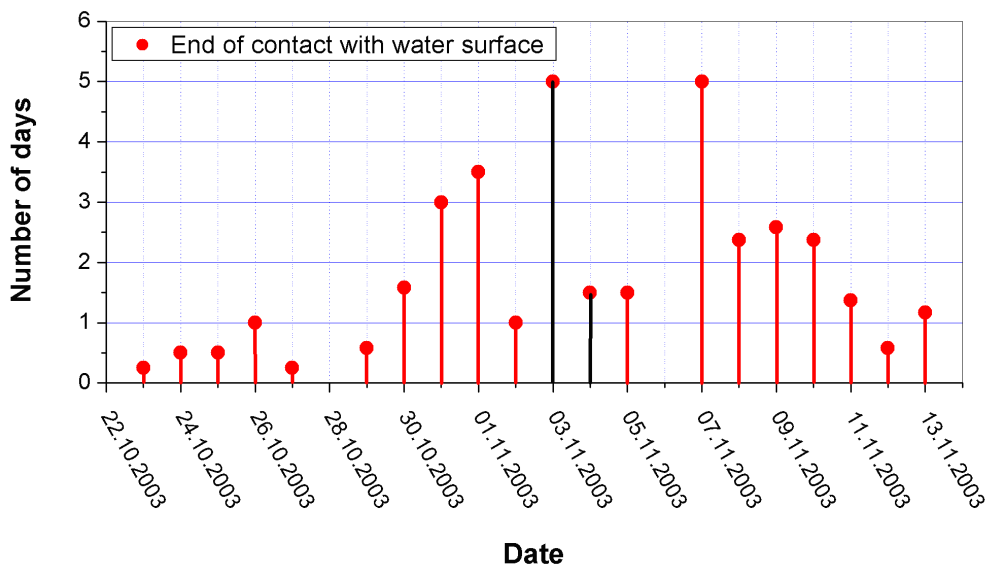


Figure 6.15: A series of time periods when back trajectories were in contact with sea surface (in days). The vertical lines indicate the duration when the (20m a.s.l.) back trajectories were in contact with the water surface. Red vertical lines indicate days with measurements and the black vertical lines indicate days with no BrO data.

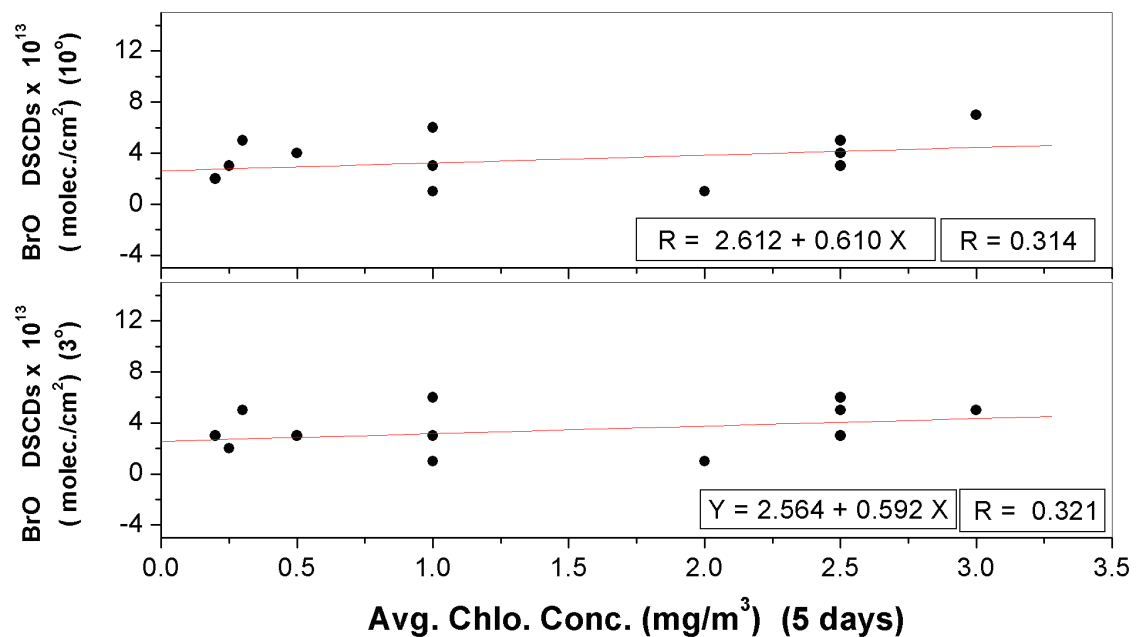


Figure 6.16: The correlation of BrO (DSCDs) (molec./cm<sup>2</sup>) with the average chlorophyll concentrations (mg/m<sup>3</sup>) along the tracks of back trajectories.

The products of these two factors determine the amount of exposure of air masses to BrO precursors from the ocean algae and phytoplankton. The first product will be:

Product 1 = (Water surface contact time x Average chlorophyll concentration along the back trajectory).

The second product will be:

Product 2 = (Water surface contact time x Maximum chlorophyll concentration along the back trajectory).

Figure 6.19 shows the correlation of BrO (DSCDs) at elev. angles 3° and 10° with Product 1 while Figure 6.20 shows the correlation of the BrO (DSCDs) with Product 2. Correlation coefficients of Product 1 with BrO (DSCDs) at elevation angles 3° and 10° are (R= 0.433) and (R = 0.154) respectively. Correlation coefficients of Product 2 with BrO (DSCDs) at elevation angles 3° and 10° are (R= 0.627) and (R = 0.355) respectively.

In order to have an overview on the correlations mentioned above, the correlation coefficients of BrO (DSCDs) with the different chlorophyll parameters are plotted together in Figure 6.21.

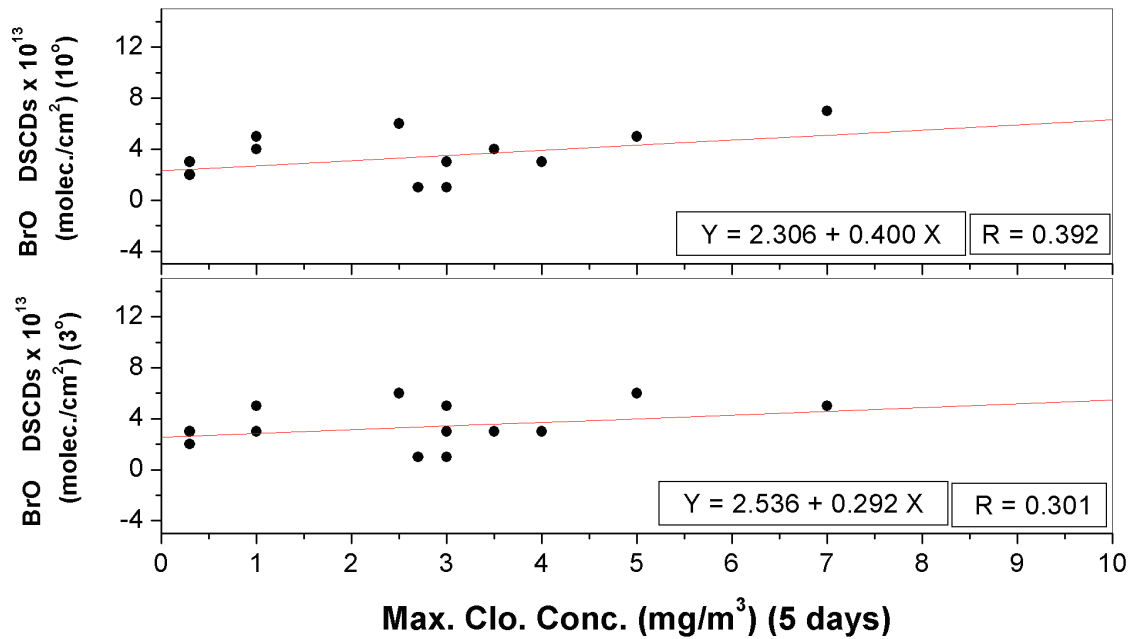


Figure 6.17: The correlation of the BrO (DSCDs) (molec./cm<sup>2</sup>) at elevation angles 3° and 10° with the maximum chlorophyll concentrations (mg/m<sup>3</sup>) along the tracks of back trajectories [current work, 2003 data set].

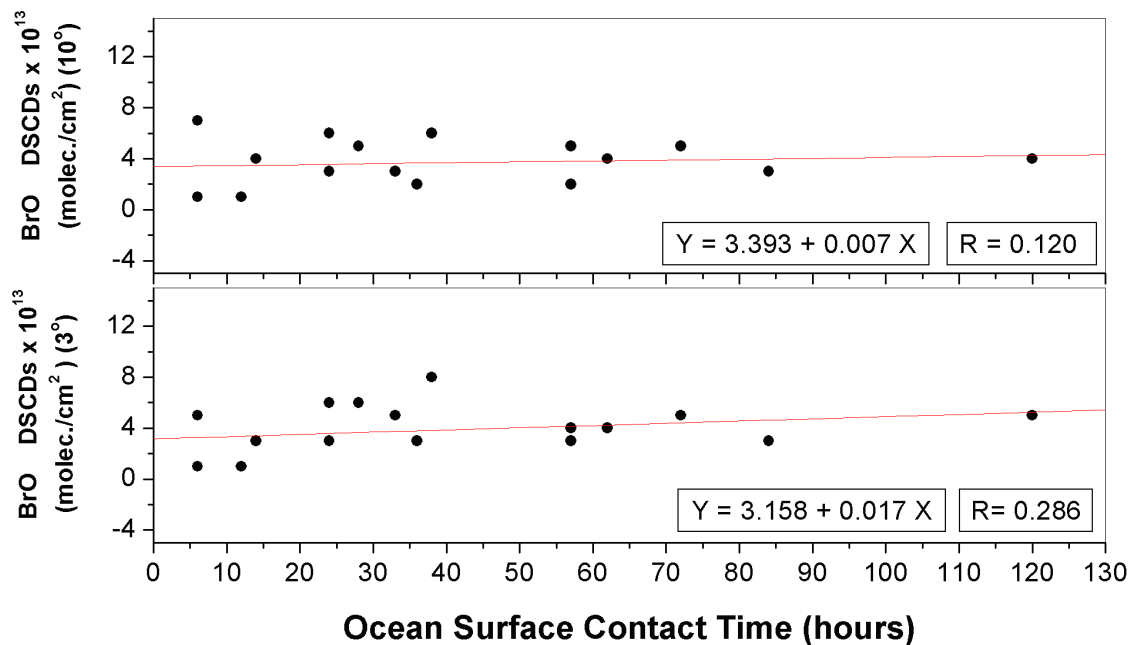


Figure 6.18: The correlation plots of the BrO (DSCDs) at elev. angles 3° and 10° with the water surface contact time (in hours).

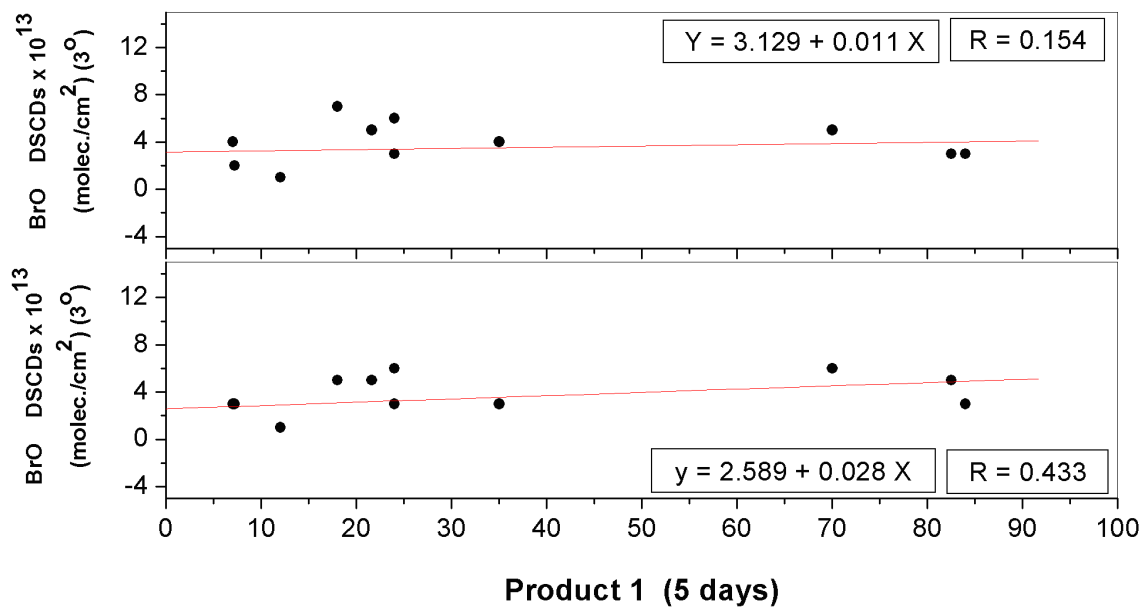


Figure 6.19: the correlation of BrO (DSCDs) at elev. angles 3° and 10° with Product1.

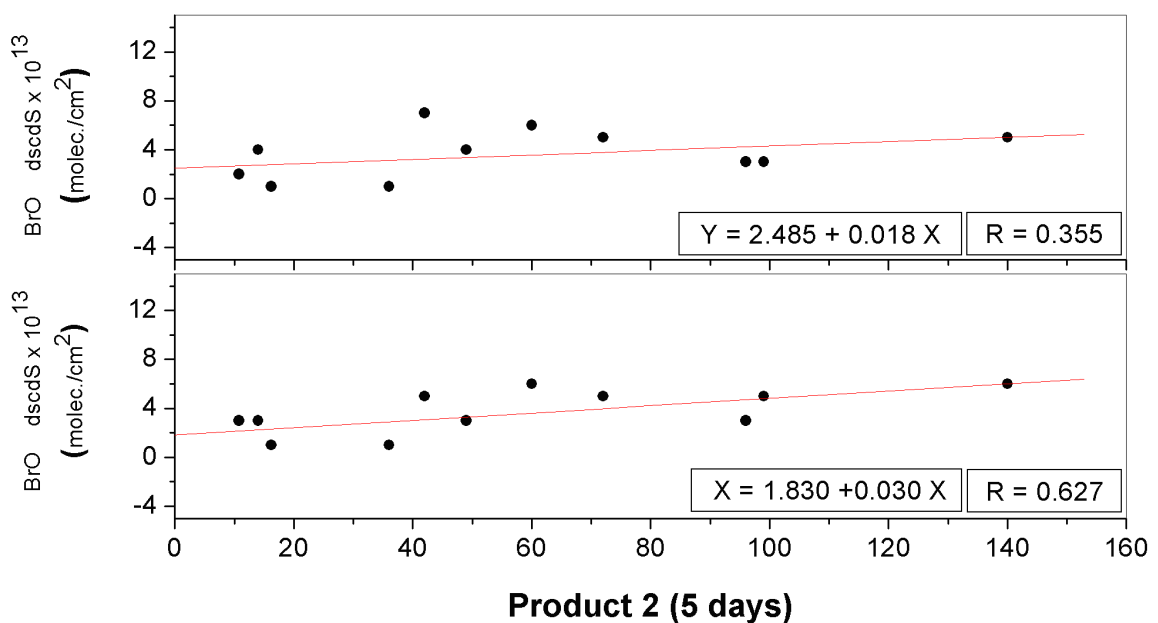


Figure 6.20: The correlation of the BrO (DSCDs) at elev. angles 3° and 10° with Product 2.

From this figure, the weak - but always positive - correlations between the BrO (DSCDs) and the different chlorophyll parameters are observed. The correlation coefficients are not significantly different between local chlorophyll correlation and the average and maximum chlorophyll concentrations along the tracks of back trajectories.

At this point of the investigation, a new set of questions arise:

(1) Which factor has more effect on the BrO formation: local chlorophyll concentrations, the chlorophyll concentrations upwind from the measurements location or a combination of both?

(2) Within the category of chlorophyll concentrations upwind from the measurements location, how long do the air masses need to be in contact with the water surface to be a significant contributor to BrO formation?

Having the current size of data (small statistical sample size), it is difficult to try to answer these two questions to any suitable degree of precision. However, to derive more insight into these questions, we investigated correlations with chlorophyll values (average and maximum) along the back trajectories for two particular groups of back trajectories:

(1) Trajectories with duration of sea water surface contact one day directly before measurement day.

(2) Trajectories with duration of sea water surface contact two days directly before measurement day.

Then similar correlation plots could be done with the chlorophyll parameters from these two specific groups of trajectories. They are not shown here in order to avoid having too many graphs. Instead, the correlation coefficients from these graphs are shown in Figure 6.22 as will follow. Figure 6.22 shows correlation coefficients between BrO (DSCDs) and local chlorophyll concentrations, average and maximum chlorophyll concentrations along the back trajectories, Product 1 and Product 2 calculated from the first one and two days back in time. Also it shows the same correlation coefficients from Figure 6.21 for comparison.

From Figure 6.22: again, no clear dependence on the selected water contact duration is found. However, the slight decrease of the correlation coefficient from (local) to (1 day) average chlorophyll concentration (second panel from top) might indicate that the local chlorophyll concentrations have the strongest influence on the BrO production. Thus the correlation coefficient for longer time periods should be interpreted with care.

Having the small statistical sample size mentioned above, the need to investigate these correlations with more experimental data becomes desirable. Using the

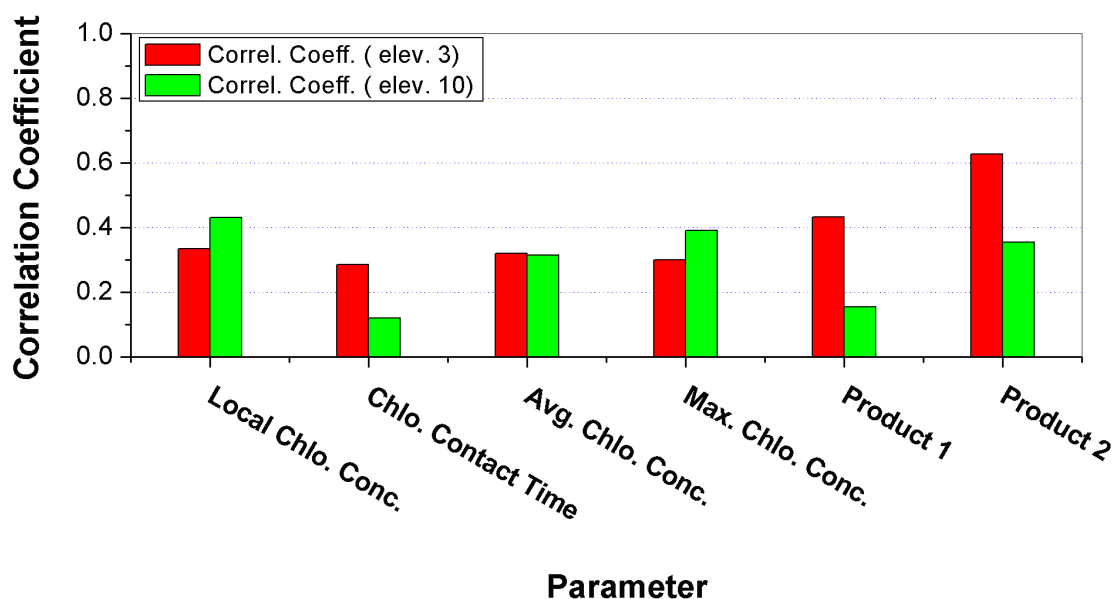


Figure 6.21: Correlation coefficients of different parameters with BrO (DSCDs) from the two elevation angles 3° and 10°.

experimental data from measurements of MAX-DOAS performed using the same instrument would be the optimum choice in this respect.

For this purpose, experimental data from (M. Martin Diploma thesis 2007) have been used here for the purpose of comparison of the findings here in this work. Measurements of M. Martin were done on board the research vessel RV Poseidon during the cruise P348 in February 2007. The route of this cruise started from Las Palmas, Gran Canaria via the Cape Verde Islands then back to Las Palmas (along the West African Coast). Figure 6.23 shows the route of the cruise and daily positions of the RV Poseidon.

The red thick lines indicate the daily path of RV Poseidon during the daylight time. For this data set, a similar approach will be applied to study the different correlations mentioned above.

Figure 6.24 shows the time series of detected BrO tropospheric (DSCDs) along the route of the cruise of RV Poseidon between 08.02.2007 and 24.02.2007. Figure 6.25 shows two examples of calculated back trajectories with HYSPLIT model for the two days 14.02.2007 and 18.02.2007.

During both days, the main wind directions were North East and the air masses were mainly coming from above continental areas then they passed by coastal areas before they reached the measurements' locations. A time series of the duration of back trajectories in contact with sea water surface is shown in Figure 6.26.

Figure 6.27 shows the weekly average chlorophyll concentrations at the RV Po-

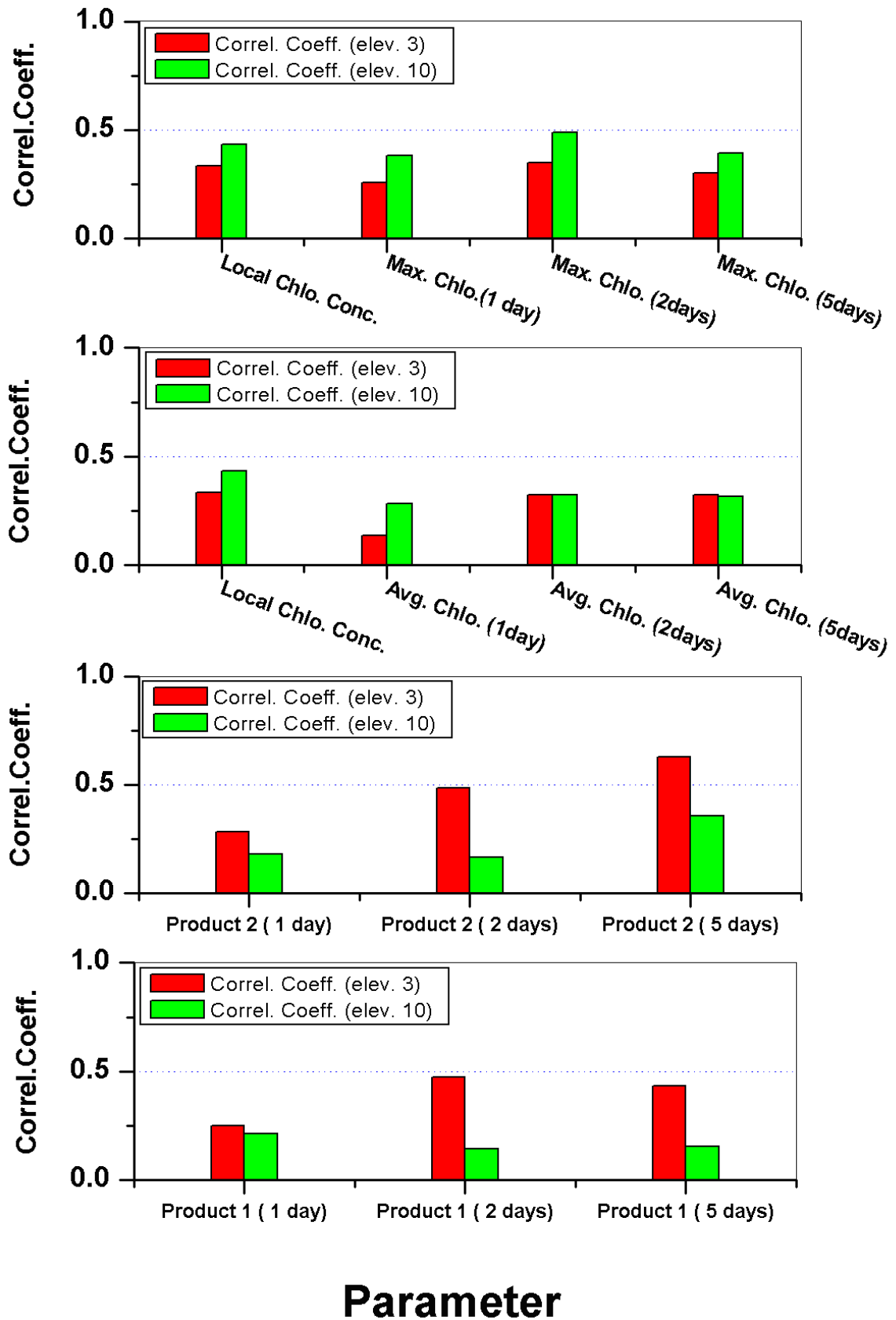


Figure 6.22: Correlation coefficients of BrO (DSCDs) at elev. angles  $3^\circ$  and  $10^\circ$  with chlorophyll parameters calculated from the first one and two days back in time. Also Correlation coefficients from Figure 6.21 are shown for comparison.

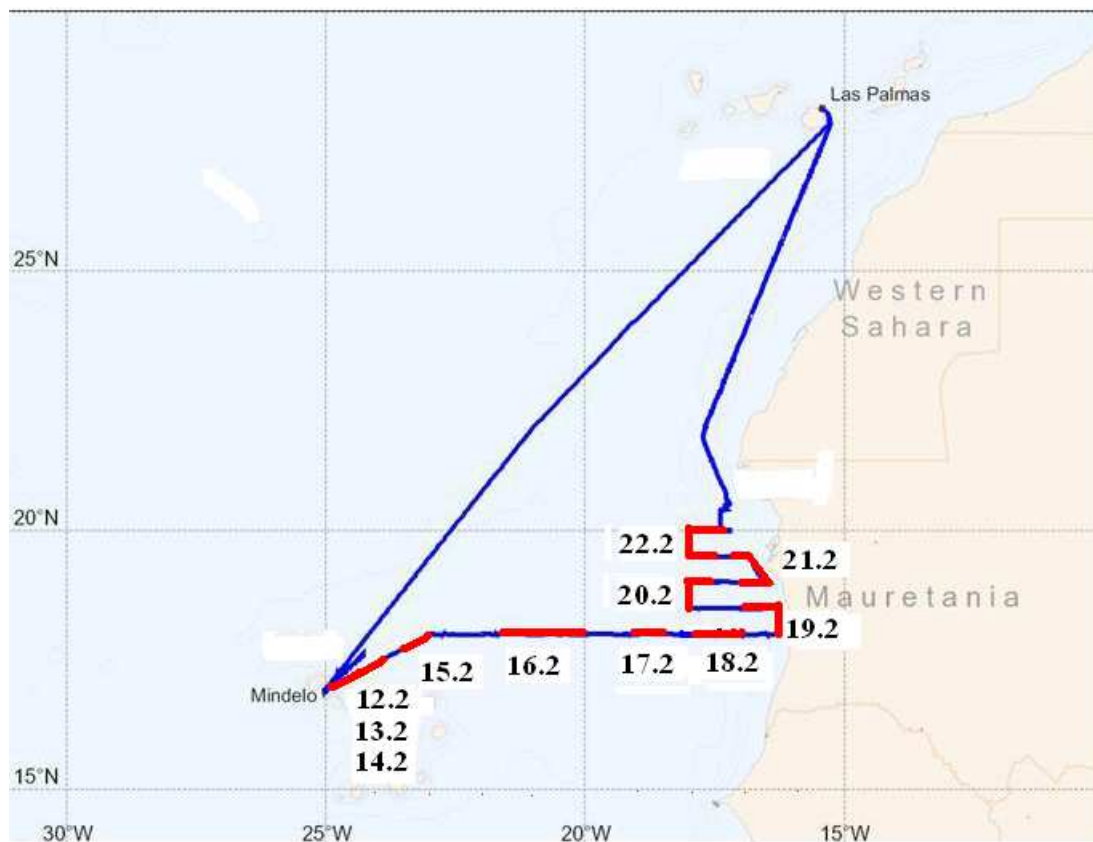


Figure 6.23: The route of the cruise and daily positions of the RV Poseidon between 08.02.2007 and 24.02.2007. [M.Martin, 2007].

seidon measurements area during the three weeks (2-9 Feb. 2007, 10-17 Feb. 2007 and 18-25 Feb. 2007) respectively from left to right (from SeaWifs). These three weeks are coincident with the measurements days on board RV Poseidon (8-24 Feb. 2007). These three satellite maps give a good indication of the spatial and temporal changes in chlorophyll concentrations. Using the same procedure here as above and overlaying daily back trajectory graphs (e.g. Figure 6.25) over the satellite maps of chlorophyll weekly average concentrations. The average and maximum chlorophyll concentrations along the tracks of back trajectories are deduced from the satellites maps (considering only the time span the back trajectories were in contact with water surface). The values of chlorophyll concentrations are deduced with an error margin of  $\pm 10\%$  ( $0.02 - 2 \text{ mg/m}^3$ ). Then correlation plots were established. Figure 6.28 shows the correlation between the BrO (DSCDs) ( $\text{molec./cm}^2$ ) at the  $6^\circ$  elevation angle (M. Martin 2007) and the local chlorophyll concentrations ( $\text{mg/m}^3$ ) at the positions of the RV Poseidon on the corresponding days. The graph shows a positive correlation between the two quantities with a correlation coefficient of (R

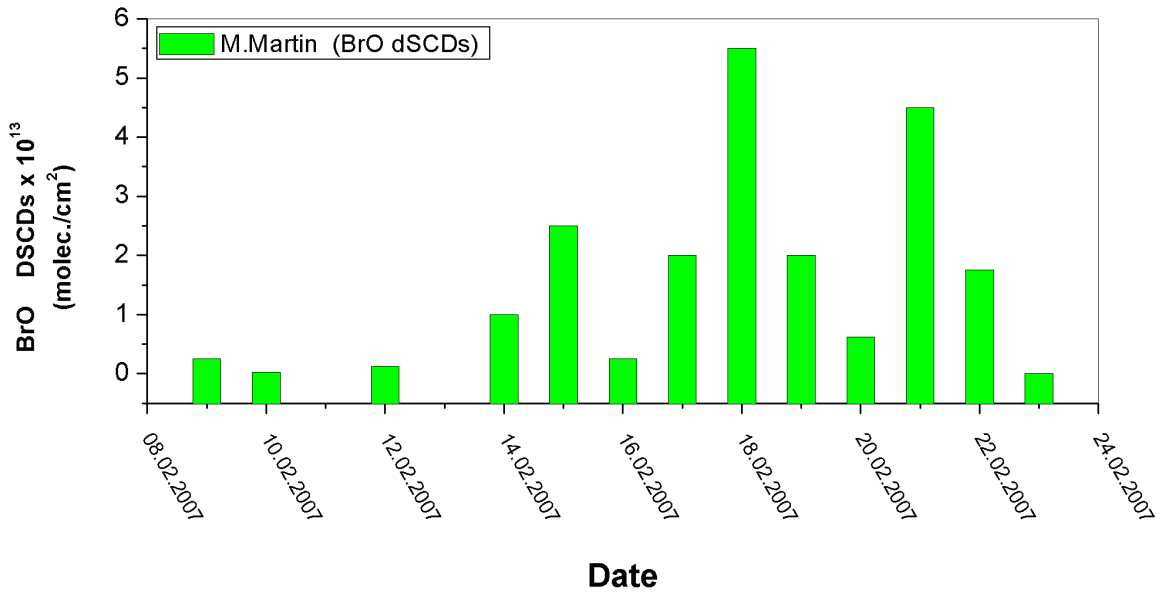


Figure 6.24: The time series of detected BrO tropospheric (DSCDs) along the route of the cruise of RV Poseidon between 08.02.2007 and 24.02.2007. [M.Martin, 2007].

= 0.853).

Figure 6.29 shows the correlation plot of the BrO (DSCDs) at the 6° elevation angle (M. Martin 2007) with the water surface contact time (deduced from HYSPLIT back trajectories). The graph shows a negative correlation between the two quantities with a correlation coefficient of ( $R = -0.618$ ). The apparent negative correlation in Figure 6.29 is believed to be due to two reasons: (1) The directions of winds during measurements: Most of the back trajectories calculated with HYSPLIT are coming from above continental areas over Africa. So following the back trajectories back in time (starting from measurements locations), the parts of trajectories above the ocean water would be "truncated" very shortly by reaching the coast. The air masses spent very short periods of time over the ocean surface compared to those of the current work mentioned above. See Figures 6.14, 6.15 and Figures 6.25, 6.26 for comparison. (2) The locations of measurement: The measurement locations during Poseidon cruise P348 were much closer to the coast than the measurements of the current work. See Figure 6.12: (left panel) and Figure 6.23 for comparison. Since the highest BrO (DSCDs) were detected at the nearest points from the coast (usually where high chlorophyll concentrations exist), these close locations to the coast mean also very short paths over the ocean water for the air masses. Figure 6.30 shows the correlation between the BrO (DSCDs) (molec./cm<sup>2</sup>) at the 6° elevation angle (M.Martin 2007) and the average and maximum chloro-

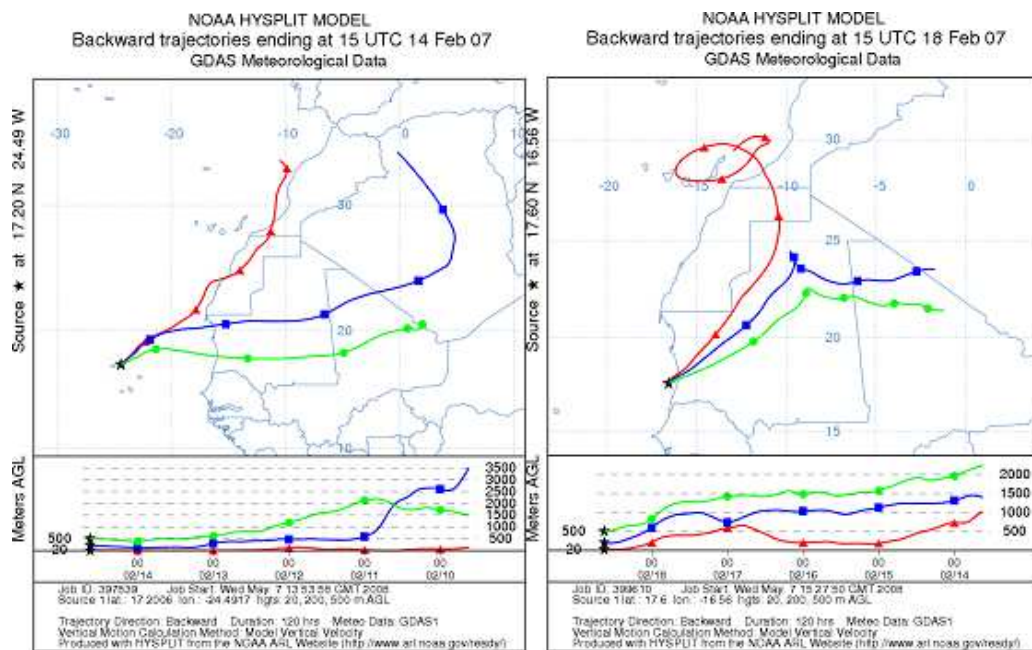


Figure 6.25: Two examples of calculated back trajectories with HYSPLIT model for the days 14.02.2007 and 18.02.2007 for the data from (M.Martin 2007).

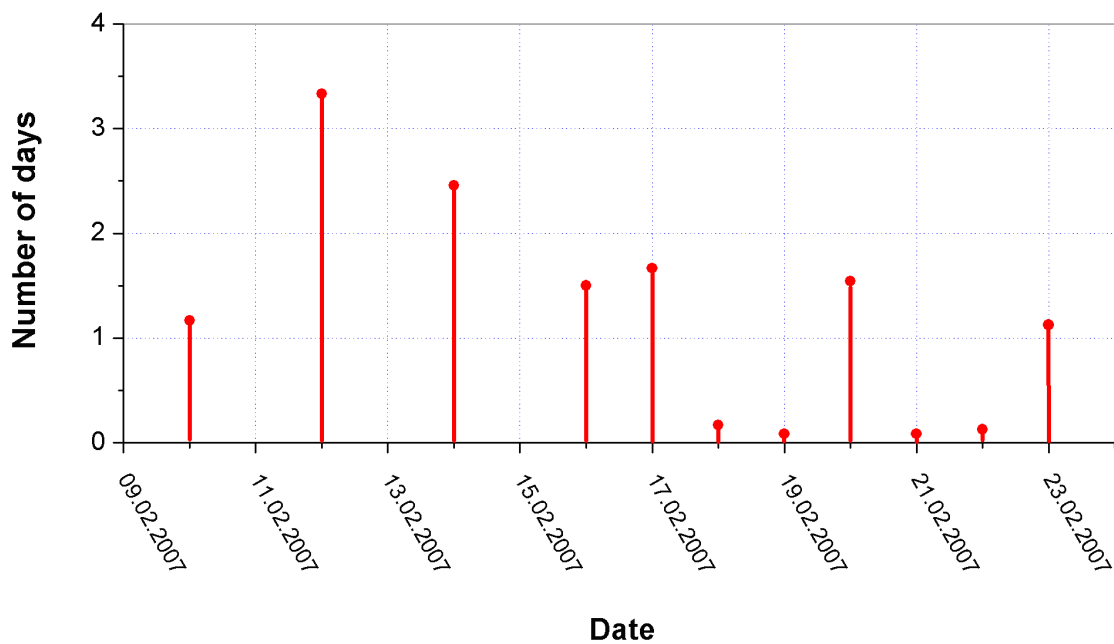


Figure 6.26: Time series of duration of back trajectories contact with water surface. The black lines indicate days with no BrO data. [M.Martin, 2007].

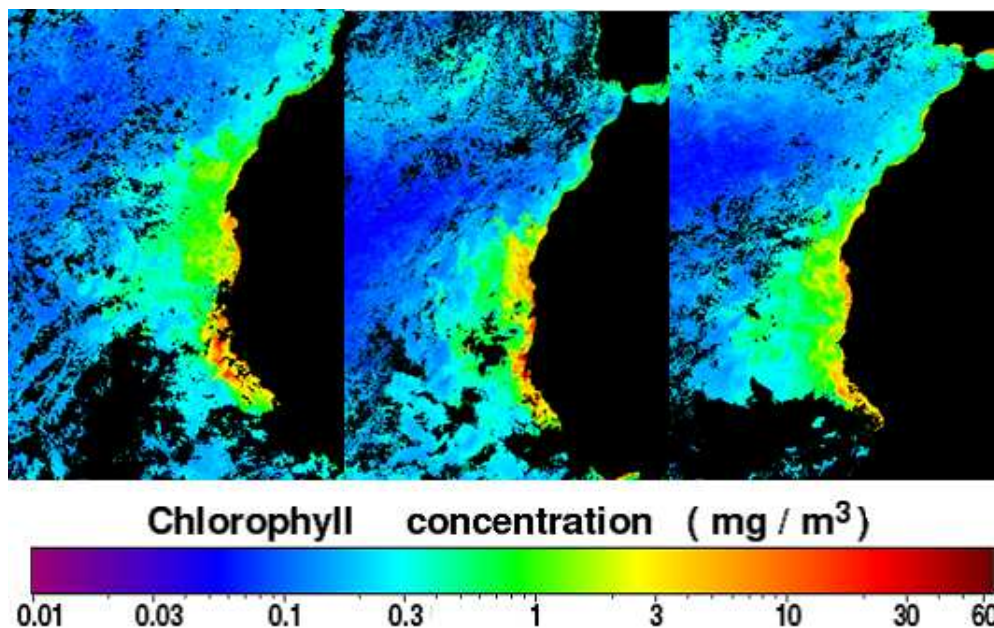


Figure 6.27: *The weekly average chlorophyll concentrations at the RV Poseidon measurements area during the three weeks (2-9 Feb. 2007, 10-17 Feb. 2007 and 18-25 Feb. 2007) respectively from left to right.*

phyll concentrations ( $\text{mg}/\text{m}^3$ ) along the back trajectories. The graph shows positive correlations with average and maximum chlorophyll concentration with correlation coefficients of ( $R=0.816$ ) and ( $R=0.758$ ) respectively. In order to give an overview on the correlations mentioned above, the correlation coefficients of BrO (DSCDs) with different chlorophyll parameters are plotted together in Figure 6.31. The figure indicates positive correlations with local chlorophyll concentrations and average and maximum chlorophyll concentrations along the back trajectories of air masses. Since the correlation coefficient with water surface contact time is negative, the correlations are also negative with the two parameters product 1 and Product 2. These negative correlations should be interpreted as mentioned above. They are mentioned here only for completeness of the review.

Comparing the information in Figure 6.31 with the information in Figure 6.21, both data sets agree in showing positive correlations with local chlorophyll concentrations and average and maximum chlorophyll concentrations along the back trajectories of air masses.

Taking into consideration that the two experimental data sets are from different times (autumn 2003 and late winter 2007) and different locations (routes of Polarstern and of Poseidon). Their agreement about these positive correlations with chlorophyll concentrations is important in confirming these correlations.

Also taking into consideration the statistical errors in calculating correlation coef-

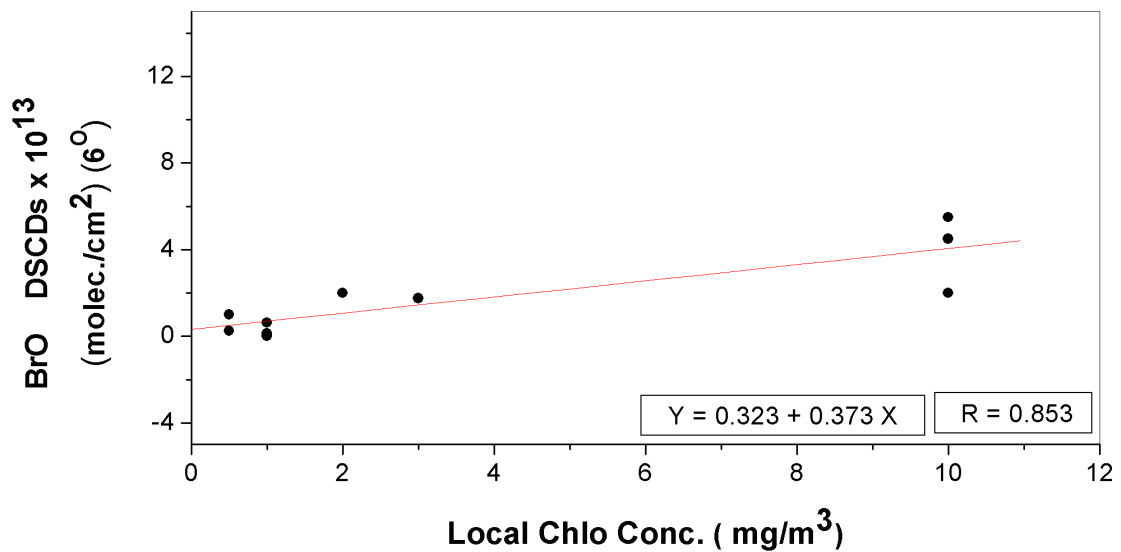


Figure 6.28: *The correlation of the BrO (DSCDs) (molec./cm<sup>2</sup>) at 6° elevation angle (M.Martin 2007) with the local chlorophyll concentrations (mg/m<sup>3</sup>).*

ficients, the strength of each correlation relative to the others cannot be absolutely determined from these two data sets because of small statistical sample sizes.

Figure 6.32 shows the same correlation coefficients with the same parameters in Figure 6.22 for the data of (M.Martin 2007). From comparing Figure 6.22 with Figure 6.32, it is noticed that the values of correlation coefficients between BrO (DSCDs) and all these different parameters do not significantly change with different duration of air masses contact with sea water surface.

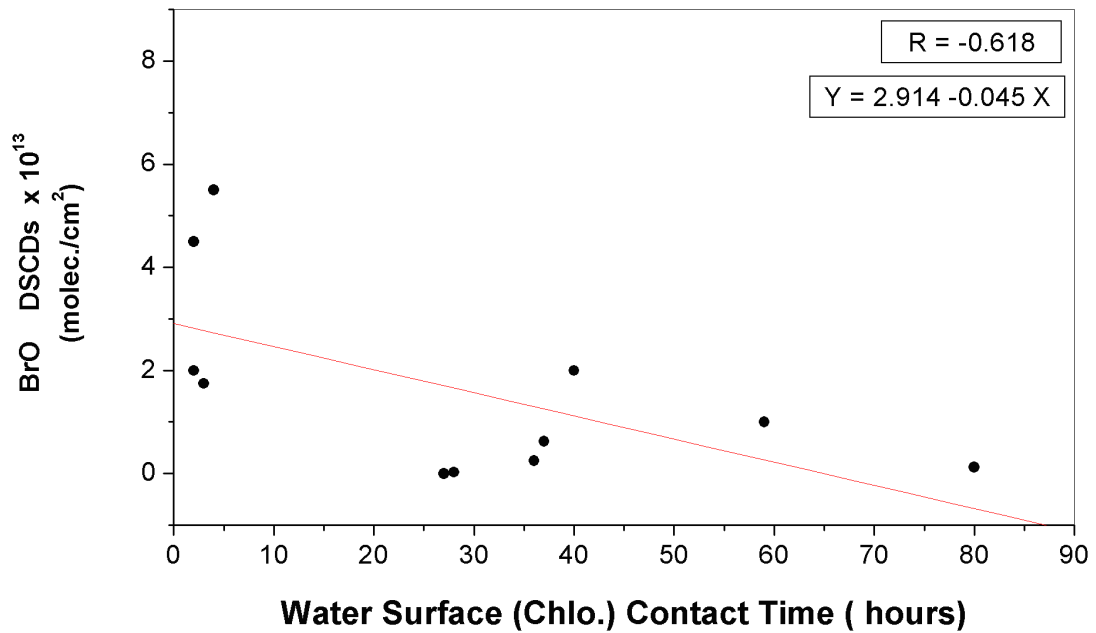


Figure 6.29: The correlation plots of the BrO (DSCDs) at 60 elevation angle (M.Martin 2007) with the water surface contact time.

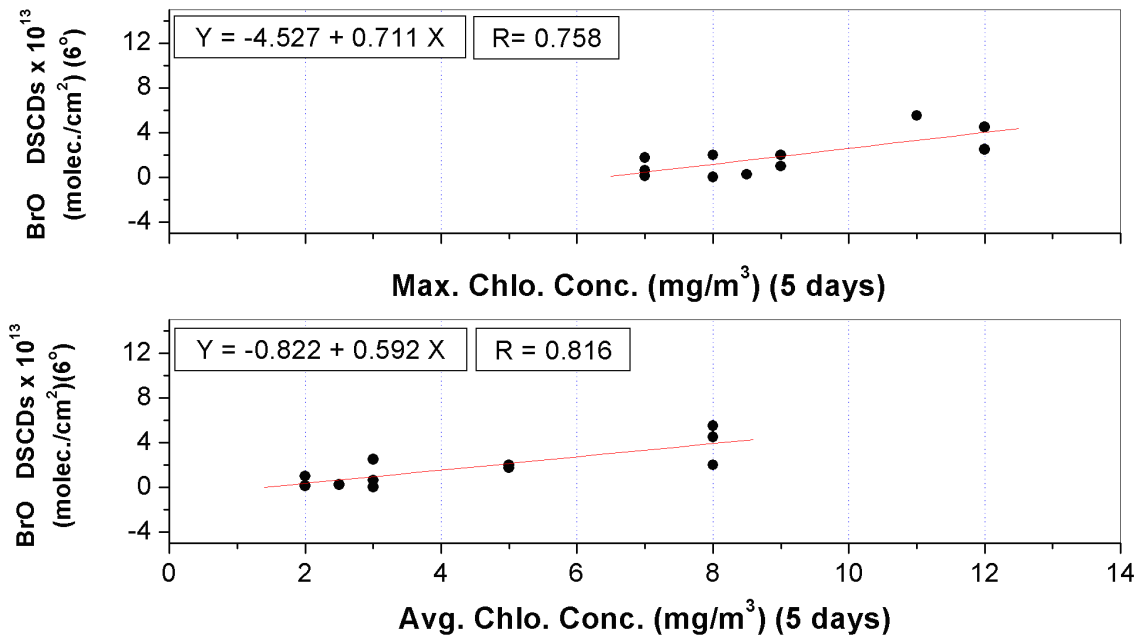


Figure 6.30: The correlation of BrO (DSCDs) (molec./cm<sup>2</sup>) at 60 elevation angle (M.Martin 2007) with the average and maximum chlorophyll concentrations (mg/m<sup>3</sup>) along the tracks of back trajectories.

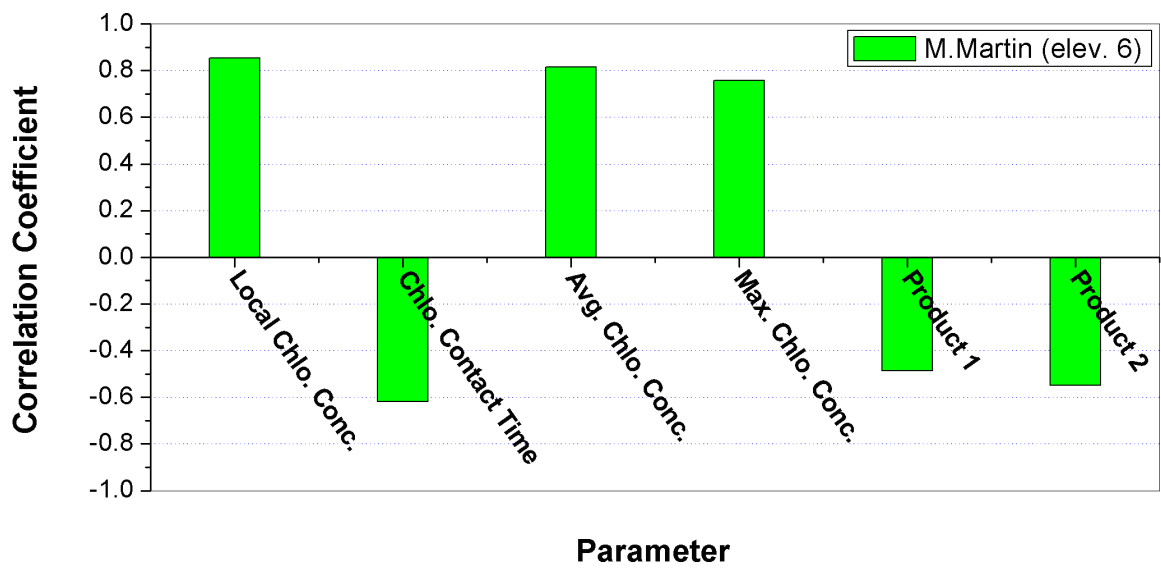


Figure 6.31: Correlations coefficients of different chlorophyll parameters with BrO (DSCDs) (M. Martin 2007).

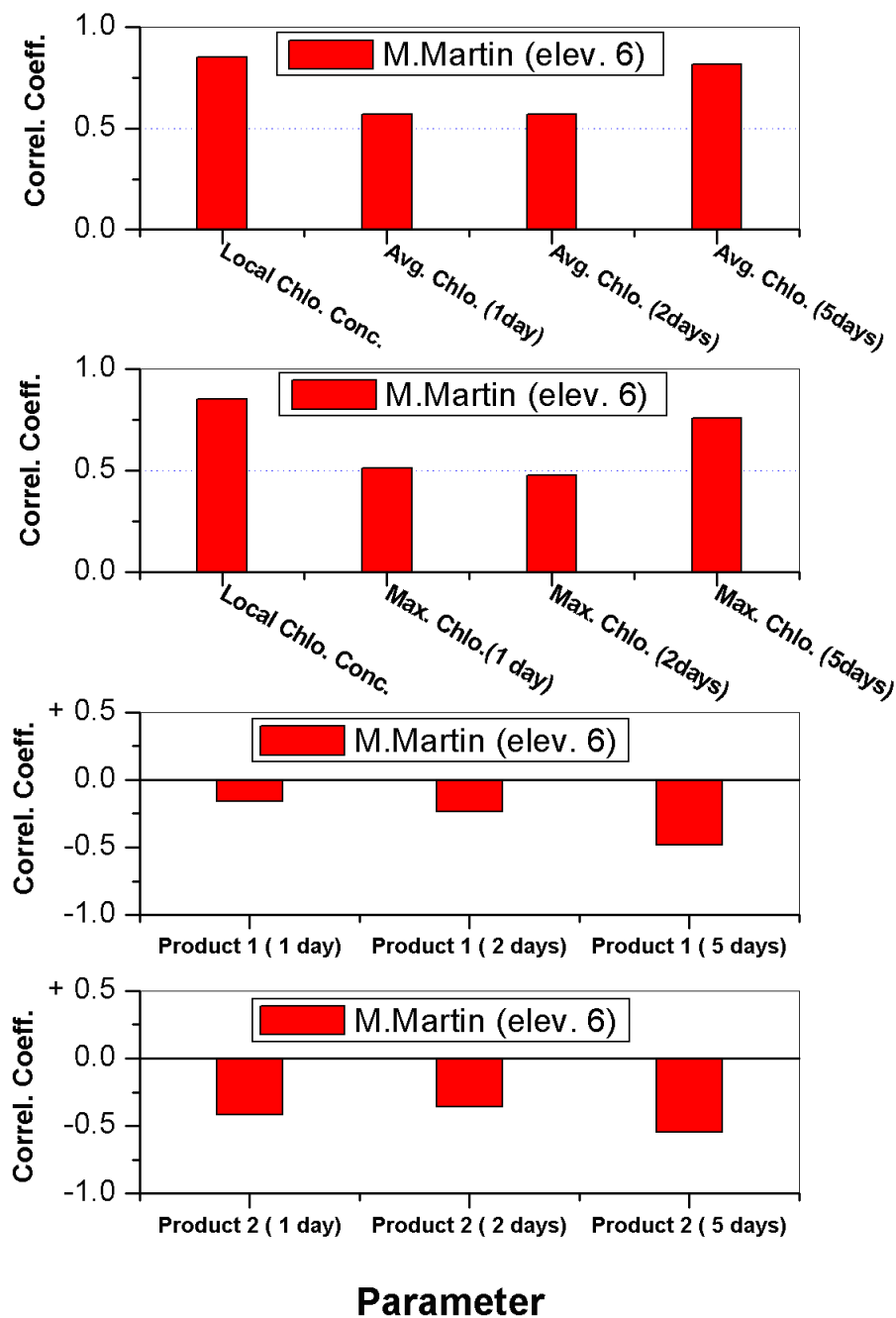


Figure 6.32: The correlation coefficients of BrO (DSCDs) with local chlorophyll concentrations, average and maximum chlorophyll concentrations of the first one and two days back in time and for the whole five days back trajectories. The correlation coefficient of product 1 and product 2 are also shown (M. Martin 2007).

### Summary of BrO-chlorophyll correlations

Overall, from all the correlations discussed above, we can draw the following conclusions:

There are positive correlations between BrO (DSCDs) and the local chlorophyll concentrations as well as the average and maximum chlorophyll concentrations along the back trajectories of air masses.

The strengths of different correlations were not significantly different for the calculated back trajectories for five days, two days or one day. This means the effect of contact time between air masses and sea water surface could not be so far observed as a significant parameter for BrO formation. The effect of local chlorophyll concentration seems to play the major role in BrO formation but this needs further investigation using more experimental data.

The overall rather low correlation coefficients and fluctuations in their values [in the data set of current work (2003 data)] can be attributed to three reasons:

1. The small statistical sample sizes of the two data sets used in this study so far.
2. In general, chlorophyll (and in turn, algae and phytoplankton) are not the only sources of BrO precursors.
3. The chlorophyll concentration data used in this study were weekly averages not daily averages. This also has its effects on the precision of the chlorophyll data used in correlation studies.

From the data set of M. Martin (2007), it was more clear that the local chlorophyll concentrations were probably the most significant contributors to BrO elevated values. The extremely short distance the air back trajectories spent in contact with ocean surface support the idea that the contributions from distant chlorophyll aggregations upwind are not as much significant as the local ones.

From both data sets used in this study, elevated BrO (DSCDs) were observed for short periods of time (few hours) during some measurements days. This corresponds to a few tens of kilometers of spatial extent of areas with elevated BrO levels. This also supports the idea that distant chlorophyll aggregations from a certain location are not significant sources of the detected BrO at these locations.

### 6.5.2 BrO-Aerosol Correlations

It is interesting to study correlations between the observed BrO (DSCDs) and several important aerosol parameters. Several marine aerosol parameters were measured by Bill Keene et al. simultaneously with MAX-DOAS measurements on Polarstern during the cruise leg ANTXXI/1 (2003). From these parameters, three interesting ones were chosen to study their covariance (possible correlations) with BrO (DSCDs): marine aerosols pH number, percentage and absolute particulate  $Br^-$  deficit in aerosols relative to sea salt.

Figures 6.33 and 6.34 show the correlation between BrO (DSCDs) at elevation angles  $3^\circ$  and  $10^\circ$  and the sea-salt aerosol pH inferred from the measured phase partitioning of HCl and measured during day time and night time respectively. The night measurements on any particular day were done at the early hours of the day before sunset.

The negative correlation with the pH number means a positive correlation with acidity of aerosols. Aerosol acidity is an important factor for the auto catalytic oxidation of marine aerosols. This process releases  $Br^-$ , which subsequently forms BrO in the MBL. Figures 6.35 and 6.36 show the correlation between BrO (DSCDs) at elevation angles  $3^\circ$  and  $10^\circ$  and the percentage deficit in particulate ( $Br^-$ ) marine aerosols relative to sea salt (measured during the day time and night time respectively).

Figures 6.37 and 6.39 show the correlation of BrO (DSCDs) at elevation angles  $3^\circ$  and  $10^\circ$  with absolute particulate  $Br^-$  deficit relative to sea salt during day time and night time respectively. The positive correlations with  $Br^-$  deficit in marine aerosols are an indication of an increase in the volatile inorganic  $Br^-$  (i.e. an increase in the release of  $Br^-$  from marine aerosols into the gas phase) and subsequent formation of BrO in the MBL.

To study the possible correlation with dust aerosol, the aerosol optical depth (AOD) values over the ocean from SeaWifs satellite maps were used. The AOD values are weekly averages of the corresponding weeks of measurements and detected at wavelength of 865 nm. Briefly this is called AOD (865 nm). For this purpose, satellite maps of the average AOD of the three weeks (24-31 Oct. 2003, 1-8 Nov. 2003 and 9-16 Nov. 2003) were used. See Figure 6.40 By overlaying the maps of daily locations of the RV Polarstern (See Figures 6.40 left panels) on the satellite maps of (AOD 865 nm), the corresponding daily values of (AOD 865 nm) could be deduced. Then the correlation between the two quantities could be established. Figure (25) shows the correlation of BrO (DSCDs) at elevation angles  $3^\circ$  and  $10^\circ$  with the dust Aerosol Optical Depth (AOD 865nm) of dust from (SeaWifs) satellite maps in a similar procedure.

A summary of all the correlation coefficients of BrO (DSCDs) with different aerosol parameters is shown in Figure (26). Also to study the possible correlation between BrO (DSCDs) from the data set of M. Martin diploma thesis (2007) with dust aerosol

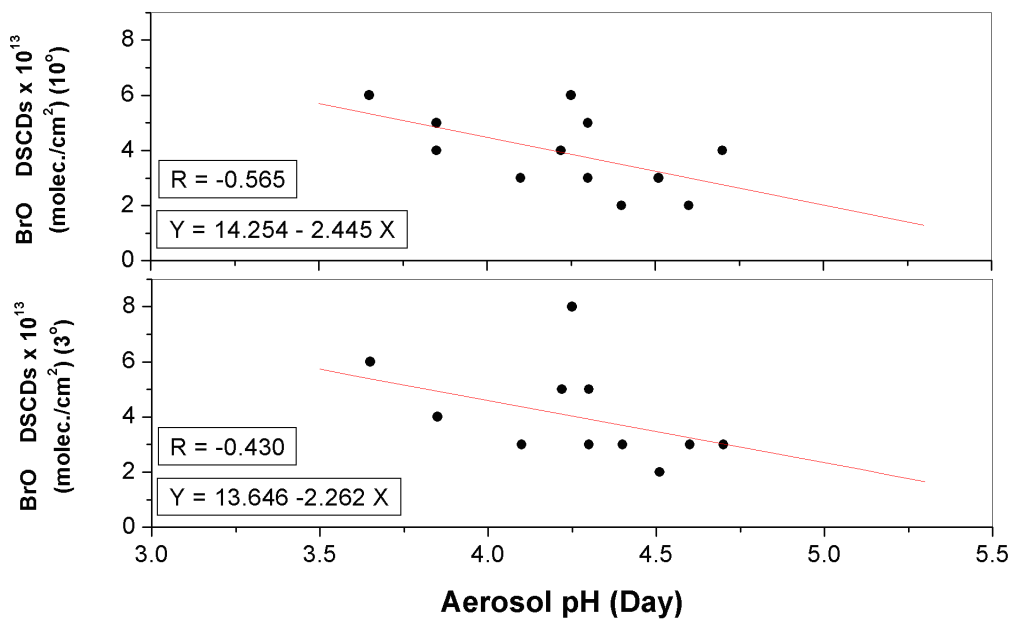


Figure 6.33: Correlation of BrO (DSCDs) at elevation angle  $3^\circ$  and  $10^\circ$  with aerosol pH number measured during day time. [aerosol data adapted from W.Keene et al., 2004]

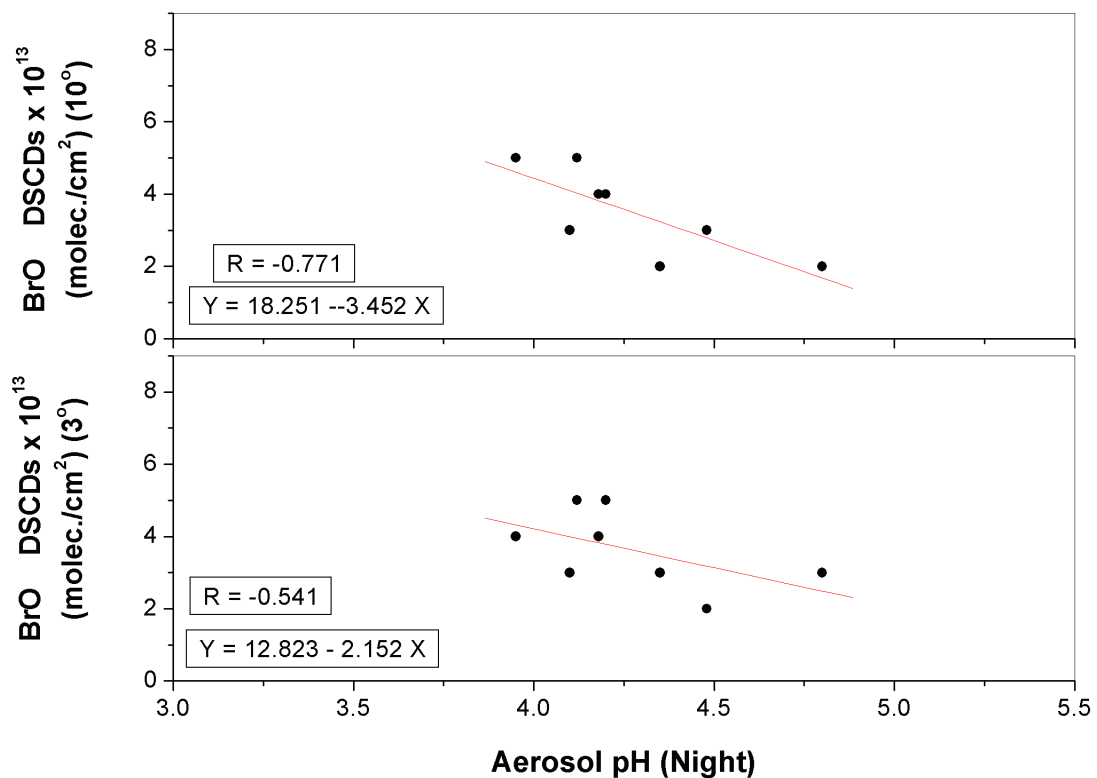


Figure 6.34: Correlation of BrO (DSCDs) at elevation angle  $3^\circ$  and  $10^\circ$  with aerosol pH number measured during night time. [aerosol data adapted from W.Keene et al., 2004]

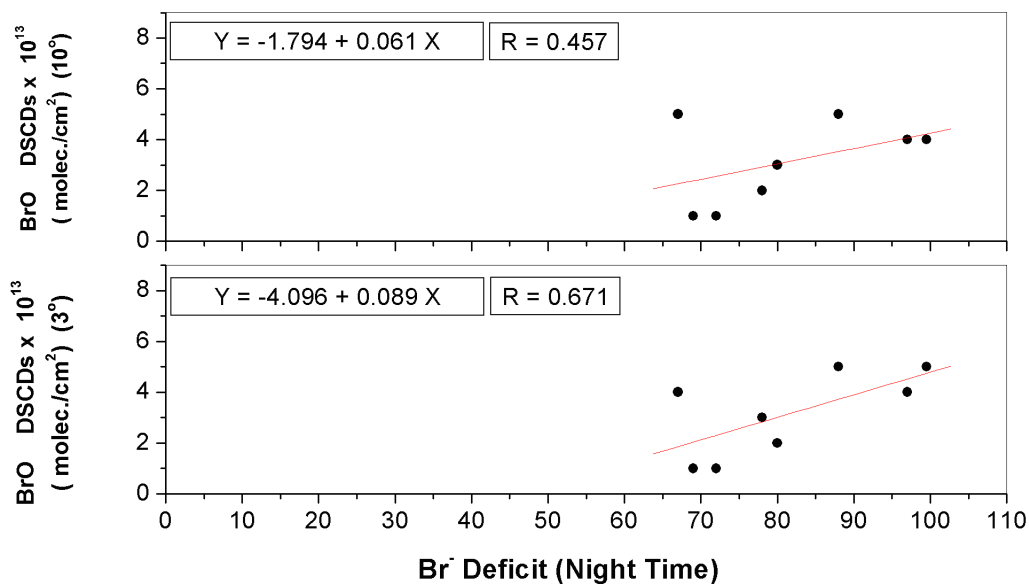


Figure 6.35: The correlation of BrO (DSCDs) at elevation angles  $3^\circ$  and  $10^\circ$  with percentage deficit in particulate ( $Br^-$ ) marine aerosols relative to sea salt (during day time). [aerosol data adapted from W.Keene et al., 2004]

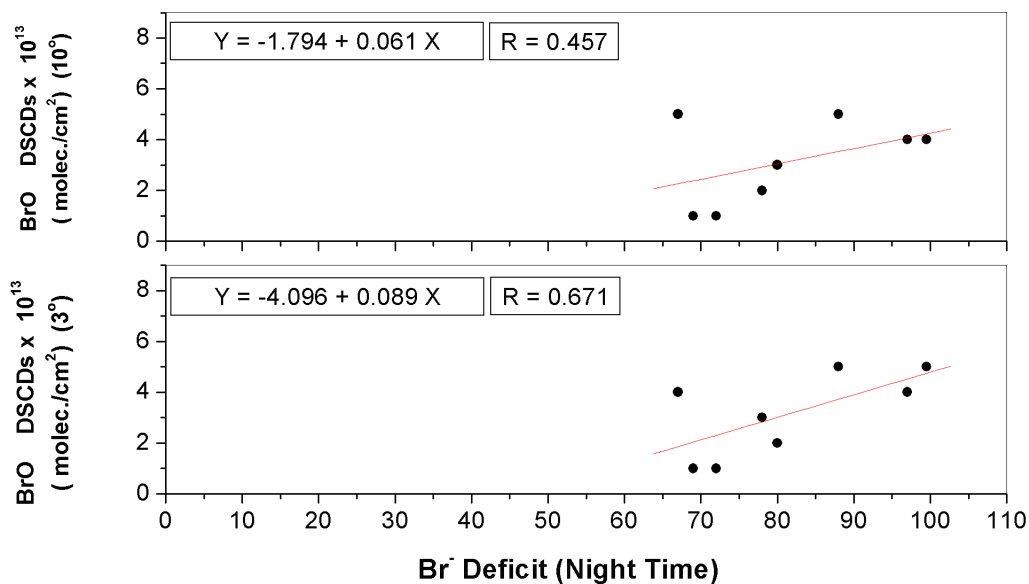


Figure 6.36: The correlation of BrO (DSCDs) at elevation angles  $3^\circ$  and  $10^\circ$  with the percentage deficit in particulate ( $Br^-$ ) marine aerosols relative to sea salt (during the night time). [aerosol data adapted from W.Keene et al., 2004]

optical depth (AOD 865 nm), SeaWifs satellite maps were used as above.

Figure (27) shows the satellite maps of (AOD 865 nm) from SeaWifs for the three weeks (2-9 Feb, 10-17 Feb and 17-25 Feb. 2007 respectively) and also the daily positions of the RV Poseidon during measurements.

The correlation between BrO (DSCDs) from M. Martin data set and the (AOD 865 nm) is shown in Figure (28). The negative correlation between the two quantities can be observed from the graph with a correlation coefficient of ( $R = - 0.793$ ).

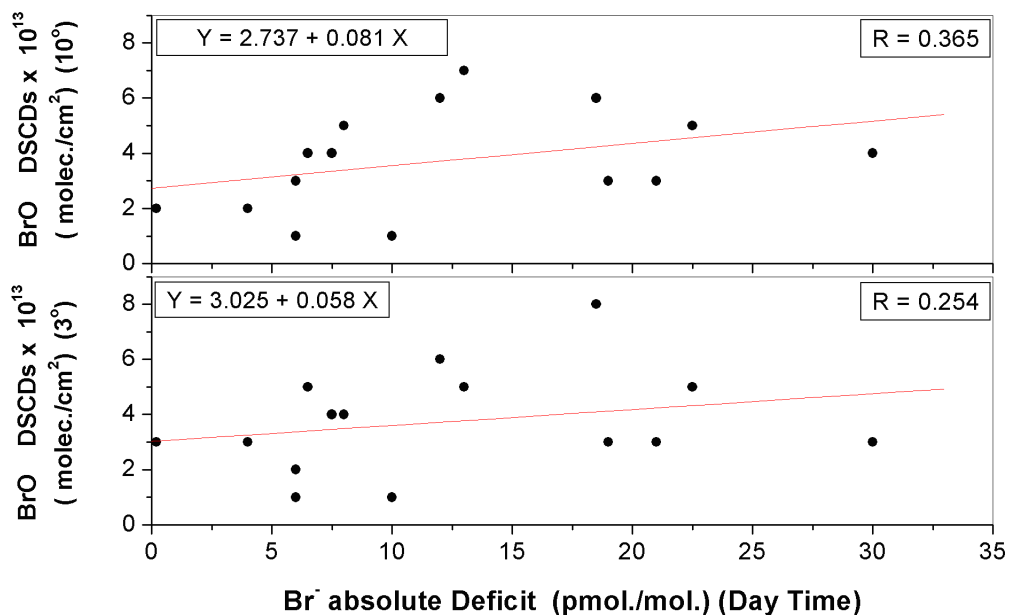


Figure 6.37: The correlation of BrO (DSCDs) at elevation angles 3° and 10° with absolute particulate Br<sup>-</sup> deficit relative to sea salt during day time. [aerosol data adapted from W.Keene et al., 2004]

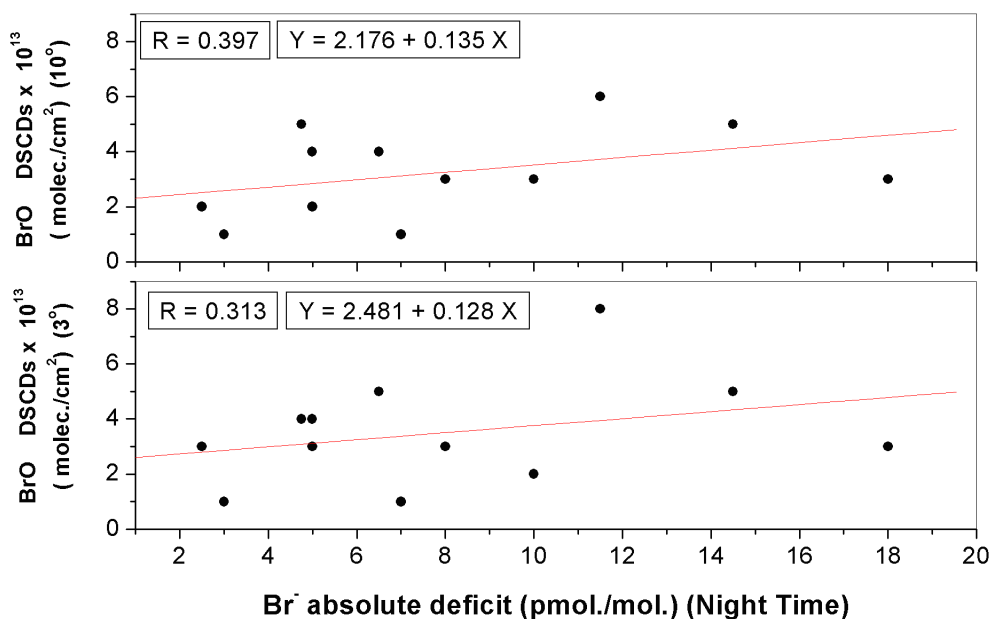


Figure 6.38: The correlation of BrO (DSCDs) at elevation angles 3° and 10° with absolute particulate Br<sup>-</sup> deficit relative to sea salt during night time. [aerosol data adapted from W.Keene et al., 2004].

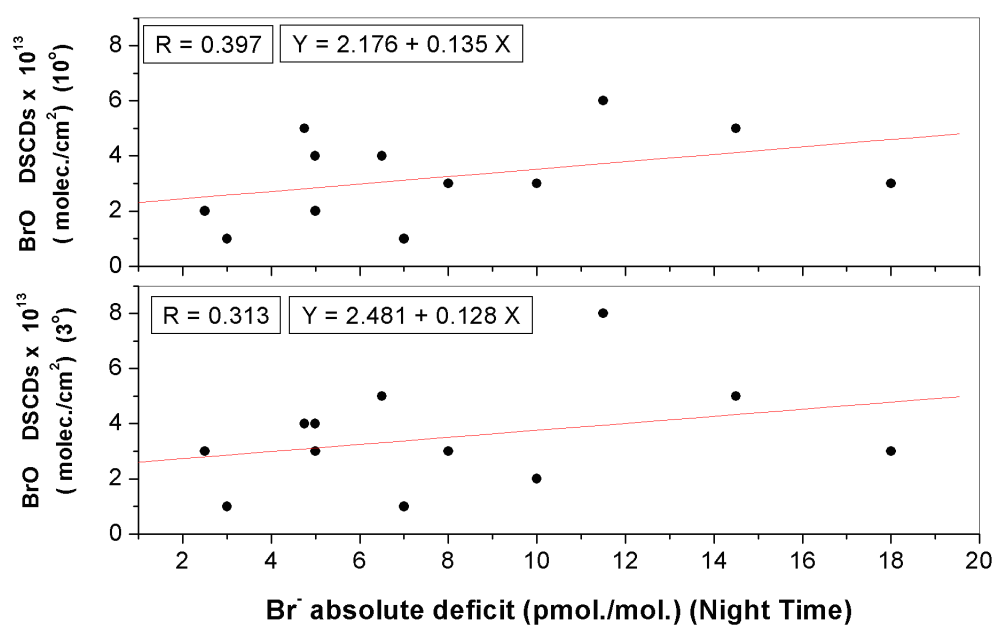


Figure 6.39: The correlation of BrO (DSCDs) at elevation angles 3° and 10° with absolute particulate Br<sup>-</sup> deficit relative to sea salt during night time.

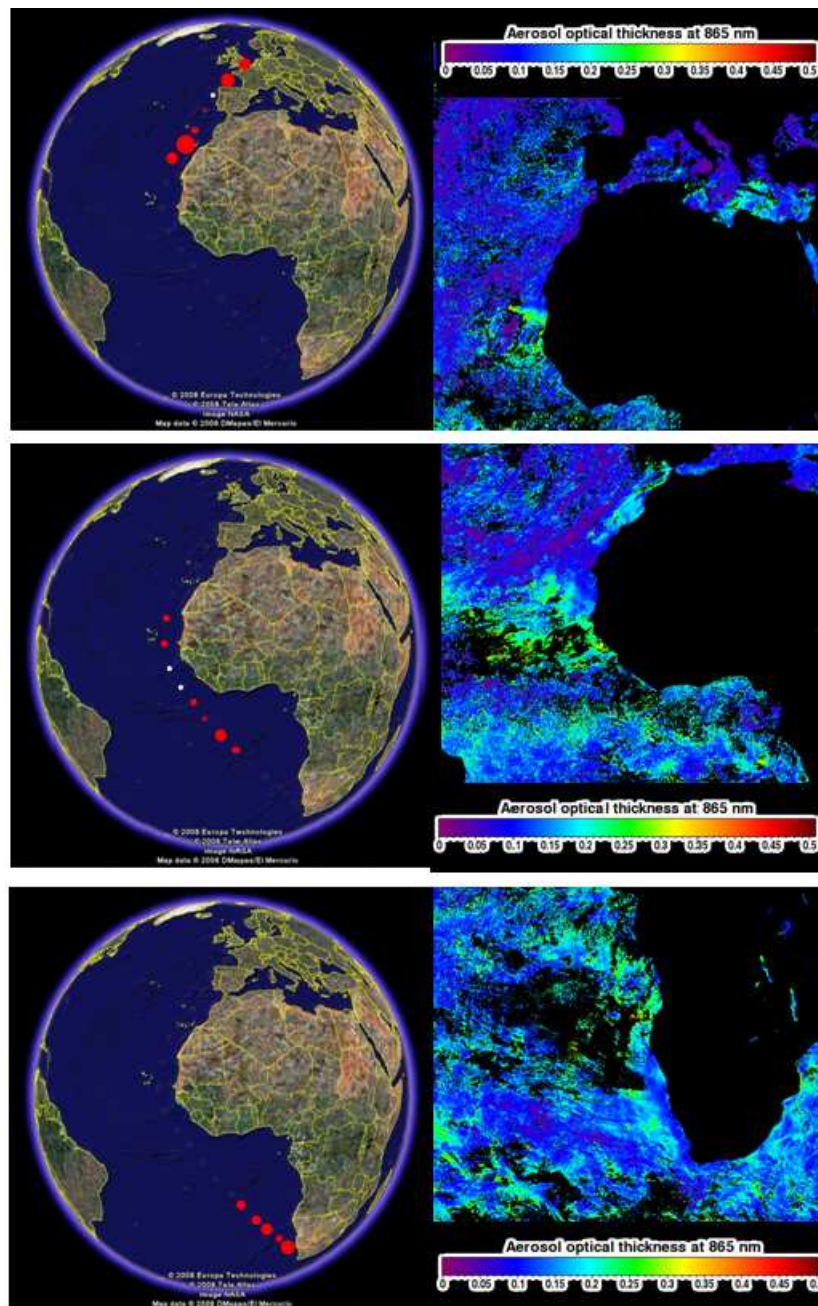


Figure 6.40: *Left panels show the positions of the RV Polarstern during the three weeks of measurement. Right panels show the weekly average of (AOD 865nm) during the three weeks(23.10.2003 - 01.11.2003)(01.11.2003 - 08.11.2003)(09.11.2003 - 16.11.2003). Please notice that the measurements ended on 13.11.2003.*

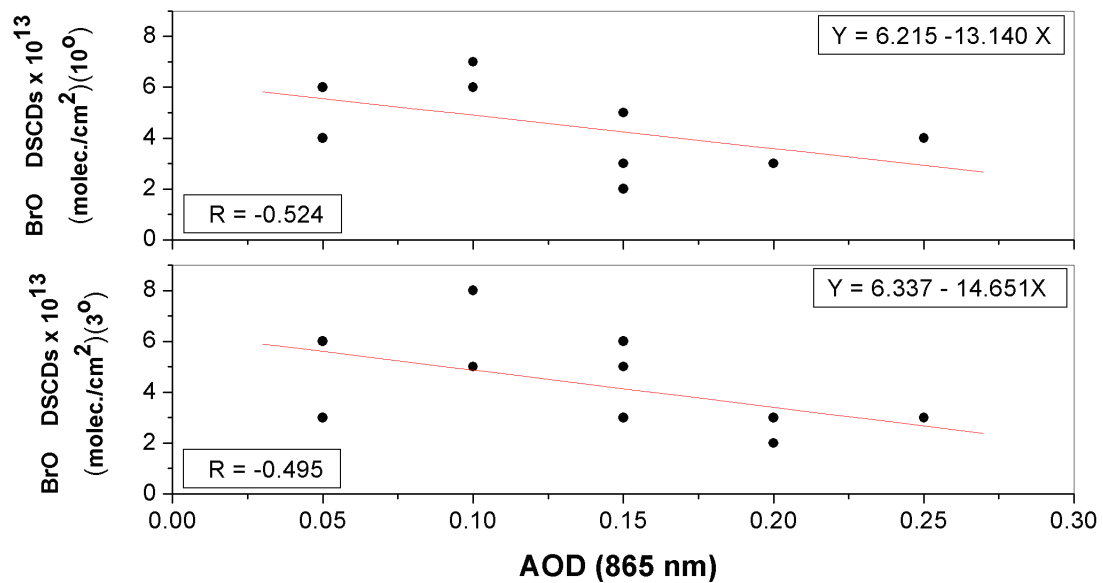


Figure 6.41: The correlation of BrO (DSCDs) at elevation angles 3° and 10° with the dust Aerosol Optical Depth (AOD 865nm) from SeaWifs satellite maps.

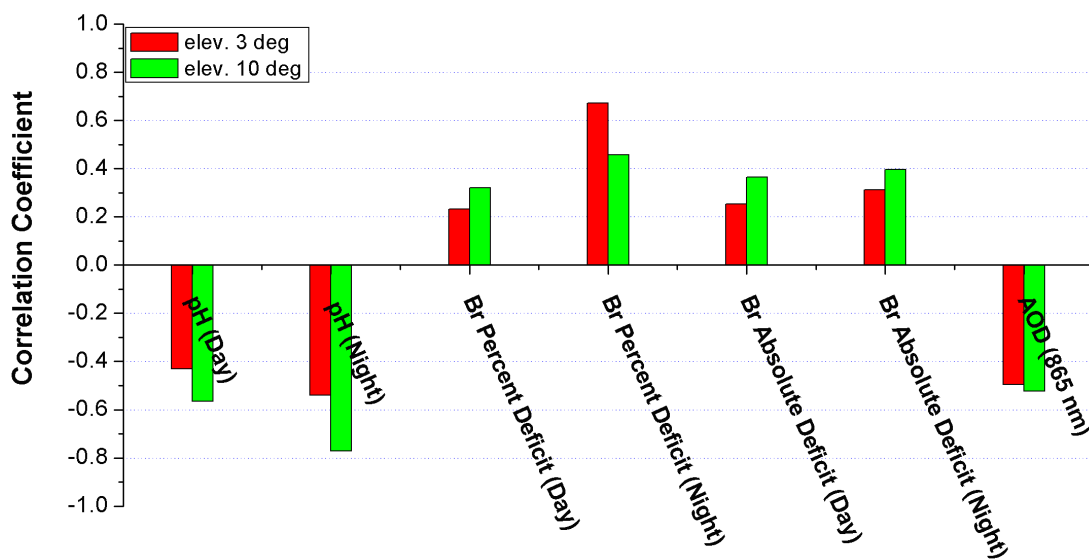


Figure 6.42: Correlation coefficients of BrO ( DSCDs) with the different aerosol parameters.

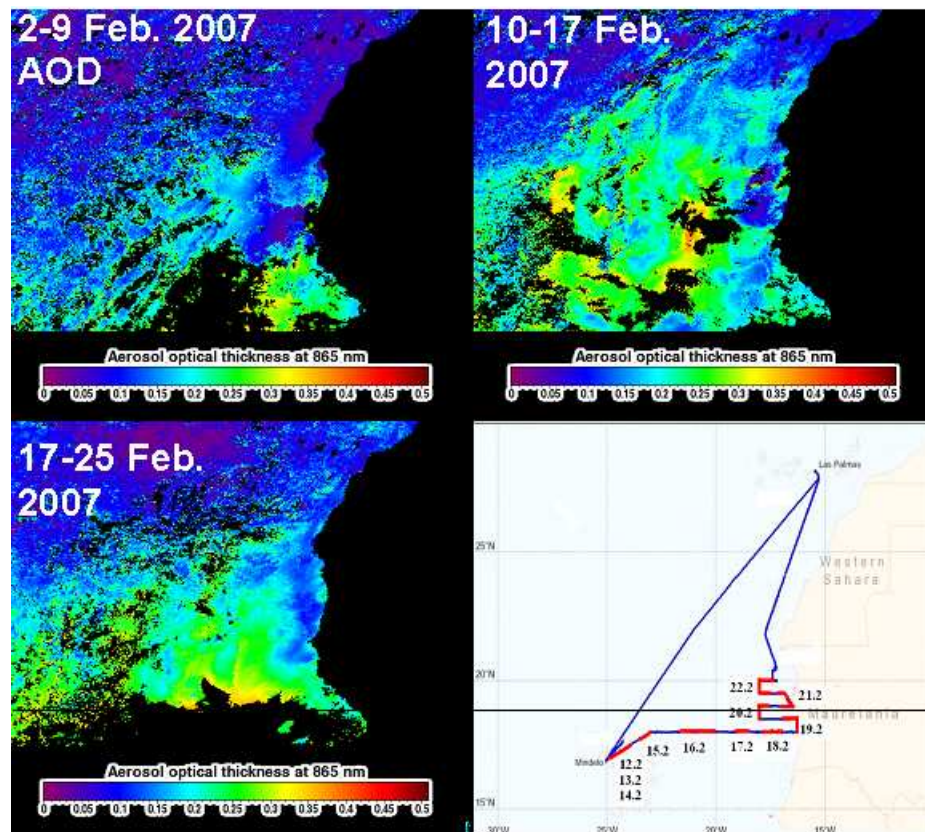


Figure 6.43: Satellite maps of (AOD 865 nm) from SeaWiFS for the three weeks (2-9 Feb., 10-17 Feb. and 17-25 Feb.) and also the daily positions of the RV Poseidon during measurements.

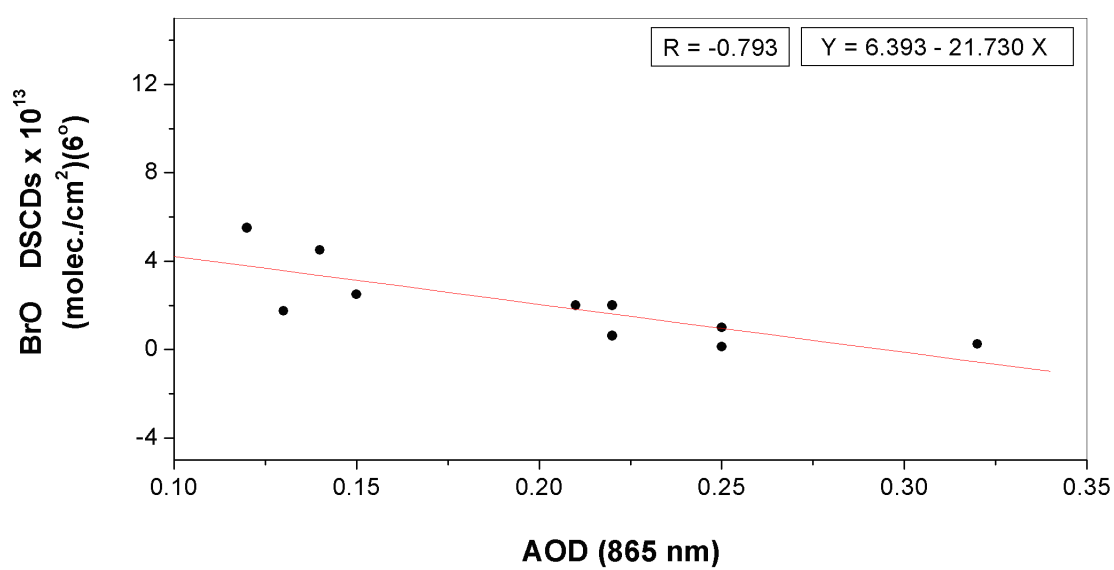


Figure 6.44: *The correlation of BrO ( DSCDs) with dust Aerosol Optical Depth (AOD 865 nm) (M. Martin 2007).*

### Summary of BrO-aerosol correlations

From all the BrO-aerosol correlations discussed above, the following can be concluded:

There is a positive correlation between BrO (DSCDs) and the acidity of marine aerosols (deduced from the negative correlation to the pH number).

There is a positive correlation between BrO (DSCDs) and the particulate  $Br^-$  percentage and absolute deficiencies in the marine aerosols relative to sea salt. This indicates more  $Br^-$  release from the aerosol phase into the gas phase and its possible contribution to BrO formation in the MBL.

There is a negative correlation between BrO (DSCDs) and dust Aerosols Optical Depth (AOD 865nm). This negative correlation is observed for both of the data sets used here. This could indicate some chemical processes related to dust aerosols in the MBL which seems to affect BrO negatively.

# 7 Results from Auto-MAX-DOAS measurements

## 7.1 Introduction

The MAX-DOAS instruments can be mounted on different types of stationary and mobile platforms. In this chapter, the results of atmospheric trace gas measurements of the ground-based mobile MAX-DOAS (Auto-MAX-DOAS)<sup>1</sup> are presented. The Auto-MAX-DOAS has some advantages as a platform and a tool for atmospheric trace gas measurements:

(1) **Provides good spatial resolution:** Auto-MAX-DOAS provides a better spatial resolution than that of Satellites : Since the spatial resolutions of satellites instruments are of order of tens of kilometers (e.g. 30x60 km for SCIAMACHY satellite instrument)<sup>2</sup>.

(2) **Mobile:** Auto-MAX-DOAS enables encircling pollution sources with measurements (e.g. power plants, industrial areas and even whole cities). Auto-MAX-DOAS also can be driven under pollution plumes to take cross-section measurements across them. These advantages don't exist in stationary ground-based instruments.

(3) **Available at any time:** Auto-MAX-DOAS is easy to install on a car top in less than 20 minutes and this makes it very suitable for going to detect pollution near/downwind from the source in case of any pollution event. Auto-MAX-DOAS readiness to go any time as a platform is an advantage because it does not need much logistical requirements and scheduled times for operation like airborne instruments.

(4) **Economic:** Much cheaper in its operation than airborne and satellite instruments.

---

<sup>1</sup>In this work, the term: (Auto-MAX-DOAS) refers to the MAX-DOAS instrument and the carrying platform (e.g. a car or a mini-bus)

<sup>2</sup>Scanning Imaging Absorption Spectrometer for Atmospheric CHartography

In this work, Auto-MAX-DOAS has been successfully used to carry out the following measurements:

1. Carry out measurements along the roads between some cities in Europe and detect  $\text{NO}_2$  along the road between them. Passing several different environments: heavy traffic, industrial and urban areas. These measurements covered a regional/continental scale.
2. Encircle industrial areas of significant  $\text{NO}_2$  emissions. The Auto-MAX-DOAS could detect and quantify the dSCDs of emitted  $\text{NO}_2$  in areas upwind and downwind from the source. These measurements were carried on in the Rhein-Neckar Valley area.
3. Carry out measurements of a big plume caused by a big fire which covered large regions of Europe (see below). These measurements covered regional/continental scale.

The common factor in all above measurements is the ability to reach the polluted areas and perform measurements around them and across the trace gas plume once or more. In the following sections, each of the above three measurement types will be discussed in detail.

## 7.2 Results from measurements along the roads

### 7.2.1 Brussels-Heidelberg measurements

In order to acquire some knowledge about the levels of  $\text{NO}_2$  pollution over urban/industrial areas in Europe, measurements along the road between Brussels (Belgium) and Heidelberg (Germany) were carried out. These measurements and their results are discussed in this section.

On 05.09.2006, measurements using Auto-MAX-DOAS were carried out on the road between Brussels (Belgium) and Heidelberg (Germany). The distance between the two cities is about 350 km .

The route of driving crossed the territories of three European countries in series: Belgium, Holland then Germany. Figure 7.1 shows the route taken for measurements by Auto-MAX DOAS between the two cities.

Continuous measurements were carried out during driving and the sequence of elevation angles was ( $22^\circ$ ,  $22^\circ$ ,  $22^\circ$ ,  $22^\circ$ ,  $40^\circ$ ,  $90^\circ$ ). Figure 7.2 shows the  $\text{NO}_2$  dSCDs from measurements along the road between Brussels (Belgium) and Heidelberg (Germany). The two vertical lines on the graph show the time when the borders were crossed. It is noticeable from the graph that there is a high-narrow peak shortly

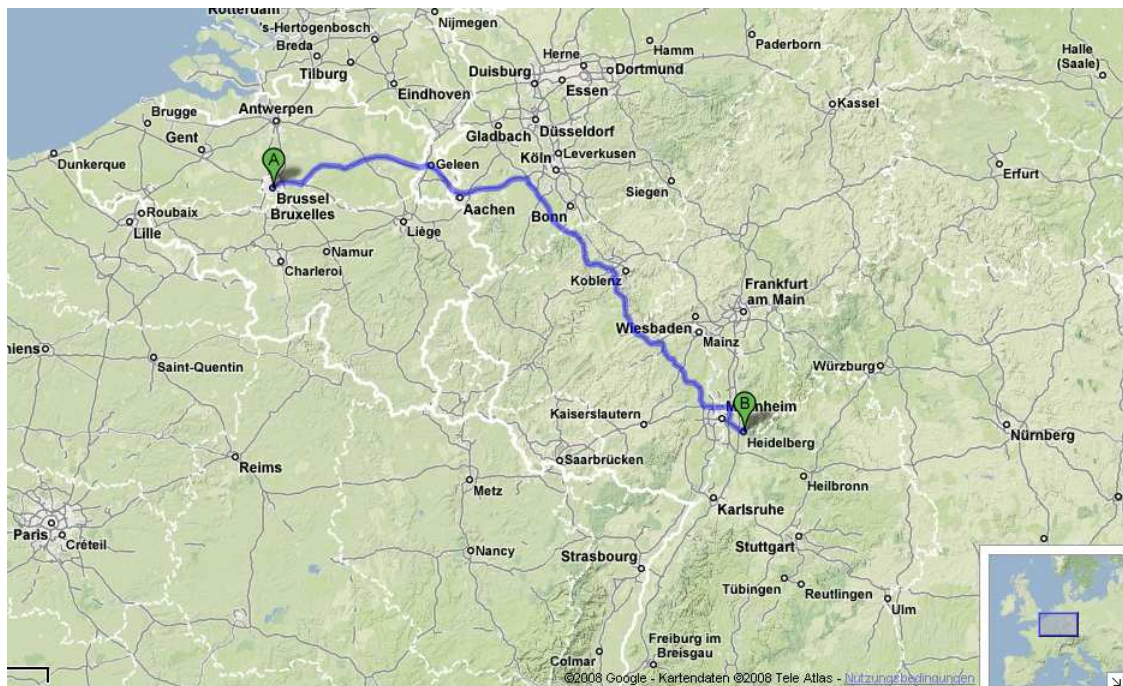


Figure 7.1: *The road between the Brussels and Heidelberg which was used by Auto-MAX-DOAS for  $\text{NO}_2$  measurements. Continuous measurements were carried out during driving.*

after crossing the Holland-Germany borders. Checking the location of driving at that time, it was immediately after driving north of Aachen city in Germany. After investigation, using maps and google earth<sup>TM</sup>, it was found that it is the big power plant (Weisweiler power plant) which works with fossil fuel (coal and natural gas)<sup>3</sup>. Figure 7.3 shows the location of the power plant (from google earth<sup>TM</sup>) and the big plume of water vapor emitted from its stacks. Also it is noticeable that the wind direction in this picture is coming from southeast. During measurements, the wind direction was from west/north-west.

Investigating the  $\text{NO}_2$  dSCDs peak caused by this power plant, it continued for about 10 minutes between 15:45 and 15:55 o'clock (see Figure 7.2). With a driving speed of about 100km/h on the highway it can be deduced that the plume was observed by the Auto-MAX-DOAS for about 15 kilometers. This means the plume was not crossing the plane of the road vertically (as if the wind is blowing from north) but rather was somehow tangentially overlapping with the line of the road so it could be observed for an extended time (10 minutes). This is consistent with the wind direction coming from the west/north-west.

<sup>3</sup>See: <http://www.rwe.com/generator.aspx/rwe-power-icw/standorte/braunkohle/kraftwerke/weisweiler/language=de/id=9674/weisweiler-page.html>.

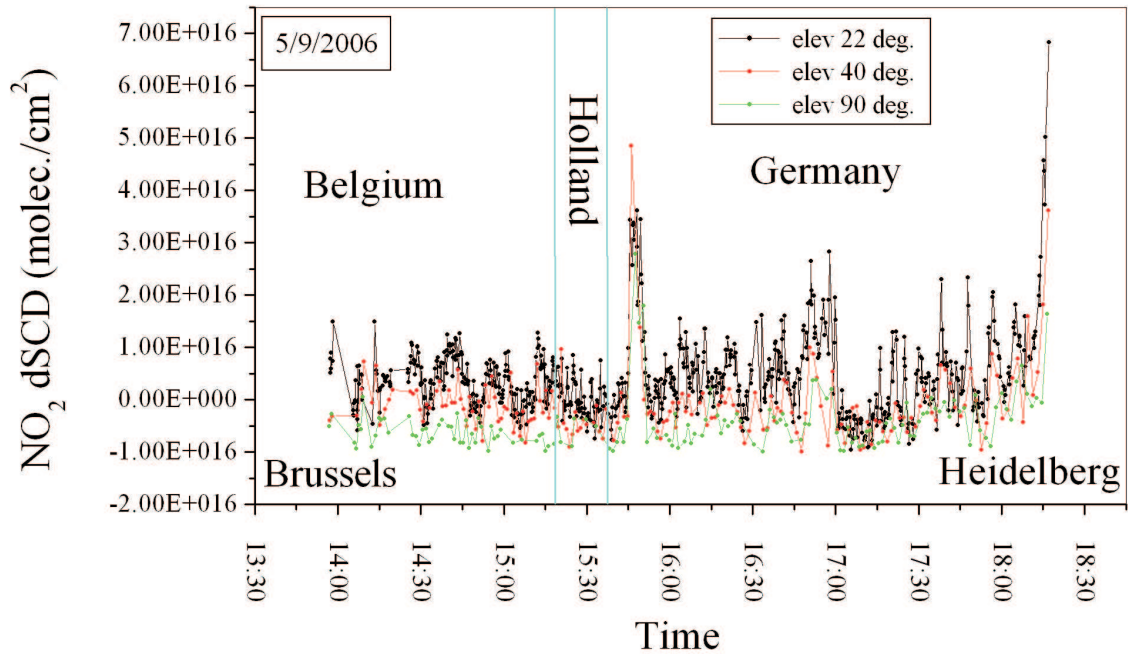


Figure 7.2: The  $\text{NO}_2$  dSCDs from measurements along the road between Brussels (Belgium) and Heidelberg (Germany) on 5.9.2006.



Figure 7.3: the location of the power plant (from google earth ) and the big plume of water vapor emitted from its stacks. The height of the stack is 180 m and it is about 500m off the road.

### 7.2.2 Vertical Column Densities Calculation Method

To relate the observed Slant Column Densities (S) to the vertical Column Density (V)[Platt, 2008], The Air Mass Factor (A) can be expressed as:

$$A = \frac{S}{V} \quad (7.1)$$

Since (S) can be measured at different elevation angles, then (S) from a certain elevation angle ( $\alpha$ ) will be noted as ( $S_\alpha$ ).

Assuming we need to calculate tropospheric slant column density ( $S_{trop.}$ ), then we have:

$$A_{trop.} = \frac{S_{trop.}}{V_{trop.}} \quad (7.2)$$

Since  $S_{trop.}$  can be expressed as:

$$S_{trop.} = S_\alpha + S_{ref.} - S_{strat.} \quad (7.3)$$

Where:

$S_{ref.}$  is the slant column density of the reference spectrum (FRS) used in spectral evaluation and it is an unknown quantity because the absorption in the reference spectrum can not be directly estimated.

$S_{strat.}$  is the stratospheric slant column density, which is also an unknown quantity<sup>4</sup>.

Then from equations (7.2) and (7.3),  $V_{trop.}$  can be expressed as:

$$V_{trop.} = \frac{S_\alpha + S_{ref.} - S_{strat.}}{A_{trop.}} \quad (7.4)$$

---

<sup>4</sup>Note that while ( $S_{ref.}$ ) is constant,  $S_{strat.}$  is time-dependent: First, because the stratospheric VCD is changing, and second because the stratospheric AMF is changing.

Since  $V_{trop.}$  can also be expressed as:

$$V_{trop.} = \frac{S_{\alpha} - S_{90}}{A_{trop.} - 1} \quad (7.5)$$

Where  $S_{90}$  is the slant column density at elevation angle  $90^{\circ}$  from the same measurement sequence of  $S_{\alpha}$ .

Then equating both equations (7.4) and (7.5), we get:

$$V_{trop.} = \frac{S_{\alpha} + S_{ref.} - S_{strat.}}{A_{trop.}} = \frac{S_{\alpha} - S_{90}}{A_{trop.} - 1} \quad (7.6)$$

Since  $V_{trop.}$ ,  $S_{\alpha}$ ,  $S_{strat.}$  and  $S_{90}$  are time-dependent quantities, equation (7.6) can be re-written as:

$$V_{trop.}(t) = \frac{S_{\alpha}(t) + S_{ref.} - S_{strat.}(t)}{A_{trop.}} = \frac{S_{\alpha}(t) - S_{90}(t)}{A_{trop.} - 1} \quad (7.7)$$

Then simplifying these two sides together, in a few steps, we get:

$$S_{ref.} - S_{strat.}(t) = \frac{S_{\alpha}(t) - (A_{trop.})(S_{90}(t))}{A_{trop.} - 1} \quad (7.8)$$

From equation 7.8, the two unknown quantities on the left hand side (LHS) can be expressed in terms of the known quantities on the right hand side (RHS). The quantities on the RHS ( $S_{\alpha}$  and  $S_{90}$  are known from measurements) and ( $A_{trop.}$ ) is calculated knowing the elevation angle ( $\alpha$ ).

From equation 7.8 and taking  $A_{trop.}$  to be equal to  $(1/\sin\alpha)$ , where  $\alpha$  is the elevation angle, we get:

$$S_{ref.} - S_{strat.} = \frac{S_{\alpha}(t) - (\frac{1}{\sin\alpha})(S_{90}(t))}{\frac{1}{\sin\alpha} - 1} \quad (7.9)$$

Applying this to the NO<sub>2</sub> results from Brussels-Heidelberg measurements:

This formula is applied to the NO<sub>2</sub> dSCDs ( $S_{\alpha}$ ) from elevation angles  $\alpha = 22^{\circ}$  and  $40^{\circ}$ . Since we have a sequence of measurements at elevation angles ( $22^{\circ}, 22^{\circ}, 22^{\circ}, 22^{\circ}, 40^{\circ}, 90^{\circ}$ ), this means we have four spectra at  $22^{\circ}$  elevation angle, one spectrum at  $40^{\circ}$  and finally one spectrum at  $90^{\circ}$ .

Concerning the four successive spectra taken at  $22^{\circ}$ :

Dividing the data into four groups, the closest in time to the  $90^{\circ}$  is the group number one and the farthest in time is the group number four.

Using data from these four groups (columns) and substituting them in equation 7.8, we can get the unknown term ( $S_{ref.} - S_{strat.}$ ). Plotting the resulting time series of applying the four data groups into the equation ??, we get four time series of data as shown in Figure 7.4.

First we have to remove the (outlier) from the data before applying the polynomial (see the oval shape in Figure 7.4). This outlier is because of the high peak from Weisweiler power plant (see above). Then we apply a polynomial of the second degree to these four series of data to get the best fit which represents the unknown term ( $S_{ref.} - S_{strat.}$ ).

By applying the polynomial, the values of  $R^2$  of the fit of the four series are different as seen in Figure 7.5. It is largest for the measurements closest in time to the  $90^{\circ}$  elevation angle and smallest for those with largest temporal difference. The fitted polynomial shows the expected behavior: the lowest values occur at the end of the measurements due to the increasing stratospheric NO<sub>2</sub> Slant Column Density ( $S_{strat.}$ ) with time approaching the sunset while the  $S_{ref.}$  is constant (see above).

The coefficients of the fitted polynomial are now used to approximate the term ( $S_{ref.} - S_{strat.}$ ) as follows:

From the polynomial equation (see Figure 7.5) and substituting each X with time of the day, we can get a time-series of the values of the time-dependent term ( $S_{ref.} - S_{strat.}$ ). Then substituting this time series into equation (7.4) for the individual measurements, we get a time series of the NO<sub>2</sub> VCDs with a high temporal resolution.

Repeating the same calculations for the  $40^{\circ}$  and  $90^{\circ}$  elevation angles too, we get a time-series of the NO<sub>2</sub> VCDs from the three elevation angles  $22^{\circ}$ ,  $40^{\circ}$  and  $90^{\circ}$ . Figure 7.6 shows the tropospheric NO<sub>2</sub> VCDs from the three elevation angles  $22^{\circ}$ ,

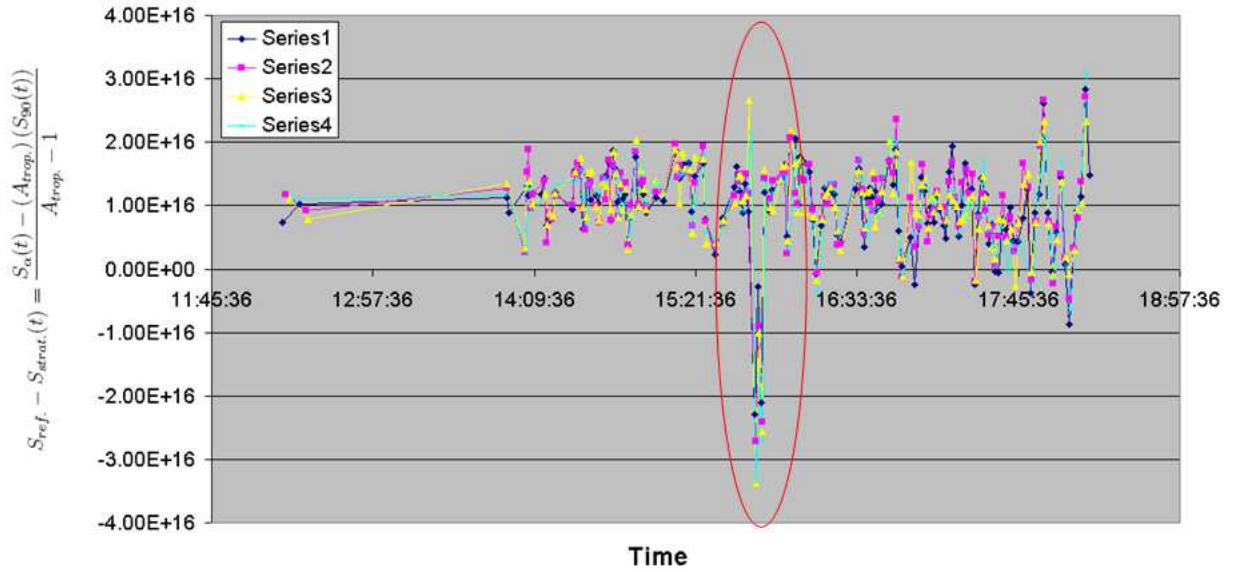


Figure 7.4: The term  $(S_{ref.} - S_{strat.})$  as a function of time. The oval shape shows the outlier of the data caused by the peak from Weisweiler power plant (see text).

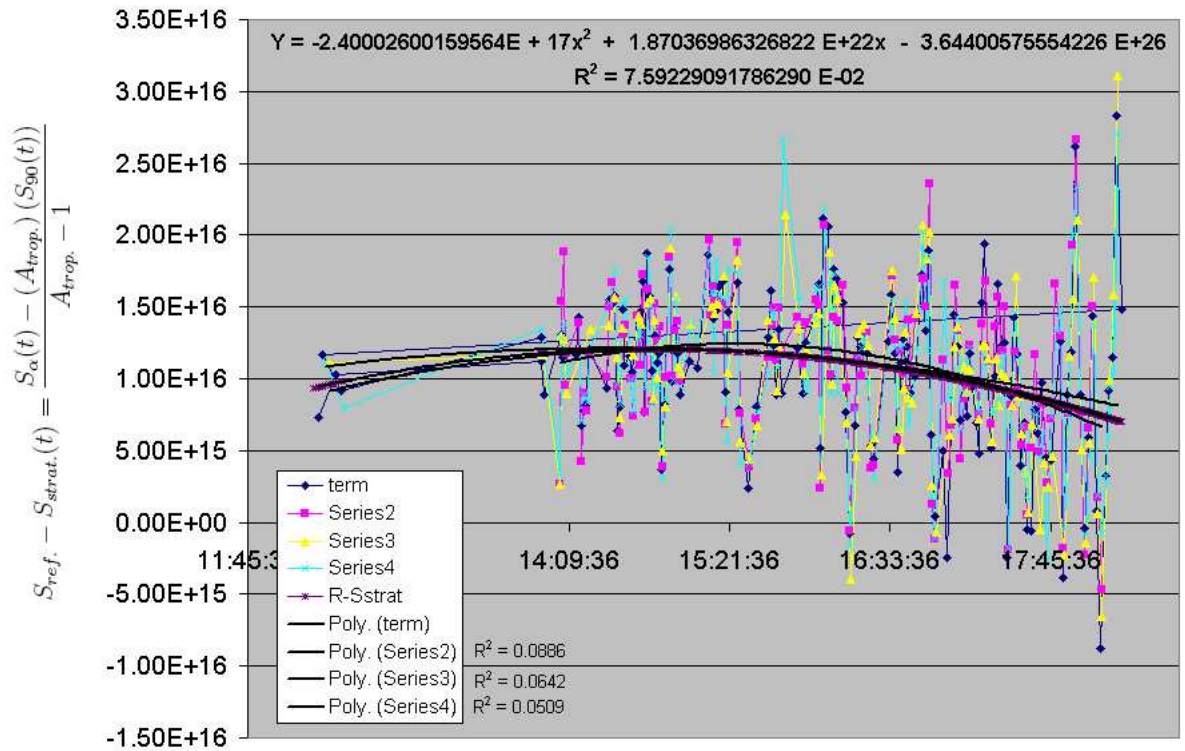


Figure 7.5: The different polynomial fits of the term  $(S_{ref.} - S_{strat.})$

40° and 90° versus time and the consistency of the VCD values is visible from the graph.

This method makes benefit of the absolute determination of the tropospheric NO<sub>2</sub> VCD from the combination of different elevation angles.

This method is used to calculate the NO<sub>2</sub> VCDs for measurements the following sections also.

Figure 7.7 shows the route from Brussels to Heidelberg with the NO<sub>2</sub> VCDs color coded along the route according to their values. Notice the high VCDs north-east of Aachen because of the Weisweiler power plant and also the relatively elevated VCDs near from Brussels, Koblenz, Heidelberg and in the Rhein Valley area.

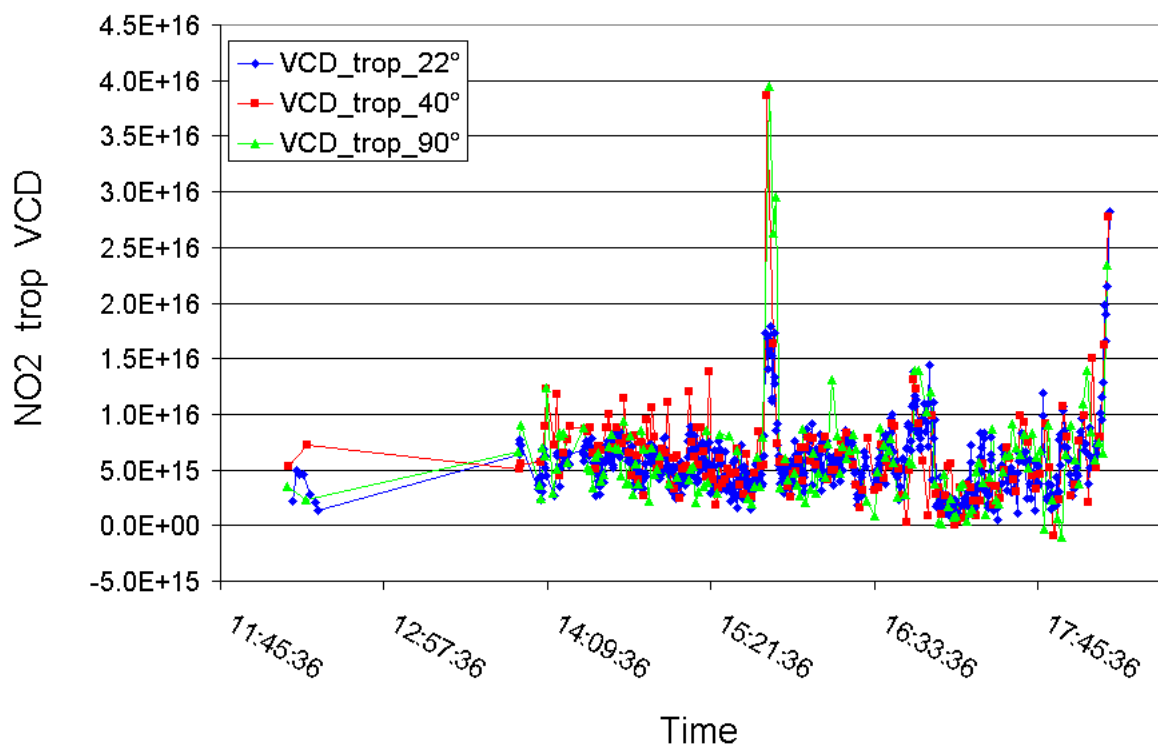


Figure 7.6: The tropospheric NO<sub>2</sub> VCDs from the three elevation angles 22°, 40°, 90° and the consistency of the VCD values from different elevation angles.

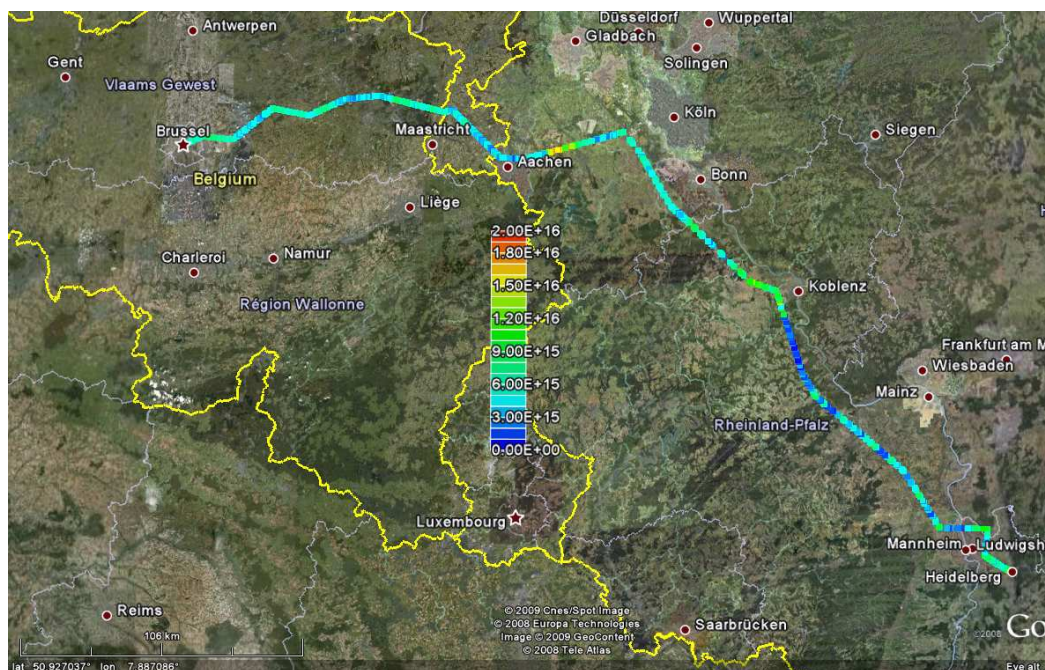


Figure 7.7: The route from Brussels to Heidelberg with the  $\text{NO}_2$  VCDs color coded along the route according to their values. Notice the high VCDs north-east of Aachen because of the Weisweiler power plant (see text) and also the relatively elevated  $\text{NO}_2$  VCDs near from Brussels, Koblenz and in the Rhein Valley area.

### 7.2.3 Comparison with Satellites

It is also interesting to compare ground-based MAX-DOAS measurements with satellite measurements of tropospheric trace gases ( $\text{NO}_2$  here). Figures 7.8 and 7.9 show the comparison between Auto-MAX DOAS  $\text{NO}_2$  VCDs and SCIAMACHY Satellite Tropospheric  $\text{NO}_2$  VCDs (TVCDs). The maximum on the color scale of SCIAMACHY graph is  $1 \times 10^{16}$  molec./ $\text{cm}^2$ . The relative agreement in the VCDs is visible from comparing the two graphs. Figure 7.10 shows also cloud-free  $\text{NO}_2$  TVCDs from OMI satellite data<sup>5</sup>.

<sup>5</sup>Ozone Monitoring Instrument.

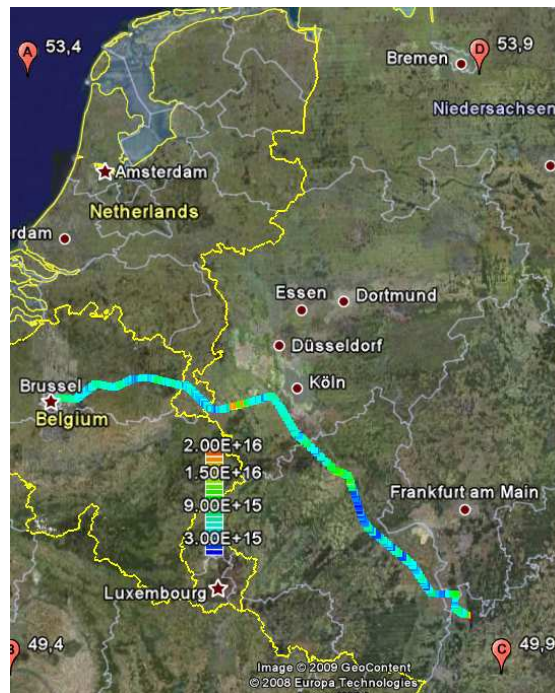


Figure 7.8: The route from Brussels to Heidelberg with the  $\text{NO}_2$  VCDs color coded along the route according to their values. The area shown in this graph is the same area of the SCIAMACHY pixel (see the graph below).

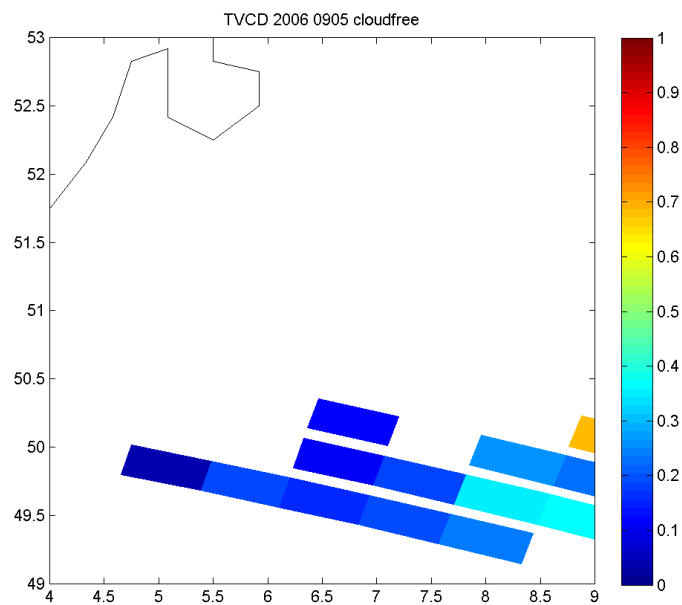


Figure 7.9: Tropospheric  $\text{NO}_2$  VCDs from cloud free pixels of SCIAMACHY.

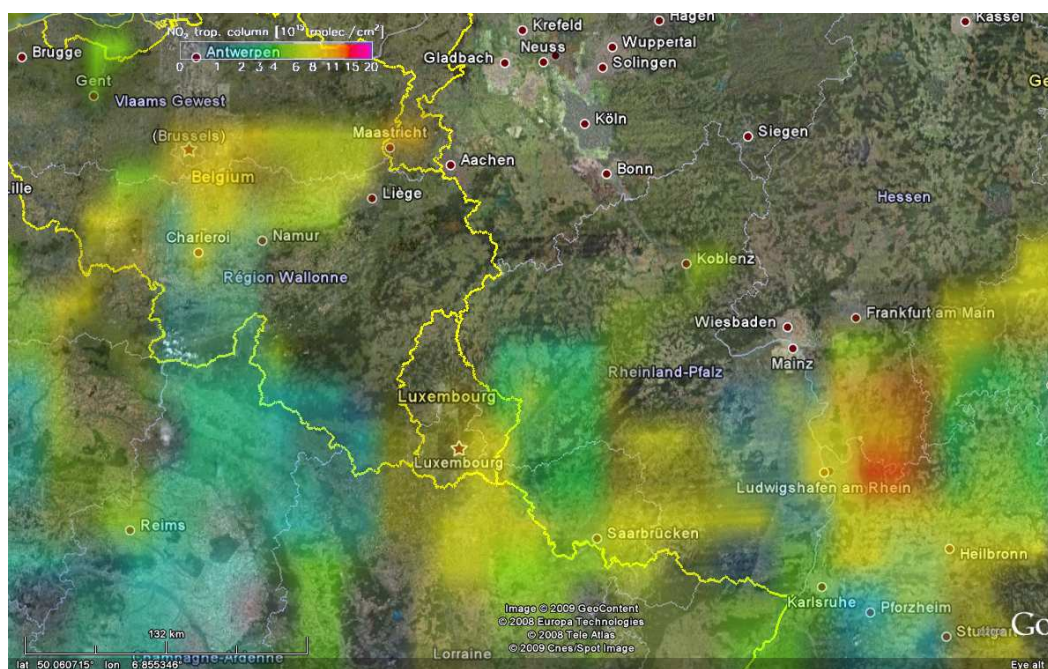


Figure 7.10: *Cloud-free  $\text{NO}_2$  TVCDs from OMI satellite data.*

## 7.2.4 Hemel Hempstead Fire

### The start of the fire

At approximately 6:01 am on Sunday 11.12.2005, there was a major explosion and subsequent large-scale fires at the Buncefield oil depot near Hemel Hempstead north west from London, United Kingdom (51.766°N, 0.428°W). Further smaller explosions followed the first one at 6:24 am, 6:26 am and 6:30 am. The fire flames rose more than 60 meters into the sky<sup>6</sup>.

Buncefield oil depot is a major distribution terminal storing refined oil and petrol, as well as kerosene supplies for airports across the region, including Heathrow and Luton. This disaster is believed to be the worst explosion at a petrochemical plant in the UK since the Flixborough disaster of 1974 [Der Spiegel magazine, Dec. 2005] and the largest industrial fire in Europe for over 50 years. Figure 7.11 shows a detailed map of the Buncefield Oil Depot area.

Reports said the explosion, which registered 2.4 on the Richter scale, was heard as far away as Oxford and Central London which is 60 km away. Figure 7.12 shows the strong fire in the Buncefield Oil Depot area a few minutes after the explosions and Figure 7.13 shows the intense plume emerging from the fire at Buncefield Oil Depot.

### Meteorological conditions and timeline of events

Due to the intense heat of the fire, the plume was highly buoyant and rose rapidly and vertically within the atmosphere penetrating the temperature inversion at the top of the Boundary Layer (BL) into the Free Troposphere (FT). Figures 7.14 (a) and (b) show the penetration of the plume into the free troposphere and Figures 7.14 (c) and (d) show the horizontal extent of the plume as seen from passenger airplanes flying over London on 11.12.2005.

The plume could readily be seen by satellites because of its large horizontal extent over south east England. Figure 7.15 shows a satellite image of the plume on 11.12.2005. The plume took the fan-like appearance because of significant wind shear, with north-westerly winds at lower levels in the Boundary Layer and north-easterly winds aloft in the Free Troposphere. Figure 7.16 shows two satellite image of south east England: One day before the fire (10.12.2005) and on the fire day (11.12.2005). Also the wind shear effect of the plume shape is shown in the bottom image.

---

<sup>6</sup>Source: Initial review of air quality aspects of the Buncefield Oil Depot explosion. A report prepared by Meteorological Office of UK (Met Office), Health Protection Agency of the UK, and AEA Technology. This report is produced for the Department for Environment, Food and Rural Affairs, the Scottish Executive, the Welsh Assembly Government and the Department of the Environment in Northern Ireland. For simplicity, It will be referred to this report with: [Init. report]

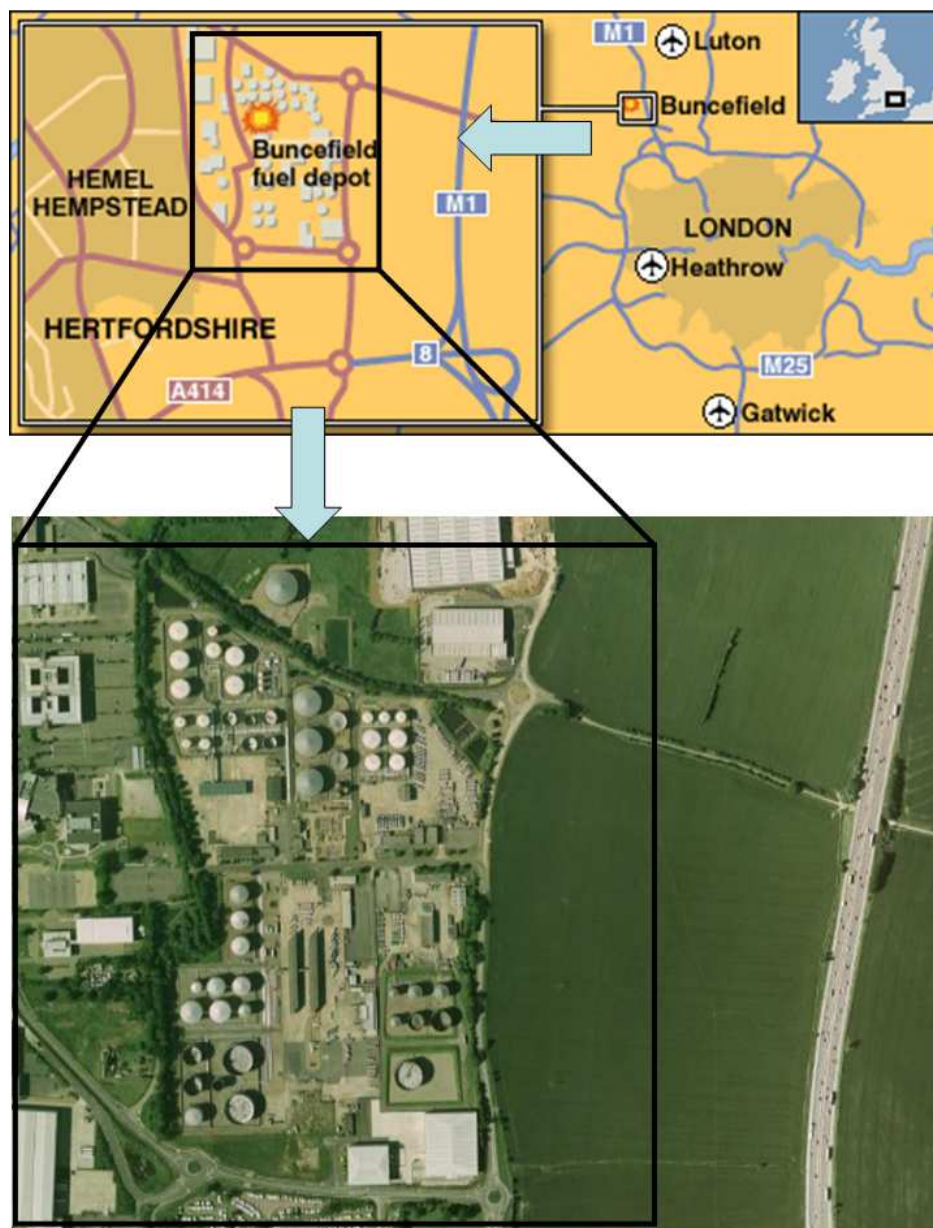


Figure 7.11: A detailed map of the Buncefield Oil Dept area. Top: The location of the Buncefield Oil Depot relative to London city, Heathrow and Luton airports (right) with a detailed map in the frame (left) [Source: BBC News]. Bottom: A more detailed google earth satellite image of the same area. The Oil storage tanks are clear in the image.

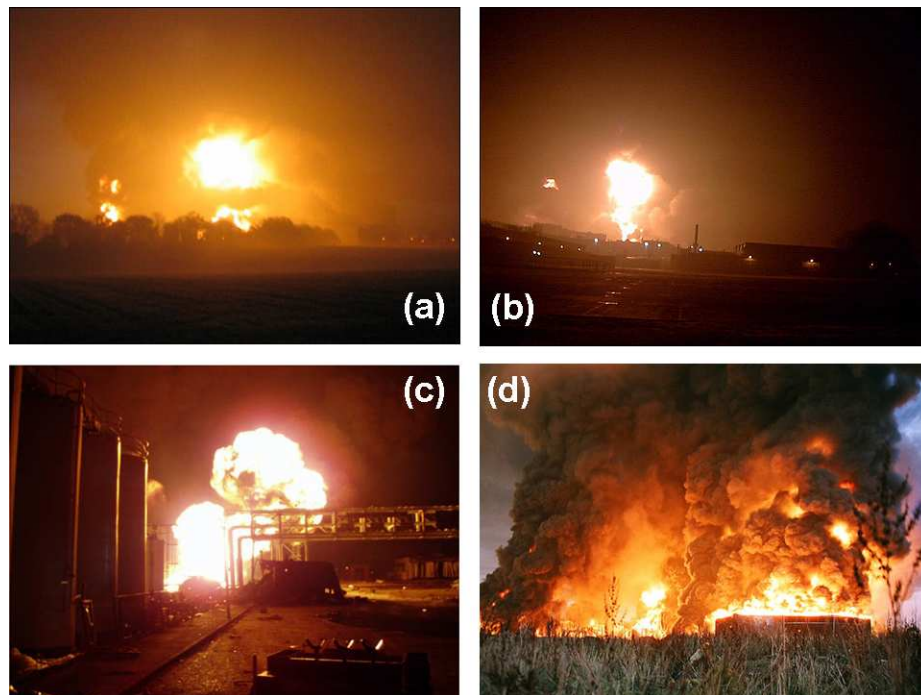


Figure 7.12: *The strong fire in the Buncefield Oil Depot area a few minutes after the explosions early in the morning of 11.12.2005. [Source: (a), (b) and (d) : Times online, and (c): CCTV screen shot from the Buncefield Oil Depot site (adapted from [www.fireworld.com](http://www.fireworld.com)).]*

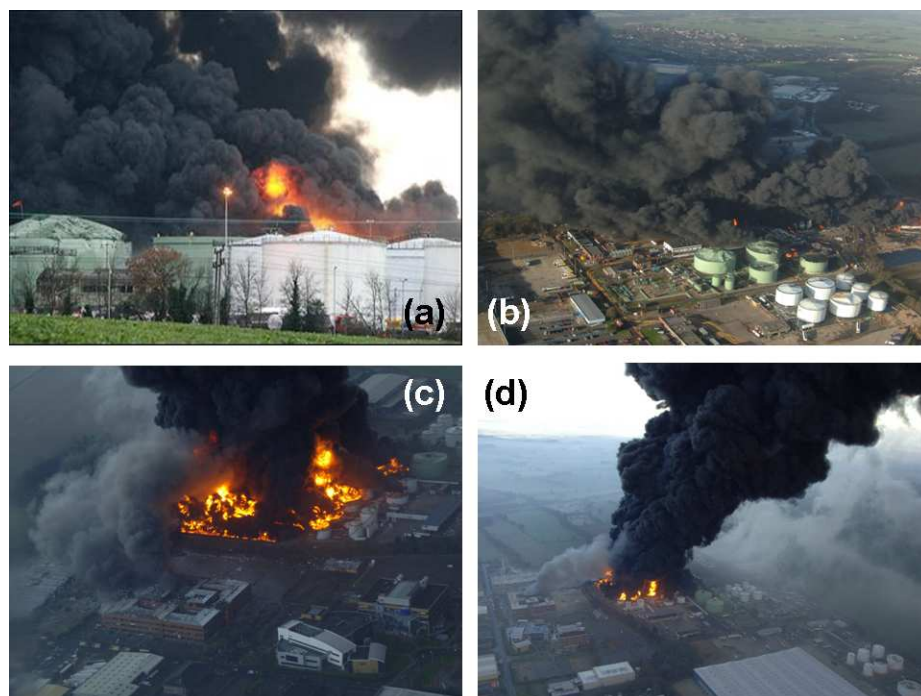


Figure 7.13: *The intense plume emerging from the fire at Buncefield Oil Depot on 11.12.2005 [Courtesy of Royal Chiltern Air Support Unit].*

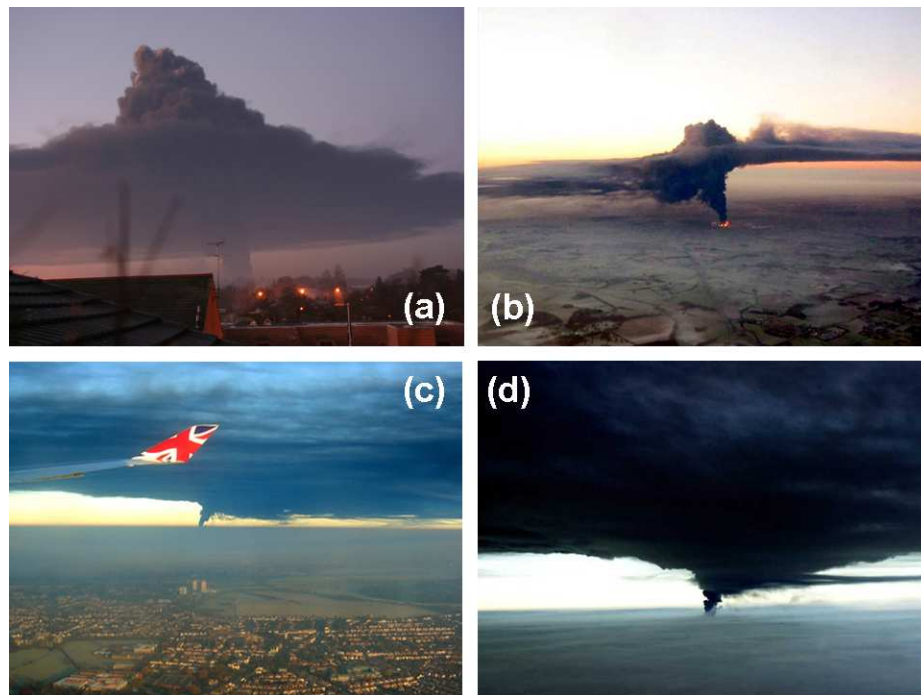


Figure 7.14: *The large extent of the plume over London and the south east England [Source: Spiegel online]. Photo (a) shows the penetration of the plume into the Free Troposphere. Photos (b), (c) and (d) show the horizontal extent of the plume as seen from passenger airplanes flying above London on 11.12.2005.*

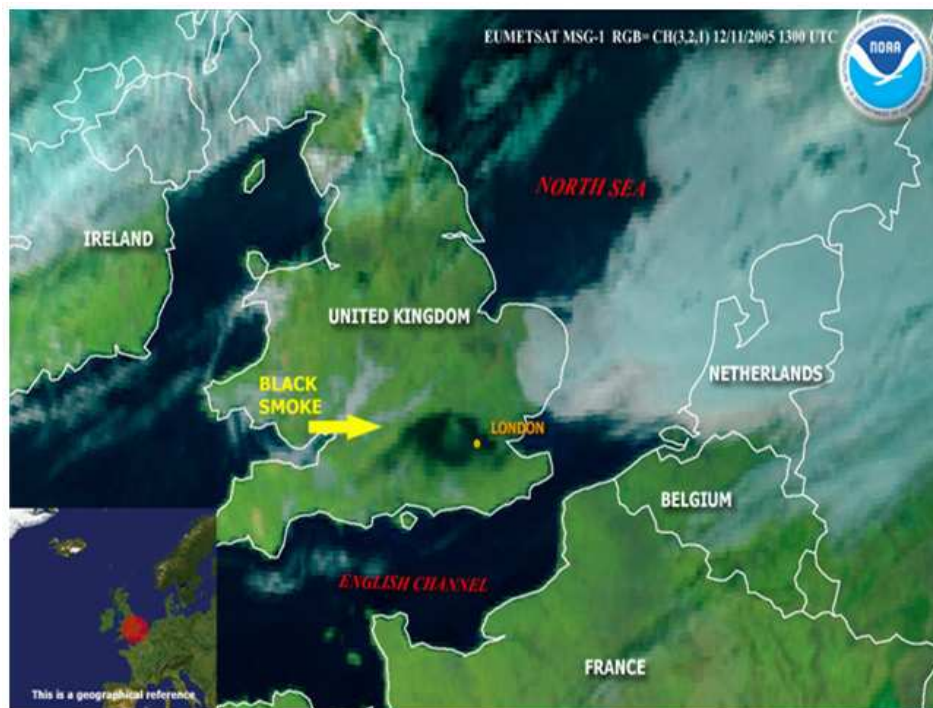


Figure 7.15: *A satellite image of Buncefield Oil Depot plume on 11.12.2005. The horizontal extent of the plume covered large areas over south east England [Source: National Oceanic and Atmospheric Administration (NOAA)].*

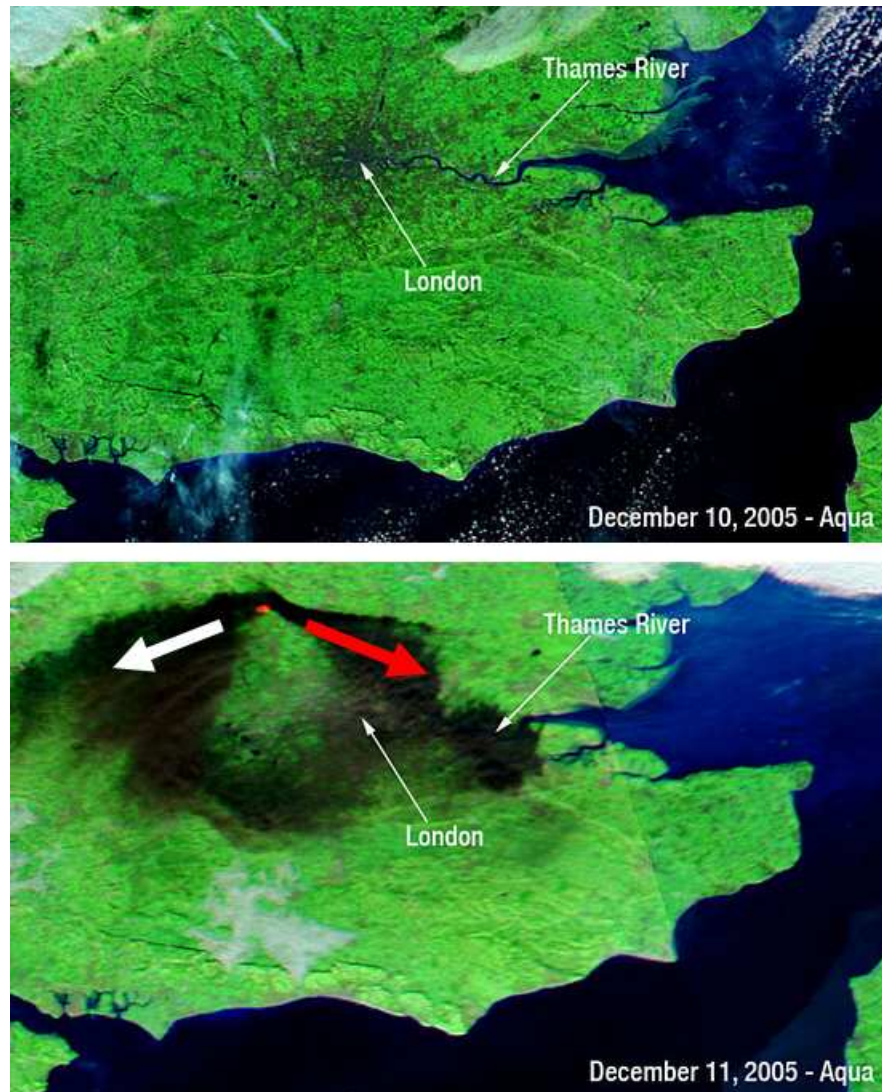


Figure 7.16: *Top: A satellite image of south east England one day before the Buncefield Oil Depot fire (10.12.2005). Bottom: A satellite image of the same area on (11.12.2005). [Source: NASA]. The red and white arrows show the wind direction at the Boundary Layer level and the Free Troposphere level respectively (see text).*

The anticyclonic conditions of the day resulted in a stable atmosphere; as a result, there was little mixing within the boundary layer, with most of the plume transport occurring in the free troposphere.

During the morning of Monday 12.12.2005, a weak frontal system moved through the area. Following the clearance of the front, there were north-easterly winds at all levels over the source [Init. report].

On Tuesday 13.12.2005, there was considerably more cloud, which reduced the availability of satellite imagery of the plume. The winds were north/north-easterly, resulting in the plume being advected south.

On 13.12.2005, we decided to try to detect the plume using Auto-MAX-DOAS since it's able to cover large enough distances during measurements. Also such a plume would be expected to have considerable amounts of  $\text{NO}_2$ . It was practically impossible to try to measure it in the UK because time was so short and the firefighting efforts were going on so it might be completely finished before we arrive there to measure the plume. So it was chosen to try to detect the plume at the northern coast of France. Before 13.12.2005, the plume was not reported to breach the northern French coast.

Early in the morning of 14.12.2005 driving with the Auto-MAX-DOAS started heading from Heidelberg towards Calais (France). The plan was to drive and measure along the north coast of France until the end of the daylight.

The Auto-MAX-DOAS reached Calais at around 13:00 O'clock and measurements started immediately at that time.

Driving for about 250 kilometers along the north coast of France on the highways. The driving speed was about 100 km/h. Figure 7.17 shows the route from Heidelberg to Le Havre via Calais.

Measurements were done in a sequence of elevation angles ( $45^\circ, 45^\circ, 45^\circ, 90^\circ$ ) and the number of scans per spectrum was fixed at 100 scans. Integration time (for one spectrum of 100 scans) was between 15 and 100 seconds according to the light intensity. The telescope of the Mini-Max-DOAS instrument was directed in the direction of driving (the same vertical plane). Figure 7.20 shows the  $\text{NO}_2$  dSDCs from the measurements during driving the Auto-MAX-DOAS between Calais and Le havre on the north coast of France on 14.12.2005.

By Thursday 15.12.2005, only small fires remained at the Buncefield Oil Depot site [Init. report]. Winds became north-westerly and stronger. The remainder of the plume was therefore transported to the south-east and rapidly dispersed in the moderate winds. The total emissions of  $\text{NO}_2$  from the fire were estimated by the Met Office<sup>7</sup> to be around 40 tonnes (0.003% of total UK annual emissions).

Also on 15.12.2005 morning, Auto-MAX DOAS measurements were carried out on the road back from Le Havre to Calais starting at 8:45 o'clock (UT time), the telescope was directed to the left side towards England (in the vertical plane per-

---

<sup>7</sup>Meteorological Office of the UK

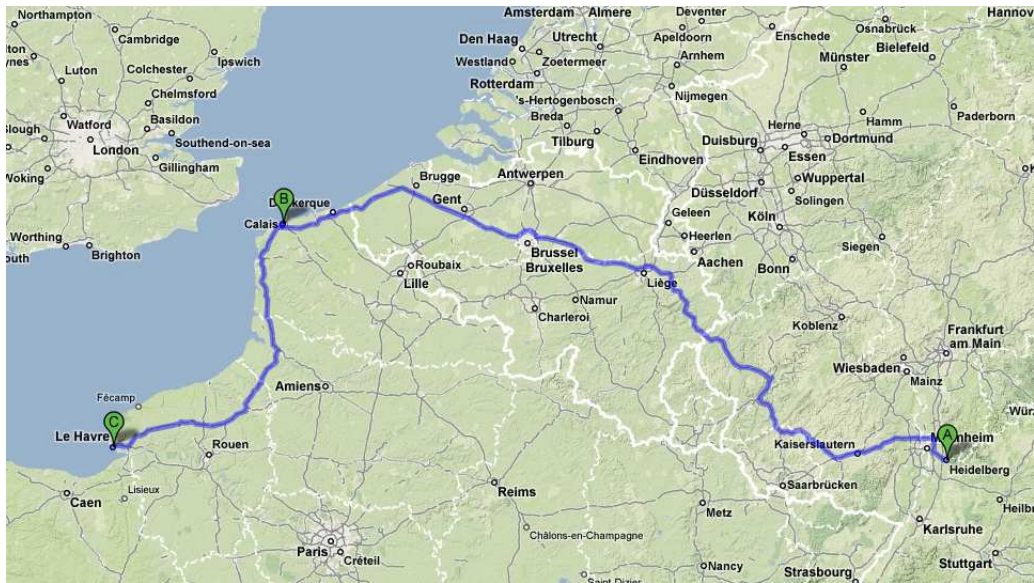


Figure 7.17: The driving route from Heidelberg to Le Havre via Calais. Labels on the map: (A) indicates Heidelberg, (B) indicates Calais and (C) Indicates Le Havre.



Figure 7.18: The driving route from Calais to Le Havre. Labels on the map: (A) indicates Calais, (B) indicates Boulogne (C) indicates Portel (D) indicates Le havre .

pendicular to the driving one). Figure 7.23 shows the route of driving on 15.12.2005 and the main cities along the road. Measurements continued until around 13:30 O'clock shortly before the Belgian City (Gents)[see Figure 7.23].

## Results and discussion

The dSCDs of NO<sub>2</sub> were obtained from evaluating the collected spectra on both days of measurements. Figure 7.20 shows the NO<sub>2</sub> dSCDs during measurements on 14.12.2005. The names of the cities reached at certain times are also indicated on the graph at the corresponding time points on the X-Axis. Figure 7.21 show the NO<sub>2</sub> VCDs from the same measurements. From Figure 7.21, there is a high peak of NO<sub>2</sub> VCDs in the distance between (Boulogne) and (Le Portel)(see Figure 7.18 too). This peak might be because of much industry in this area in northern France and this peak is of an approximate width of 30 kilometer FWHM. A second high peak of NO<sub>2</sub> VCDs of an approximate width of 100 kilometer FWHM appears between Dieppe and Le Havre too. Taking into account that the Auto-MAX DOAS speed was 100km/h, one hour on the X-Axis means 100 km of driving.

Figure ?? shows a color coded map of the VCDs as a function of Geo-location (latitude, longitude) along the measurements route on 14.12.2005.

Figure 7.24 shows the NO<sub>2</sub> dSCDs from the Auto-MAX DOAS measurements on 15.12.2005. Figure 7.26 shows the NO<sub>2</sub> VCDs from the same measurements. The graph shows one NO<sub>2</sub> VCDs peak around Calais city on the northern coast of France. The peak is about 100 km (FWHM). From measurements on both days, It is difficult to exclusively attribute the observed NO<sub>2</sub> VCDs peaks to the Buncefield fire plume only. Since the northern coast of France and Belgium has also some Urban/industrial areas. But in General, the size of extended NO<sub>2</sub> VCDs peaks (around 100 km) on both days suggests that they were due to a widely spread plume and this supports the idea that it might be the fire plume transported with the north/north-westerly winds coming from England.

In order to explore the origin of the air masses detected on both days, air back trajectories were produced using HYSPLIT<sup>8</sup> model.

The back trajectories were produced for the last 24 hours before measurements at different heights above ground level (AGL). Figures 7.27 and 7.28 show the back trajectories of air masses on 14.12.2005 at different heights above ground level. The starting point (time, location) of these back trajectories is chosen to be at the time/position of the high NO<sub>2</sub> VCDs peak between Boulogne and Le Portel (50° N, 1.72° E) (see also Figure 7.21).

Figures 7.27 and 7.30 show also the back trajectories of air masses on the same day for another starting point at the second NO<sub>2</sub> VCDs peak between Dieppe and Le Havre(49.46° N, 1° E). (see also Figure 7.21).

---

<sup>8</sup>Hybrid Single Particle Lagrangian Integrated Trajectory Model. [See <http://www.arl.noaa.gov/HYSPLIT.php>].



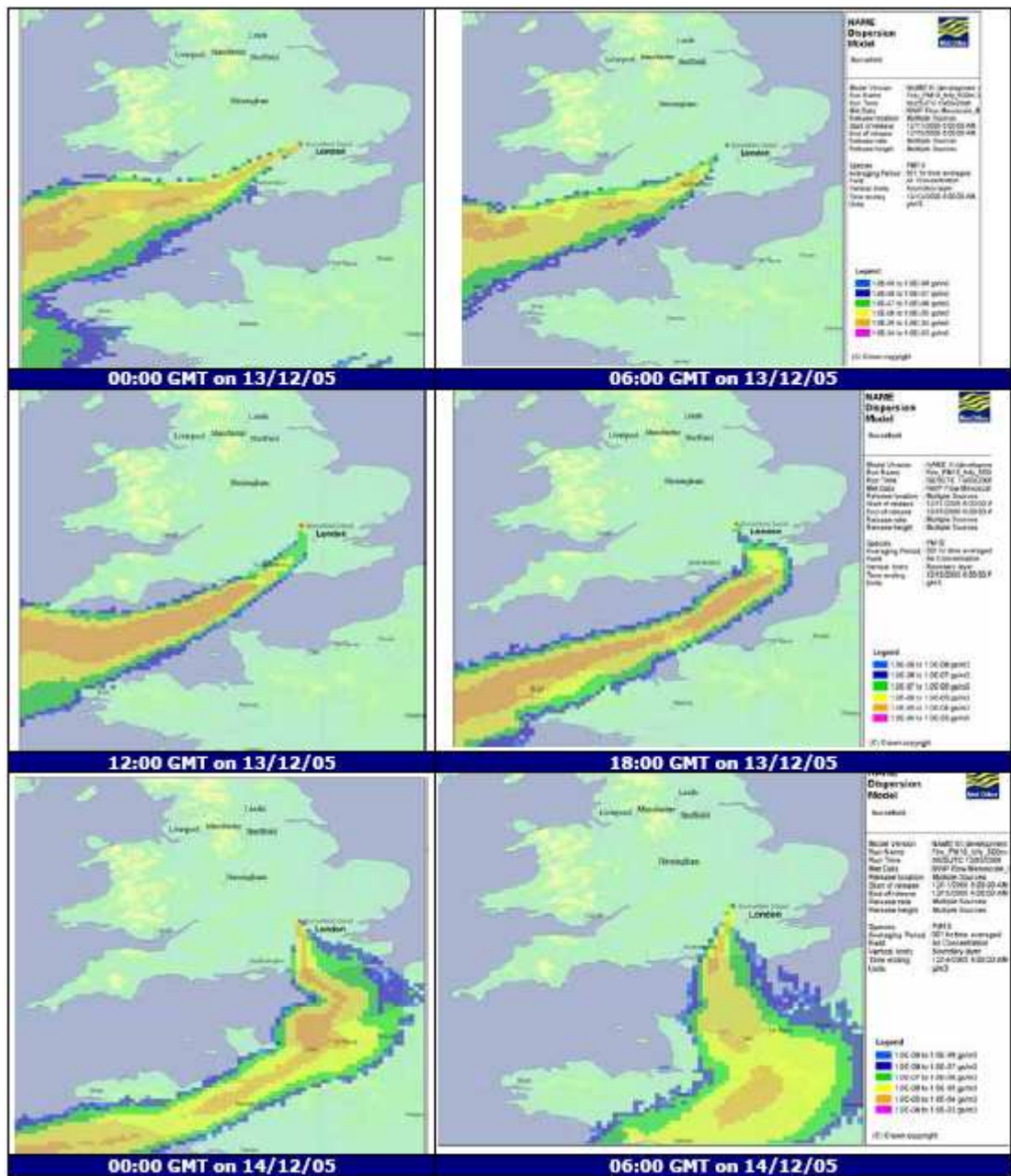


Figure 7.19: The predicted hourly averaged PM10 concentrations between 0 and 4000m. The extent of the plume is clearly to travel over France and it appears that on 14.12.2005 (bottom) at 00:00 O'clock and at 6:00 O'clock, the plume was transported over the north coast of France.

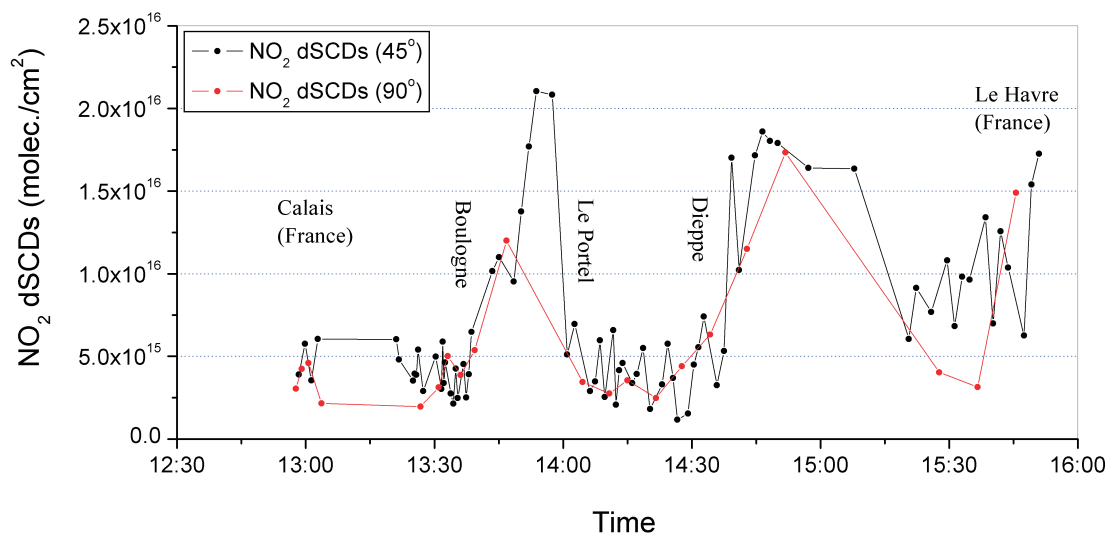


Figure 7.20: The  $\text{NO}_2$  dSCDs from the measurements during driving the Auto-MAX-DOAS between Calais and Le Havre on the north coast of France on 14.12.2005.

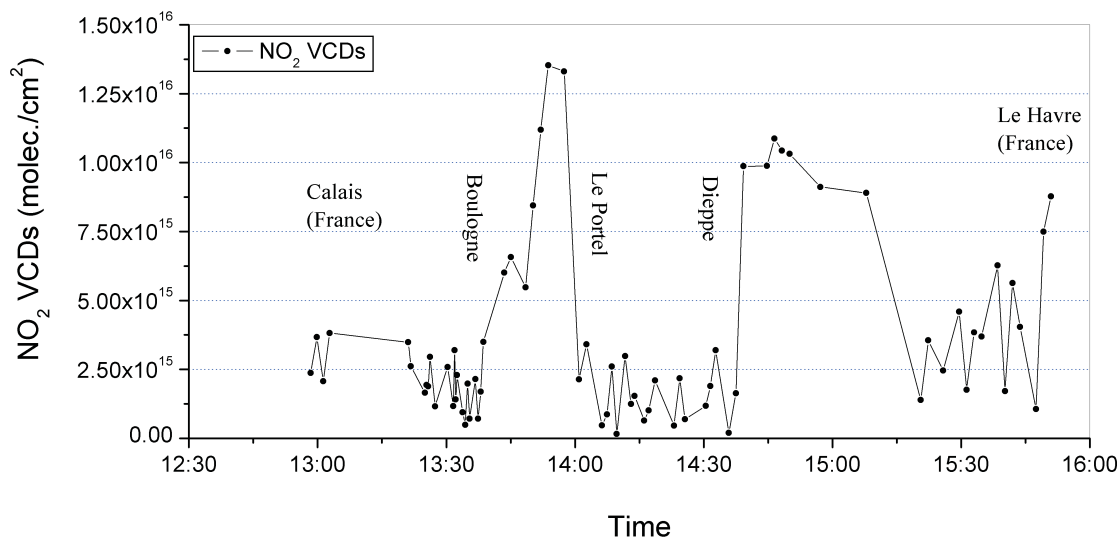


Figure 7.21: The  $\text{NO}_2$  VCDs from the measurements during driving the Auto-MAX-DOAS between Calais and Le Havre on the north coast of France on 14.12.2005.



Figure 7.22: The  $\text{NO}_2$  VCDs as a function of Geo-location along the measurement route on 14.12.2005.

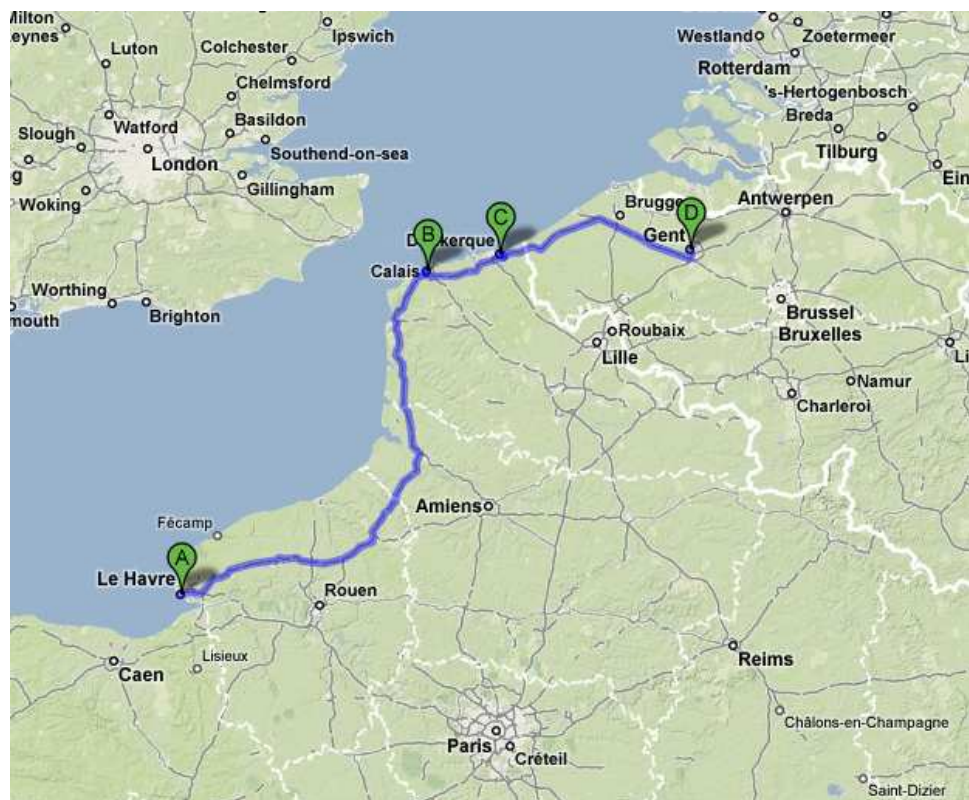


Figure 7.23: *The route of driving on 15.12.2005 and the main cities along the road. Labels on the map: (A) indicates Calais, (B) indicates Dunkerque, (C) indicates Furnes (France) and (D) indicates Gent(Belgium).*

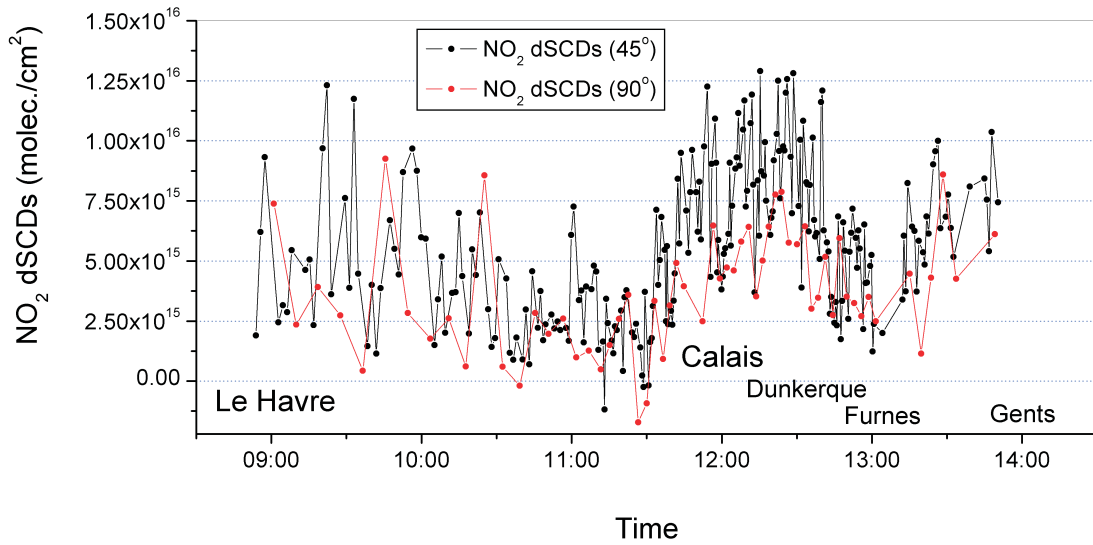


Figure 7.24: The  $\text{NO}_2$  dSCDs from the measurements during driving the Auto-MAX-DOAS between Le havre and Calais on the north coast of France on 15.12.2005.

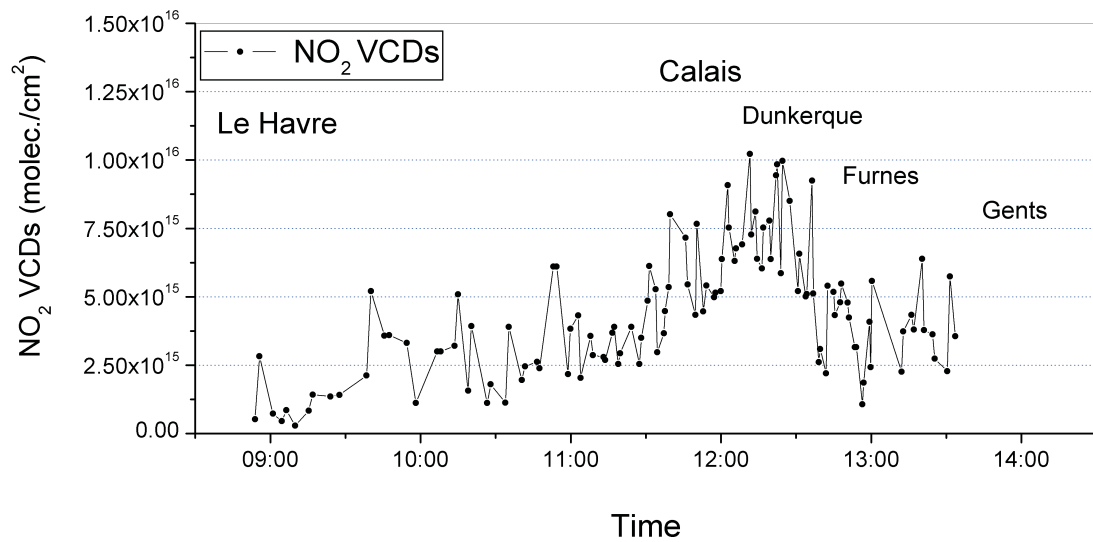


Figure 7.25: The  $\text{NO}_2$  VCDs from the measurements during driving the Auto-MAX-DOAS between Le havre and Calais on the north coast of France on 15.12.2005.

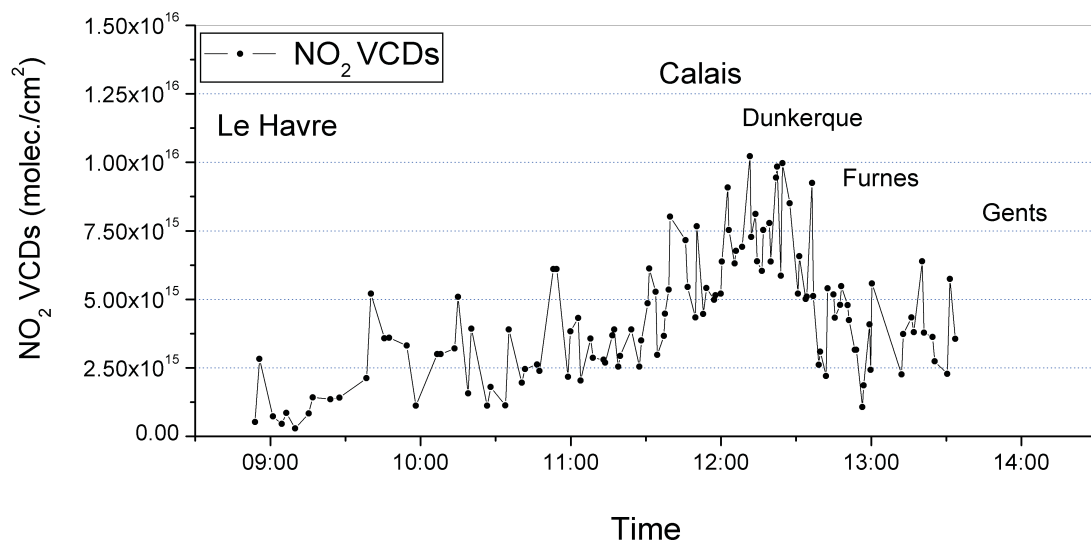


Figure 7.26: The NO<sub>2</sub> VCDs as a function of Geo-location along the measurements route on 15.12.2005.

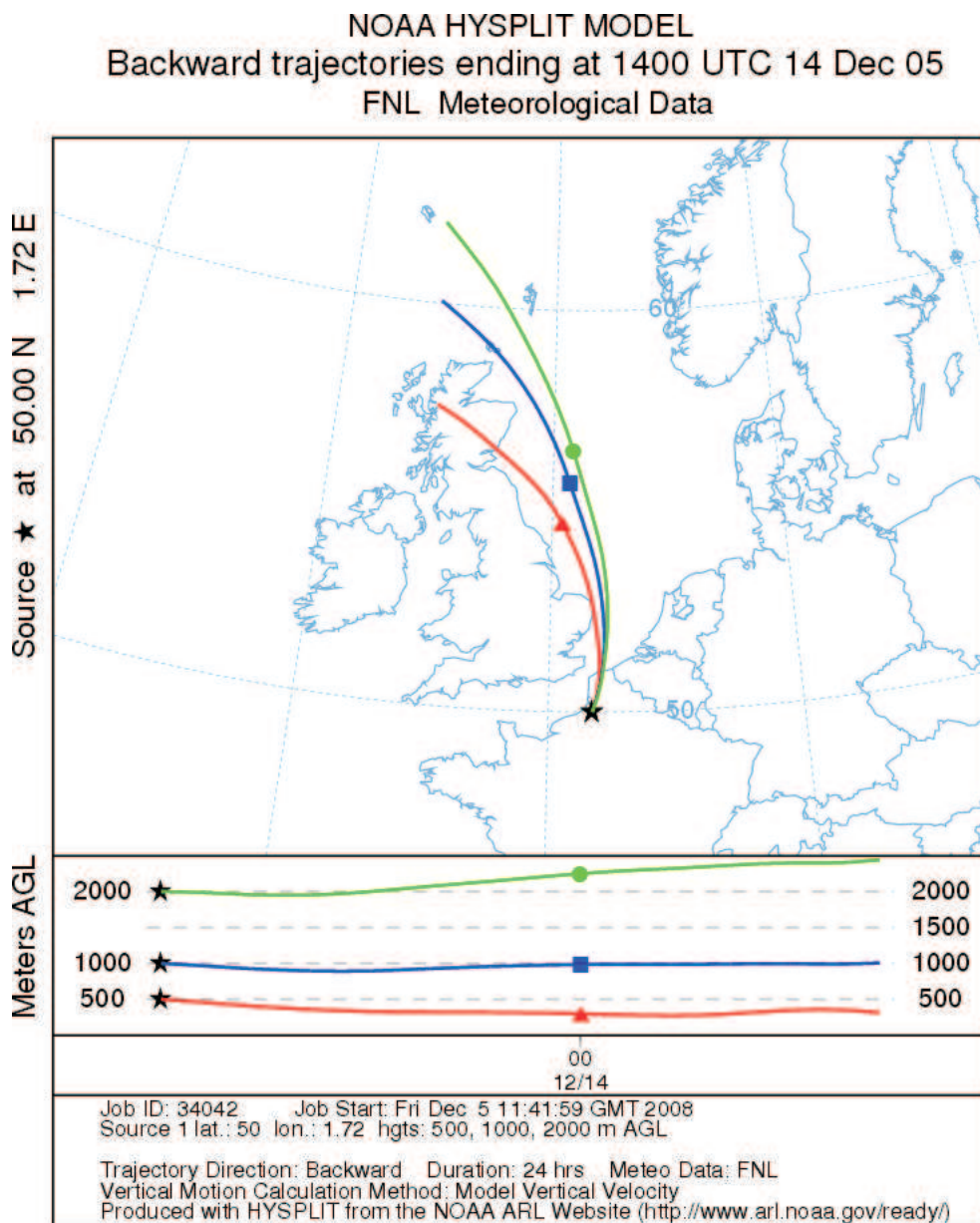


Figure 7.27: The back trajectories of air on 14.12.2005 at heights 500m , 1000m, 2000m above ground level. The starting point is at the time and position of the  $\text{NO}_2$  VCDs narrow peak between Boulogne and Le Portel on the French north coast. (See Figure 7.21)

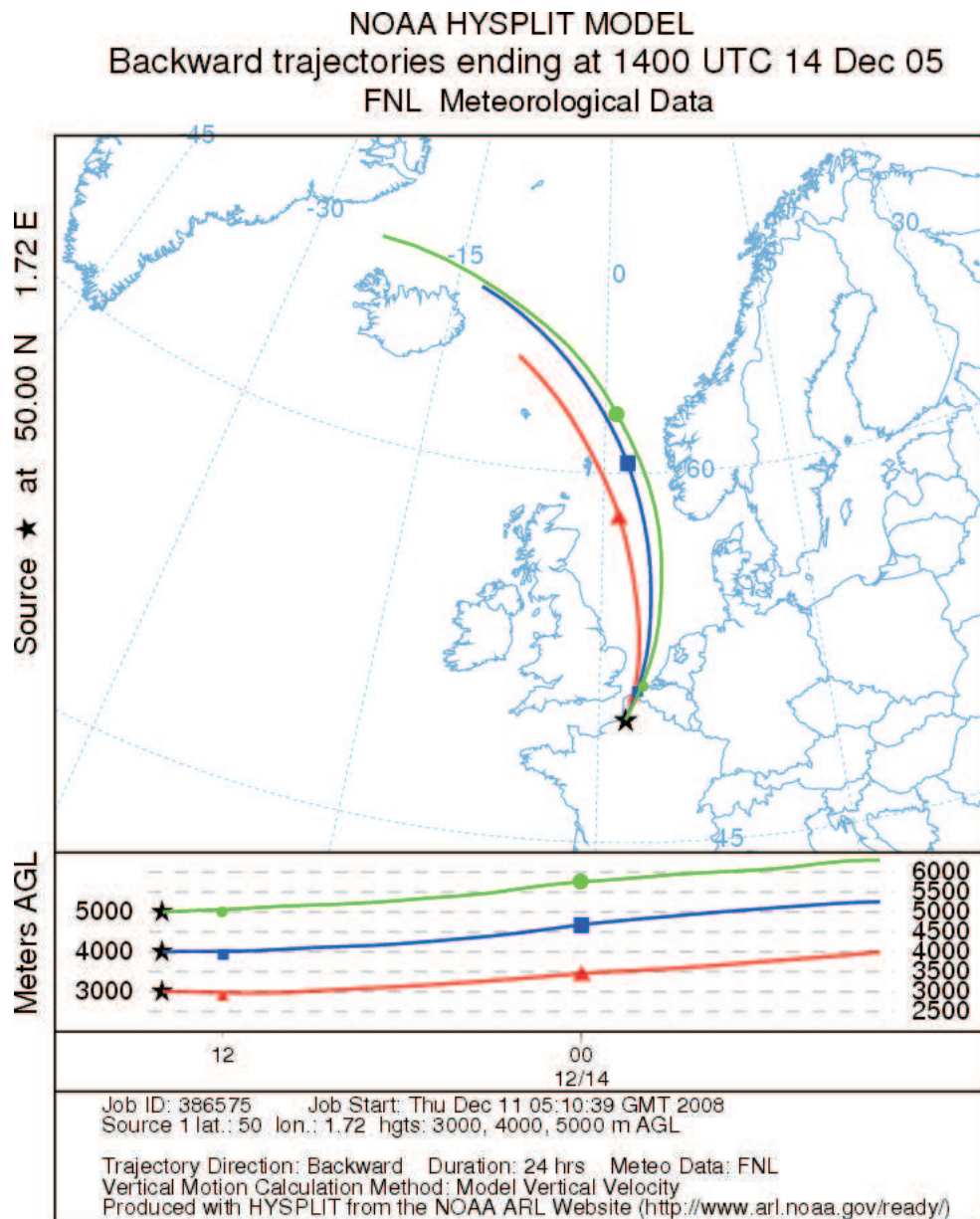


Figure 7.28: The back trajectories of air on 14.12.2005 at heights 3000m , 4000m, 5000m above ground level. The starting point is at the time and position of the  $\text{NO}_2$  VCDs narrow peak between Boulogne and Le Portel on the French north coast. (See Figure 7.21)

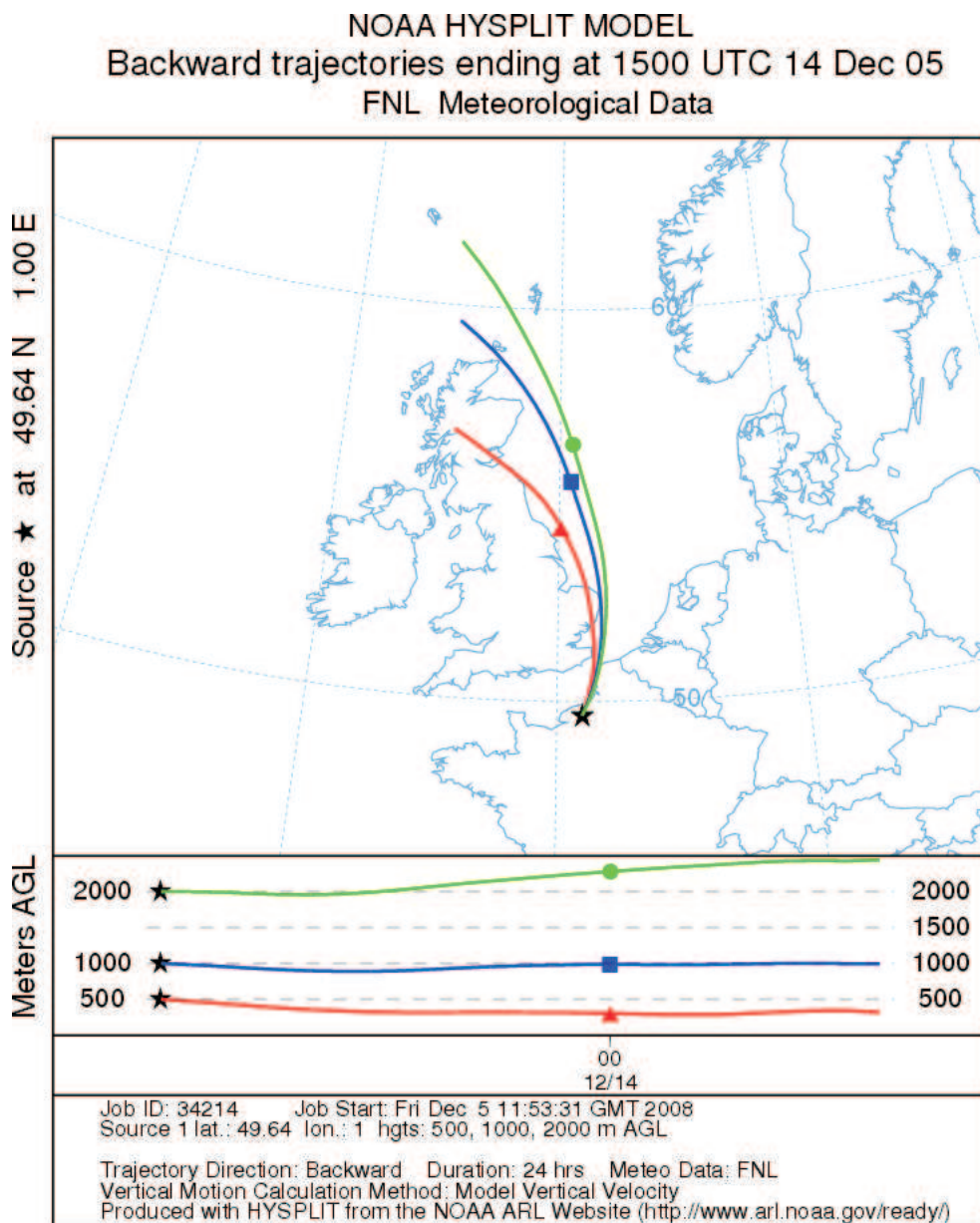


Figure 7.29: The back trajectories of air on 14.12.2005 at heights 500m , 1000m, 2000m above ground level. The starting point is at the time and position of the  $\text{NO}_2$  VCDs wide peak between Dieppe and Le Havre on the French north coast. (See Figure 7.21)

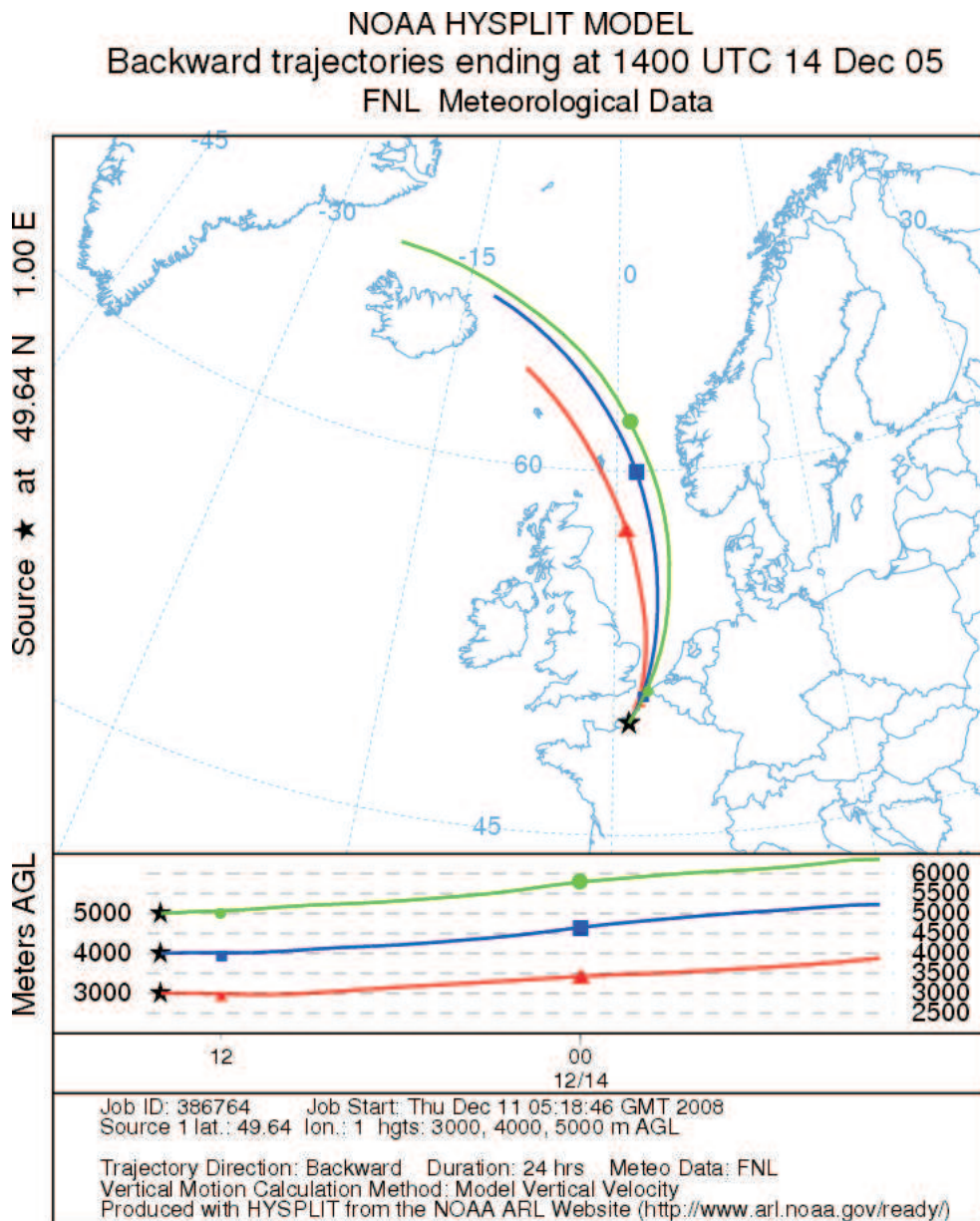


Figure 7.30: The back trajectories of air on 14.12.2005 at heights 3000m , 4000m, 5000m above ground level. The starting point is at the time and position of the  $\text{NO}_2$  VCDs wide peak between Dieppe and Le Havre on the French north coast. (See Figure 7.21)

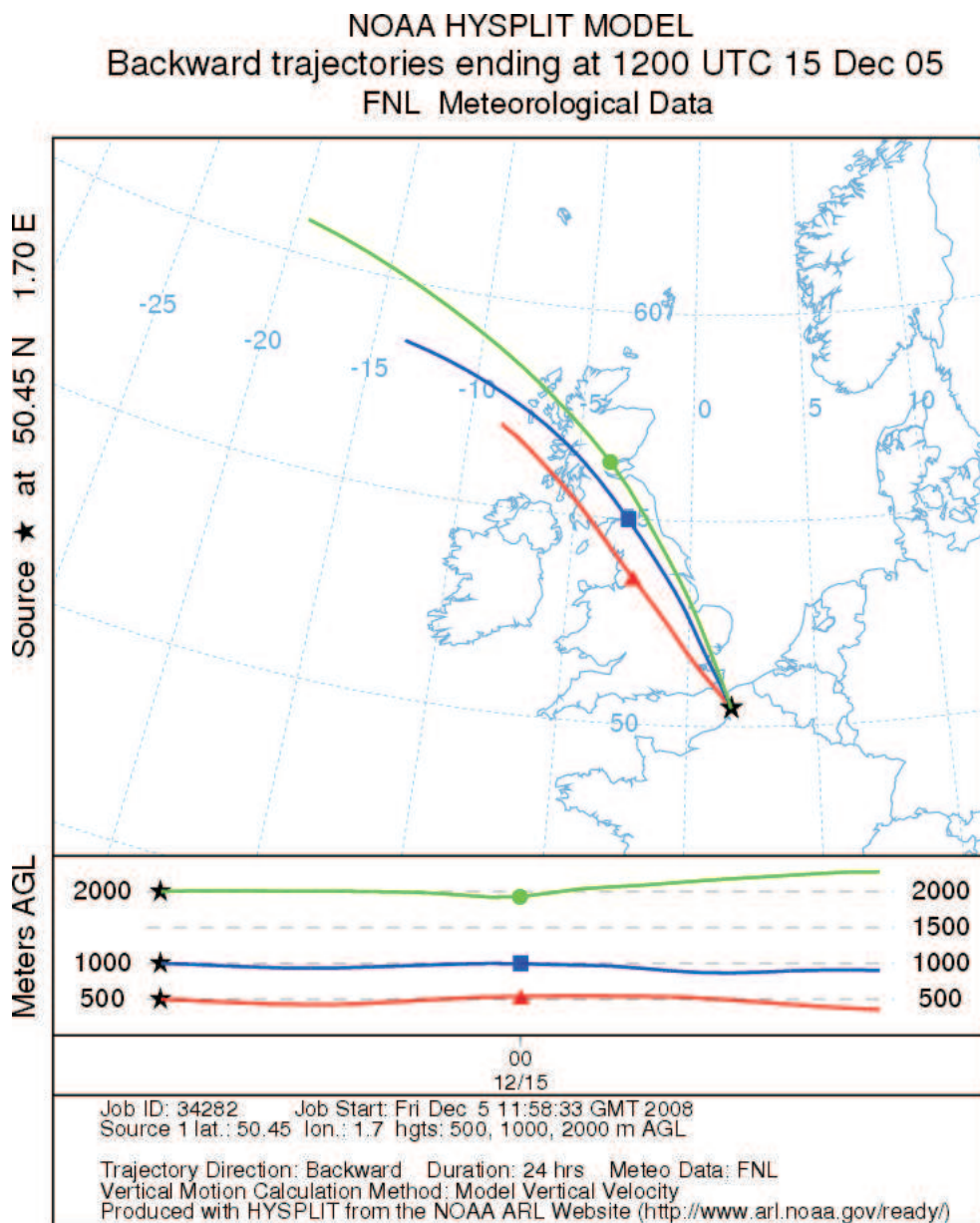


Figure 7.31: The back trajectories of air on 15.12.2005 at heights 500m , 2000m, 2000m above ground level. The starting point is at the time and position of the NO<sub>2</sub> VCDs wide peak around Calais on the French north coast. (See Figure ??)

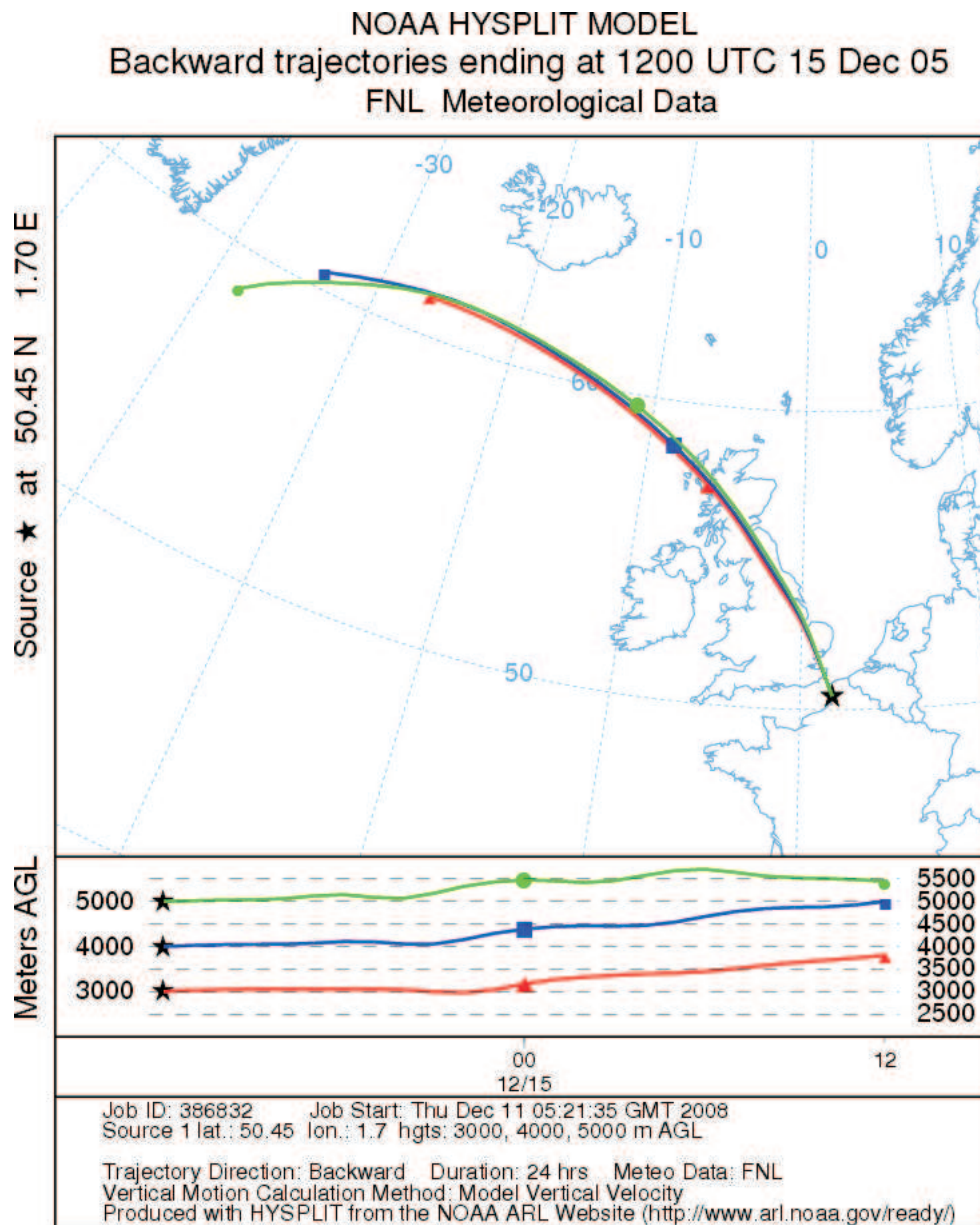


Figure 7.32: The back trajectories of air on 15.12.2005 at heights 3000m , 4000m, 5000m above ground level. The starting point is at the time and position of the  $\text{NO}_2$  VCDs wide peak around Calais on the French north coast. (See Figure ??)

## 7.3 Results from encircling pollution sources

### 7.3.1 Results From Encircling Mannheim-Ludwegshafen Area

On 23.8.2006 and 24.08.06 Auto-MAX-DOAS measurements were carried out around Mannheim-Ludwigshafen Industrial\urban area and some adjacent areas (such as Frankenthal, Mutterstadt and Schifferstadt). Figure 7.33 shows the map of the investigated area and the driving route around it (in red color). The investigated area, The measurements conditions, the meteorological conditions and results are discussed in this section.

**The investigated area:** Mannheim-Ludwegshafen Industrial\urban area has two major sources of air pollution:

The BASF industrial compound and the Big Mannheim power plant (in German: **GroßKraftwerk Mannheim GKM**). The BASF is a large chemical industry compound in this area (orange colored areas in Figure 7.33). The GKM is one of the biggest German hard coal power plants with performance of 1675  $MW_{electricity}$  [Source: [www.umweltforum-mannheim.de](http://www.umweltforum-mannheim.de)](see Figure 7.33). During measurements, the GKM was running partially with hard coal (anthracite)(blocks 7, 8) and also oil\gas (blocks 3, 4 and 6). Anthracite coal typically contains approximately 5 percent moisture, 4 percent volatile matter, 10 percent ash, less than 1 percent sulfur, less than 1 percent nitrogen, and 80 percent fixed carbon. Starting from November 2006, blocks 3, 4 and 6 were adapted to work using hard coal so the GKM started to be fully running with hard coal after that time.

**Measurements conditions:** On 23.08.2006, two complete cycles along the route were carried out while four complete cycles were carried out on 24.08.2006.

On both days, measurements were taken at a sequence of elevation angles ( $45^\circ$ ,  $45^\circ$ ,  $45^\circ$ ,  $45^\circ$ ,  $90^\circ$ ). The telescope was pointed in the plane along the driving direction taking scans at the mentioned elevation angles.

The integration time<sup>9</sup> for one spectrum was 3-25 seconds according to light intensity during driving since the sky was partially cloudy on both days of measurement (see below).

Driving under a cloud would decrease the light intensity and increase the integration time. The speed of the Auto-MAX-DOAS during measurements was 80-100  $km/h$  during all measurements. All the roads used during driving were highway roads (Autobahn) so practically the car could not be driven slower than 80  $km/h$ . The path of the Auto-MAX-DOAS around the investigated areas was reconstructed on a map using the log information of time and location collected during driving. The locations of the Auto-MAX-DOAS during driving were determined by a GPS (Global Positioning System) device and logged as a function of time. Figure 7.34 shows an

---

<sup>9</sup>In this work: Integration time is defined as the time necessary to complete one spectrum which consists of several scans.

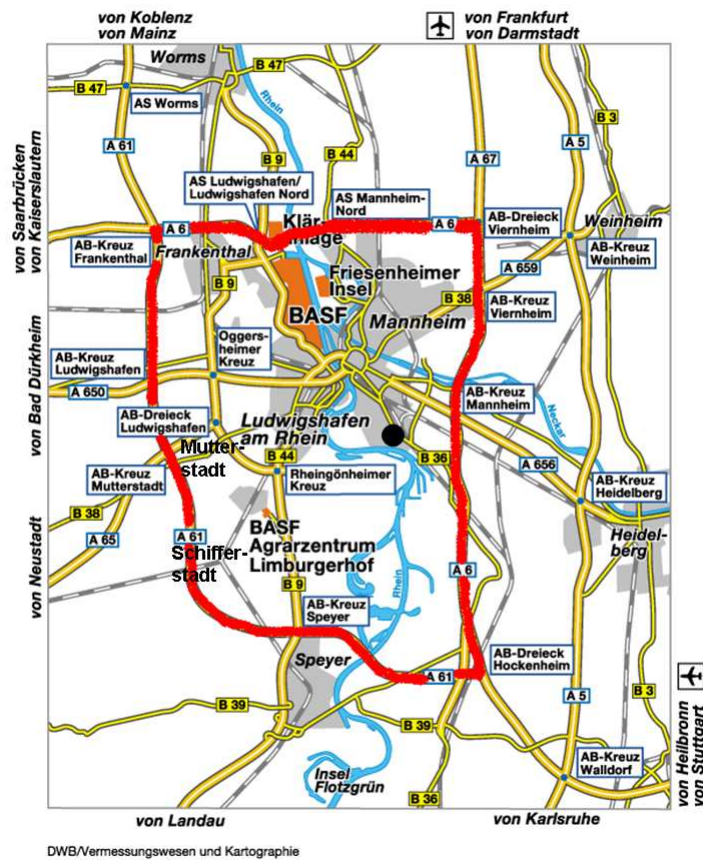


Figure 7.33: The route around Mannheim-Ludwegshaven Industrial/urban area and the nearby areas: Frankenthal, Mutterstadt and Schifferstadt. The BASF industrial area is indicated in orange color and the black dot indicates the GKM location.

example the Auto-MAX-DOAS location determination during measurements using Google earth program<sup>TM</sup> (see <http://earth.google.com/>).

**Meteorological conditions:** The sky was partially cloudy on both days of measurement. Wind direction and speed during both days of measurements are obtained from six different ground meteorological stations in the investigated area and near from it.

Figure 7.35 shows the route of driving and the locations of the meteorological stations: three stations inside the investigated area: Mannheim North, Mannheim middle, Mannheim South (respectively from north to south) and three stations are to the east of it: Wilmsfeld (Odenwald), Heidelberg and Wiesloch (respectively from north to south). [Source: The Regional Office for environment, measurements and nature protection of Baden-Württemberg (Landesanstalt fuer Umwelt, Messungen und Naturschutz Baden-Württemberg LUBW)].



Figure 7.34: The location of the Auto-MAX-DOAS during driving at 15:30:36 O'clock, local time (UT+2)

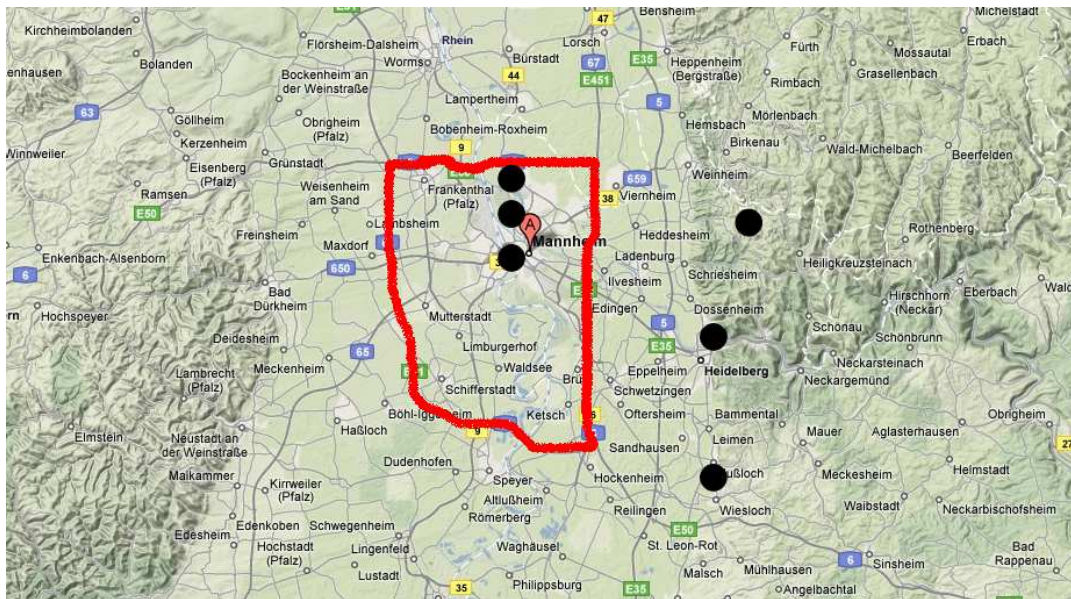


Figure 7.35: The locations of the meteorological stations: Mannheim North, Mannheim middle, Mannheim South respectively from top to bottom (inside the investigated area) and Wilmsfeld (Odenwald), Heidelberg and Wiesloch respectively from top to bottom (East of the investigated area).

Figures 7.36 and 7.37 show the wind direction during both days of measurements obtained from the six meteorological stations (half hourly averages). The red vertical lines indicate the start and the end of each driving cycle: two cycles on 23.08.2006 and four cycles on 24.08.2006.

Comparing both Figures, the wind directions on 23.08.2006 from different stations during the whole afternoon were fluctuating and inconsistent with each other. On the contrary of that, the wind directions on 24.08.2006 from different stations were consistent during the whole day and during measurements too.

Figures 7.38 and 7.39 show the wind speeds during both days of measurements. From comparing both figures, the wind speeds on 23.08.2006 (with max. 2m/sec.) were slower than those on 24.08.2006 (up to 6m/sec.). It can be deduced from the wind directions and speeds during both days that on 23.08.2006, the wind was slow and variable in direction and the wind on 24.08.2006 was faster and consistent in direction. This difference in wind conditions between the two days can be connected with the topography of the area as follows : The investigated area falls in the Rhein River valley between two high areas (see Figure 7.35):

1. Naturpark Pfalzer Wald at west\south west.
2. The Odenwald at east\north east.

When the wind is extremely slow like the case on 23.08.2006, the wind directions are easily changed by the topography of the land surface and when the wind speed is not so slow, the wind directions are not strongly affected by the surface topography. It is clear from the consistency of the wind directions on 24.08.2006 that they were not much affected by the surface topography. Since the wind directions are mostly westerly winds (ranging between north west and south west), the wind directions at the three stations outside the Mannheim-Ludwegshaven area are most likely to be affected by the land surface topography. Thus, calculating the average wind direction during measurements is restricted to the three stations in Mannheim only. After the measurements and Windoas Analysis of the collected spectra, the dSCDs of NO<sub>2</sub> could be retrieved as a function of time. Figures 7.40 and 7.41 show the NO<sub>2</sub> dSCDs along the route of driving as a function of time on 23.08.2006 and 24.08.2006 respectively.

Figures 7.42, 7.43 show the NO<sub>2</sub> VCDs during the first and second cycles respectively around the route of measurements on 23.08.2006. Figures 7.44, 7.45, 7.47 7.47 show the NO<sub>2</sub> VCDs during the first, second, third and fourth cycles respectively around the route of measurements on 24.08.2006.

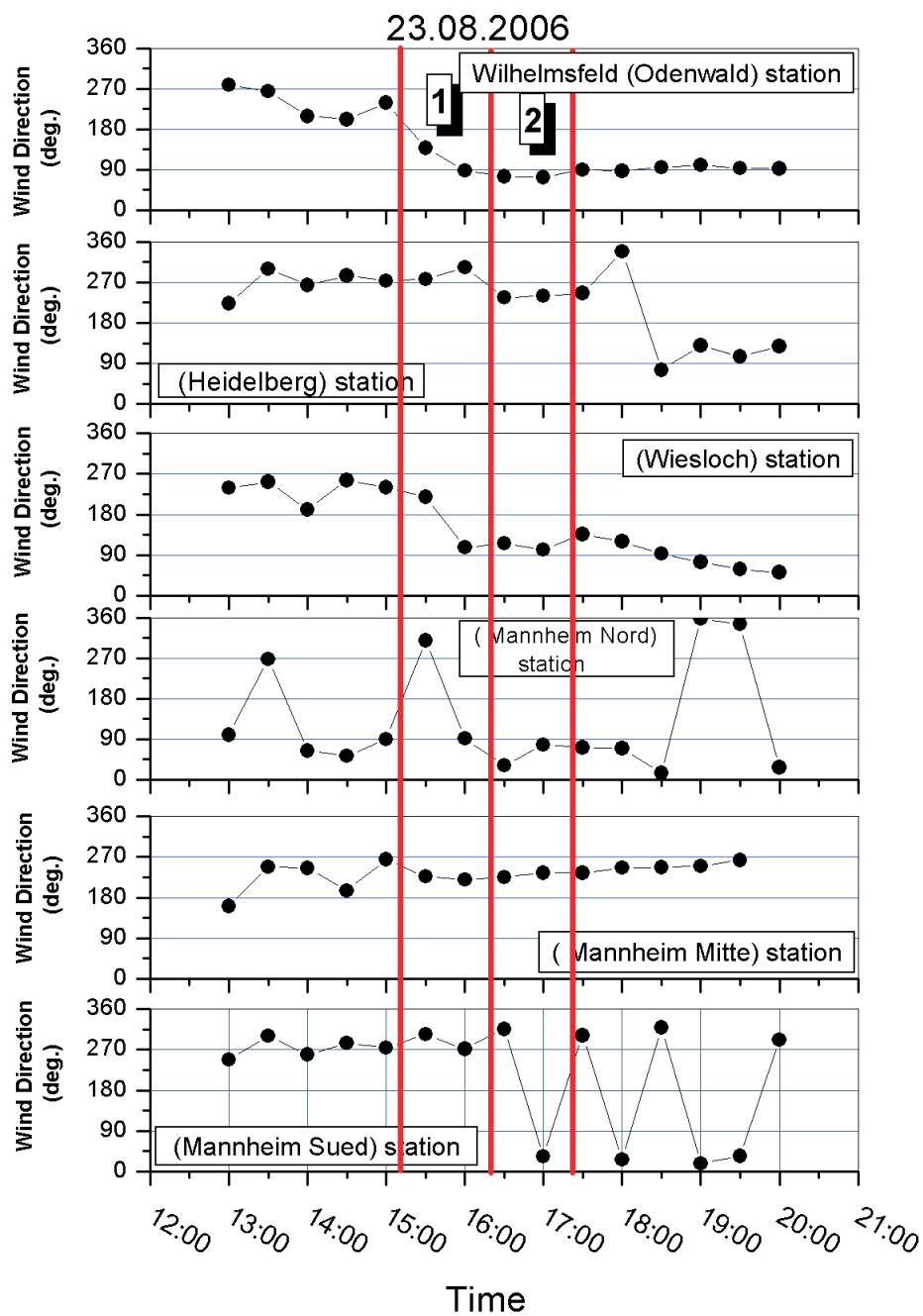


Figure 7.36: Wind directions on 23.08.2006 obtained from six different meteorological stations (half hourly averages). The red vertical lines indicate the start and the end of each of the two driving cycles.

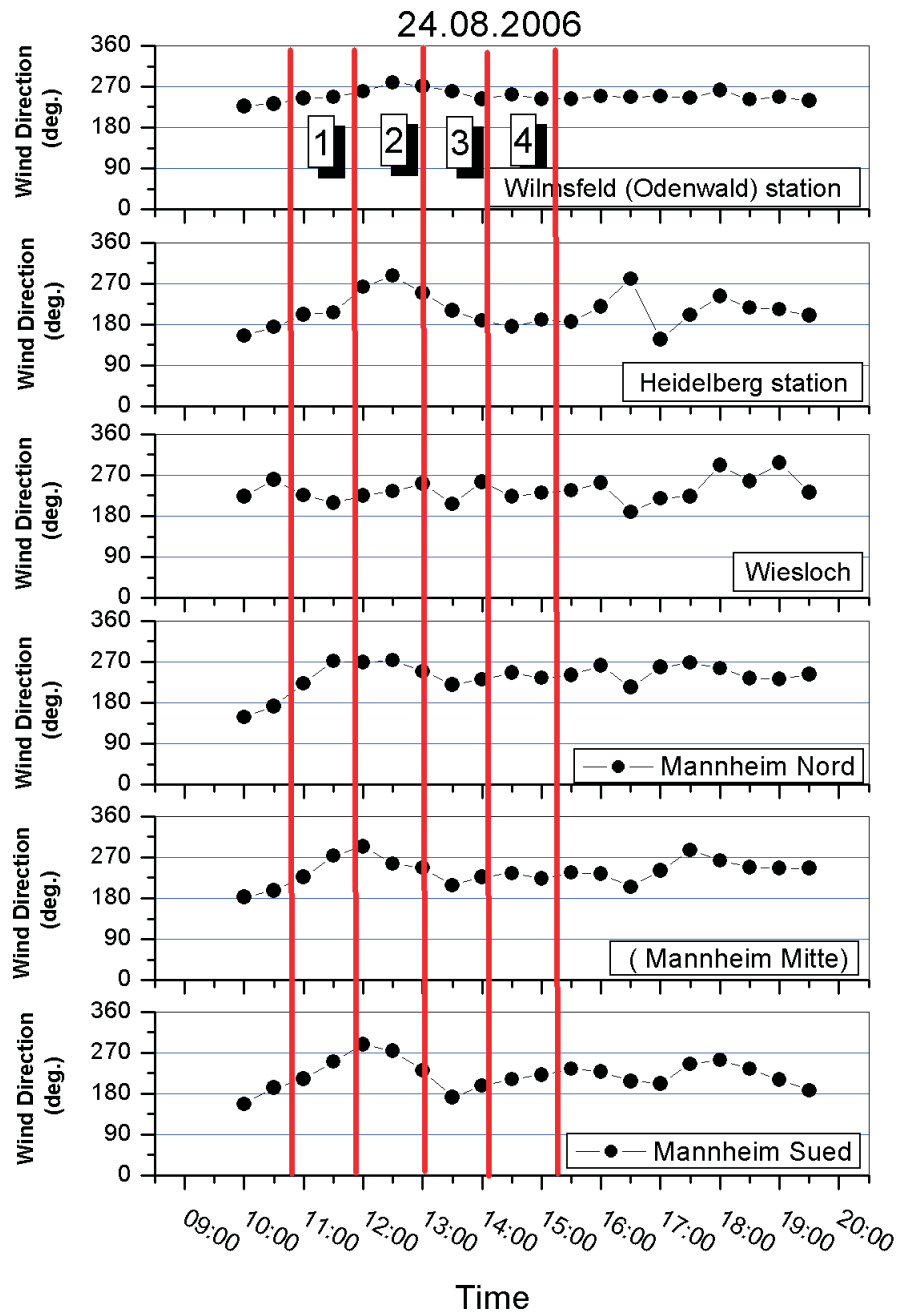


Figure 7.37: Wind directions on 23.08.2006 obtained from six different meteorological stations (half hourly averages). The red vertical lines indicate the start and the end of each of the four driving cycles.

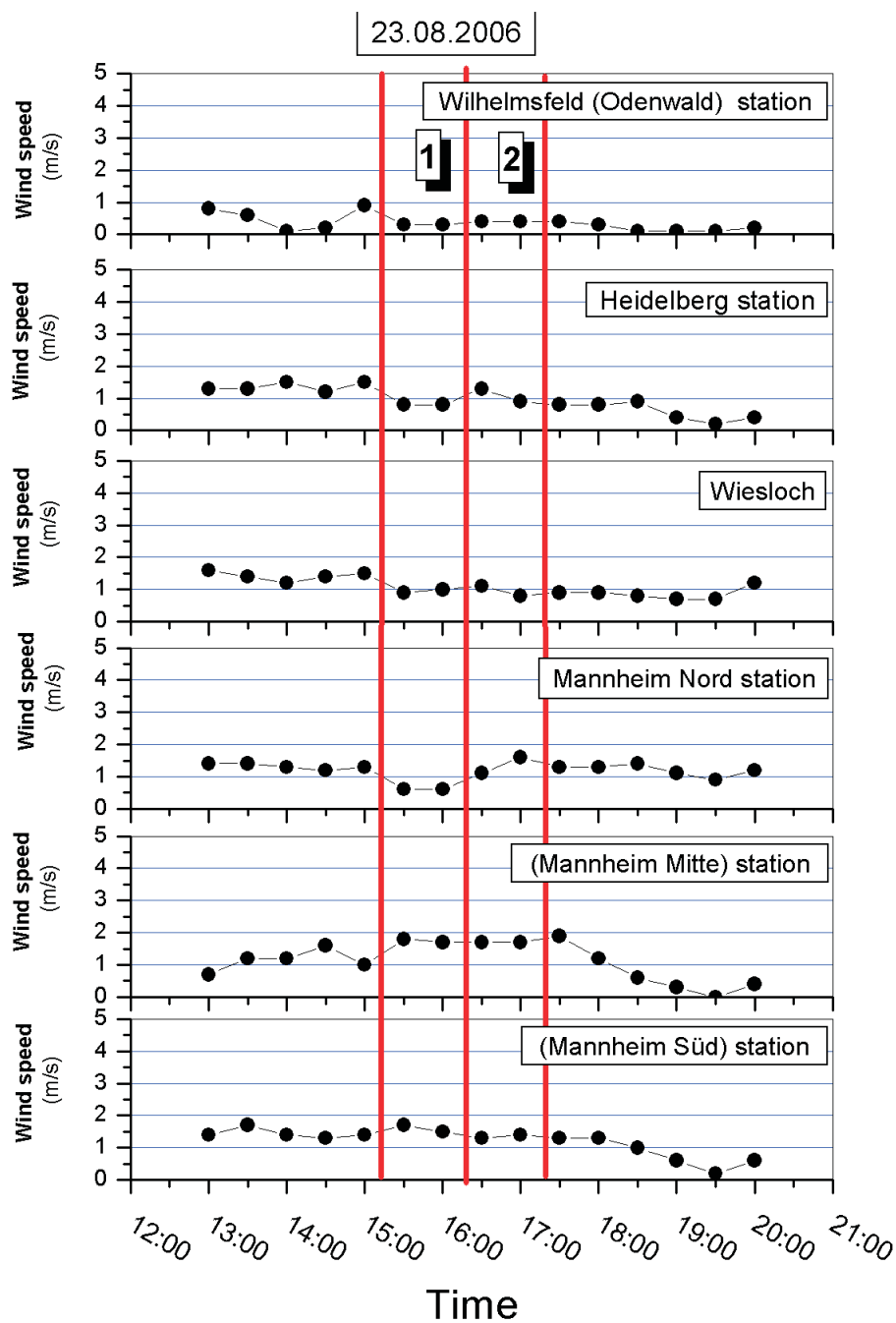


Figure 7.38: Wind speed on 23.08.2006 obtained from six different meteorological stations (half hourly averages). The red vertical lines indicate the start and the end of each of the two driving cycles.

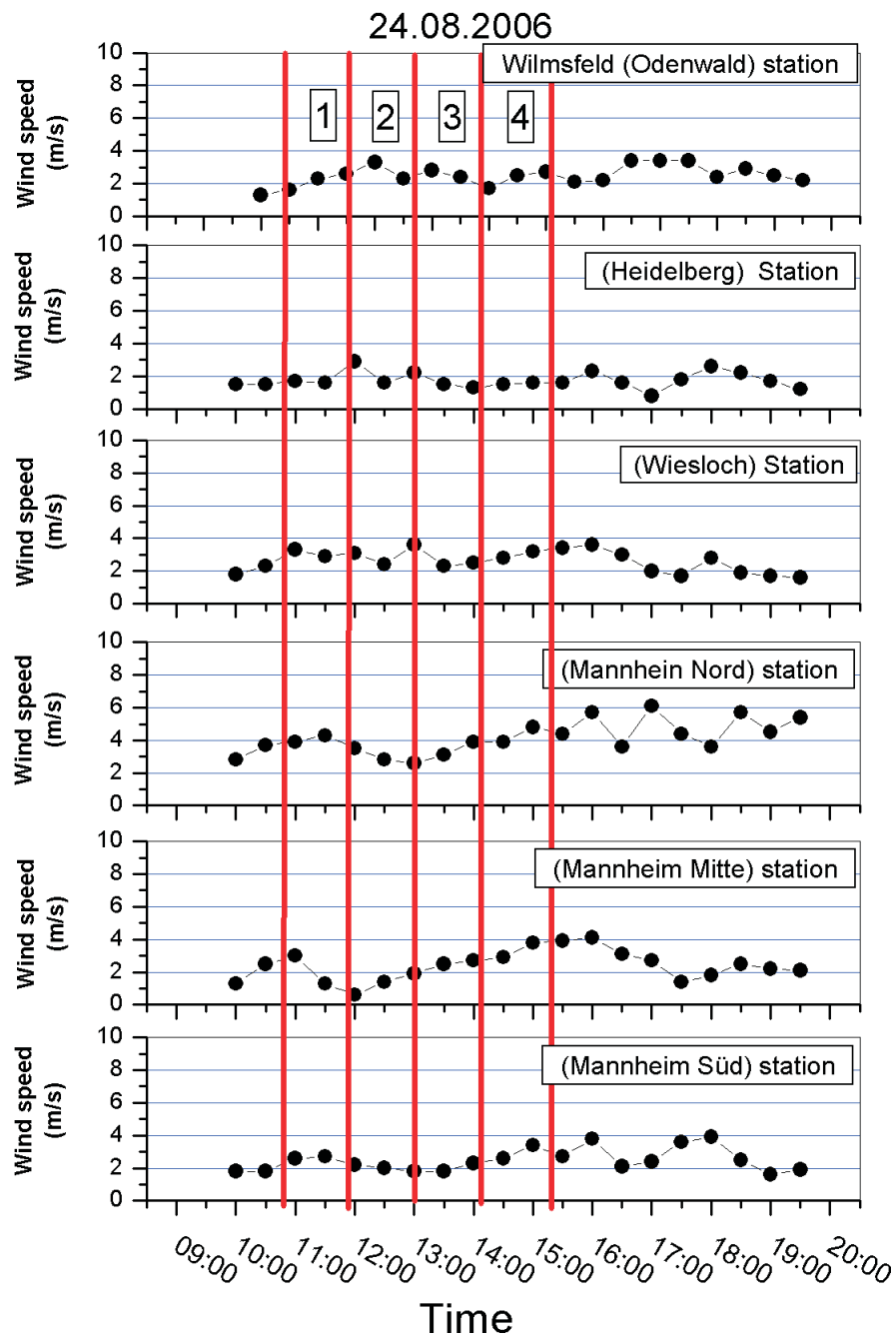


Figure 7.39: Wind speed on 24.08.2006 obtained from six different meteorological stations (half hourly averages). The red vertical lines indicate the start and the end of each of the four driving cycles.

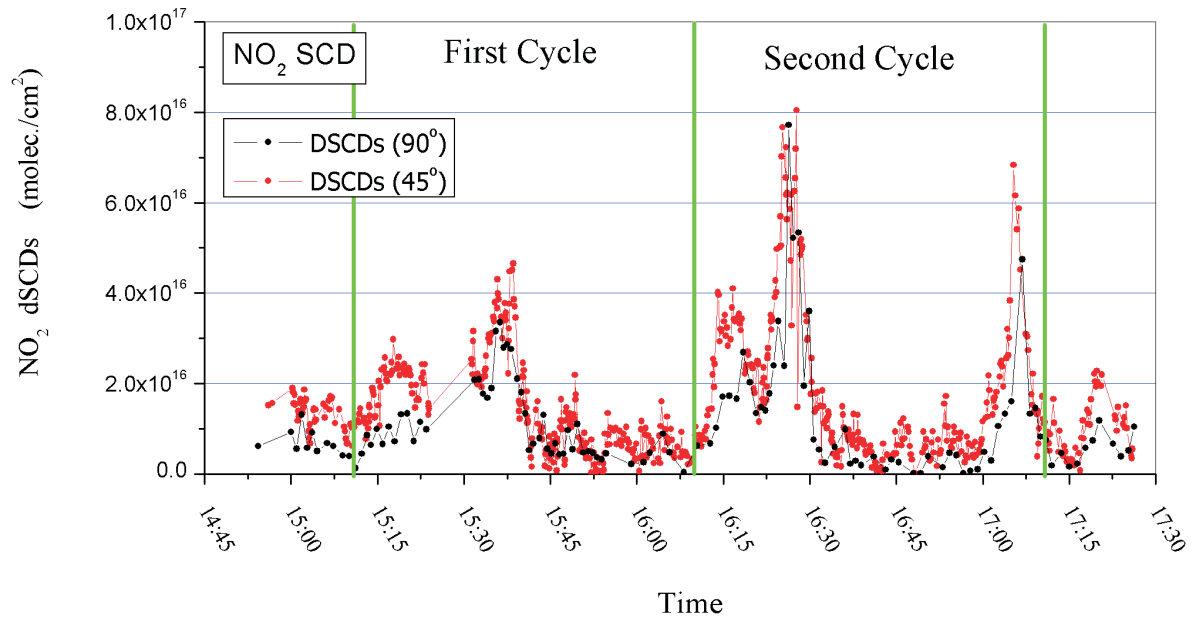


Figure 7.40: The  $\text{NO}_2$  dSCDs along the route of Auto-MAX-DOAS driving on 23.08.2006.

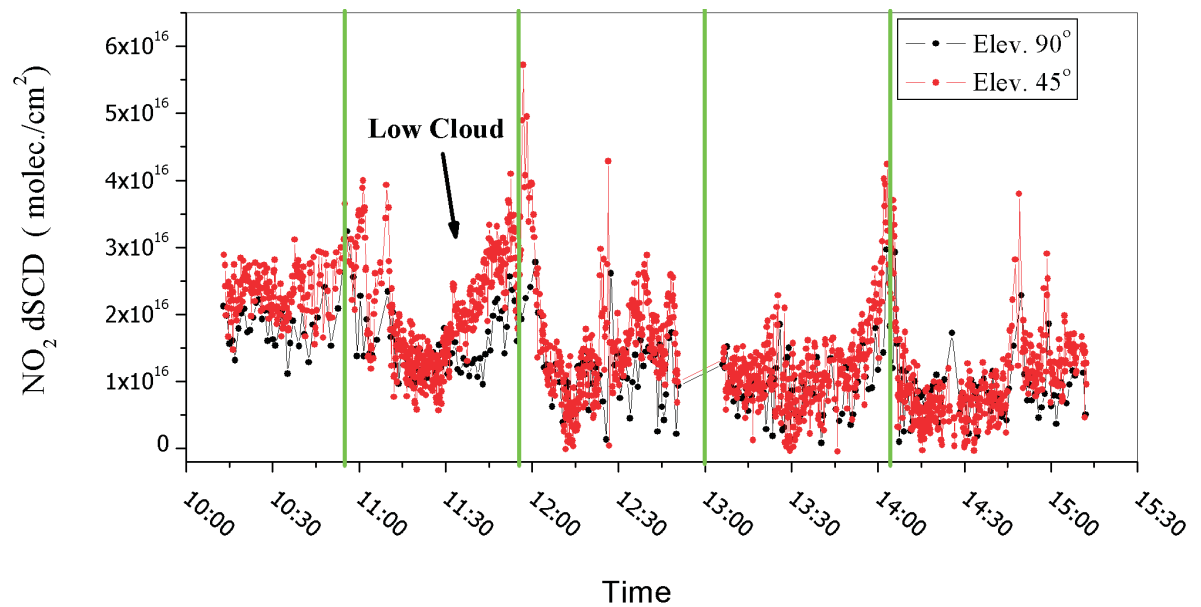


Figure 7.41: The  $\text{NO}_2$  dSCDs along the route of Auto-MAX-DOAS driving on 24.08.2006.

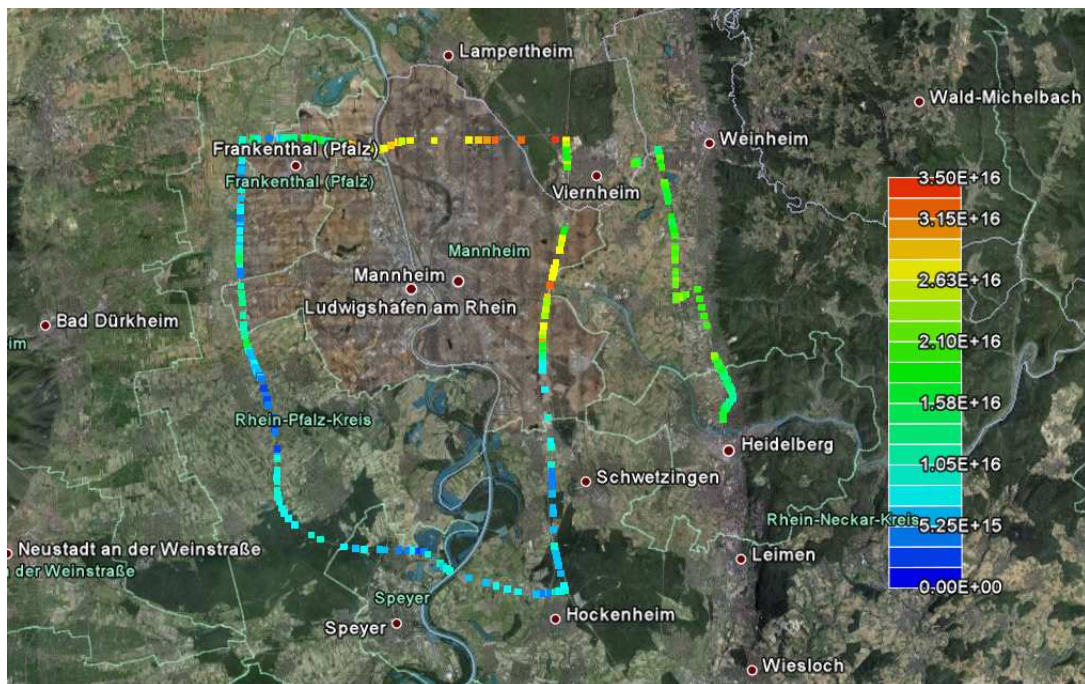


Figure 7.42: The NO<sub>2</sub> VCDs during the first cycle around the route of measurements on 23.08.2006).

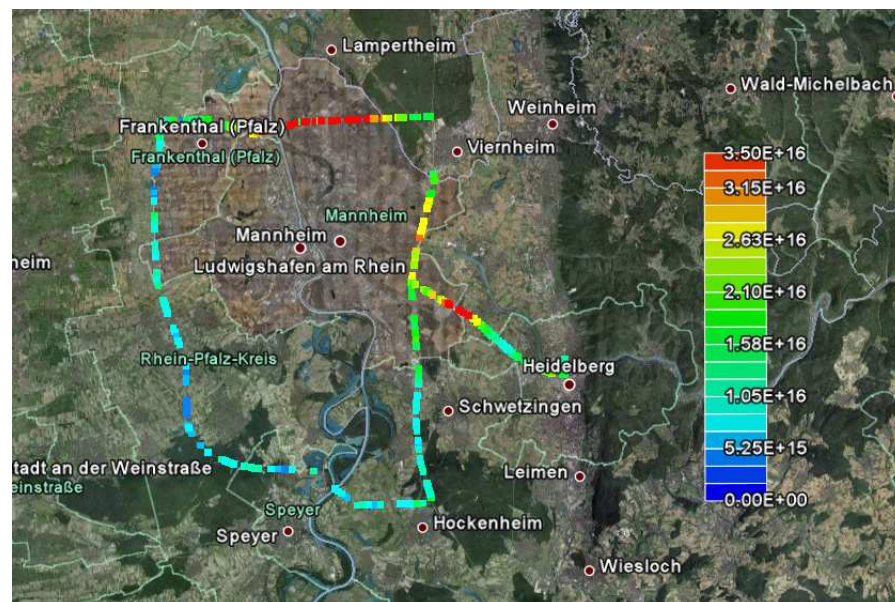


Figure 7.43: The NO<sub>2</sub> VCDs during the second cycle around the route of measurements on 23.08.2006.

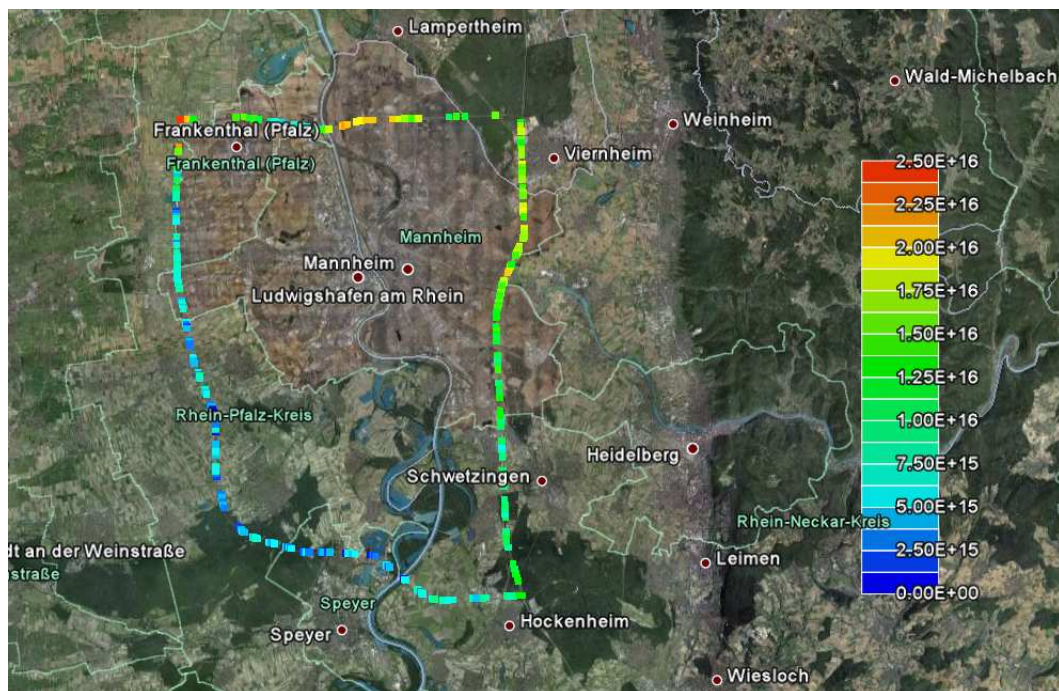


Figure 7.44: The  $\text{NO}_2$  VCDs during the first cycle around the route of measurements on 24.08.2006).

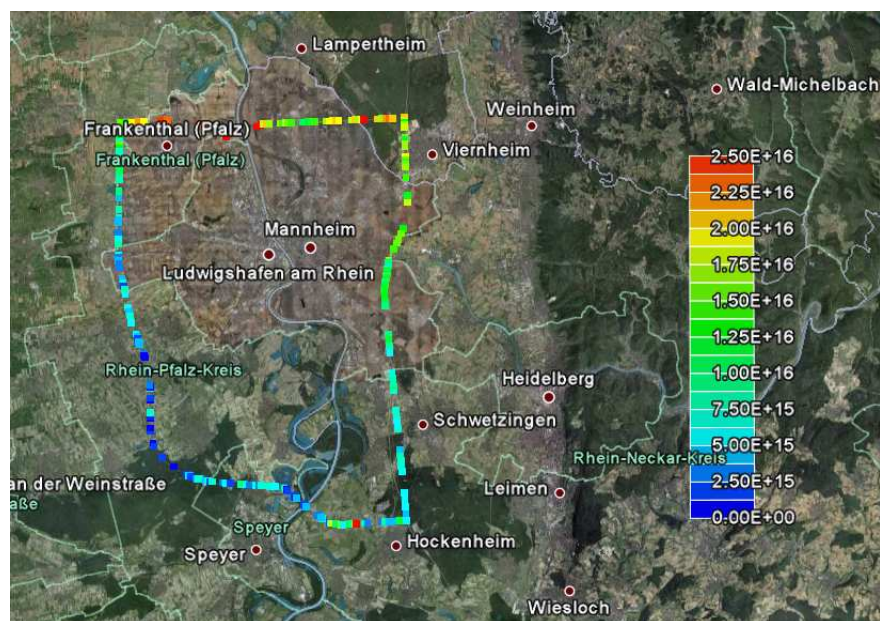


Figure 7.45: The  $\text{NO}_2$  VCDs during the second cycle around the route of measurements on 24.08.2006.

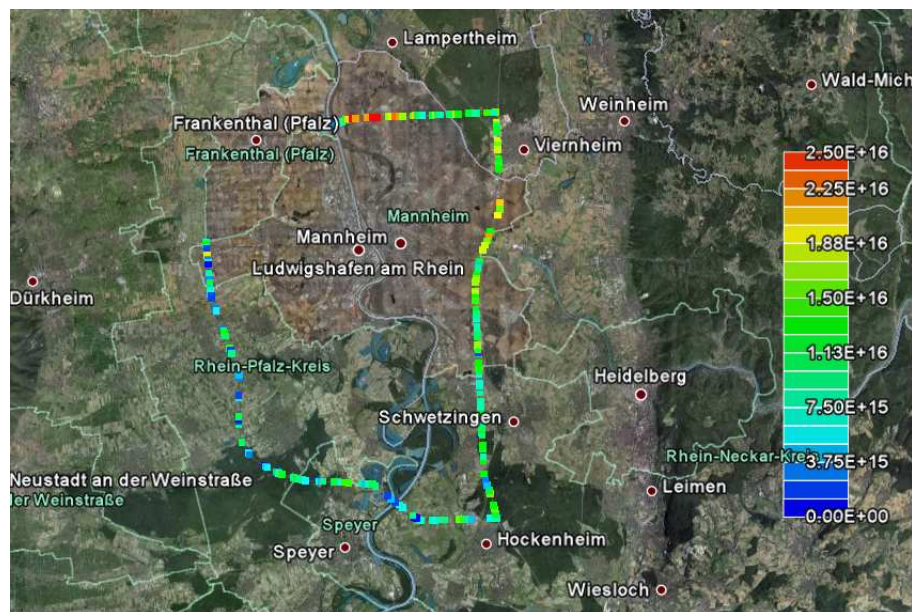


Figure 7.46: *The  $\text{NO}_2$  VCDs during the third cycle around the route of measurements on 24.08.2006.*

Figure 7.47: *The  $\text{NO}_2$  VCDs during the fourth cycle around the route of measurements on 24.08.2006.*

### 7.3.2 General Considerations for encircling measurements

In general for the encircling measurements, some considerations have to be taken into account. Also from the experience gained during the encircling measurements so far, some points could be summarized as follows:

#### The effect of driving speed of the Auto-MAX-DOAS

Driving fast has some advantages and disadvantages such as:

1. Advantage: To drive fast and encircle the investigated area before the wind direction would change during the day. Since the wind direction can change around the clock. This can affect the understanding and interpretation of the results and makes the interpretation of observations neither easy nor straightforward (see below for more details on this point).
2. Disadvantage: It would cause the spatial resolution of the measurements to be reduced: If the integration time is about  $60 \times 30$  sec., so driving too fast (e.g.

at a speed around 100km/h) would cause the so called pixel size<sup>1</sup> to be around 1.66 km. Driving at half of this speed (i.e. 50 km/h) for the same integration time would cause the spatial resolution to be twice better (i.e. pixel size = 0.83 km). For the best spatial resolution of the measurements, the integration time of one spectrum needs to be as short as possible and/or the driving speed has to be minimum.

Therefore also driving slow can enhance the spatial resolution but also might not complete a whole circle before the wind direction changes and makes calculation flux practically impossible.

### **The effect of choice of the encircling route**

It is noteworthy that the choice of the route around the investigated area has to satisfy two criteria:

1. The route should be -preferably- mostly free of traffic jams, otherwise the measurements could be distracted several times and also the pollution from the traffic would cause a systematic background error in the NO<sub>2</sub> dSCDs.
2. The route should not be very large so that it would be far from the investigated area. Also this large route would cause one cycle to take a long time and the wind direction might change before on complete cycle would be completed. This can complicate the efforts to estimate the flux of emissions to/ from the investigated area.

### **The effect of wind direction and speed**

Two extreme situations can be assumed to estimate their consequences :

1. If the wind speed is very low (e.g. below 10 km/h) and the wind direction is varying quickly, this will cause the plume in the investigated (encircled) area to move around or back and forth but not to leave the area. This makes pollution flux measurements and estimation practically impossible.
2. If the wind speed is high and the wind direction is persistent in one direction for long enough time, these would be the ideal conditions for flux estimation measurements.

---

<sup>1</sup>Pixel size is defined here in this work as: the distance covered during driving with Auto-MAX-DOAS until one complete spectrum is taken. It is expressed in length along the driving route

Actually the realistic situations are most of the time something in between these two extreme cases. While every single day of measurements is a unique situation in itself :

With its weather conditions, time of the year, cloudiness, aerosol load in the atmosphere, and several other factors. So each case needs to be considered separately and no general rule would fit for all measurements conditions. All what can be deduced from the actual experience are general trends but not more detailed rules.

### **The effect of season**

Winter has the advantage of cold air near from the ground surface so the BL would not exceed 2 kilometers anyhow at mid-latitudes. Emissions usually happen within the first 100-200 meters from the ground surface. The vertical mixing is not so active so this enables the application of some assumptions for the possible plume vertical layer extent (within the BL especially if there is a temperature inversion at the top of the BL). This would help to estimate scenarios for the vertical profile of the measured trace gas (e.g.  $\text{NO}_2$ ).

But also the big disadvantages of winter are thick clouds and rain. Rain would wash out the trace gas from the troposphere and the cloudiness would complicate the radiative transfer in the atmosphere and would complicate any AMF calculations for estimation of VCDs.

While summertime would have the advantage of less cloudiness and clear sky. But the heat near from the ground surface and the strong vertical mixing and convection would complicate the assumptions to estimate the trace gas layer height. Also there are some emission activities related to the season, for example burning wood and coal for heating are related to winter time while in summer time, such heating activities do not exist.



# 8 Results from DANDELIONS campaign

## 8.1 DANDELIONS campaign overview

DANDELIONS (Dutch Aerosol and Nitrogen Dioxide Experiments for vaLIIdation of OMI and SCIAMACHY) is a project that encompasses validation of NO<sub>2</sub> measurements by the Ozone Monitoring Instrument (OMI)<sup>1</sup> and SCIAMACHY (Scanning Imaging Absorption SpectroMeter for Atmospheric CartographY), and of aerosol measurements by OMI and the Advanced Along-Track Scanning Radiometer (AATSR)<sup>2</sup>, using an extensive set of groundbased and balloon measurements over the polluted area of the Netherlands.

During the DANDELIONS campaign, measurements were performed at the Cabauw Experimental Site for Atmospheric Research (CESAR, 51.97°N, 4.93°E 0.70 m below mean sea level). The Cabauw site has a large number of routine instruments aimed at measuring meteorological, radiative and cloud parameters. An overview of the instrumentation available during the campaign is given in Table 8.1. Most of these instruments measured on a continuous basis.

Additional measurements by NO<sub>2</sub> lidar, radio sondes, ozone sondes and the GLOBE sun photometer were performed during days with (potentially) good weather. These days became golden days if the cloud coverage during the overpass was less than 20% and most instrumentation worked well. The golden days for intensive analysis are May 27, 28, June 19, 23, 24.

There were Aura overpasses over Cabauw one or two times per campaign day, OMI operated flawlessly. The monthly spatial zoom mode was performed twice during the campaign (unfortunately during overcast situations).

For SCIAMACHY, during the campaign, an Operations Change Request was honored, that maximized the number of overpasses with nadir mode observations for Cabauw.

---

<sup>1</sup>The Ozone Monitoring Instrument (OMI) is a Dutch-Finnish instrument on board EOS- 60 Aura, that has been in space since July 15, 2004

<sup>2</sup>Advanced Along-Track Scanning Radiometer (AATSR) is one of the Announcement of Opportunity (AO) instruments on board the European Space Agency (ESA) satellite ENVISAT. It is the most recent in a series of instruments designed primarily to measure Sea Surface Temperature (SST)

Table 8.1: Participating instruments

Instrument	Group	data
OMI	KNMI/NASA	NO <sub>2</sub> columns : level 2 & level 4, AOT
SCIAMACHY	KNMI	NO <sub>2</sub> columns : TEMIS and Bremen
AATSR	KNMI	aerosol type, AOT, Ångström coefficient
NO <sub>2</sub> lidar	RIVM	NO <sub>2</sub> profiles
NO <sub>2</sub> monitor	RIVM	NO <sub>2</sub> surface concentrations
Boundary layer lidar	RIVM	aerosol extinction, backscatter profiles
MAX DOAS	IUP Bremen	NO <sub>2</sub> columns
MAX DOAS	IUP Heidelberg	NO <sub>2</sub> columns, three azimuth angles
MAX DOAS	BIRA Brussels	NO <sub>2</sub> columns
Mini MAX DOAS	BIRA Brussels	NO <sub>2</sub> columns
Mini MAX DOAS	KNMI	NO <sub>2</sub> columns
Radio sondes	KNMI	pressure, temperature, RH
Ozone sondes	KNMI	ozone profiles
Brewer spectrophotometer	KNMI	ozone columns
GLOBE spectrophotometer	KNMI	AOT
Routine aerosol instruments	TNO/KNMI	AOT

On average, two overpasses per 3–4 days were available from SCIAMACHY.

## 8.2 MAX-DOAS measurements in Cabauw

During the DANDELIONS campaigns, three multi-axis differential optical absorption spectroscopy (MAX-DOAS) instruments operated quasi continuously in Cabauw. They were the MAX-DOAS instruments of BIRA-IASB, University of Bremen and IUP Heidelberg. The three IUP-Heidelberg telescopes were directed at three different azimuth angles (325°, 235°, 145°) with respect to north. Each telescope sequentially scans 5 different elevation angles : 1°, 3°, 6°, 20° and 90° (zenith); a single measurement is taken every 90 seconds.

Figure 8.2 shows Cabauw site on the map. Figure 8.2 shows the three telescopes in the measurements location.

## 8.3 MAX-DOAS NO<sub>2</sub> results

During the whole campaign time, the measurements were continuously carried out automatically and they were followed up from Heidelberg using a remote connection software.



Figure 8.1: *Cabauw site on the map*

The data was evaluated first using Windoas software with a fixed reference for all days for comparison of the NO<sub>2</sub> DSCDs from all telescopes at different elevation angles. Comparing the DSCDs obtained from lowest elevation angles can give some information about the homogeneity of the field around the measurements site (homogeneity in NO<sub>2</sub> concentrations at the three different azimuth directions of measurements) see next section. Then the data was evaluated using MFC software using the reference spectrum from each sequence to evaluate the spectra of the sequence. Thus the NO<sub>2</sub> tropospheric DSCDs are obtained. Appendix B shows the complete series of NO<sub>2</sub> VCDs during the campaign in comparison to the other participating MAX-DOAS Instruments. Figure 8.3 shows time series of the obtained average tropospheric NO<sub>2</sub> tropospheric VCDs from one telescope.

It is clear from the Figure that the NO<sub>2</sub> VCDs were decreasing with time while going more into summer time. This could be explained by one of two simple explanations :

1. Less emissions during summer dure to holidays time.
2. More photolysis of NO<sub>2</sub> so it is photolyzed and escapes detection.



Figure 8.2: *The three Heidelberg telescopes at Cabauw measurements site directed at three different azimuth directions  $325^\circ$ ,  $235^\circ$ ,  $145^\circ$*

## 8.4 Investigation of the spatial homogeneity

Assuming that the tropospheric  $\text{NO}_2$  layer is horizontally homogenous, the observed  $\text{NO}_2$  SCDs for the different azimuth angles should be similar. In turn, from the observed differences for the various viewing directions the horizontal heterogeneity of the  $\text{NO}_2$  concentration field can be estimated. Such an estimation is a very important information for the validation of satellite instruments with ground based observations. In cases of strong horizontal gradients, ground based observations might be not representative for the average value within a satellite ground pixel. Since the horizontal extension of the absorption paths along the line of sight is largest for low telescope elevation, here, the observations at elevation angles of  $3^\circ$  are used for the estimation of the heterogeneity of the tropospheric  $\text{NO}_2$  concentration field.

### Tropospheric Vertical Column Densities of NO<sub>2</sub> (VCDs) at Cabauw – Holland during the Campaign time.

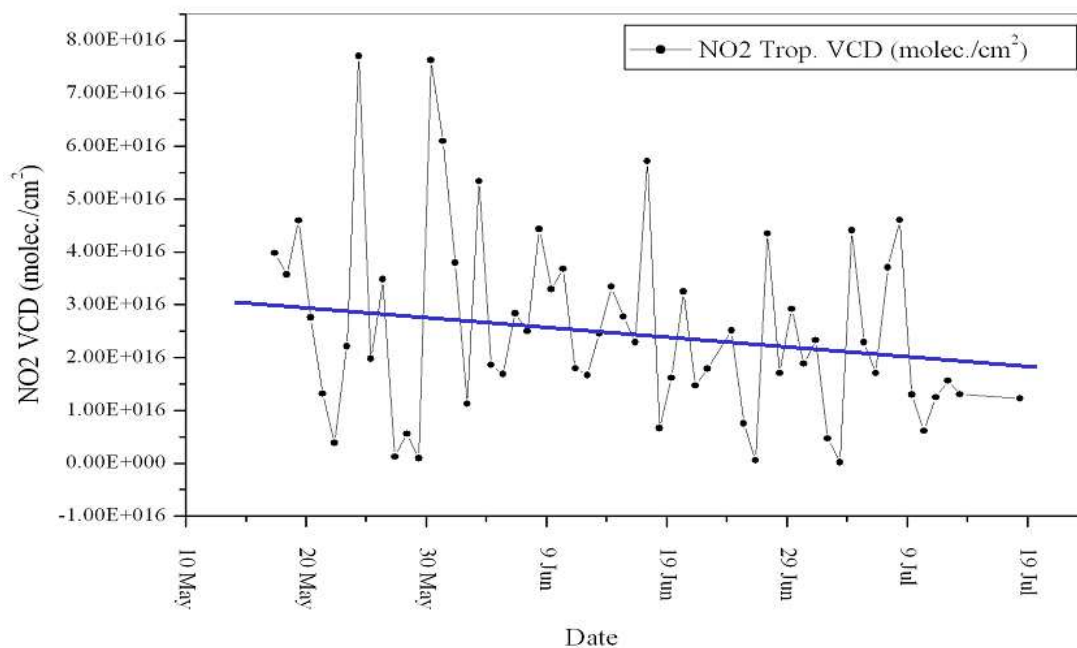


Figure 8.3: A time series of the obtained average tropospheric NO<sub>2</sub> VCDs

In principle it would be even better to use even smaller elevation angles (e.g. the telescopes at 1° elevation), but unfortunately one of the 1° observations is affected by a limited free path along the line of sight (probably due to trees).

Figure 8.4 shows one day (03.07.2005) with homogeneous field of concentration of NO<sub>2</sub> around the measurements place during the hole day. The three telescopes directed at three different azimuth directions see the same NO<sub>2</sub> DSCDs which are almost only stratospheric ones and no evidence from tropospheric NO<sub>2</sub> at that day (a clean day).

Figure 8.5 shows one day (15.05.2005) with homogeneous field of concentration of NO<sub>2</sub> around the measurements place during the first half-day where there is some tropospheric pollution with NO<sub>2</sub> and then in the afternoon the tropospheric pollution is more in the North direction (telescope 2 was directed to the NW direction).

From the observed NO<sub>2</sub> SCDs at 3° telescope elevation, the ratio of the maximum and the minimum NO<sub>2</sub> SCDs were calculated. For a horizontally homogenous concentration field, this ratio should be 1; the more this ratio deviates from unity, the larger are the horizontal gradients. In addition to the strength of the horizontal gra-

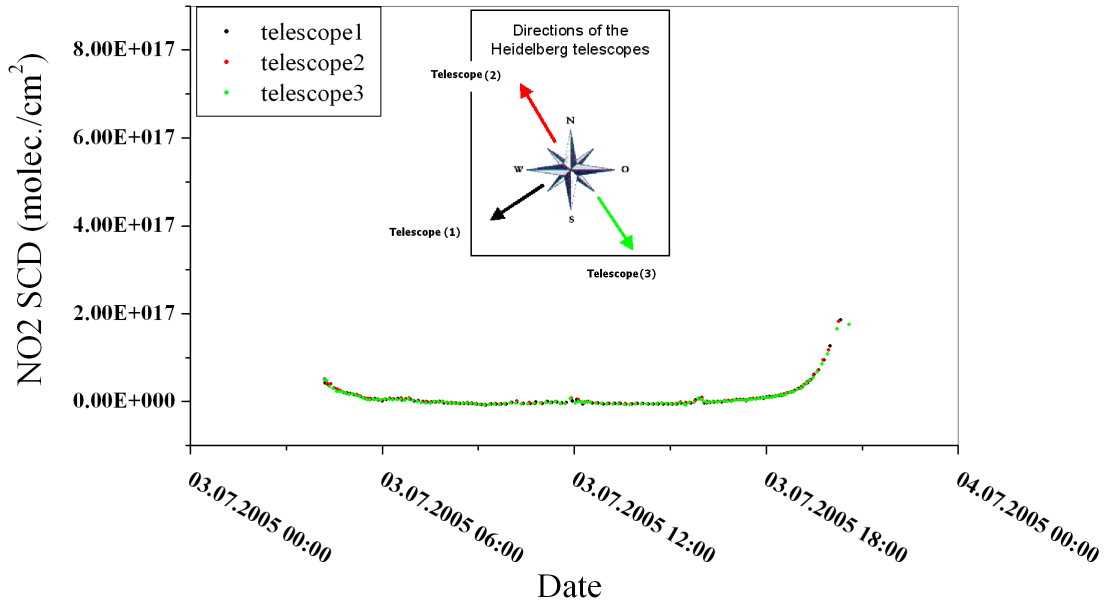


Figure 8.4: *one day (03.07.2005) with homogeneous field of concentration of  $\text{NO}_2$  around the measurements place. The three telescopes directed at three different azimuth directions see the same  $\text{NO}_2$  DSCDs which are almost only stratospheric ones and no evidence from tropospheric  $\text{NO}_2$  at that day (a clean day).*

dients, also information on the direction of the  $\text{NO}_2$  gradient can be derived. Since the instrument was operated only in three different azimuth angles, only limited information on the direction of the horizontal gradient can be derived. In future applications, it might be interesting to measure at much more azimuth angles. For the interpretation of the retrieved information on the gradient of the tropospheric  $\text{NO}_2$  concentration field, it is important to consider two effects which can affect the observed  $\text{NO}_2$  SCDs, especially for low elevation angles :

First, the sensitivity to the relative azimuth angle (between the telescope and the sun). This dependency becomes more pronounced for increasing solar zenith angle (SZA) and increasing aerosol load (see Wagner et al., 2004).

Second, the effect of the atmospheric aerosol load on the atmospheric visibility and thus on the horizontal extension of the absorption paths along the line of sight. Thus, depending on the aerosol load, the calculated ratio represents information on gradients over areas of different horizontal extension.

The magnitude of both effects was estimated by means of radiative transfer calculations using the radiative transfer model TRACY-II [Deutschmann et al., 2006;

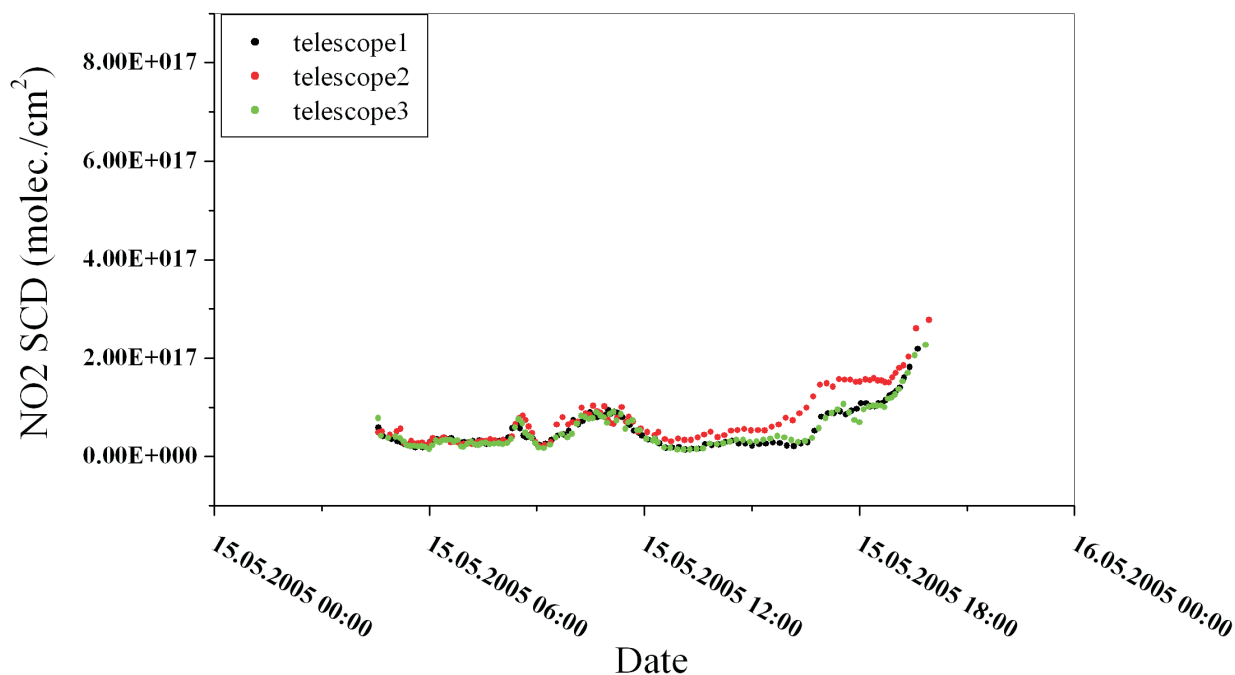


Figure 8.5: day (15.05.2005) with homogeneous field of concentration of  $\text{NO}_2$  around the measurements place during the first half-day where there is some tropospheric pollution with  $\text{NO}_2$  and then in the afternoon the tropospheric pollution is more in the North direction (telescope 2 was directed to the NW direction).

Wagner et al., 2007]. The dependence on the azimuth angle is found to be generally very small. For a pure Rayleigh atmosphere and various aerosol loads (optical depth 0.1 to 1) the variation is typically below 15% (for SZA ranging from  $20^\circ$  to  $80^\circ$ ). Thus, almost all observed ratios of the maximum and minimum  $\text{NO}_2$  SCDs (see Figure 8.6) are much larger than what could be explained by this azimuth dependence.

Figure 8.6 shows Maximum and minimum  $\text{NO}_2$  DSCD observed for an elevation angle ( $3^\circ$ ) of the Heidelberg MAX-DOAS telescopes observing under three different azimuth angles at Cabauw during the DANDELIONS campaign in 2005. High ratios indicate large horizontal gradients of the tropospheric  $\text{NO}_2$  concentration field, colors indicate the direction of the gradient (directed towards higher values).

In contrast, the effect of aerosol scattering on the horizontal extension, for which the calculated ratio is representative, can be very large. Assuming a layer height of 1km, the geometrical path length inside this layer for an elevation angle of  $1^\circ$  would be  $\sim 19\text{km}$ . For a pure Rayleigh atmosphere the molecular scattering reduces this path length to an effective path length of only  $\sim 17\text{km}$ .

For additional aerosol scattering the path length decreases further. Assuming an

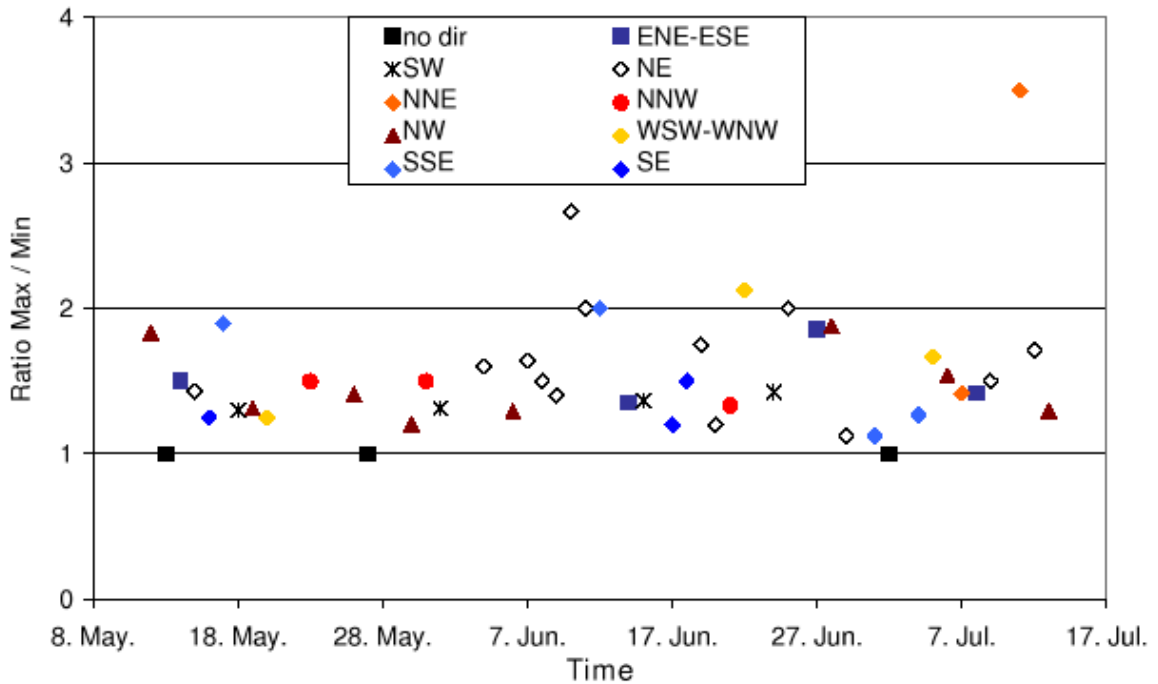


Figure 8.6: *Maximum and minimum NO<sub>2</sub> DSCD observed for an elevation angle ( $3^\circ$ ) of the Heidelberg MAX-DOAS telescopes observing under three different azimuth angles at Cabauw during the DANDELIONS campaign in 2005. High ratios indicate large horizontal gradients of the tropospheric NO<sub>2</sub> concentration field, colors indicate the direction of the gradient (directed towards higher values).*

optical depth of 0.1 (0.3, 1.0) in a layer between the surface and 1km altitude with, the effective path length would be only  $\sim 12\text{km}$  ( $\sim 8\text{km}$ ,  $\sim 4.5\text{km}$ ). Thus for typical aerosol optical depths the horizontal extension, for which the calculated ratio is representative, ranges between about 10km and 25km.

In principle, the visibility of the atmosphere could be estimated from the simultaneously measured O<sub>4</sub> absorption [Wagner et al., 2004]. However, such a detailed analysis is beyond the scope of this study and will be a subject of further studies in future.

## 8.5 MAX-DOAS ground-based results comparisons

The MAX-DOAS results from IUP Heidelberg and the other two institutes (BIRA and IUP Bremen) were done for the purpose of intercomparison of instruments together to check the reliability of the measurements. Figure 8.5 shows the Scatter-

plots of the tropospheric NO<sub>2</sub> columns retrieved during the 2005 campaign from the BIRA maxdoas instrument and, respectively, the Bremen maxdoas (top left), the Heidelberg maxdoas for the 3 pointing directions North-West (top right), South-East (bottom left) and South-West (bottom right). The regression analysis parameters are given in the legends.

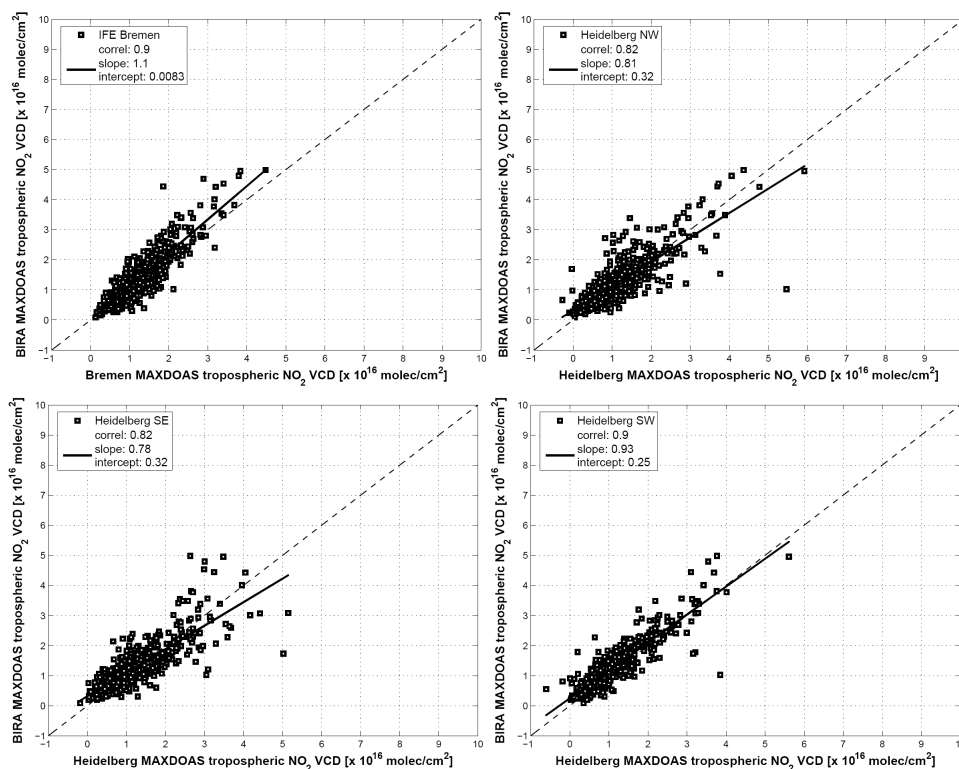


Figure 8.7: the Scatterplots of the tropospheric NO<sub>2</sub> columns retrieved during DANDELIONS campaign from the BIRA MAX-DOAS instrument and, respectively, the Bremen maxdoas (top left), the Heidelberg maxdoas for the 3 pointing directions North-West (top right), South-East (bottom left) and South-West (bottom right). The regression analysis parameters are given in the legends.

Very good agreement is found between the BIRA and Bremen data sets (Pearson correlation coefficients of 0.9 and slope of 1.1), and good agreement is also found with the three Heidelberg telescopes (correlations between 0.82 and 0.9). After further homogenisation of the BIRA and Heidelberg data sets regarding the NO<sub>2</sub> absorption cross-sections considered for the retrieval, an even better agreement is found, reaching a correlation coefficient of 0.92 and a slope of 0.99. Note that such a level of agreement is only achieved when considering the South West pointing Heidelberg telescope, since this is approximately in the same direction as the two other

instruments. This result highlights the importance of horizontal inhomogeneities in the  $\text{NO}_2$  field that in some cases strongly affect the comparisons with satellite.

## 8.6 Comparisons with Satellite results

Good agreement between the data from the three groundbased instruments was obtained. Also agreement with satellite data showed some good agreement in general. Taking into account the differences in retrieval methods, algorithms and assumed  $\text{NO}_2$  profiles during retrieval process. An example is shown in Figure 8.8, which includes also the OMI (Level 2 product) and SCIAMACHY (TEMIS product) overpass data. The gaps in the timeseries of ground-based measurements result from the application of the selection criterion based on the comparison of the  $\text{NO}_2$  columns retrieved from  $15^\circ$  and  $30^\circ$  of elevation.

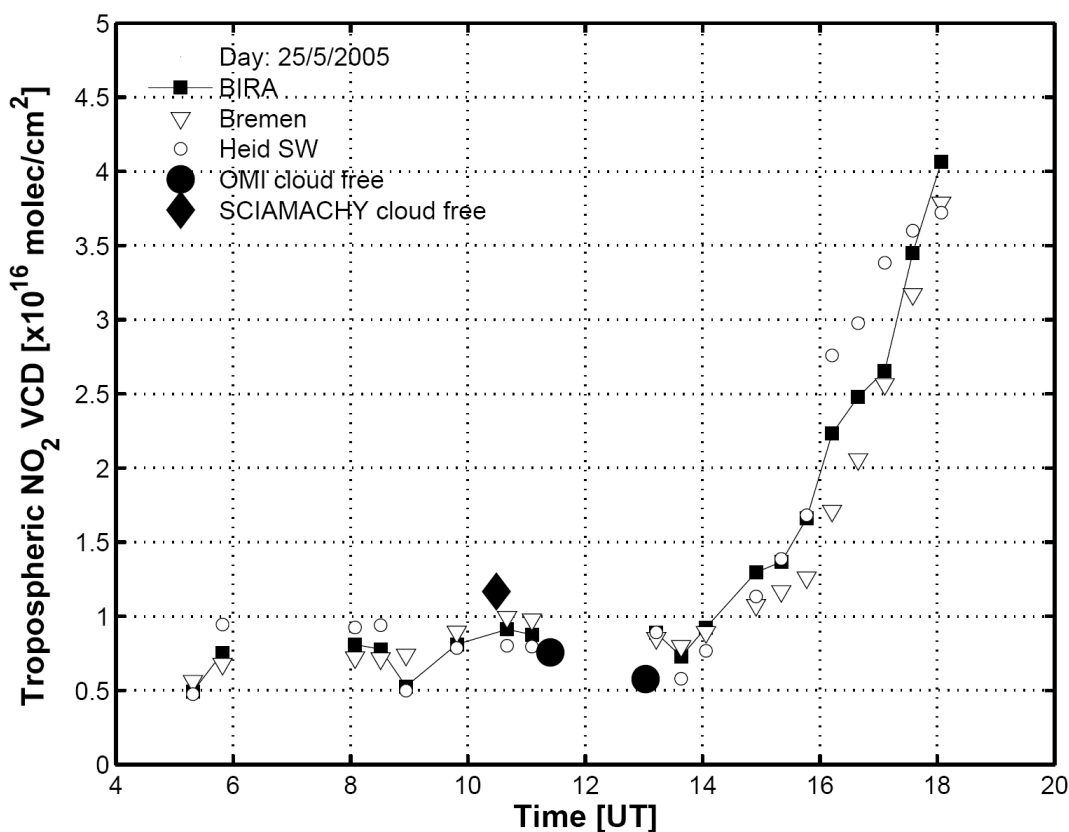


Figure 8.8: comparison between ground-based MAX-DOAS results, OMI (Level 2 product) and SCIAMACHY (TEMIS product) overpass data during the day 25.05.2005.

# 9 Summary and Outlook

## 9.1 Summary

This work consists of three parts. In the first part, results are represented from BrO measurements on board of Research Vessel Polarstern during October-November 2003 during the cruise between Bremerhaven (Germany) and Cape Town (South Africa).

In the second part, Auto-MAX-DOAS (Car DOAS) measurements were carried out at Mannheim- Ludwigshafen Industrial / urban area and on the road between Brussels (Belgium) and Heidelberg (Germany) and also on the north coast of France during a big fire event near from London (UK). NO<sub>2</sub> was detected during these measurements with the Auto-MAX-DOAS.

In the third and last part, we participated in a large international measurement campaign where we carried out long time series NO<sub>2</sub> measurements (about two months) at the Cabauw experimental site for Atmospheric Research.

In the following, the summary of the main findings and outcome of each of the three parts will be stated.

### 9.1.1 The Polarstern campaign:

BrO mixing ratios up to 18 ppt were detected in the troposphere over the Atlantic Ocean between latitudes 10° and 30° north (west of African coast). Various correlation studies were carried out to shed some light on the sources and processes which contribute the production of BrO in the Marine Boundary Layer MBL. Here is the summary of the main outcome of these investigated BrO-correlations:

#### BrO-Chlorophyll Correlations

From all the BrO-Chlorophyll correlations studied in this thesis, the following can be concluded:

- (1) There are positive correlations between BrO (DSCDs) and the local chlorophyll concentrations as well as the average and maximum chlorophyll concentrations along the back trajectories of investigated air masses.

(2) The strengths of different correlations were not significantly different for the calculated back trajectories for five days, two days or one day prior to measurement. This means that the effect of time duration of contact between air masses and sea water surface could not be a significant parameter in BrO formation.

(3) The effect of local chlorophyll concentration seems to play the major role in BrO formation but this needs further investigation using more experimental data.

The overall rather low correlation coefficients and fluctuations in their values [in the data set of current work (2003 data)] can be attributed to three reasons:

(a) The small statistical sample sizes of the two data sets used in this study so far.

(b) Chlorophyll (and in turn, algae and phytoplankton) is not the only source of BrO precursors.

(c) The chlorophyll concentrations data used in this study were weekly averages not daily averages. This also has its effects on the precision of the chlorophyll data used in correlation studies.

(4) From the data set of M. Martin (2007), it was more clear that the local chlorophyll concentrations were probably the most significant contributors to BrO elevated values. The extremely short distance the air back trajectories spent in contact with ocean surface support the idea that the contributions from distant chlorophyll aggregations upwind are not as much significant as the local ones.

(5) From both data sets used in this study, elevated BrO (DSCDs) were observed for short periods of time (few hours) during some measurements days. This corresponds to a few tens of kilometers of spatial extent of areas with elevated BrO levels. This also supports the idea that distant chlorophyll aggregations from a certain location are not significant sources of the detected BrO at these locations.

### BrO-Aerosol Correlations

From all the BrO-aerosol correlations studied in this thesis, the following can be concluded:

(1) There is a positive correlation between BrO (DSCDs) and the acidity of marine aerosols (deduced from the negative correlation to the aerosol pH).

(2) There is a positive correlation between BrO (DSCDs) and the particulate  $Br^-$  percentage and absolute deficiencies in the marine aerosols relative to sea salt. This indicates more  $Br^-$  release from the aerosol phase into the gas phase and its possible contribution to BrO formation in the MBL.

(3) There is a negative correlation between BrO (DSCDs) and dust Aerosols Optical Depth (AOD 865nm). This negative correlation is observed for both of the data sets used here. This could indicate some chemical processes related to dust aerosols in the MBL which seems to affect BrO negatively.

### 9.1.2 Auto-MAX DOAS measurements

The MAX-DOAS instruments can be mounted on different types of stationary and mobile platforms. The Auto-MAX-DOAS has some advantages as a platform and a tool for atmospheric trace gas measurements:

(1) Provides good spatial resolution : Auto-MAX-DOAS provides a better spatial resolution than that of Satellites : Since the spatial resolutions of satellites instruments are of order of tens of kilometers (e.g. 30x60 km for SCIAMACHY satellite instrument).

(2) Mobile : Auto-MAX-DOAS enables encircling pollution sources with measurements (e.g. power plants, industrial areas and even whole cities). Auto-MAX-DOAS also can be driven under pollution plumes to take cross-section measurements across them. These advantages don't exist in stationary ground-based instruments.

(3) Available at any time : Auto-MAX-DOAS is easy to install on a car top in less than 20 minutes and this makes it very suitable for going to detect pollution near/downwind from the source in case of any pollution event. Auto-MAX-DOAS readiness to go any time as a platform is an advantage because it does not need much logistical requirements and scheduled times for operation like airborne instruments.

(4) Economic : Much cheaper in its operation than airborne and satellite instruments.

In this work, Auto-MAX-DOAS has been successfully used to carry out the following measurements:

(a) Carry out measurements along the roads between some cities in Europe and detect  $\text{NO}_2$  along the road between them. Passing several different environments: heavy traffic, industrial and urban areas.

These measurements covered a regional/continental scale.

(b) Encircle industrial areas of significant  $\text{NO}_2$  emissions. The Auto-MAX-DOAS could detect and quantify the dSCDs of emitted  $\text{NO}_2$  in areas upwind and downwind from the source. These measurements were carried on in the Rhein-Neckar Valley area.

(c) Carry out measurements of a big plume caused by a big fire which covered large regions of Europe (see below).

These measurements covered regional/continental scale.

The common factor in all above measurements is the ability to reach the polluted areas and perform measurements around them and across the trace gas plume once or more.

### **Brussels-Heidelberg measurements**

Elevated  $\text{NO}_2$  VCDs north east of Aachen because of Weisweiler power plant which works with fossil fuel (hard coal and oil/gas). Also elevated  $\text{NO}_2$  VCDs near from all the populated cities in Europe along the road and also in the Rhein Valley. The two cities of departure and destination of this trip (Brussels and Heidelberg respectively) also had elevated  $\text{NO}_2$  VCDs. These results could be tested against satellite data too from SCIAMACHY and OMI and the comparison showed a good agreement in general. Taking into account that the satellite pixel is several kilometers in dimensions and that Auto-MAX DOAS measurements are more spatially resolving.

### **Encircling Mannheim-Ludwegshaven Area**

Elevated  $\text{NO}_2$  VCDs were found downwind from this area during several cycles made around it (two and four on two separate days).

### **Hemel Hempstead Fire**

Large area were found to be covered with elevated  $\text{NO}_2$  VCDs (of order of 100 km) at the northern French coast. Back trajectories and information from modeling support the assumption that the detected elevated  $\text{NO}_2$  VCDs were most probably from the big fire at Buncefield Oil Depot near from London. It is difficult to make a very surely attribution for the plume but several evidences were supporting this assumption (wind direction, modeling information and that the plume was trapped a loft which allows it to travel faster to the north coast of France).

### **9.1.3 DANDELIONS campaign**

It was mainly a validation campaign for the satellite instruments OMI and SCIAMACHY. So one main issue of this campaign was cross comparisons of ground-based instruments together besides comparison with satellite data too. Comparisons with other MAX-DOAS and with satellites showed good agreement in general between the detected  $\text{NO}_2$  VCDs.

## 9.2 Outlook

Through the course of this work, interesting results were obtained and they are opening opportunity for further investigation as follows:

### **The Polarstern Campaign:**

The BrO correlations investigated in this part are interesting to explore more in the future with much bigger statistical size of data. These correlation studies can be a frame for further studies in future with more experimental data and also more radiative transfer modeling.

Also the exceptional availability of quality meteorological data is one of the very good points about using Polarstern meteorological data as an input to these studies. This excellent capability of Polarstern gives an unprecedented set of meteorological data those could be used as input not only for correlation studies purpose, but as inputs for the radiative transfer too.

From the experience gained during Polarstern campaign data analysis and modeling, it became clear that the information about the cloud cover, ceiling and the different groups of low, middle and high clouds could be a very useful input for radiative transfer modeling.

Combining this with using the other tools used in this work (such as HYSPLIT) could give much better inputs for deeper analysis and interpretation of the results. So it is recommended to do the same study on a bigger experimental data sample (five years for example).

### **Auto-MAX DOAS measurements:**

Measurements using this excellent tool within the frame of this study was only for few days but the scientific outcome was interesting and giving a good insight about pollution with NO<sub>2</sub>.

Further measurements and more repeated measurements around the same sources for an extended time period will give an insight about the seasonal effects of emissions/dispersion of plumes and also about the possible variations in emissions during the year. Namely industrial areas like Mannheim-Ludwigshafen are excellent candidates for such a study.

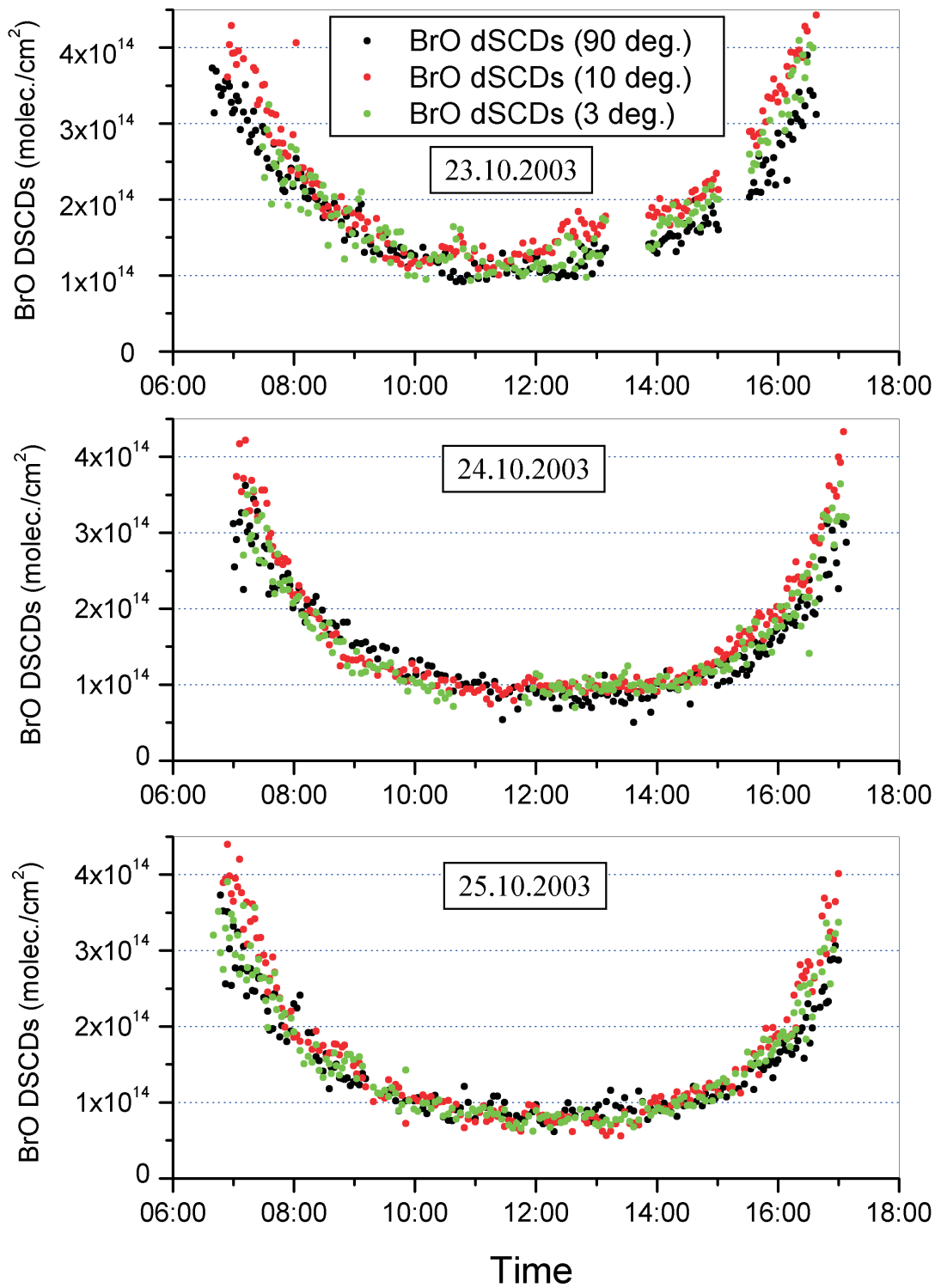
Also regular measurements would have a much bigger change of comparison with satellite data. Clouds and overpasses/coverage are major problems about the ability to compare ground-based measurements to satellite measurements.

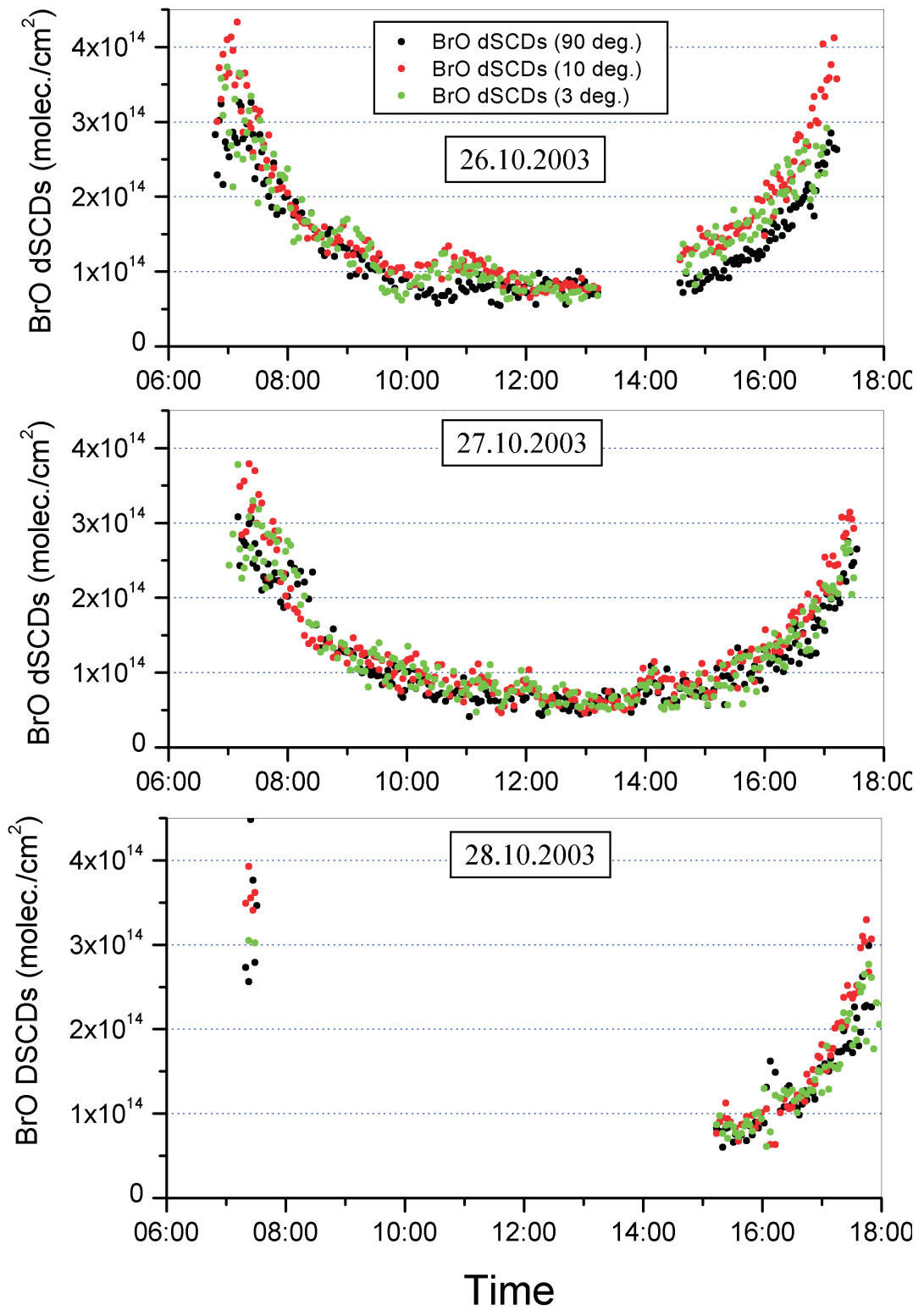


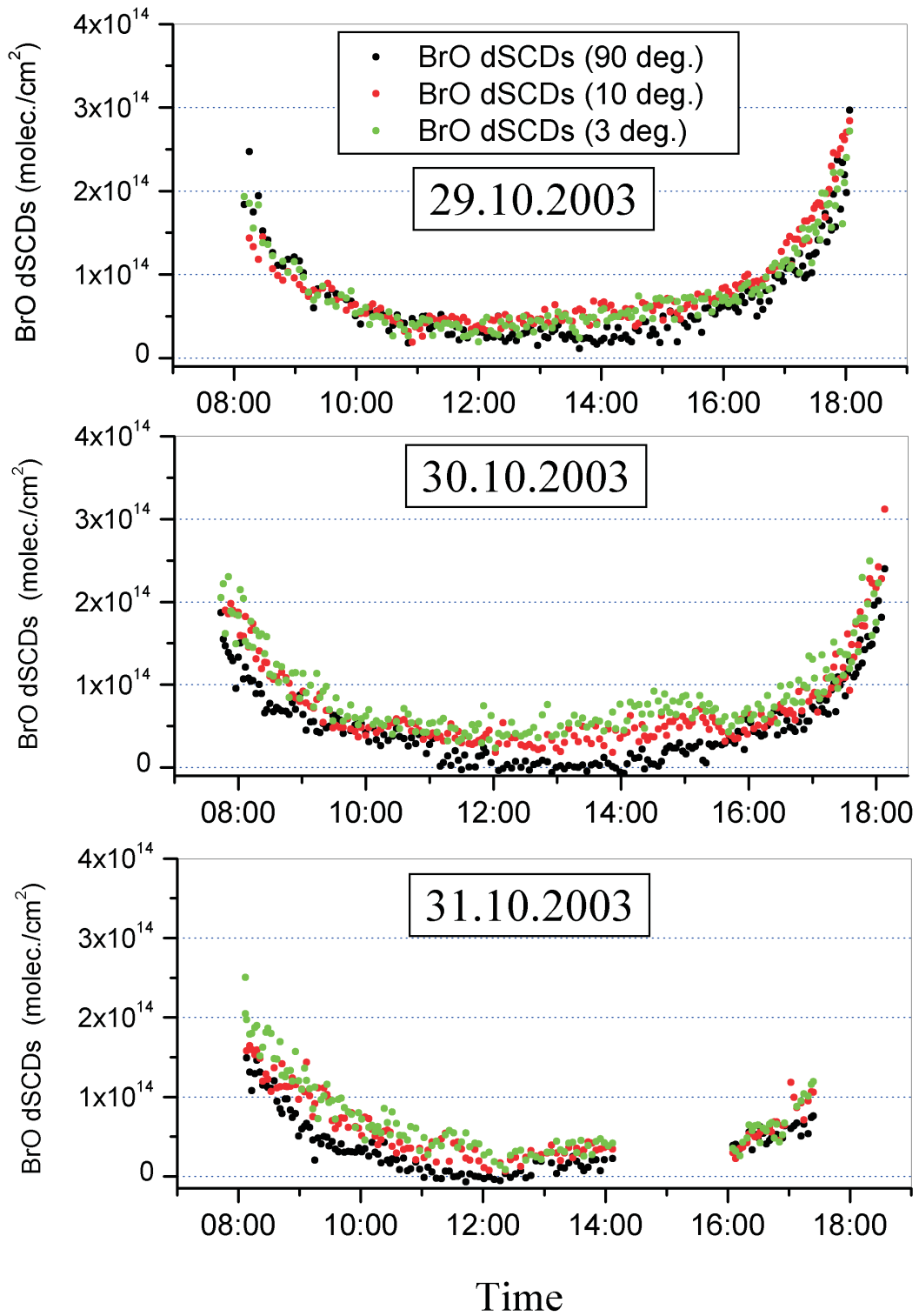
# Appendix A

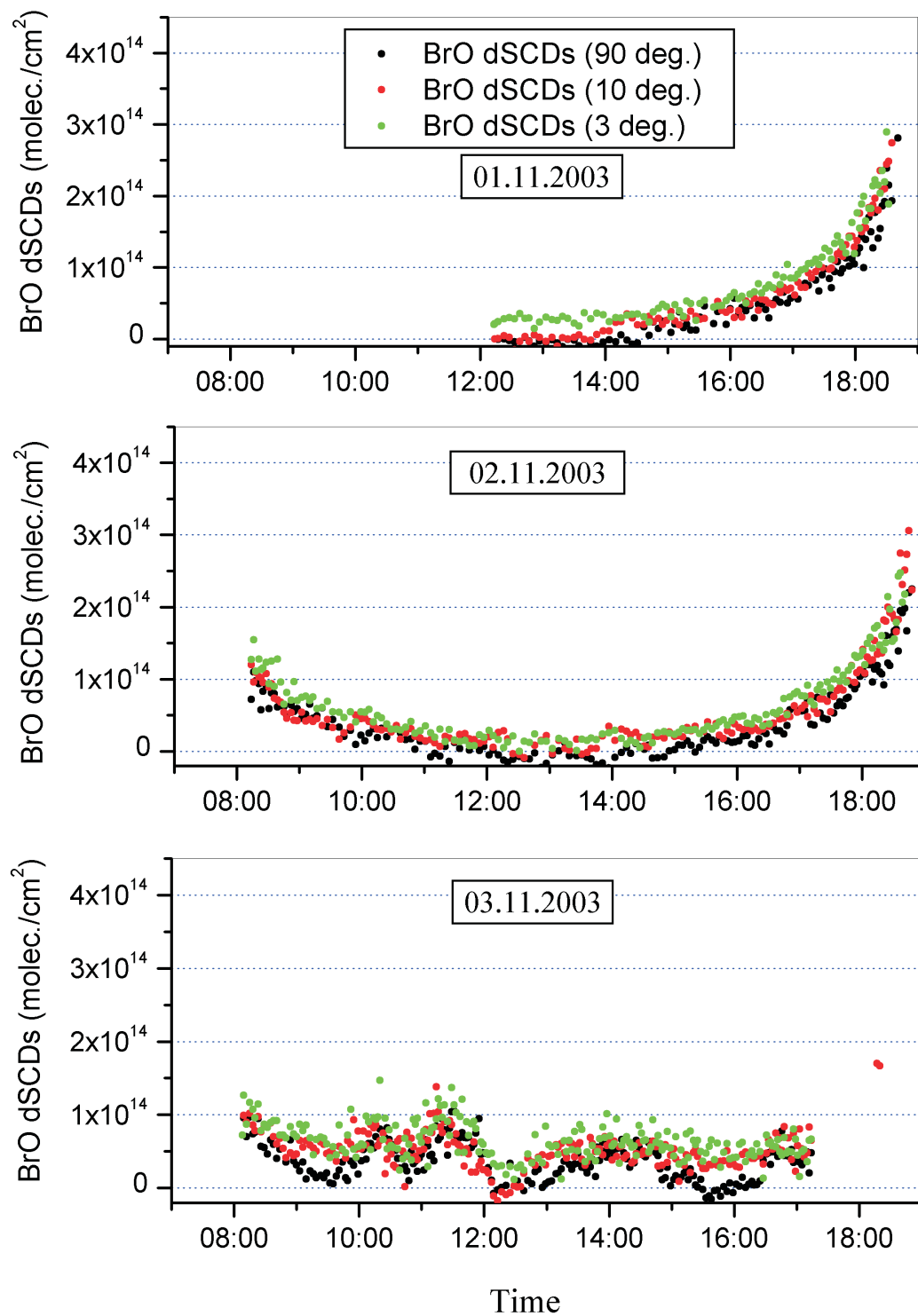
## **BrO dSCDs time series from the MAX-DOAS on board of the Polarstern RV**

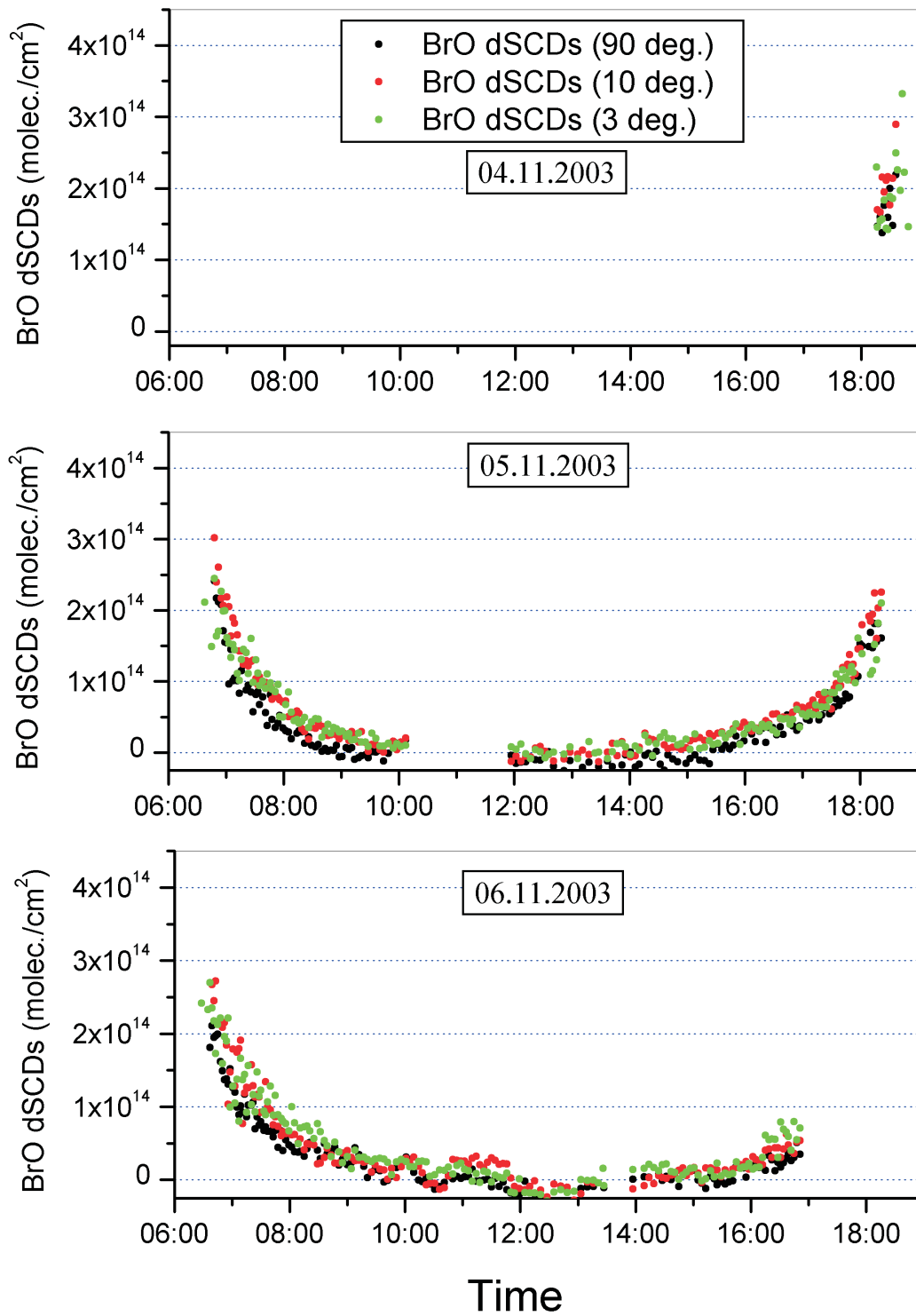
The following figures show the BrO dSCDs time series of the MAX-DOAS instrument on board of the Polarstern RV between 23.10.2003 and 14.11.2003.

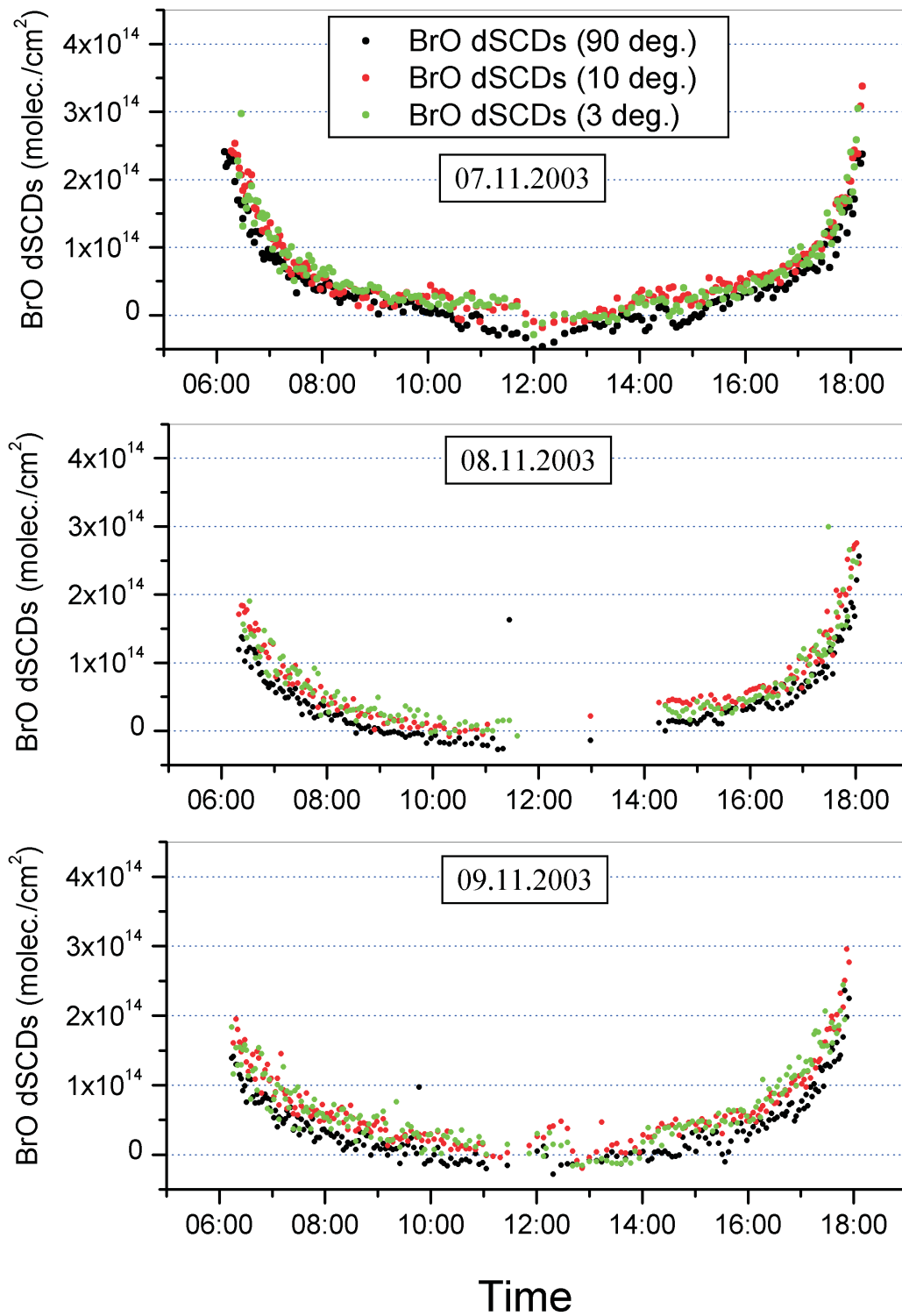


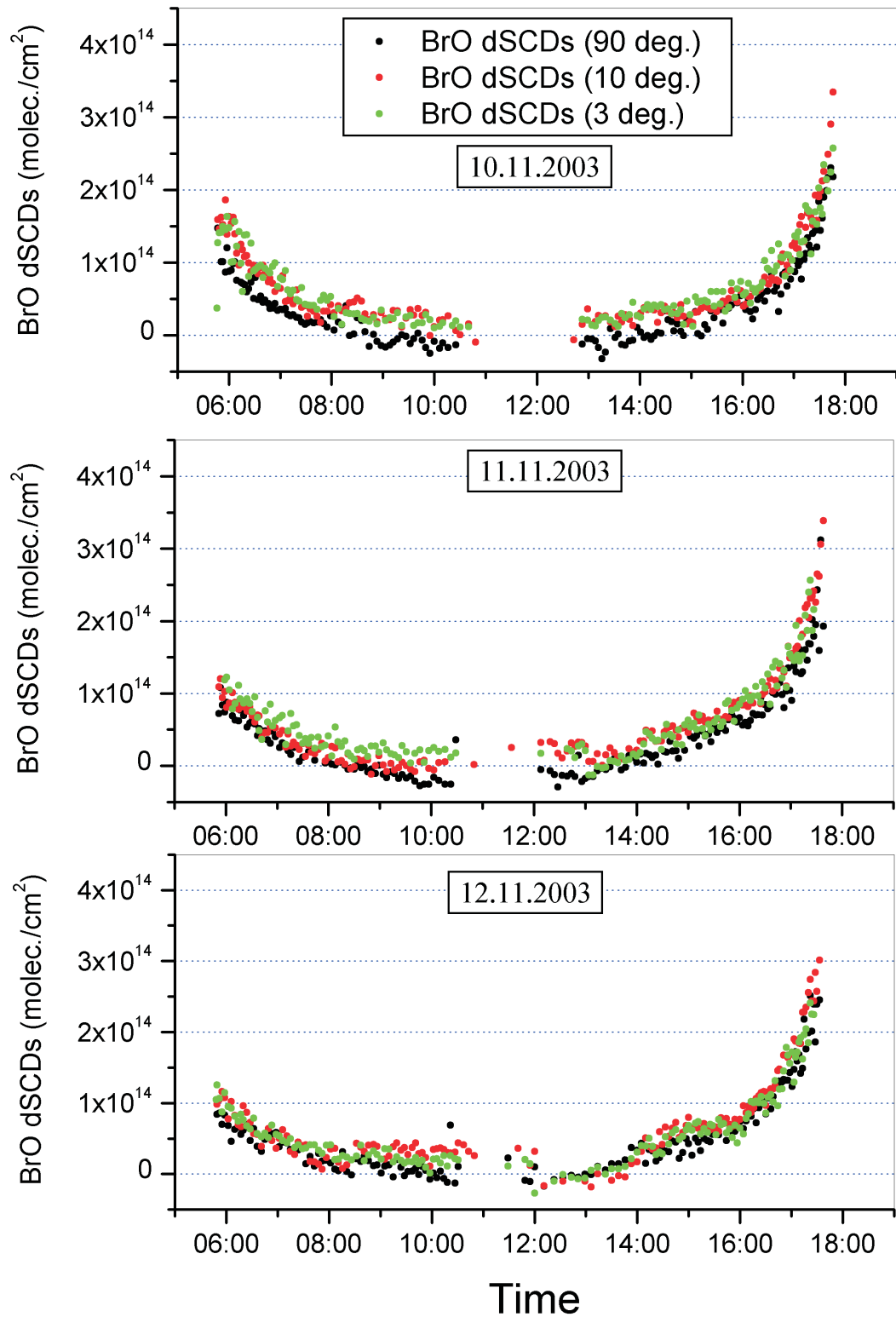








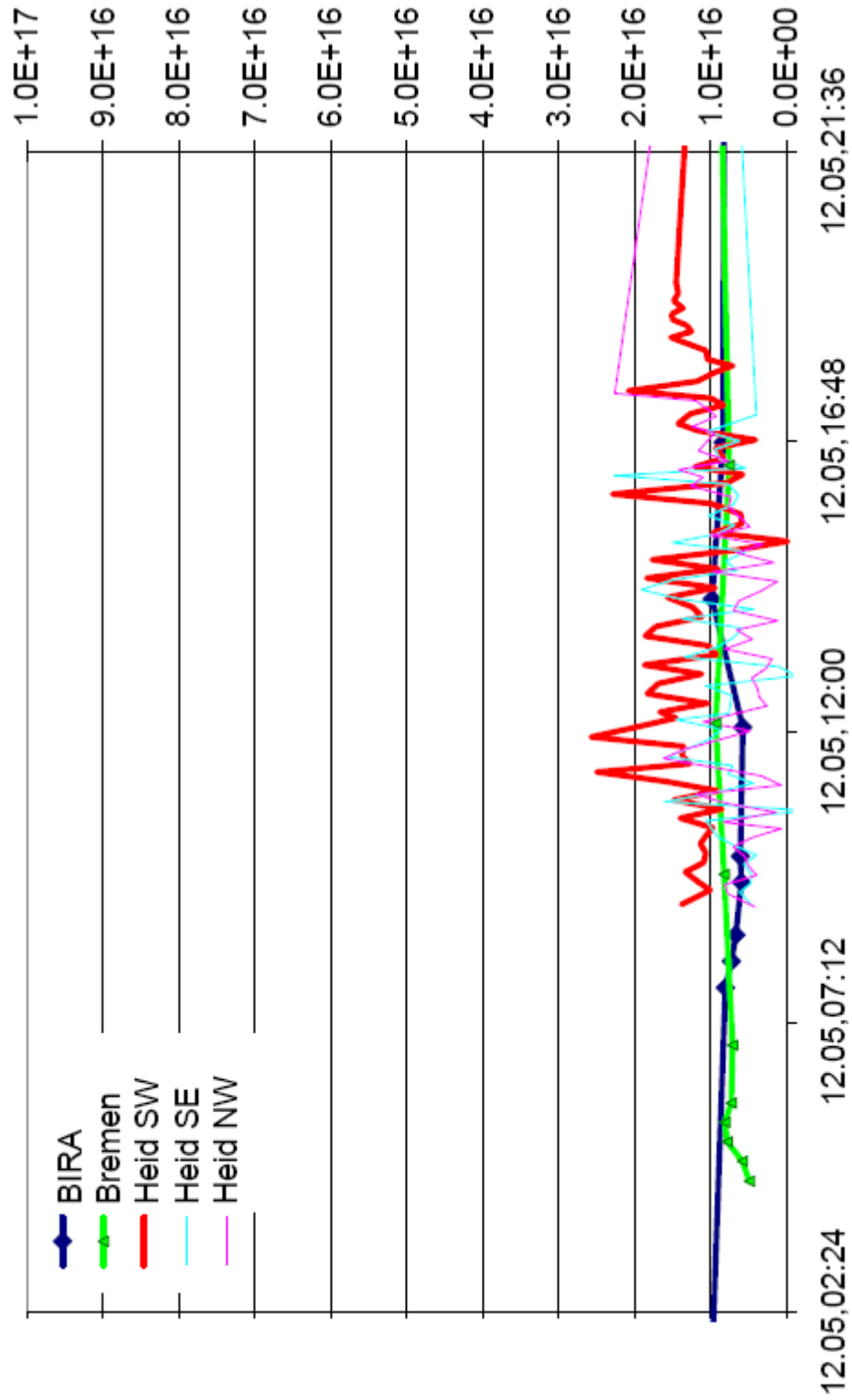


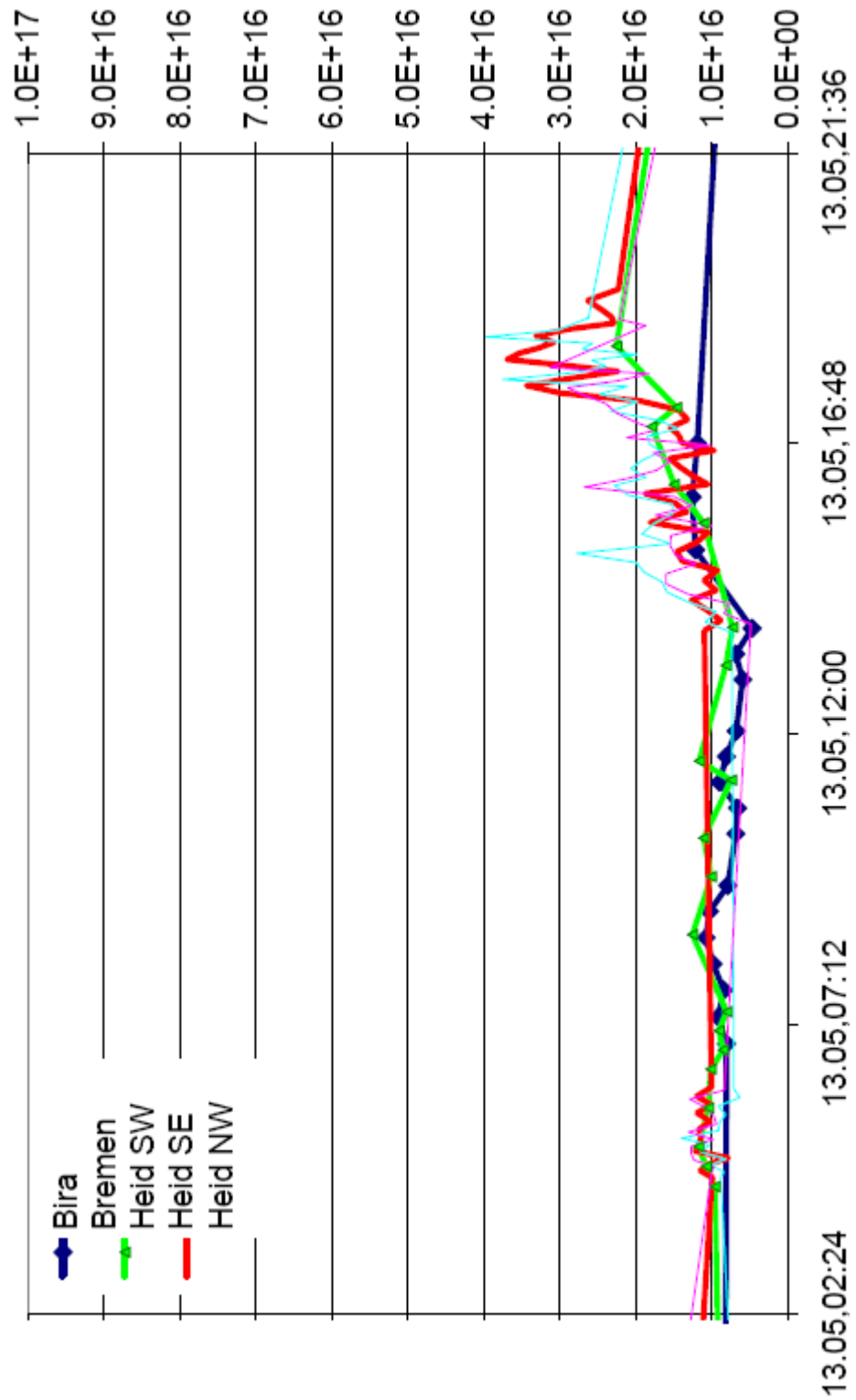


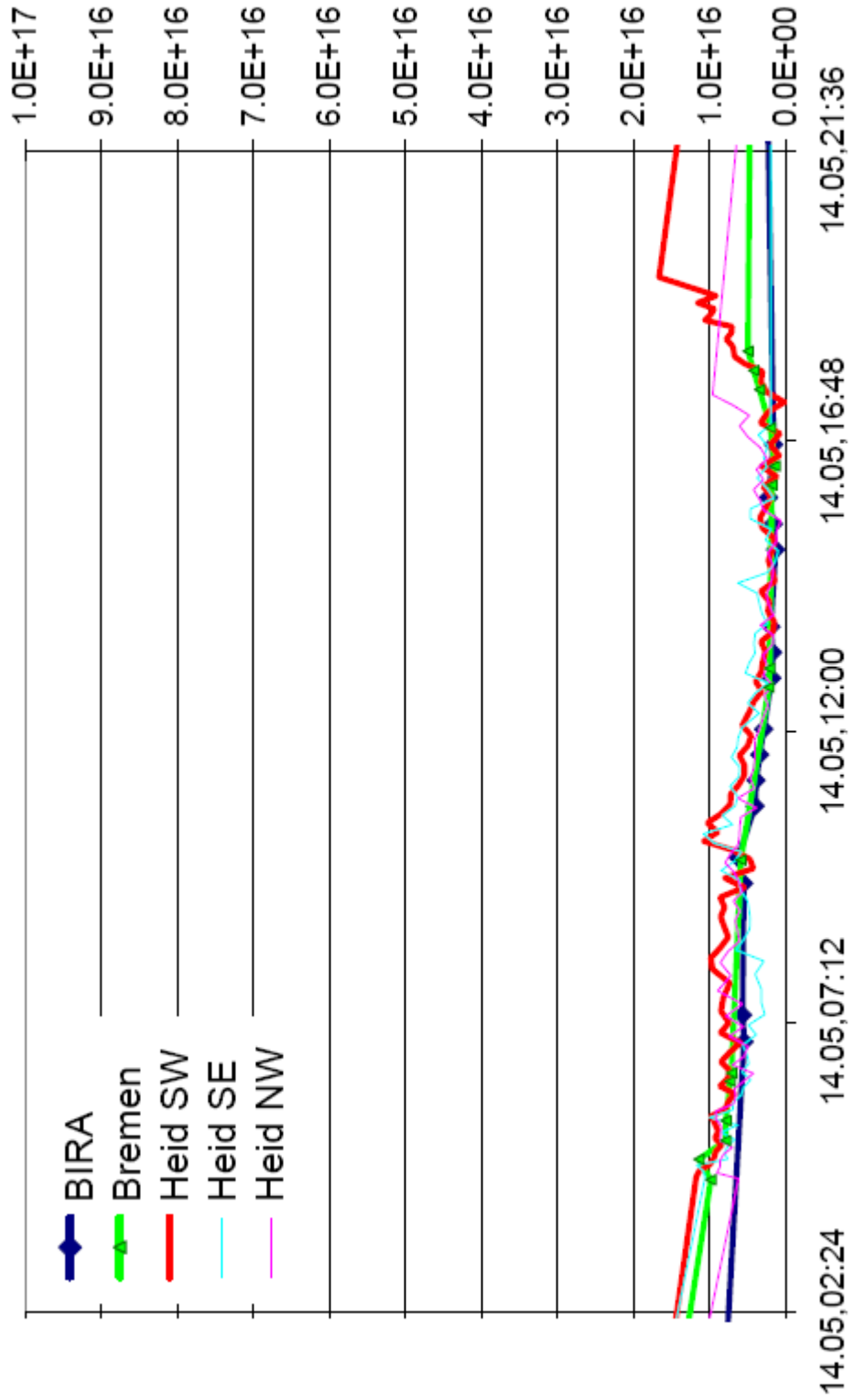
# Appendix B

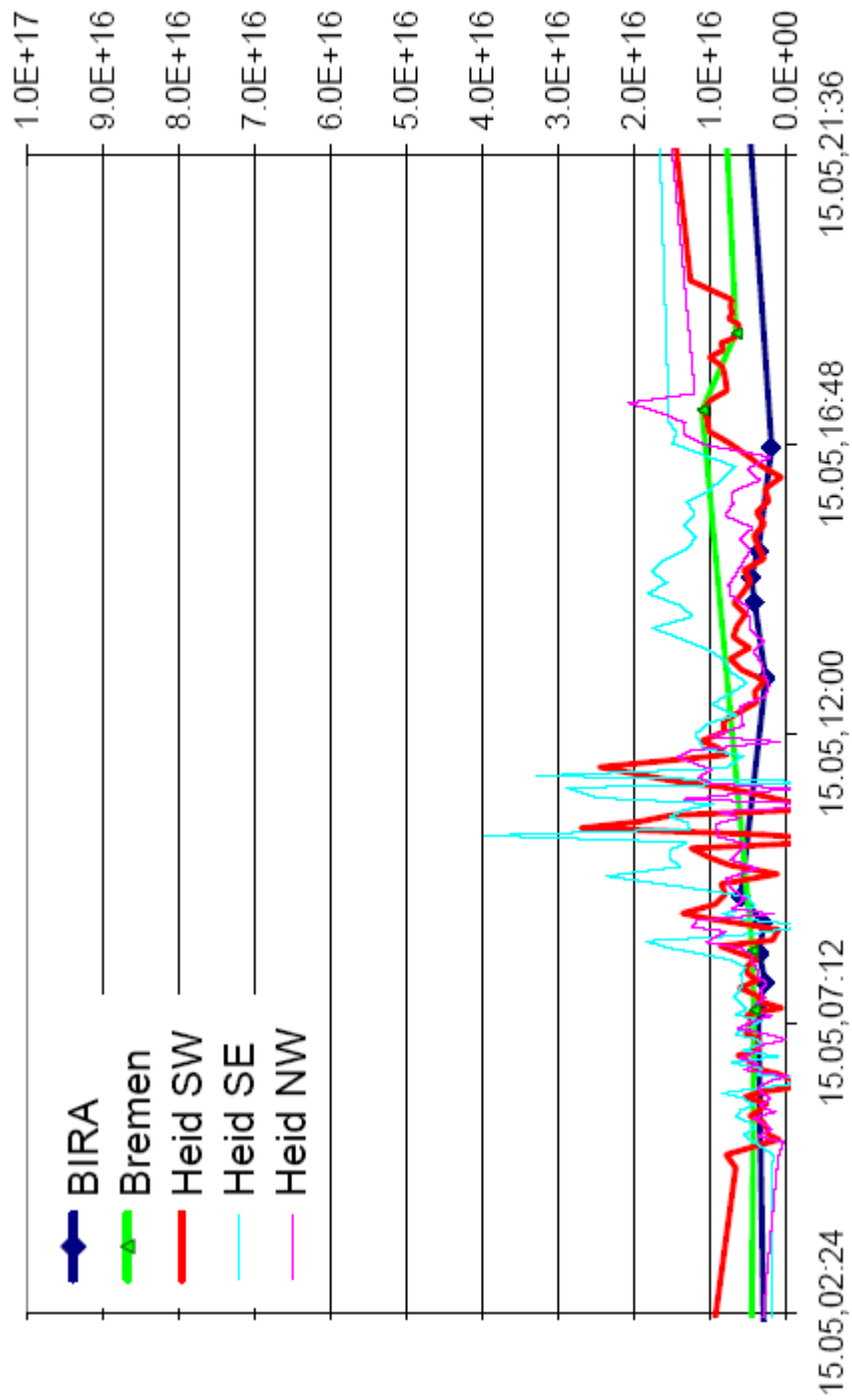
## **NO<sub>2</sub> VCDs Comparisons between MAX-DOAS Instruments**

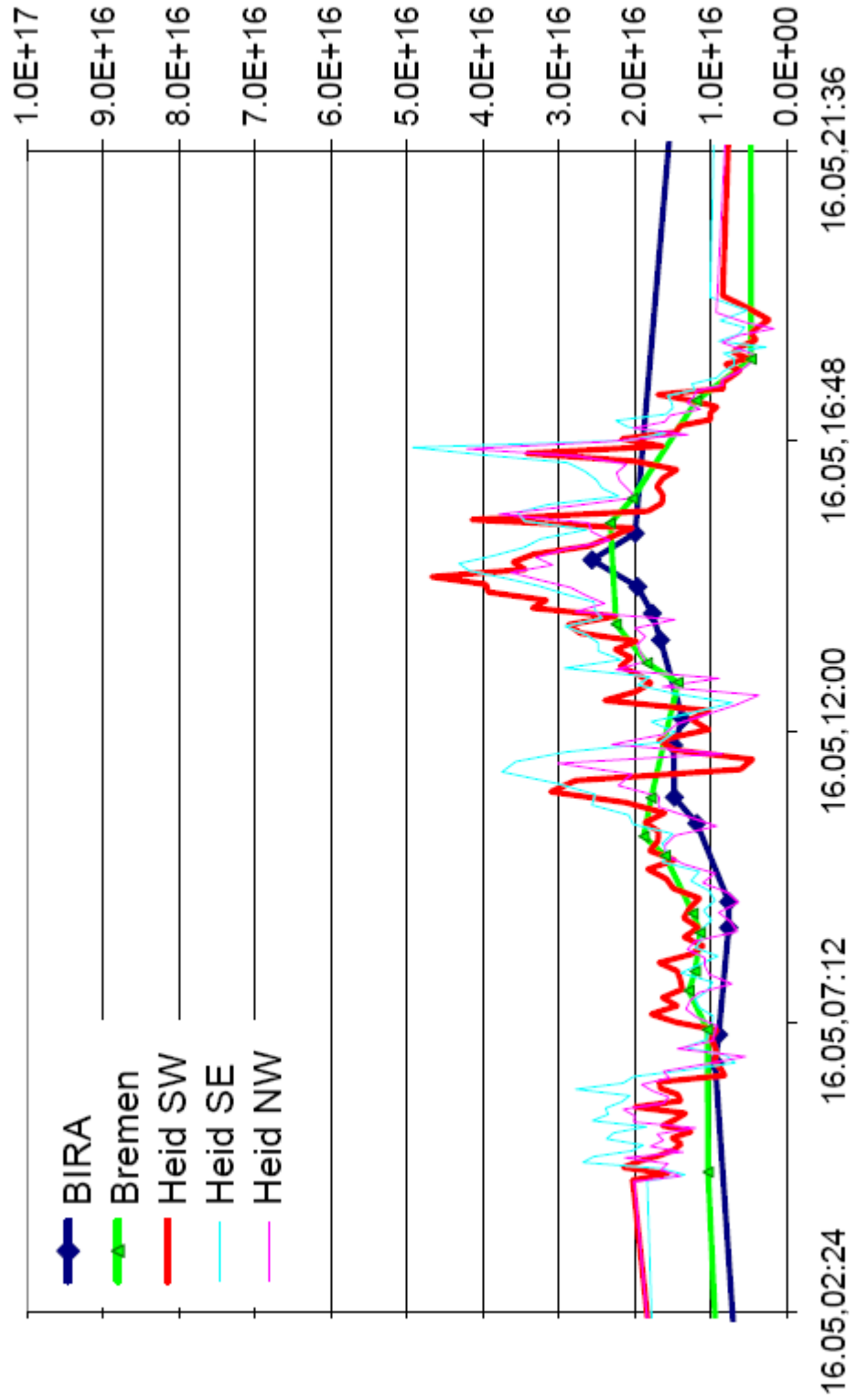
The following figures show the NO<sub>2</sub> VCDs time series of the different MAX-DOAS instruments: The Heidelberg three telescopes, The Bremen MAX-DOAS instrument and the BIRA MAX-DOAS instrument.

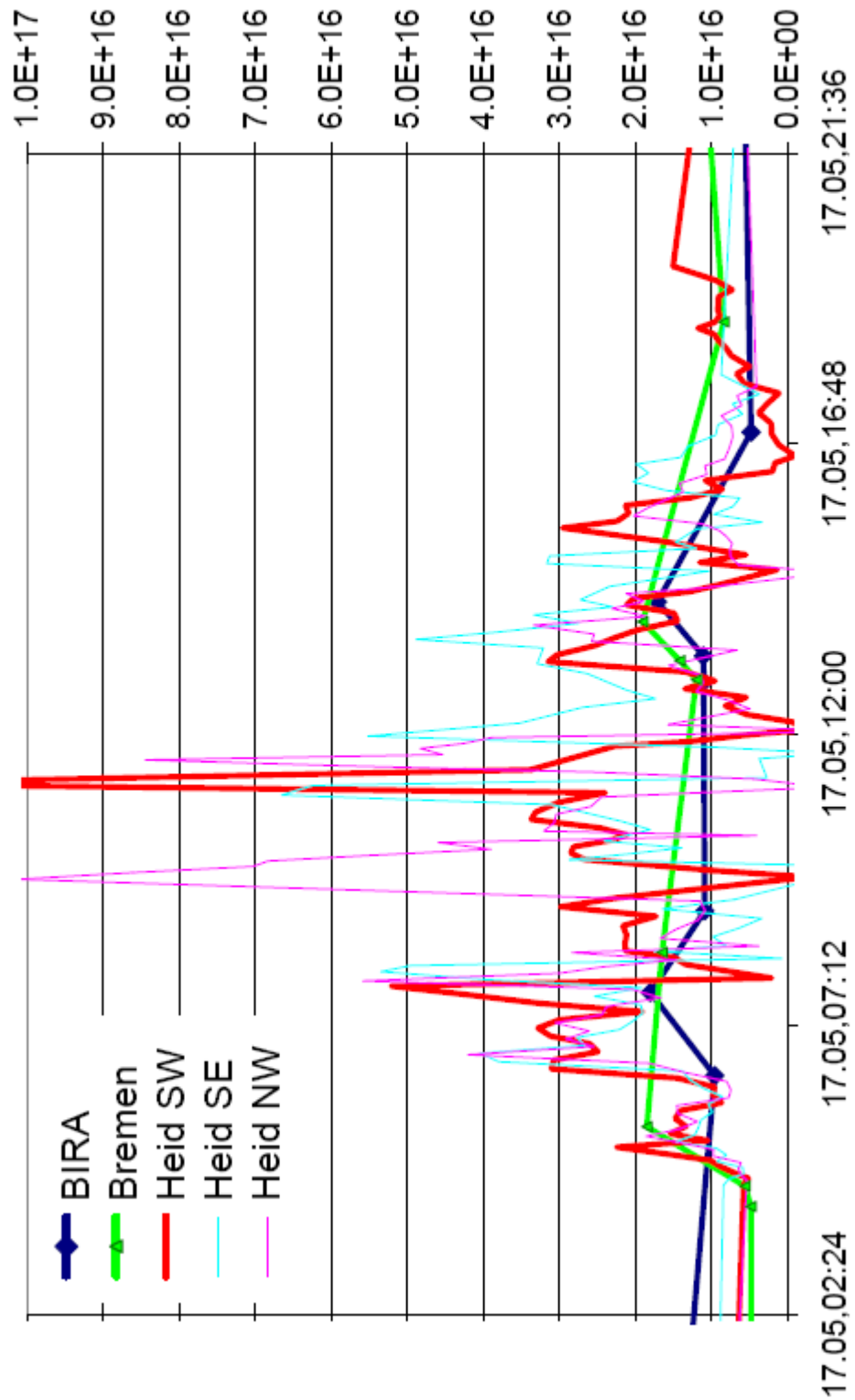


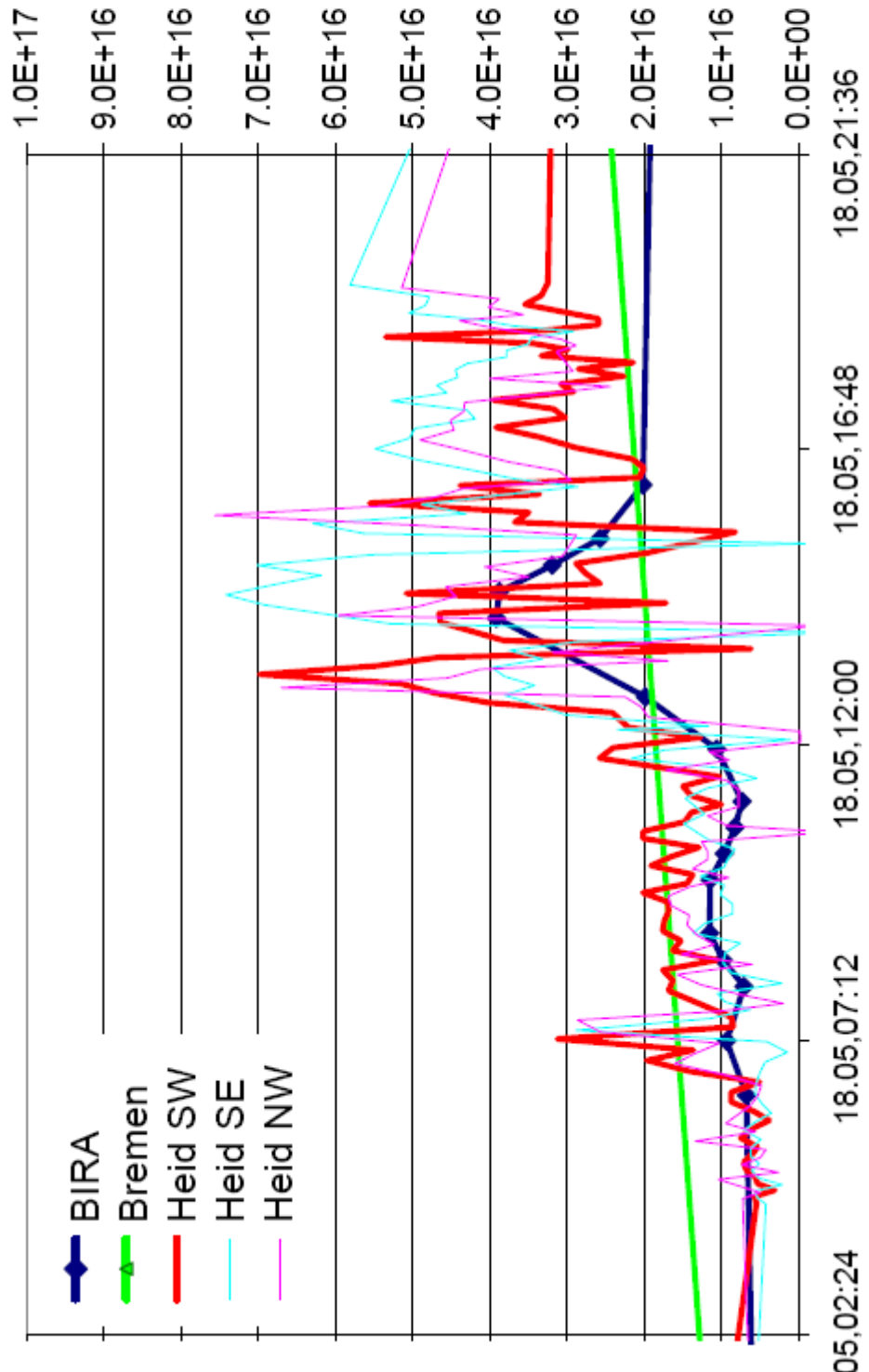


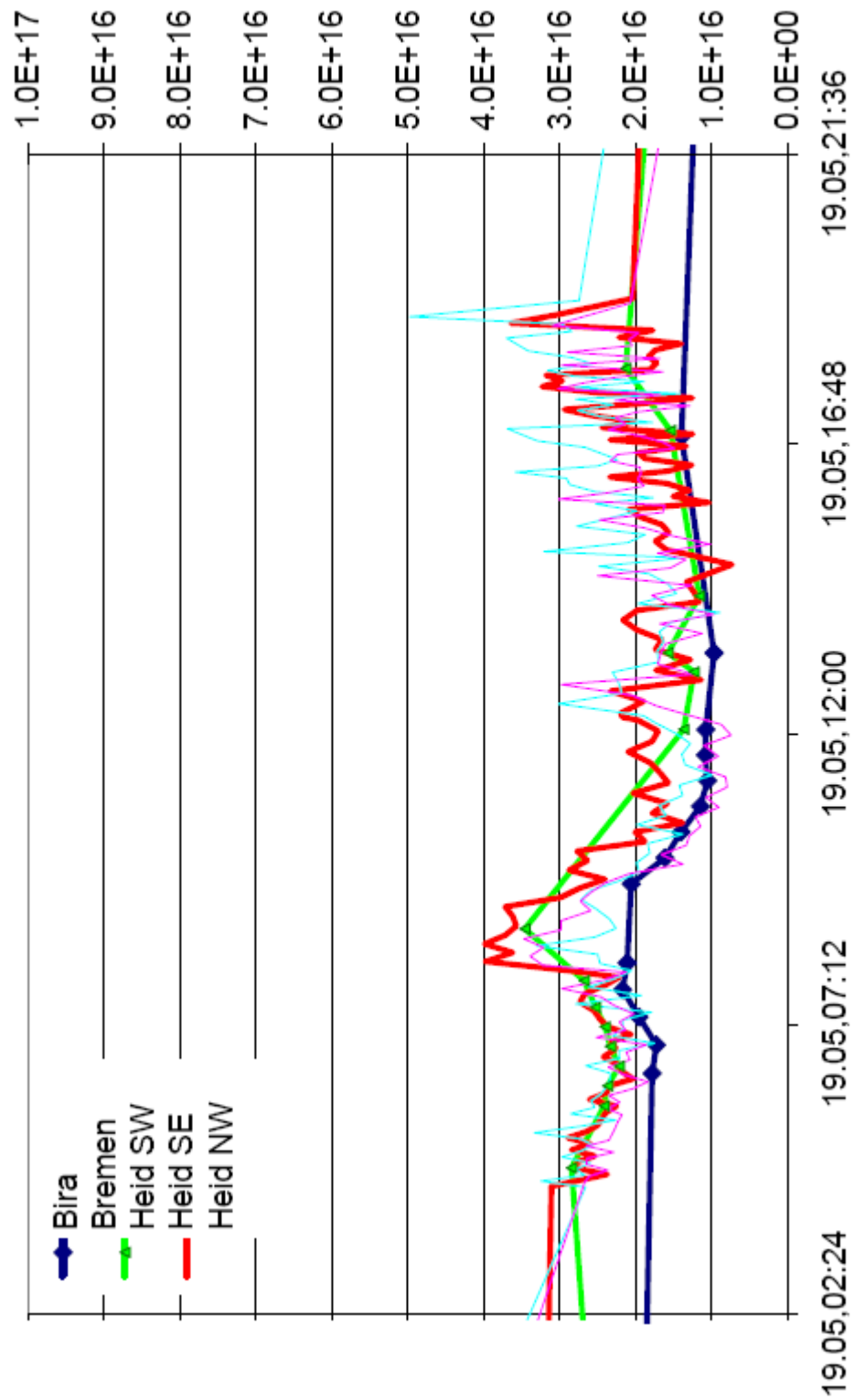


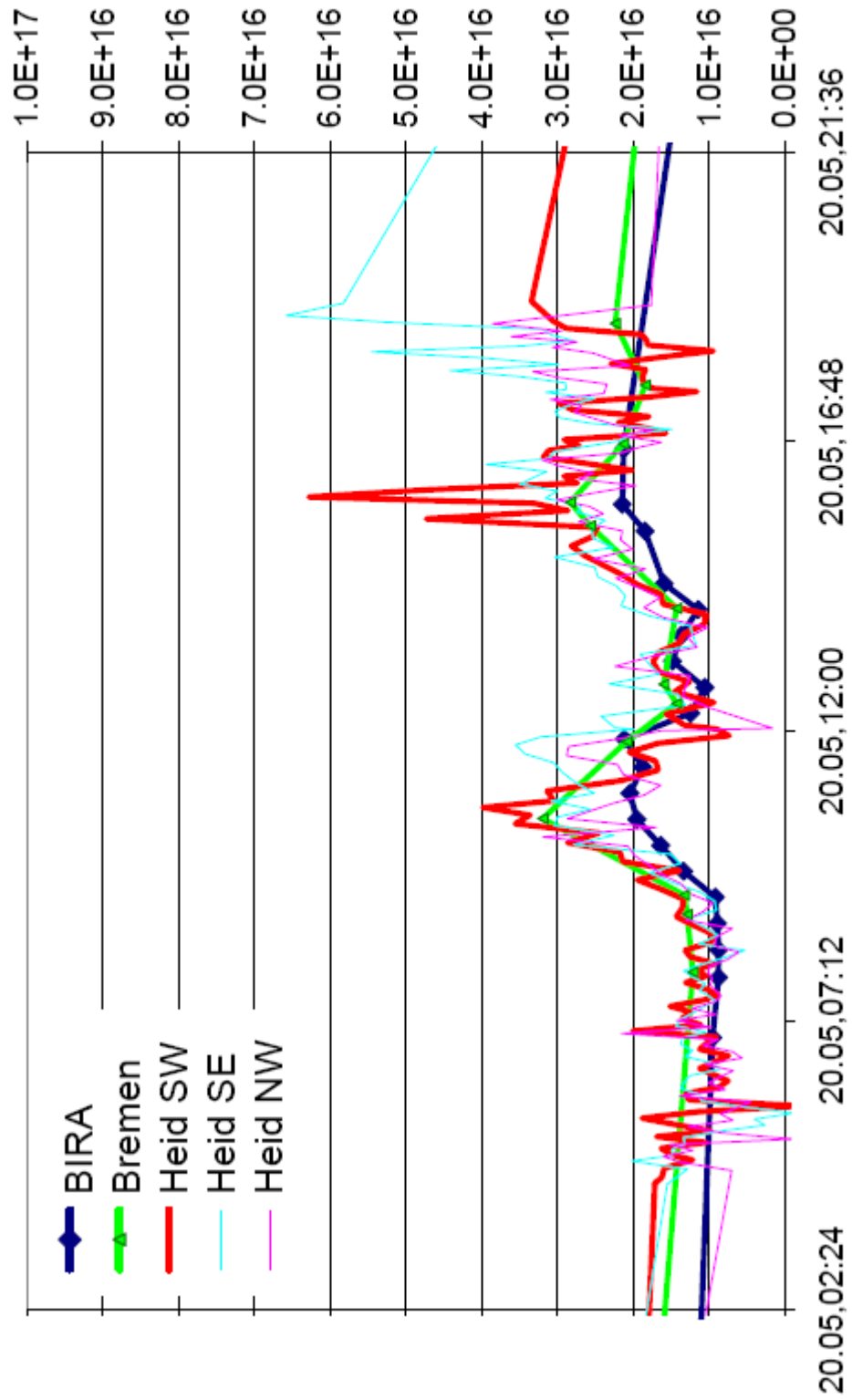


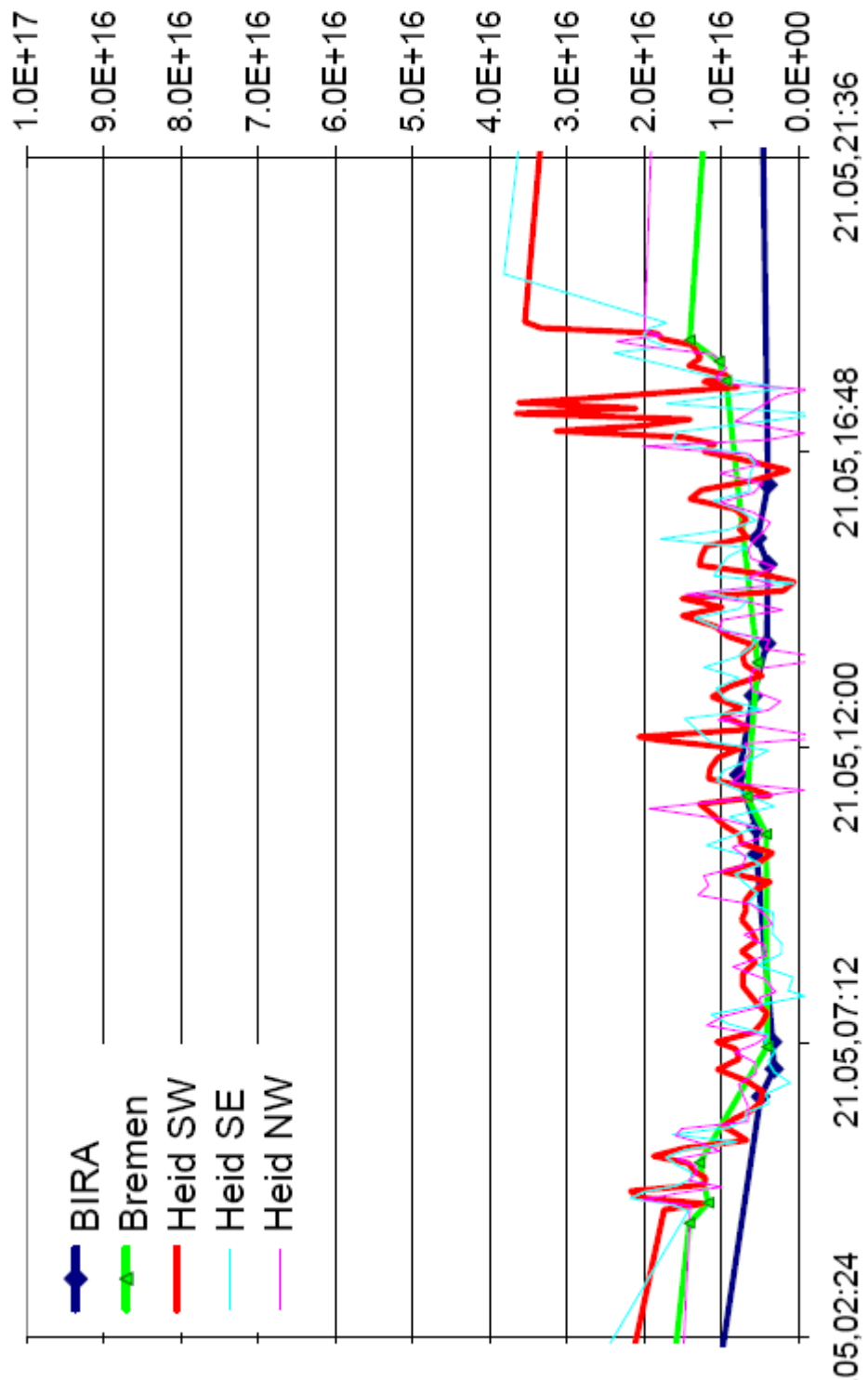


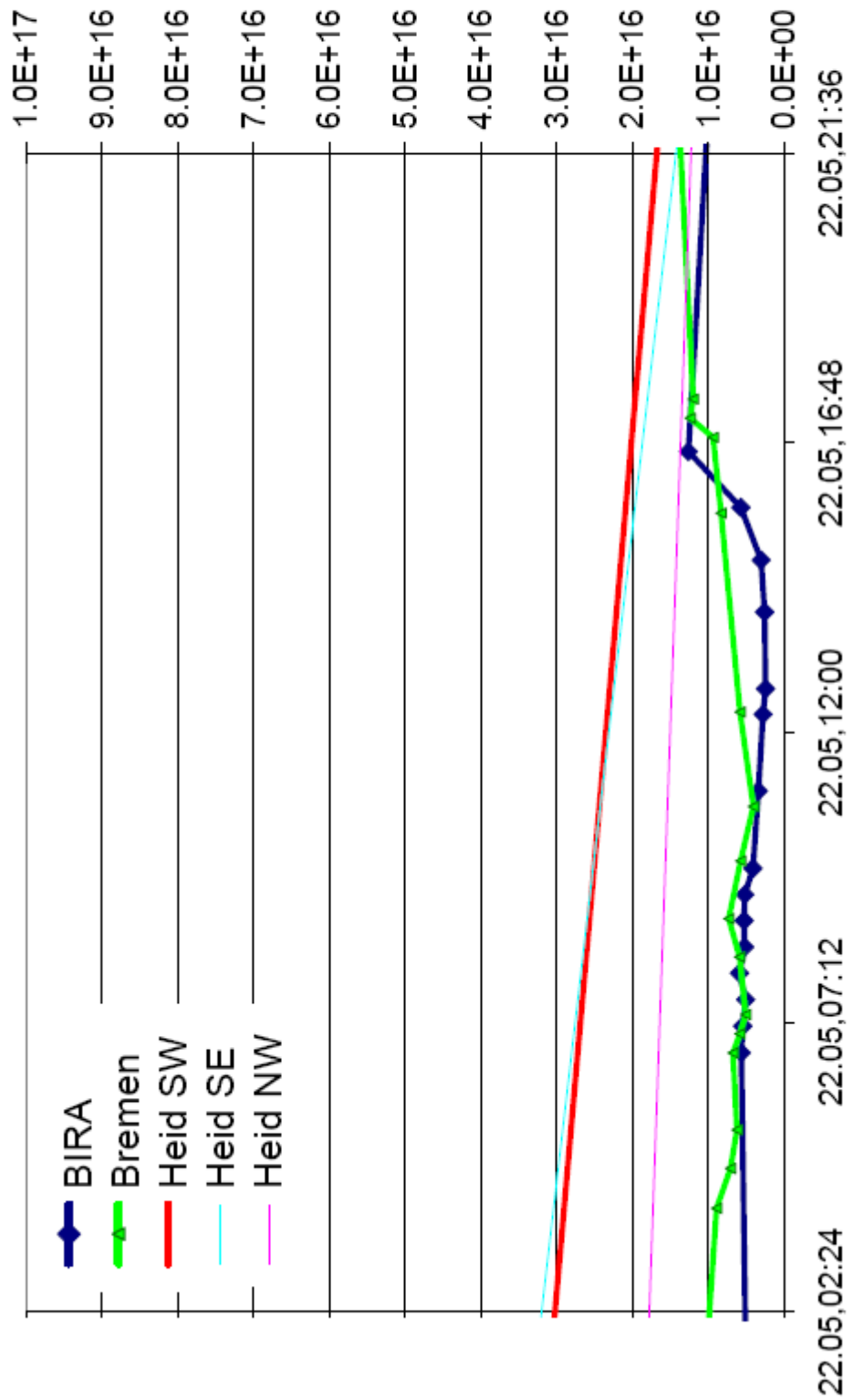


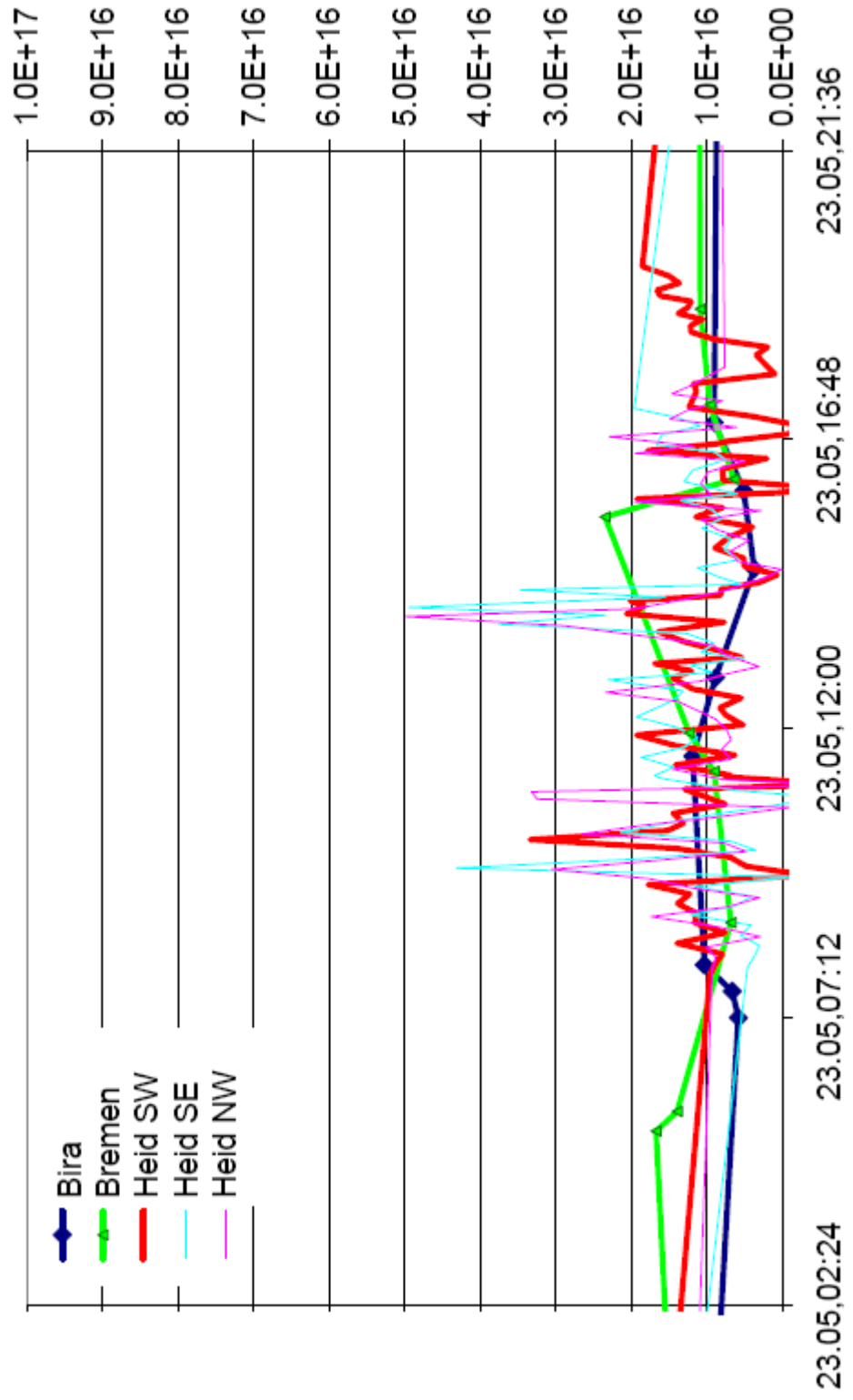


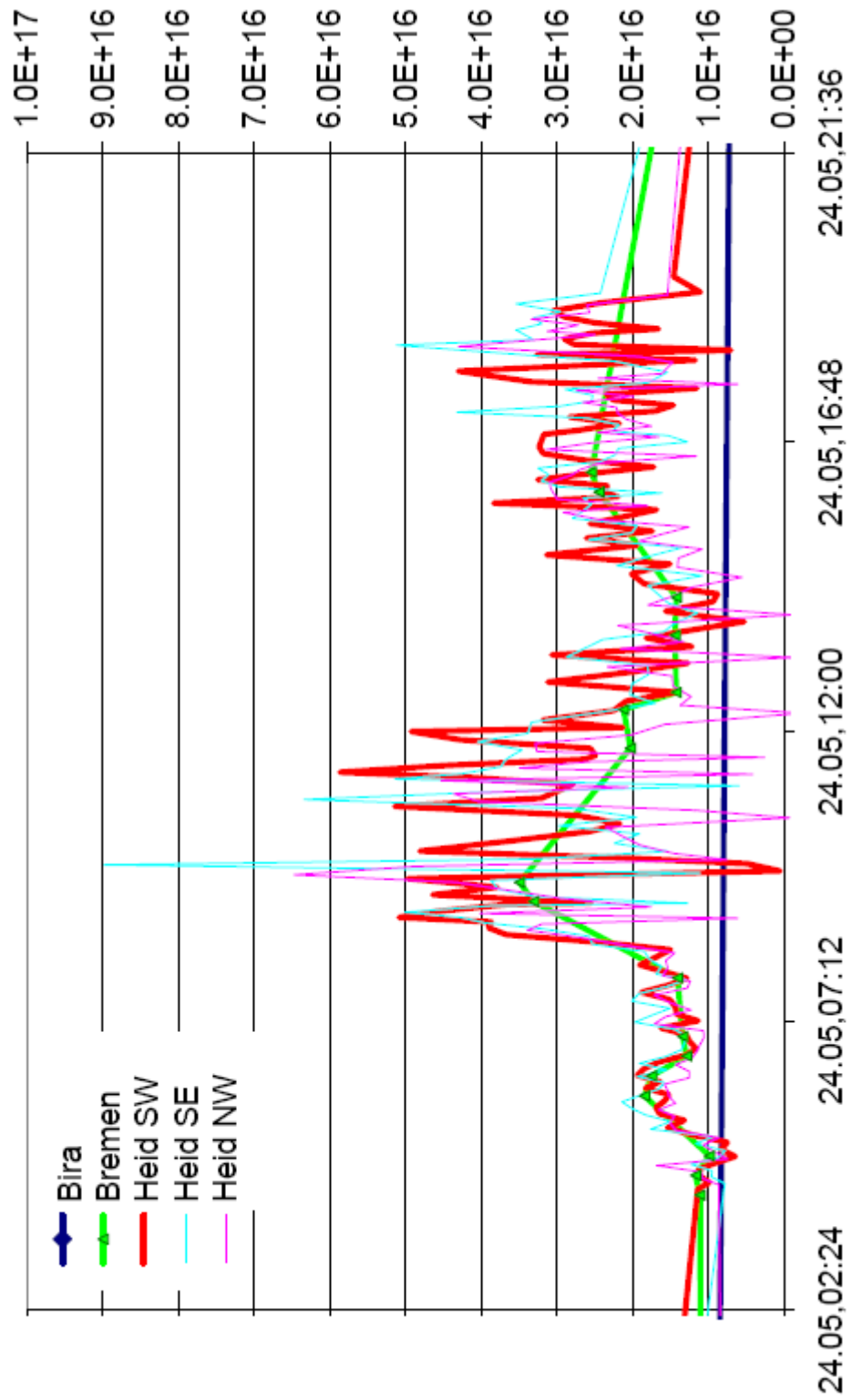


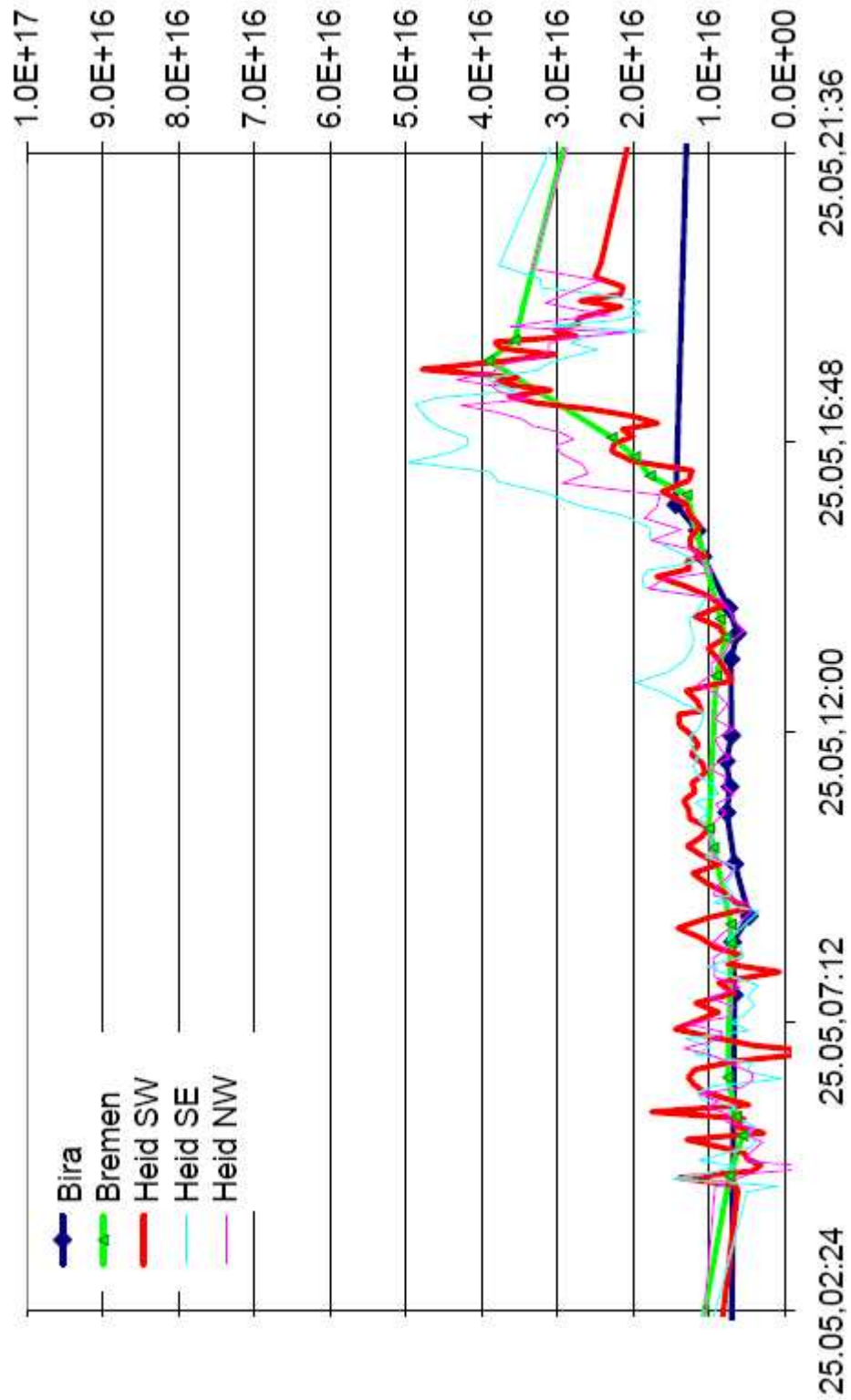


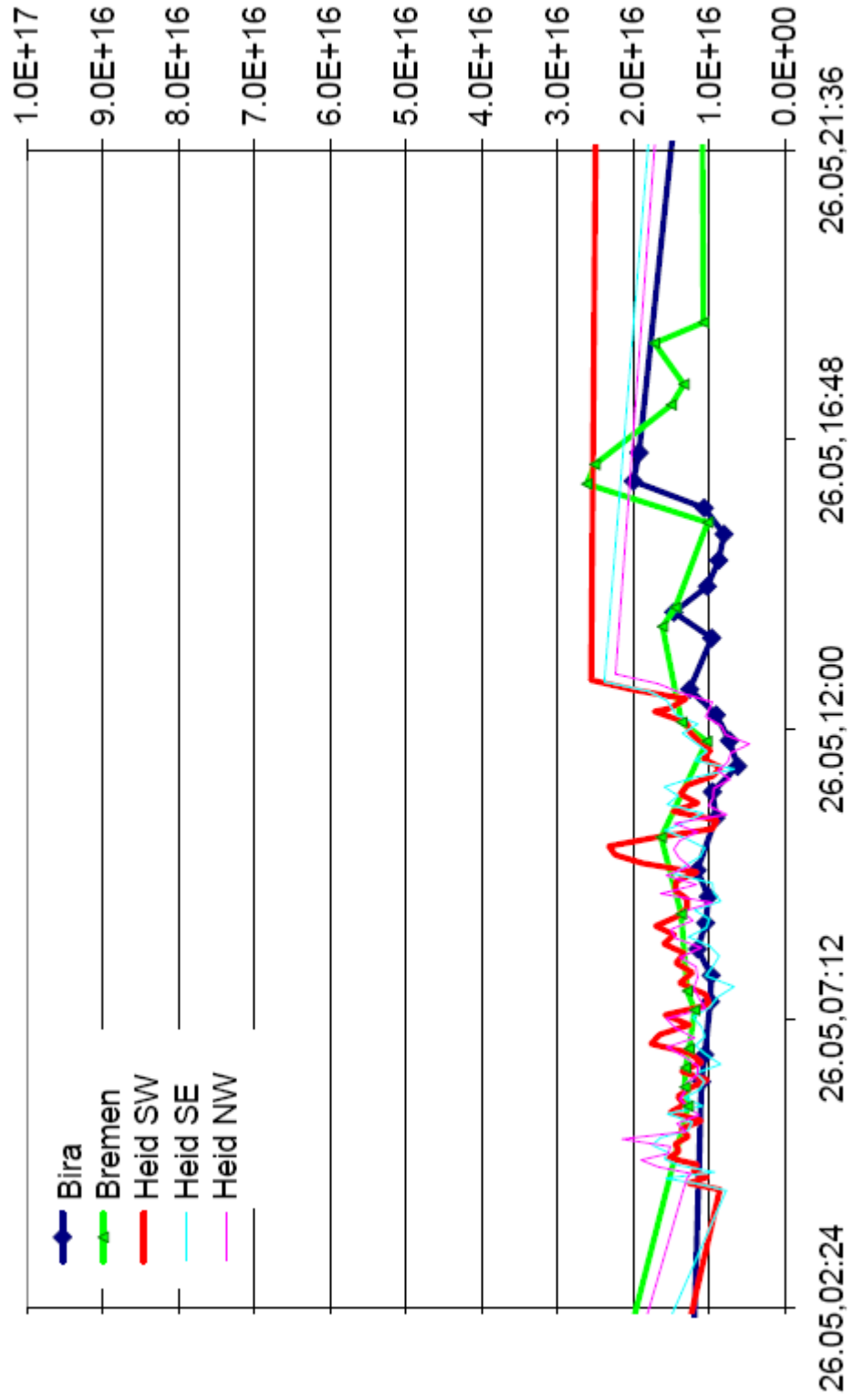


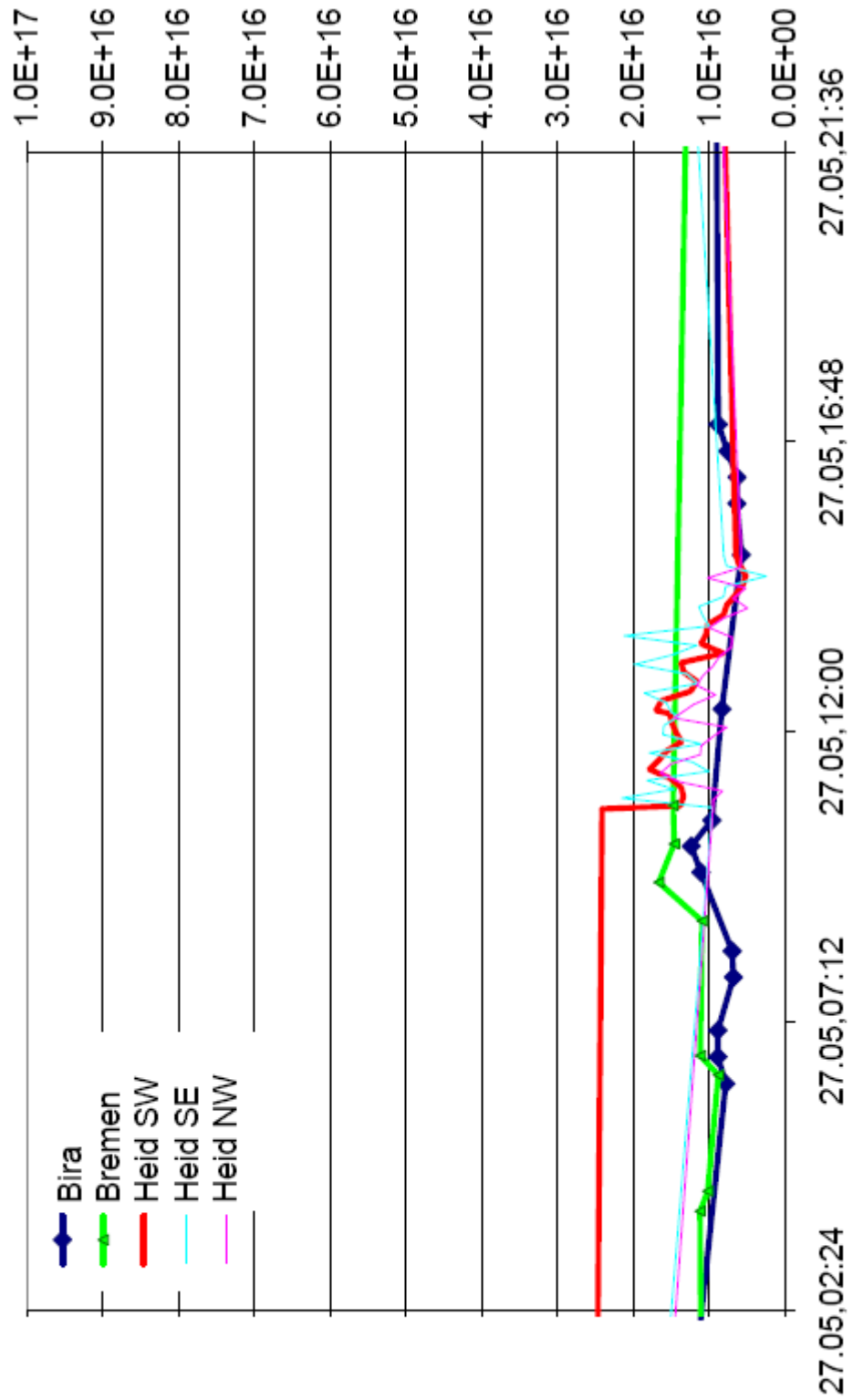


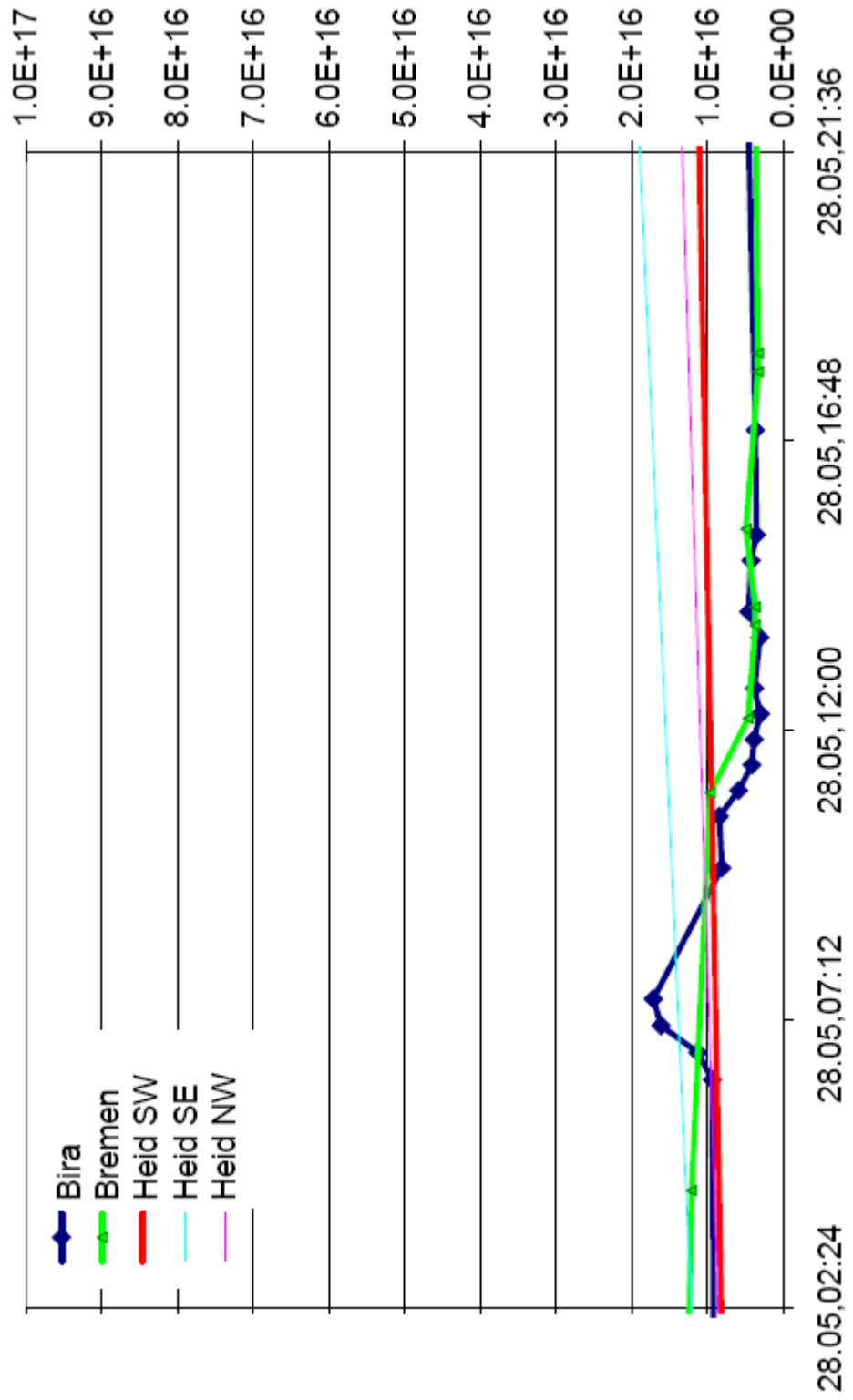


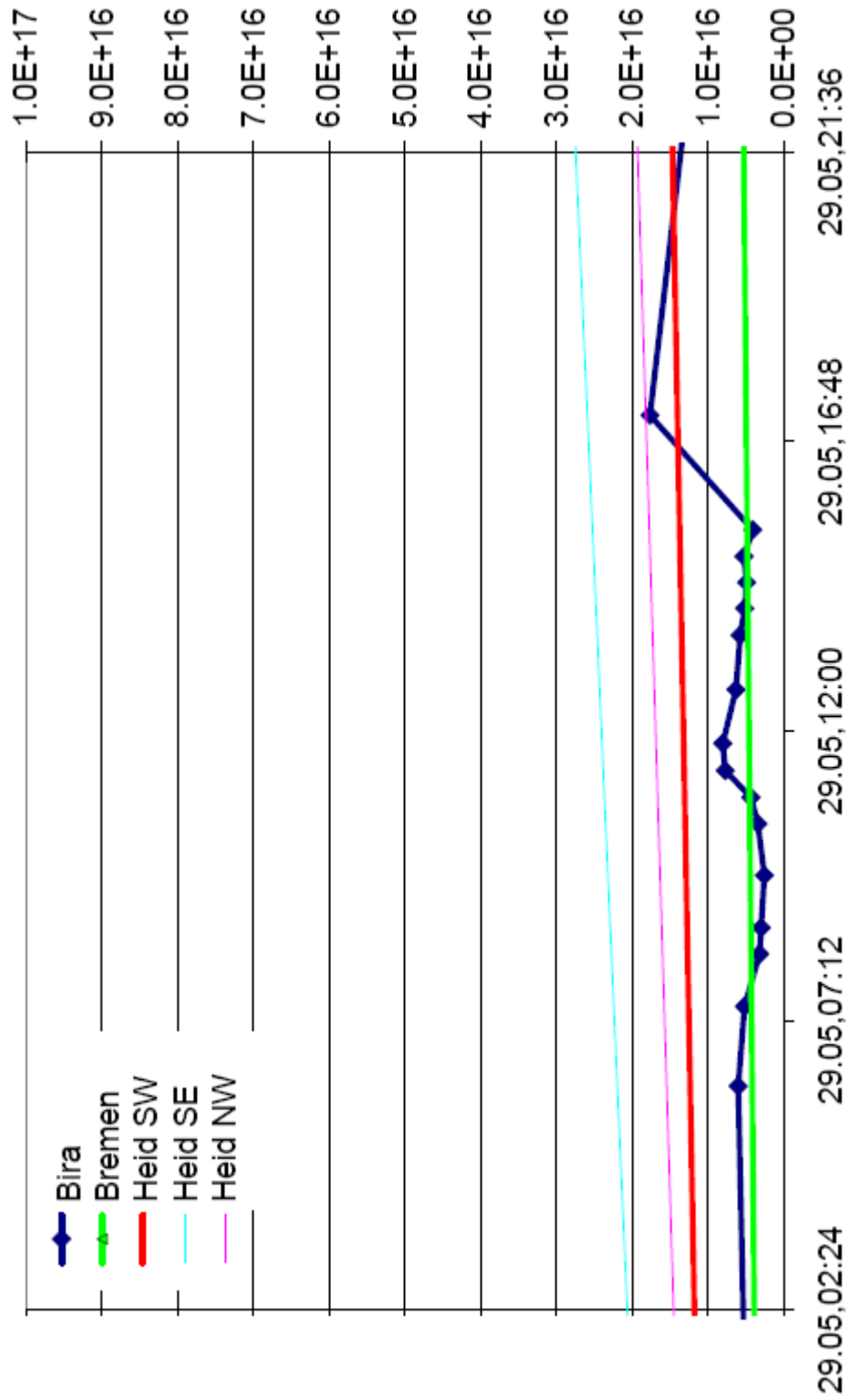


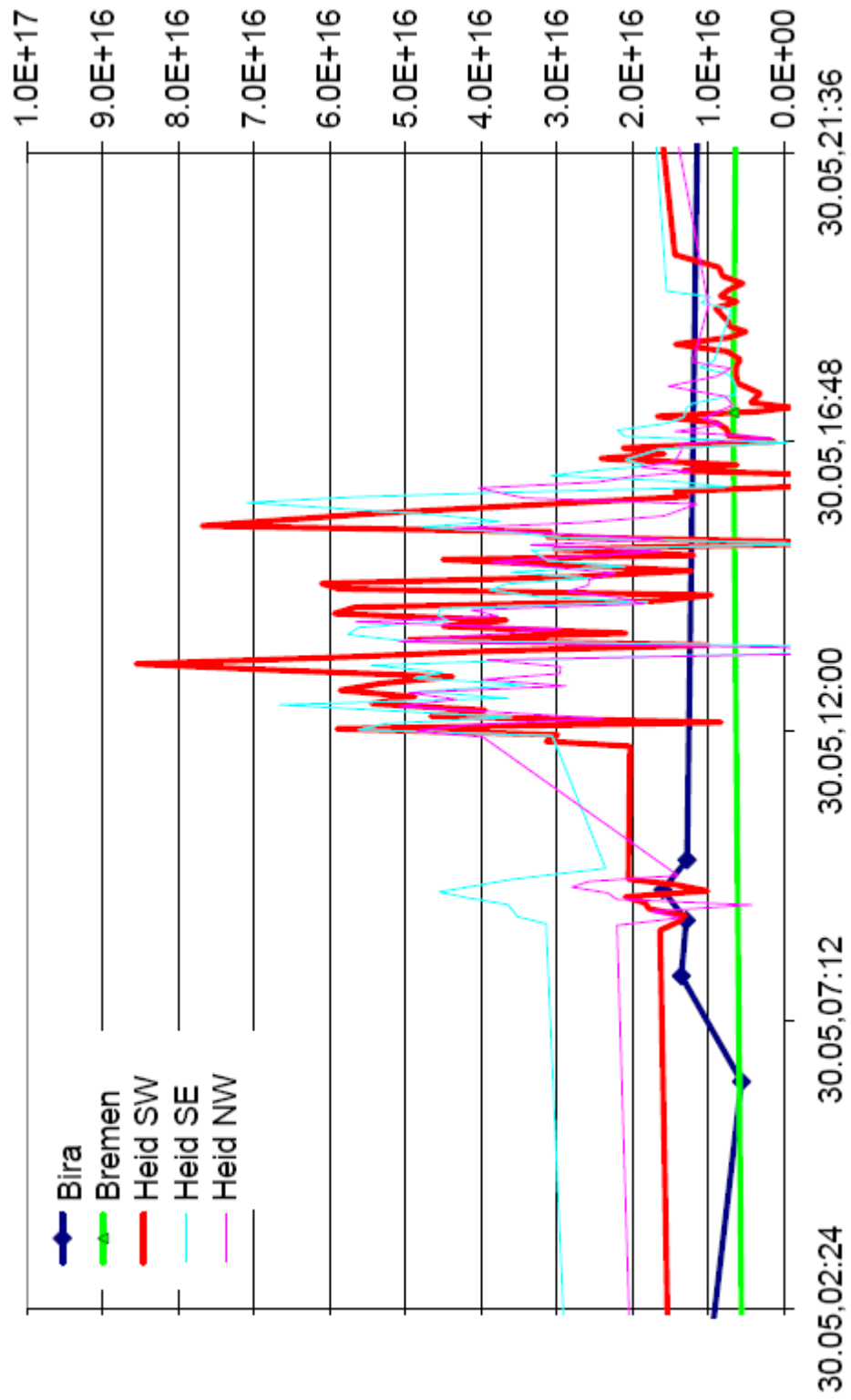


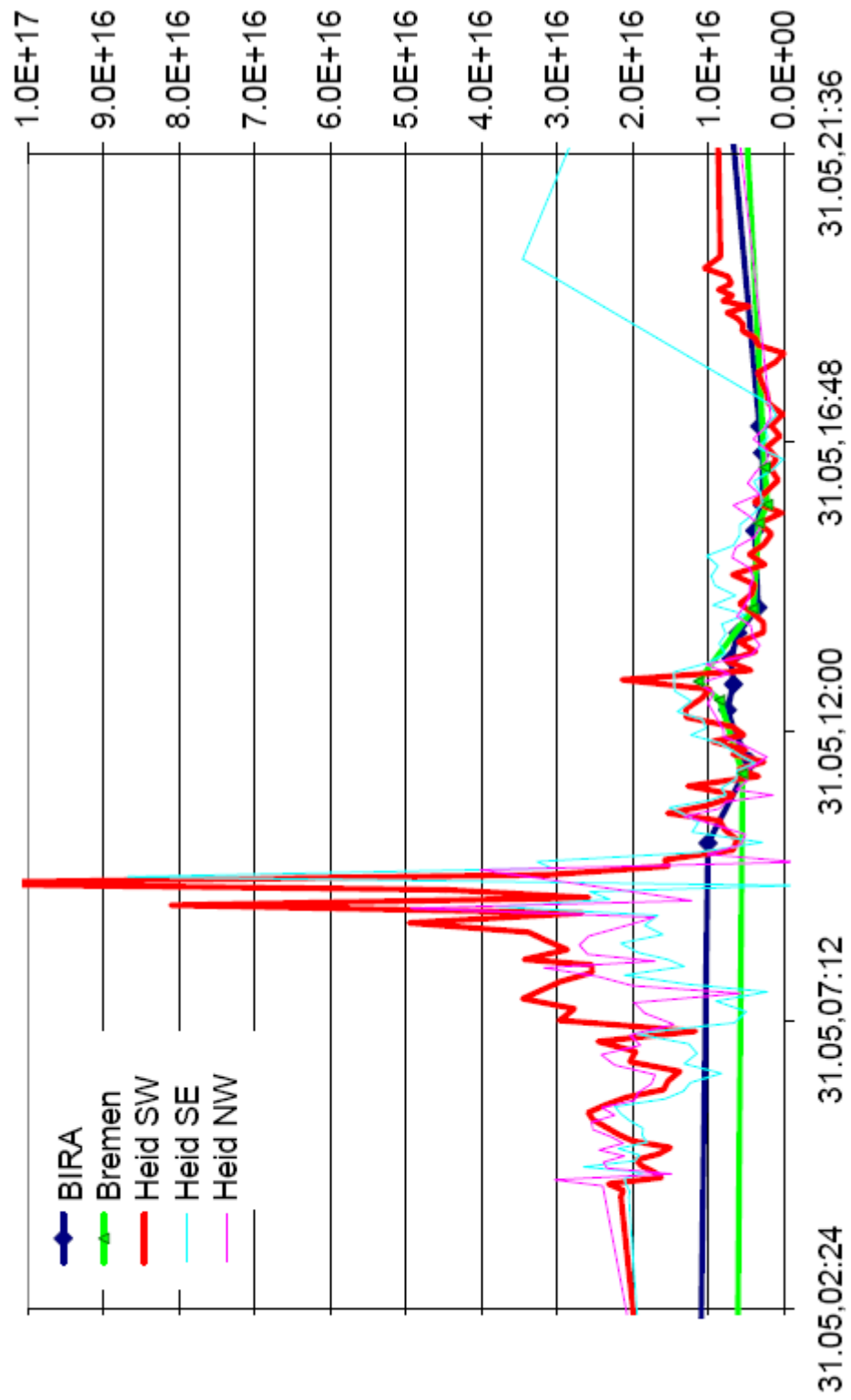


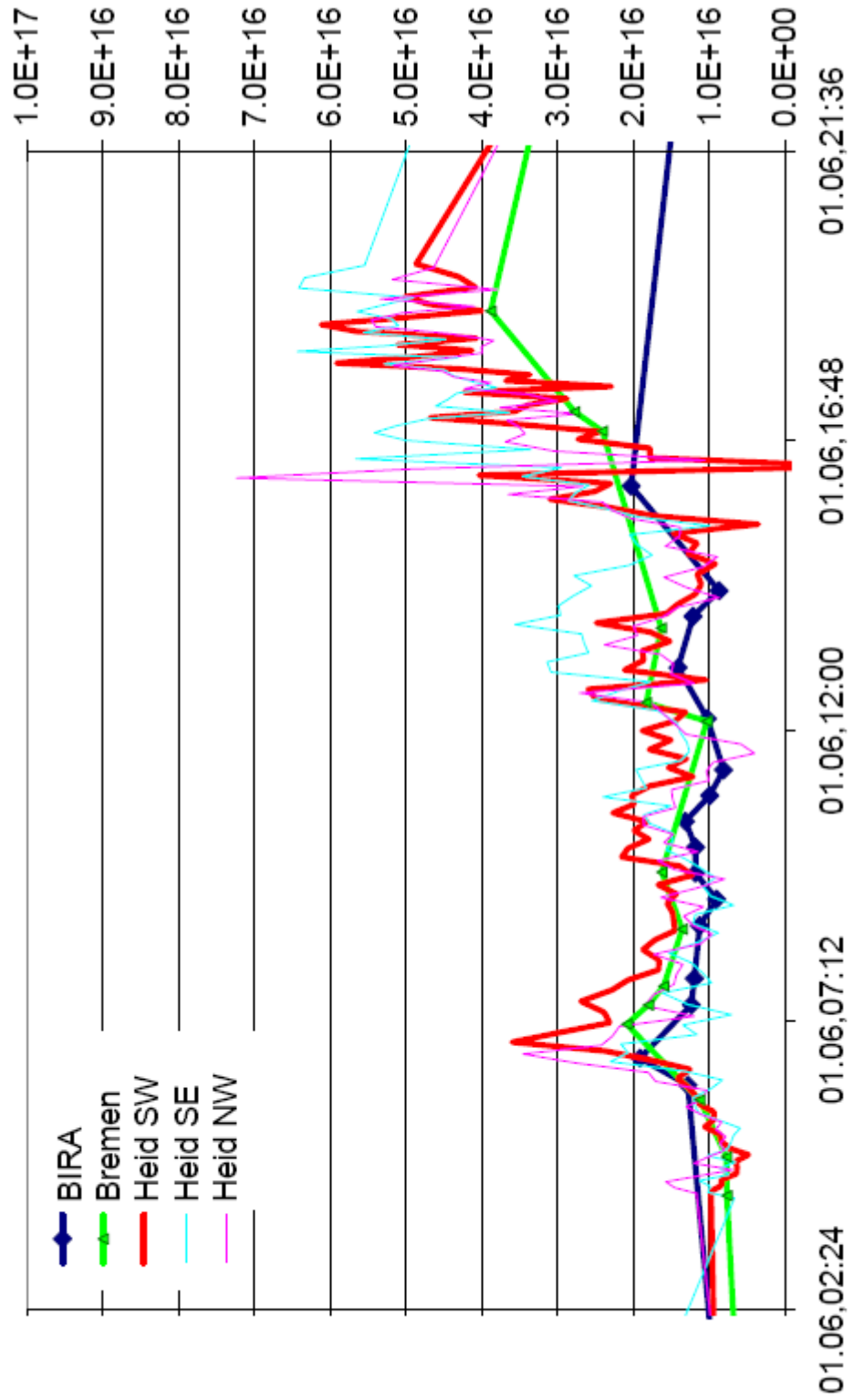


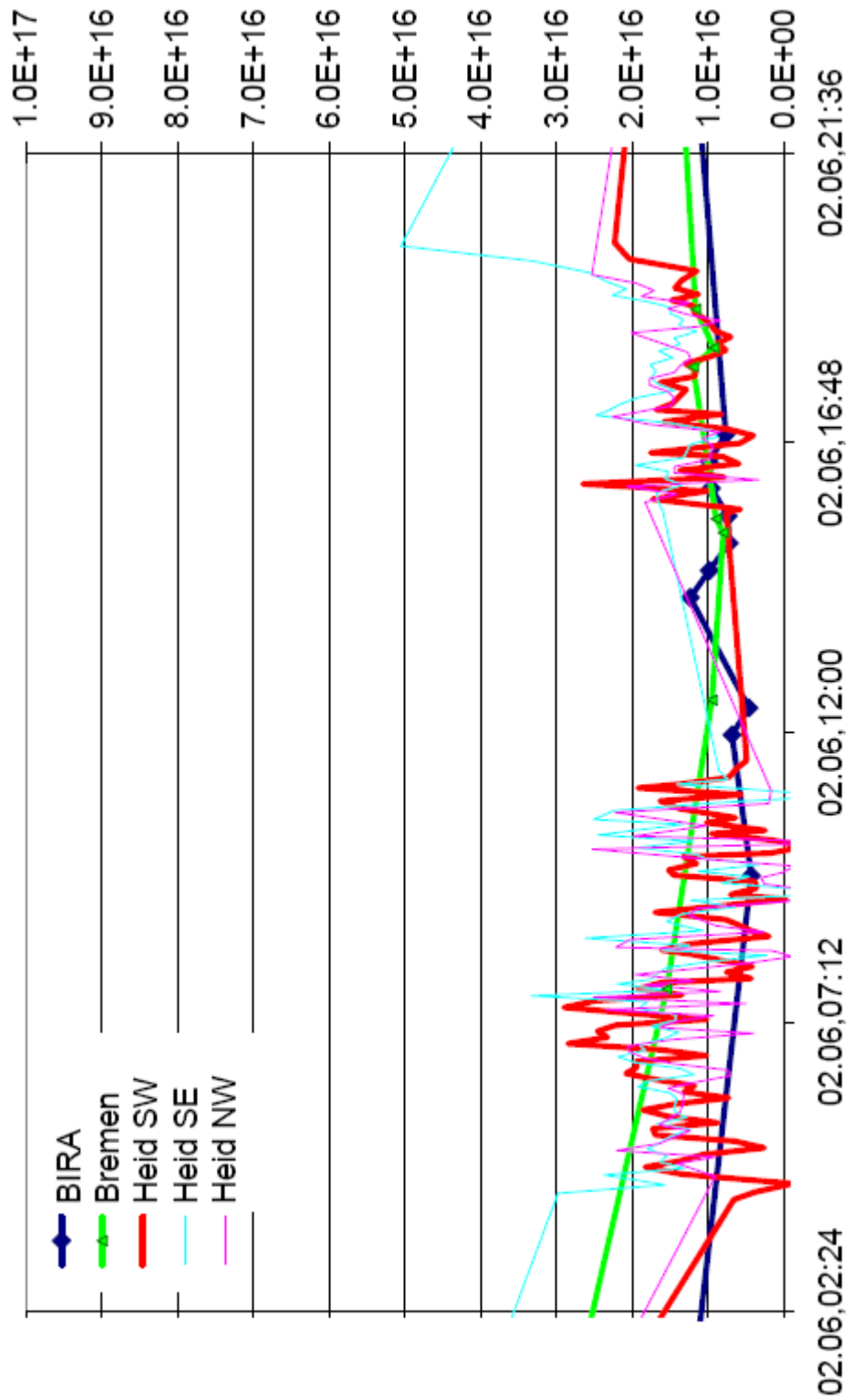


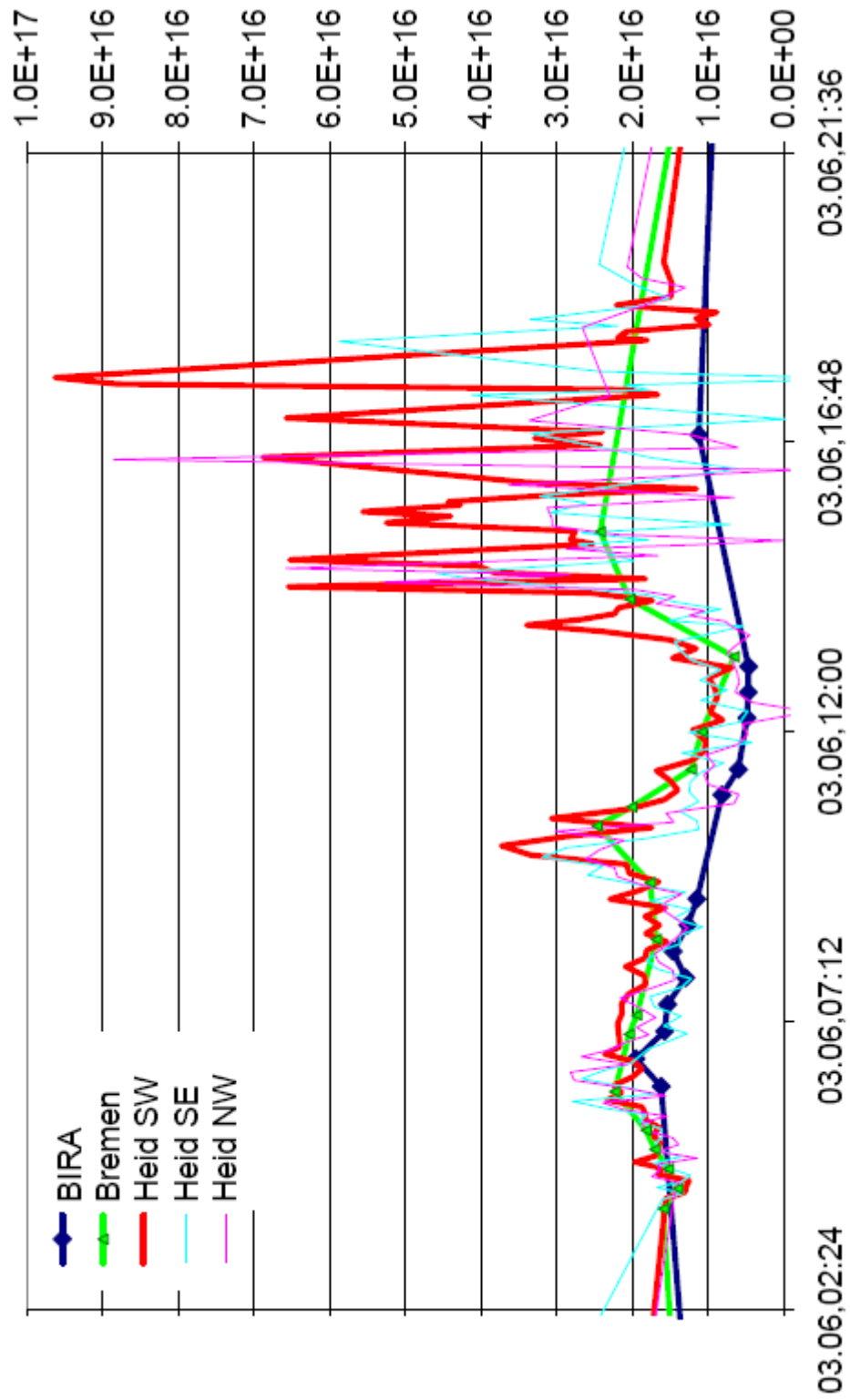


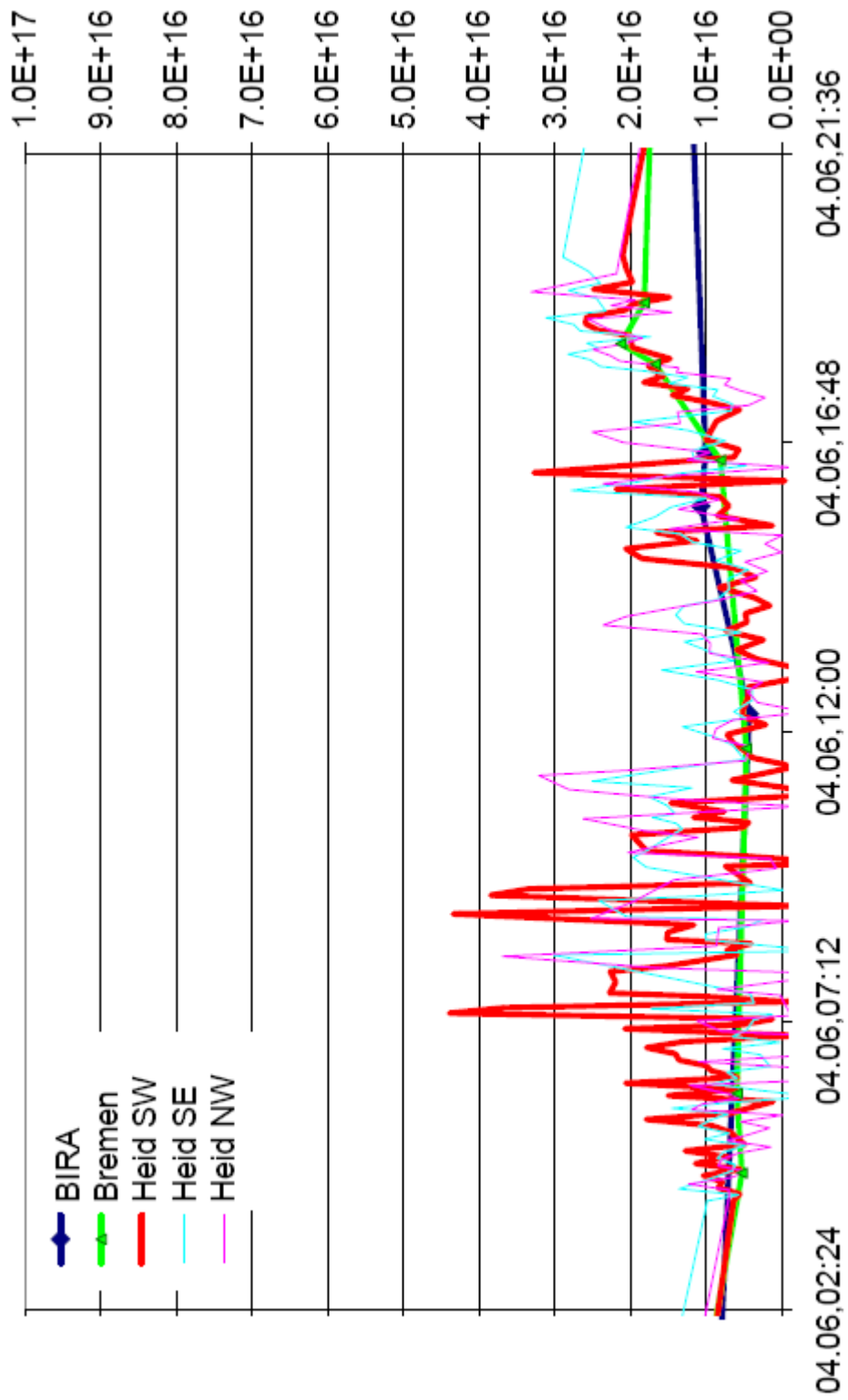


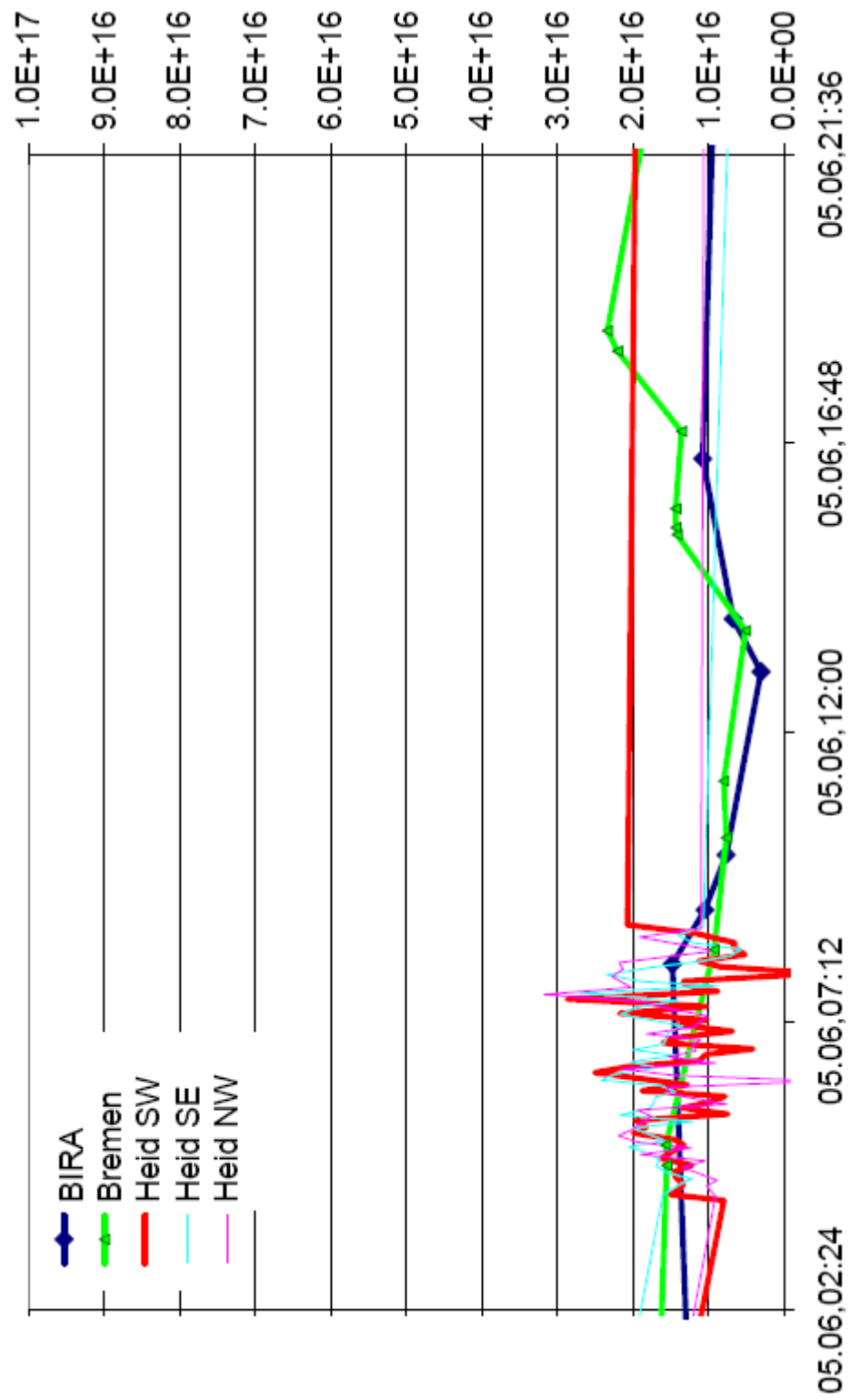


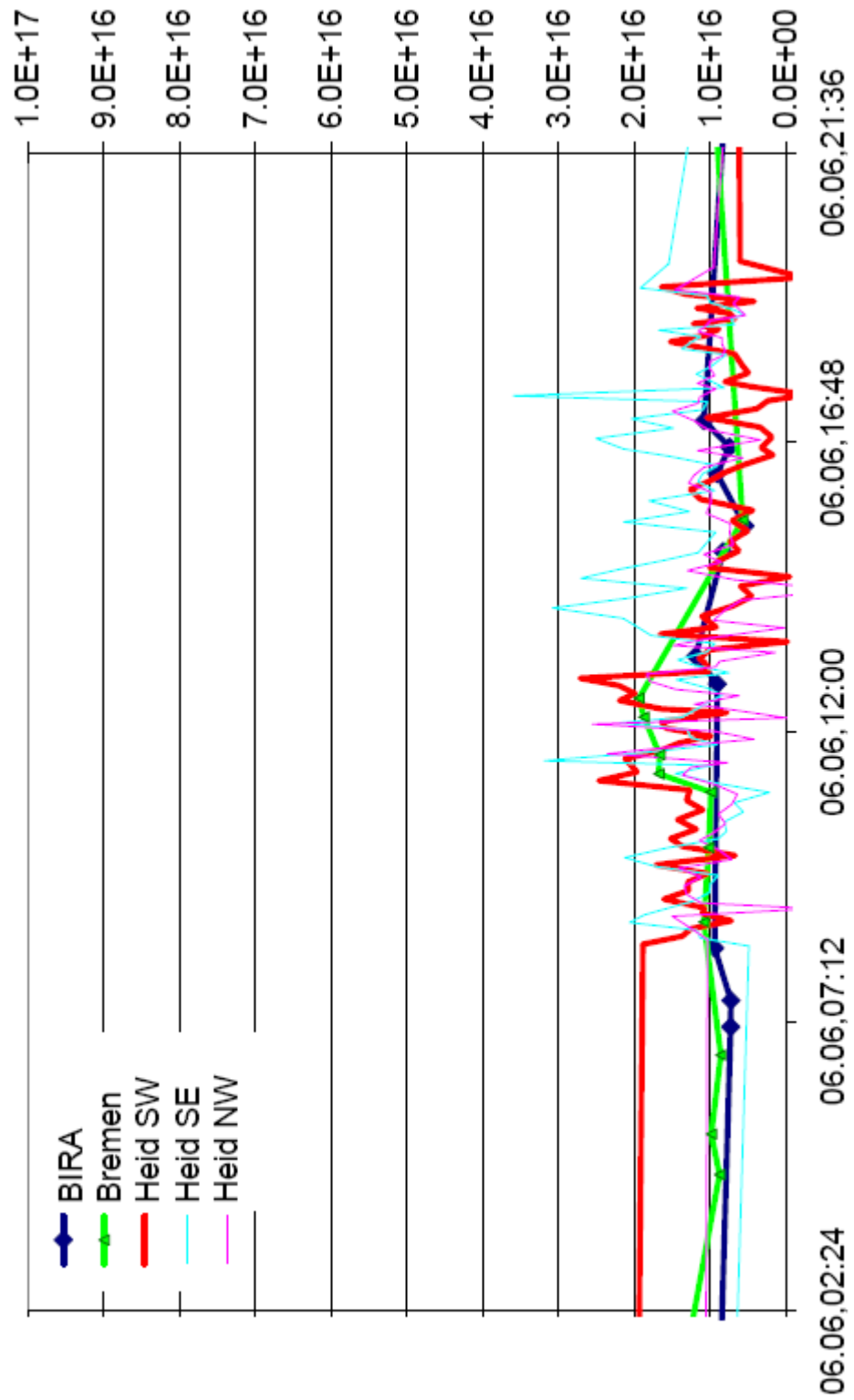


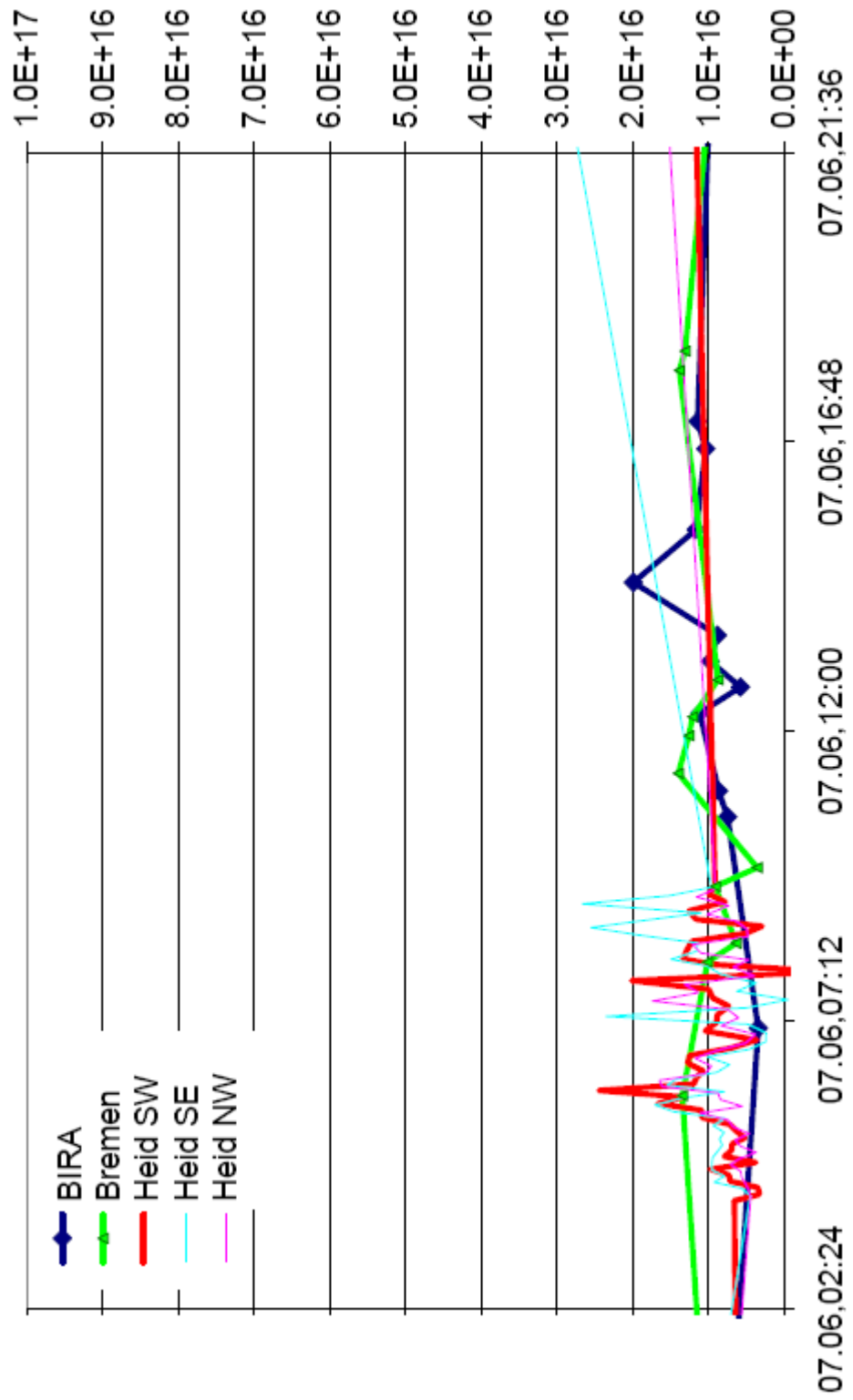


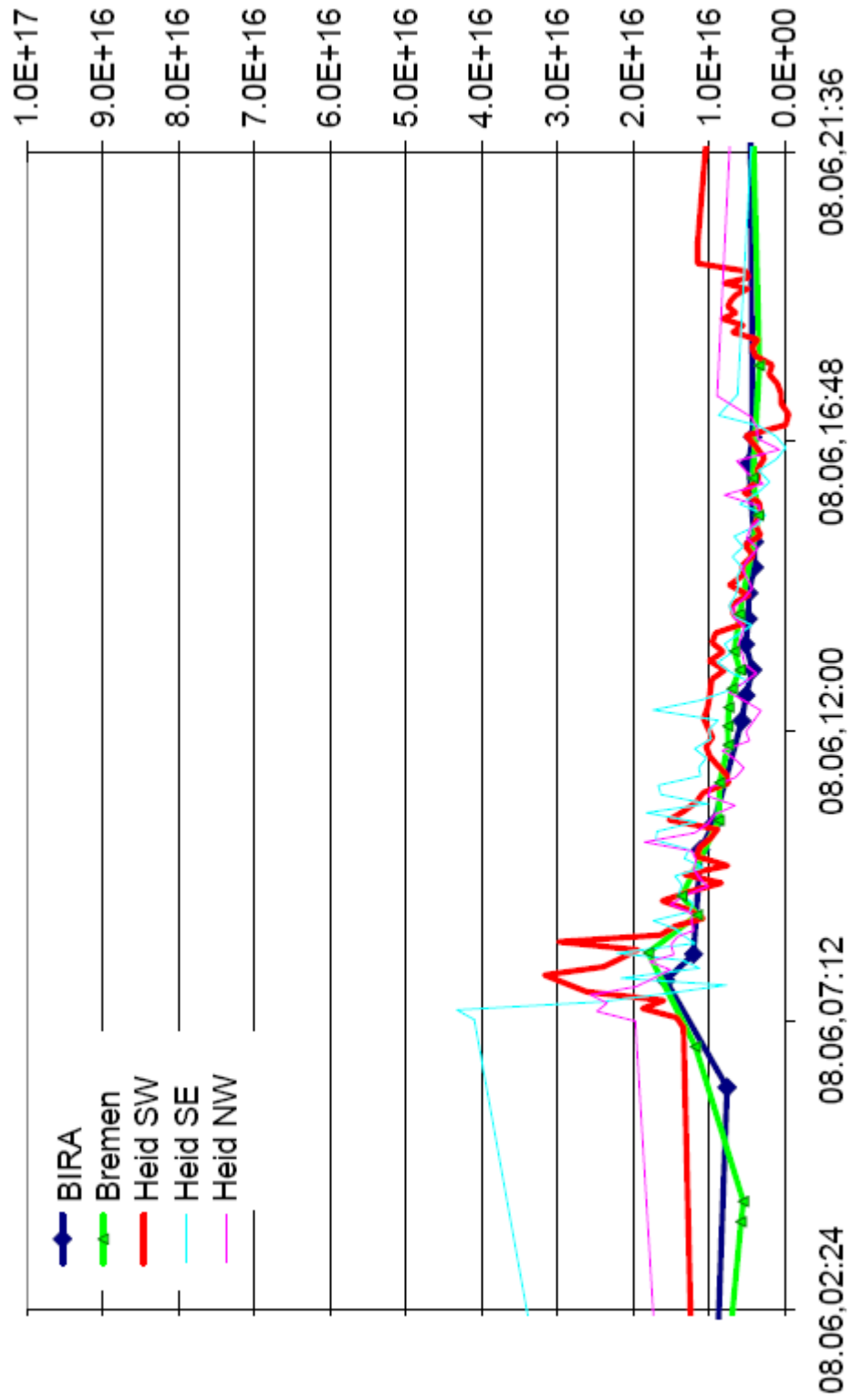


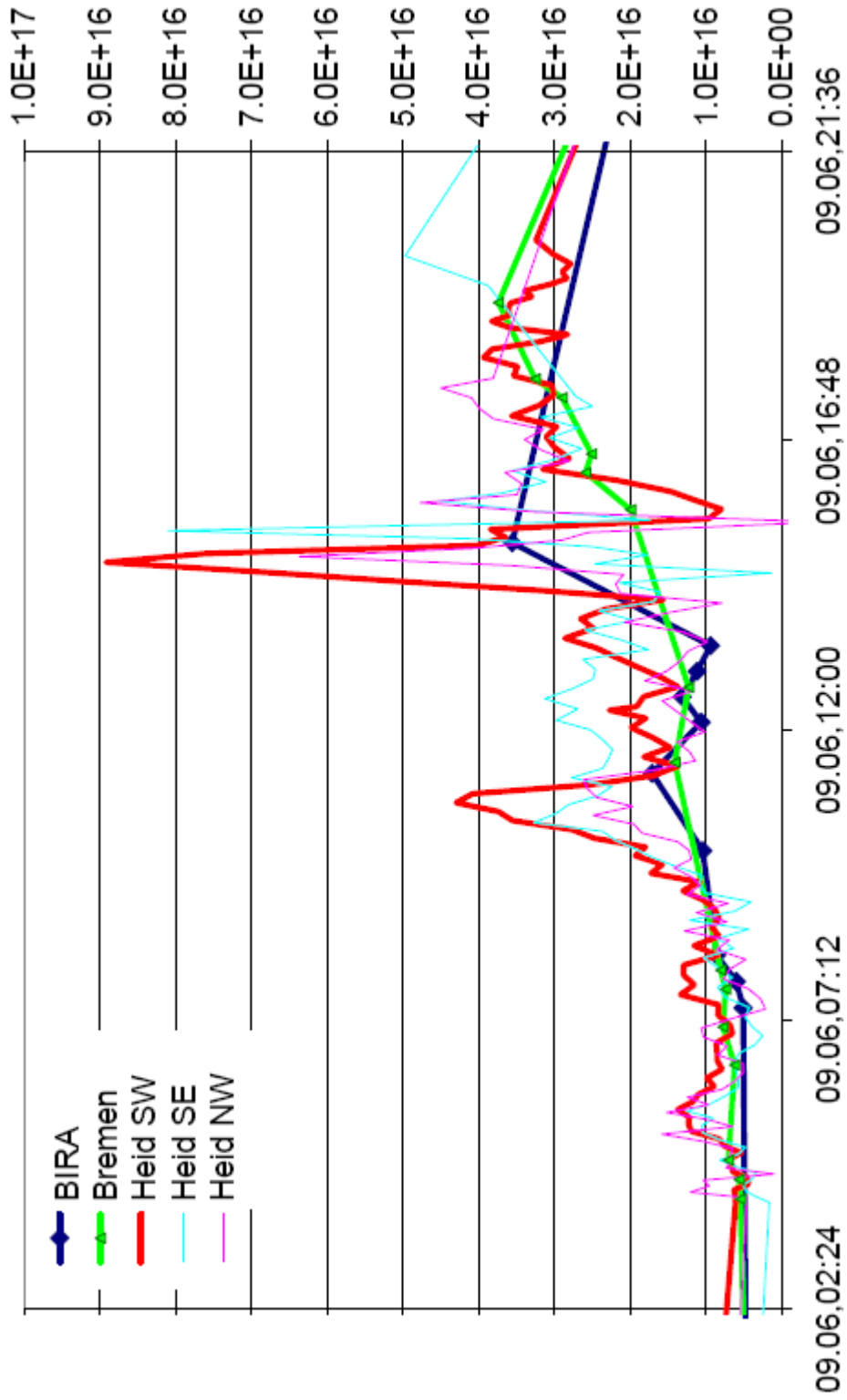


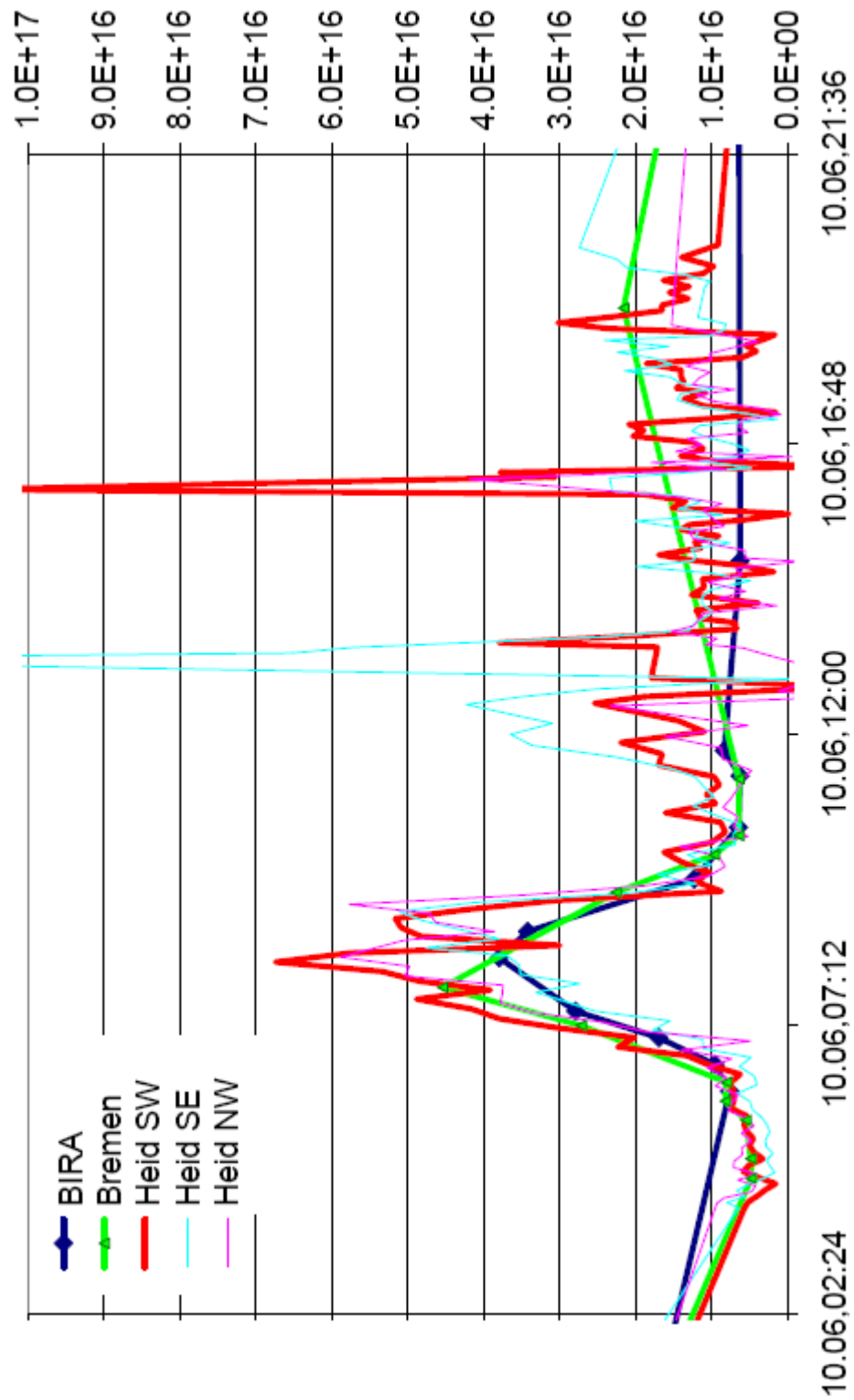


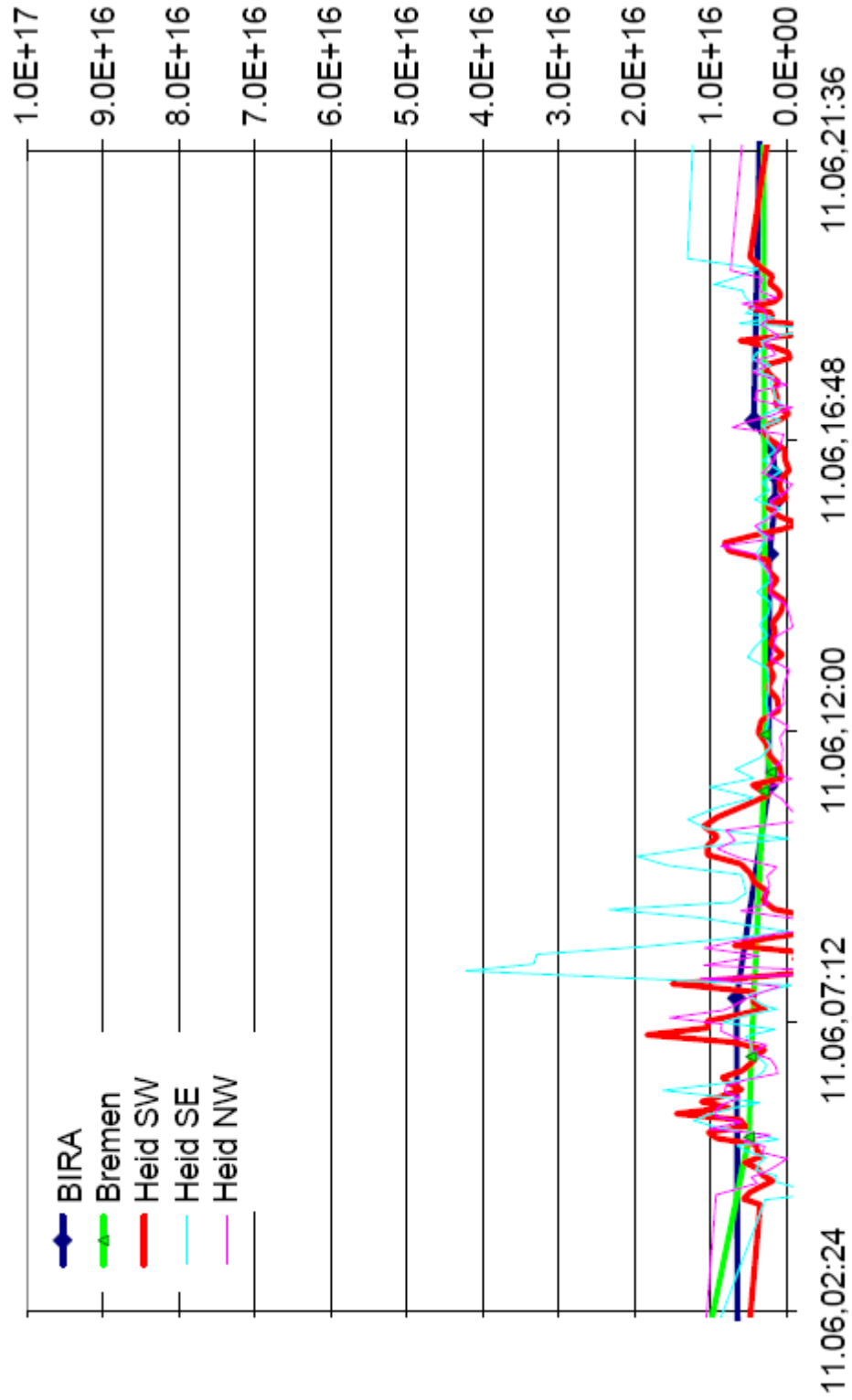


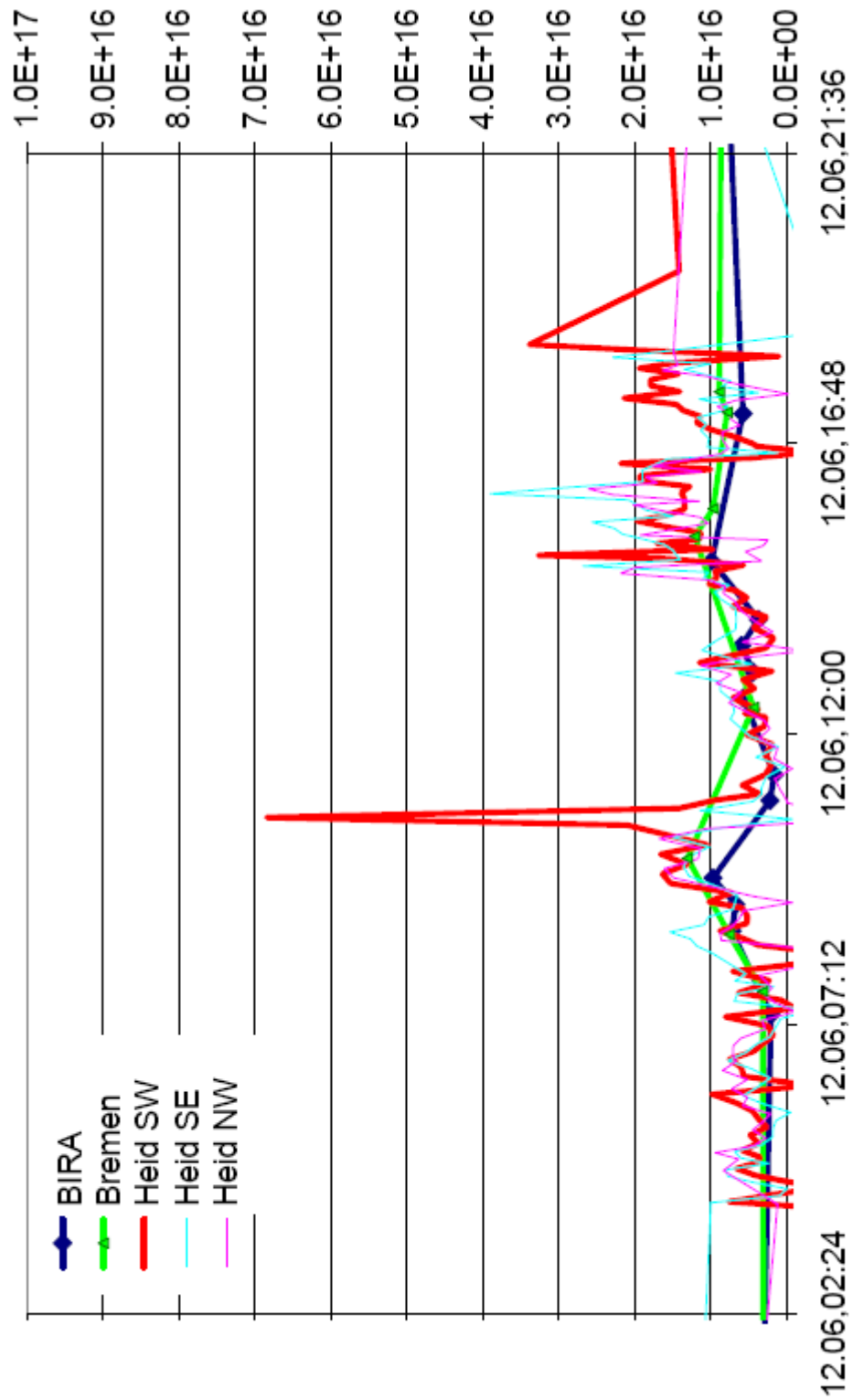


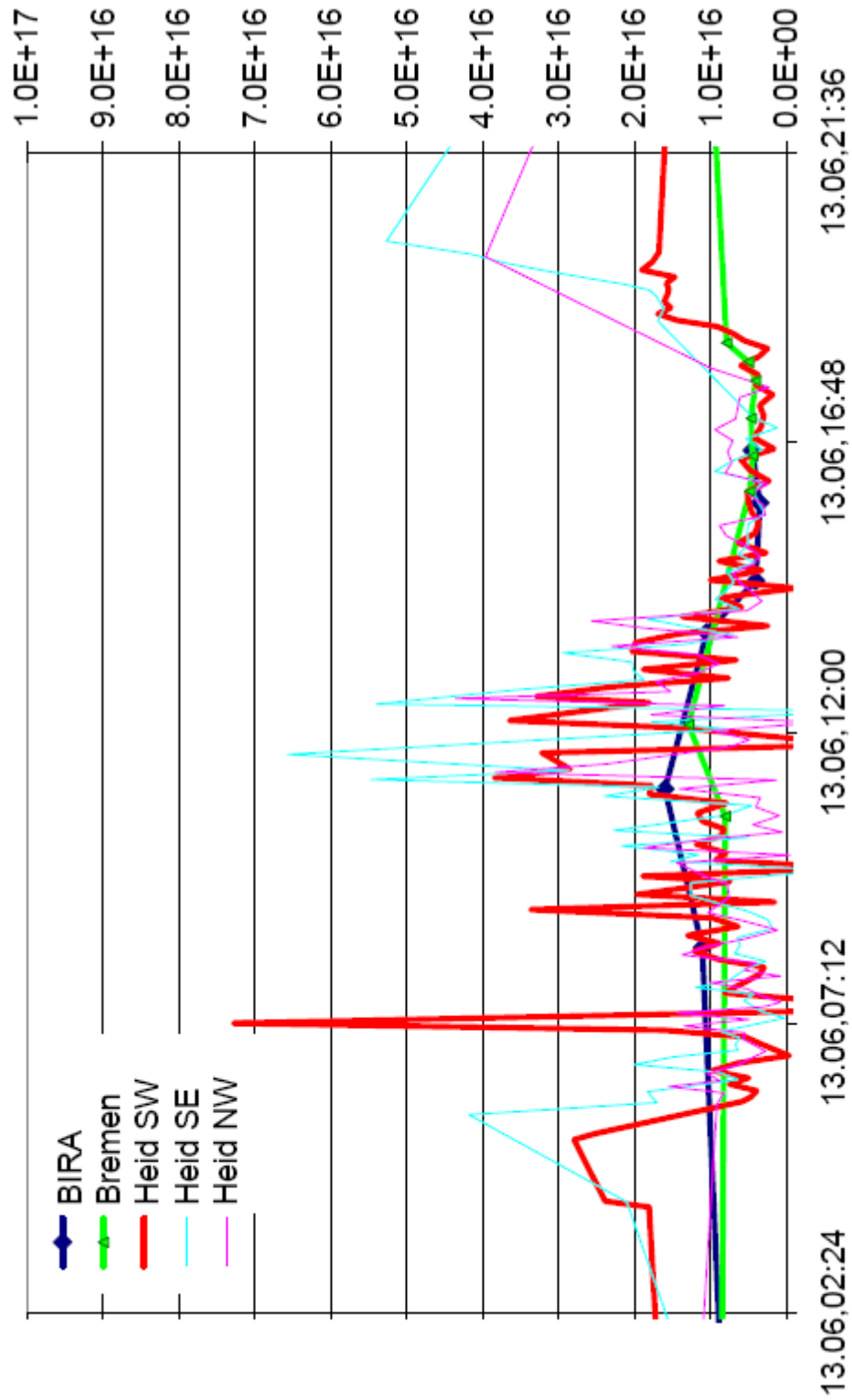


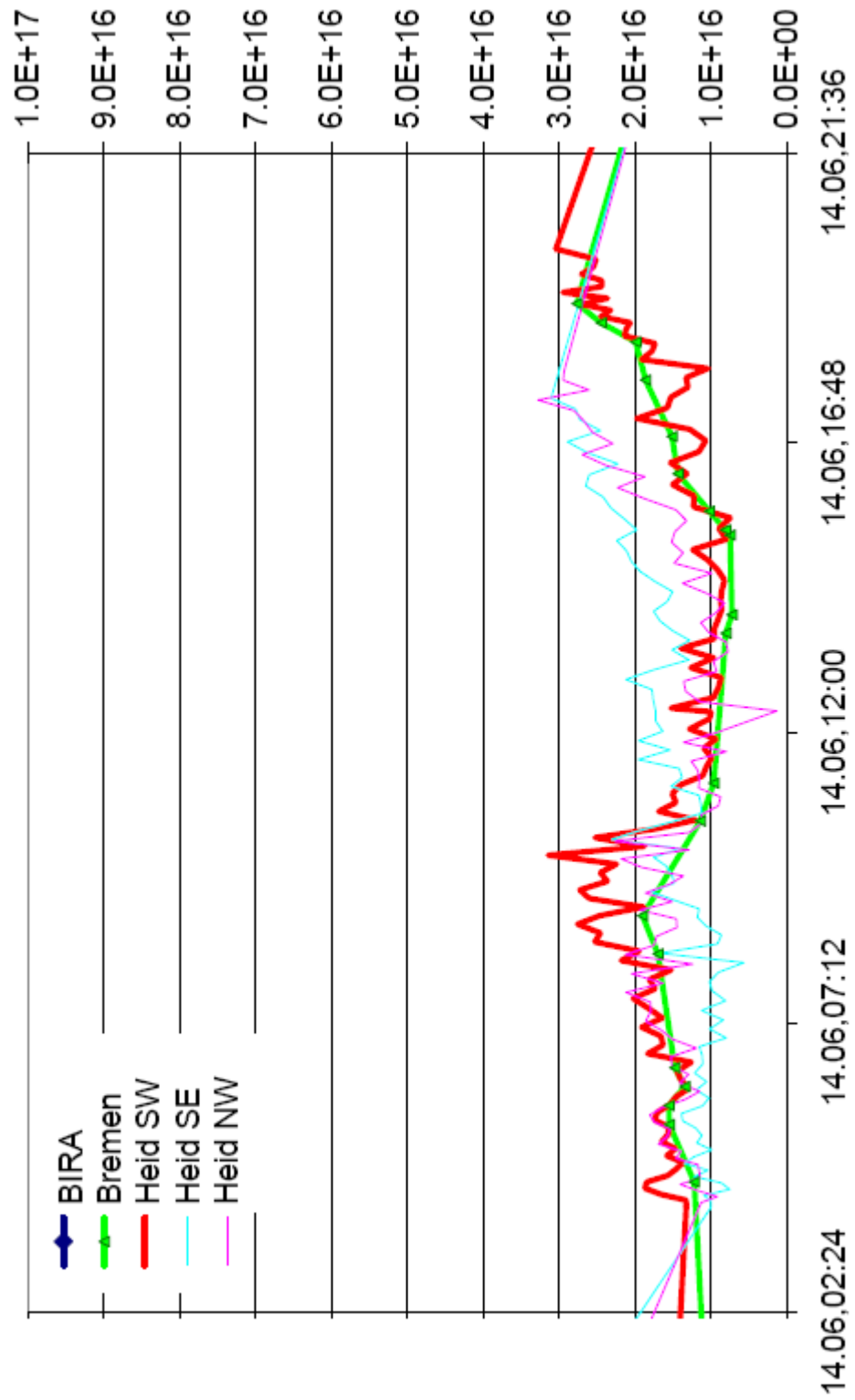


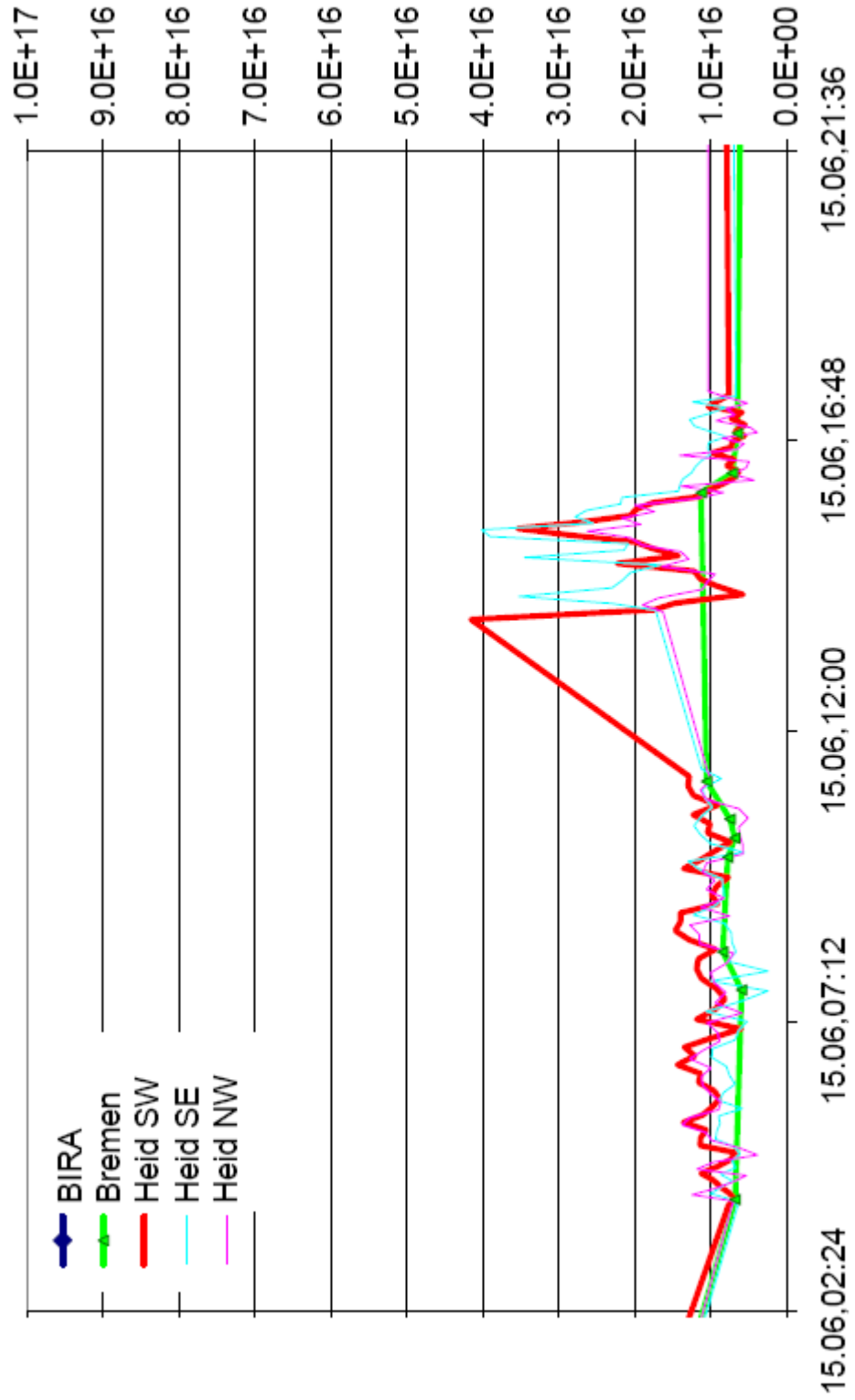


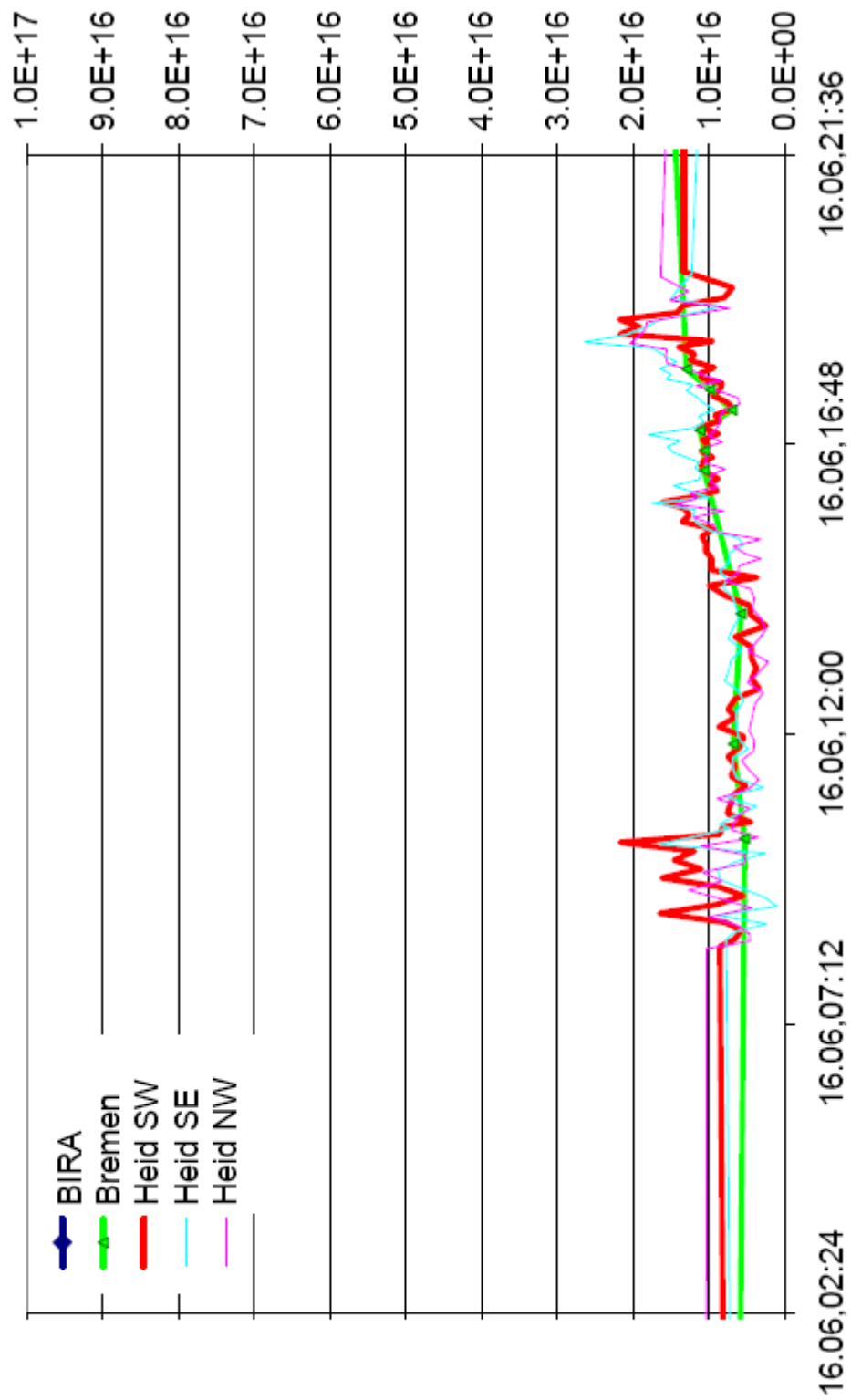


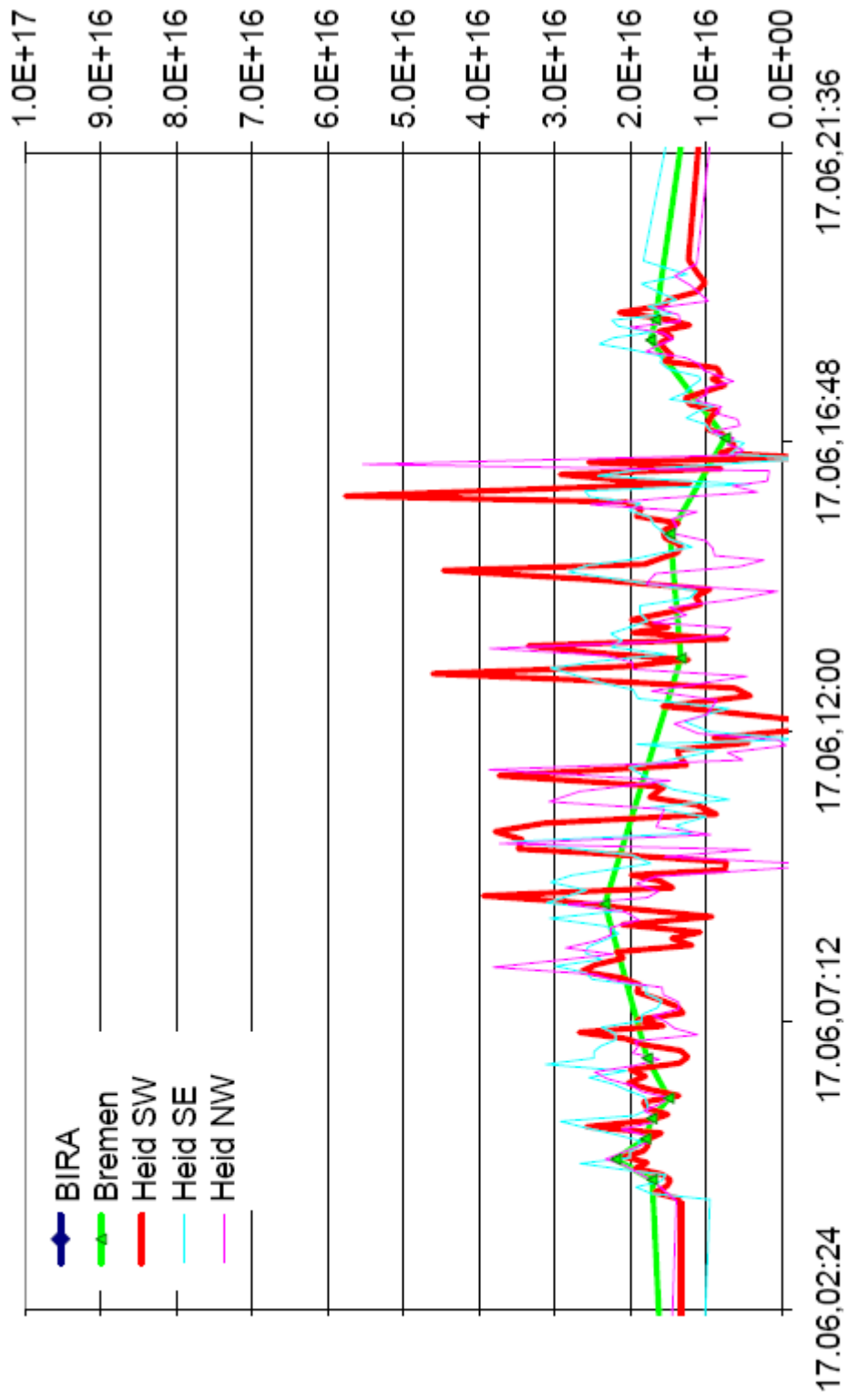


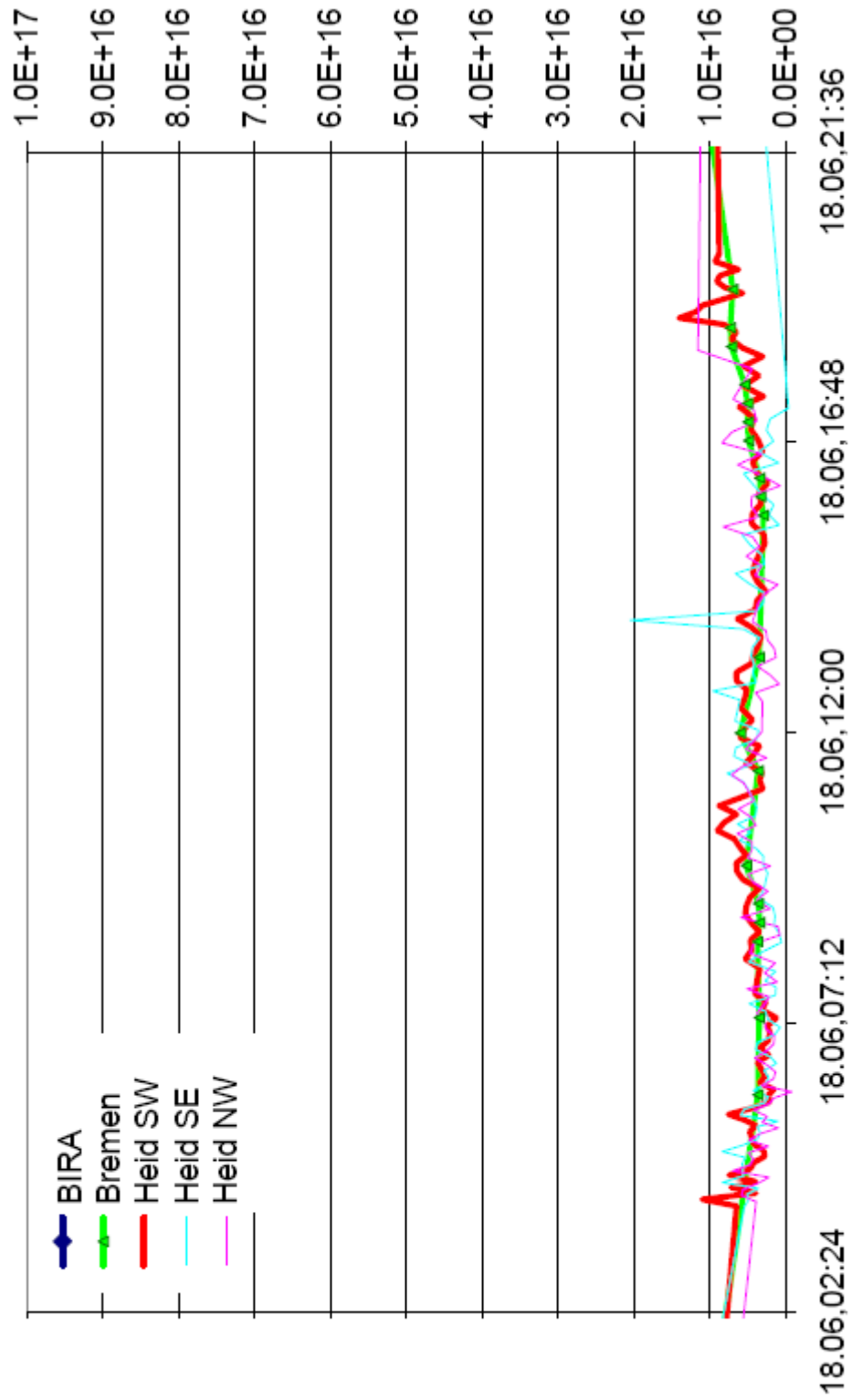


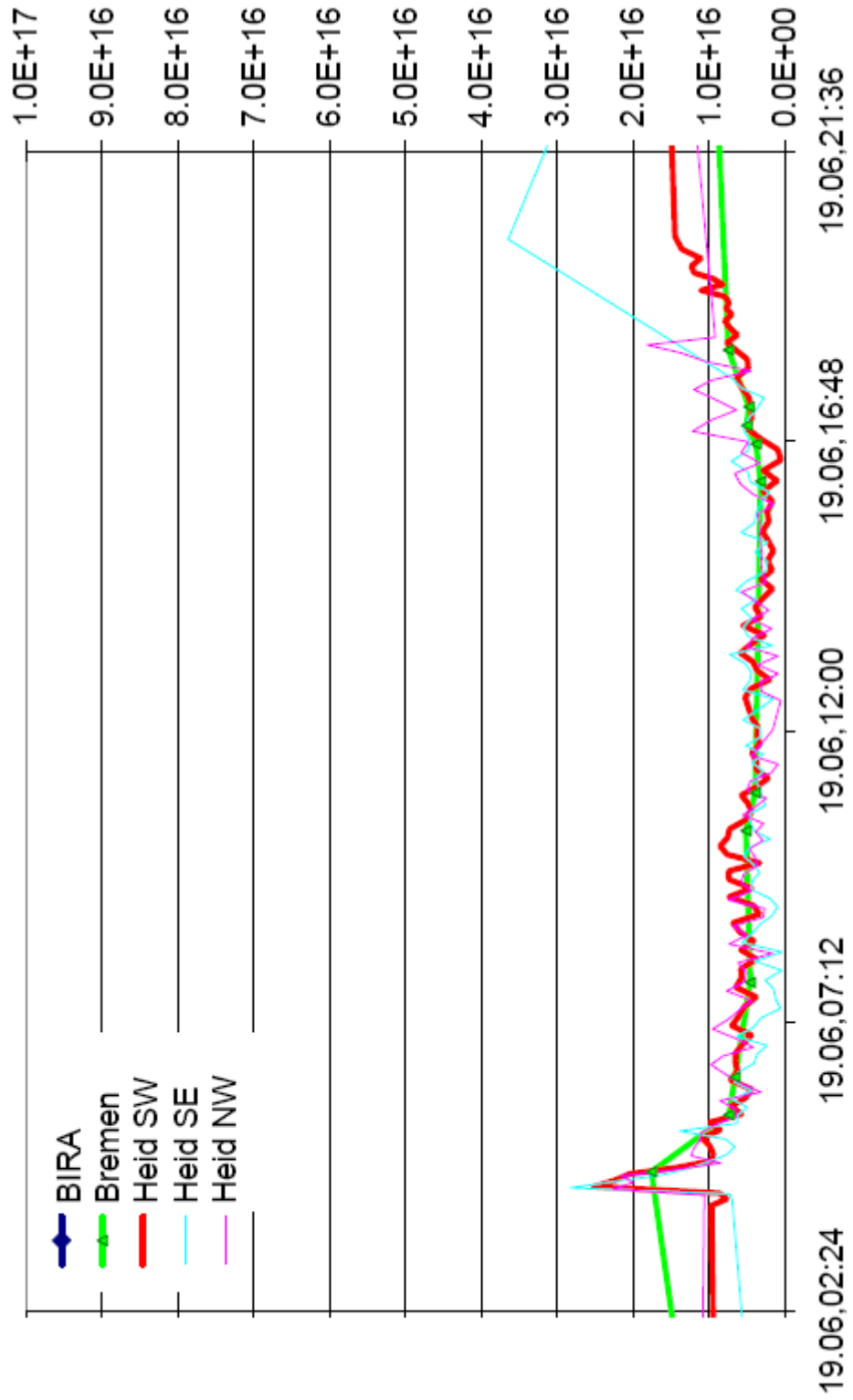


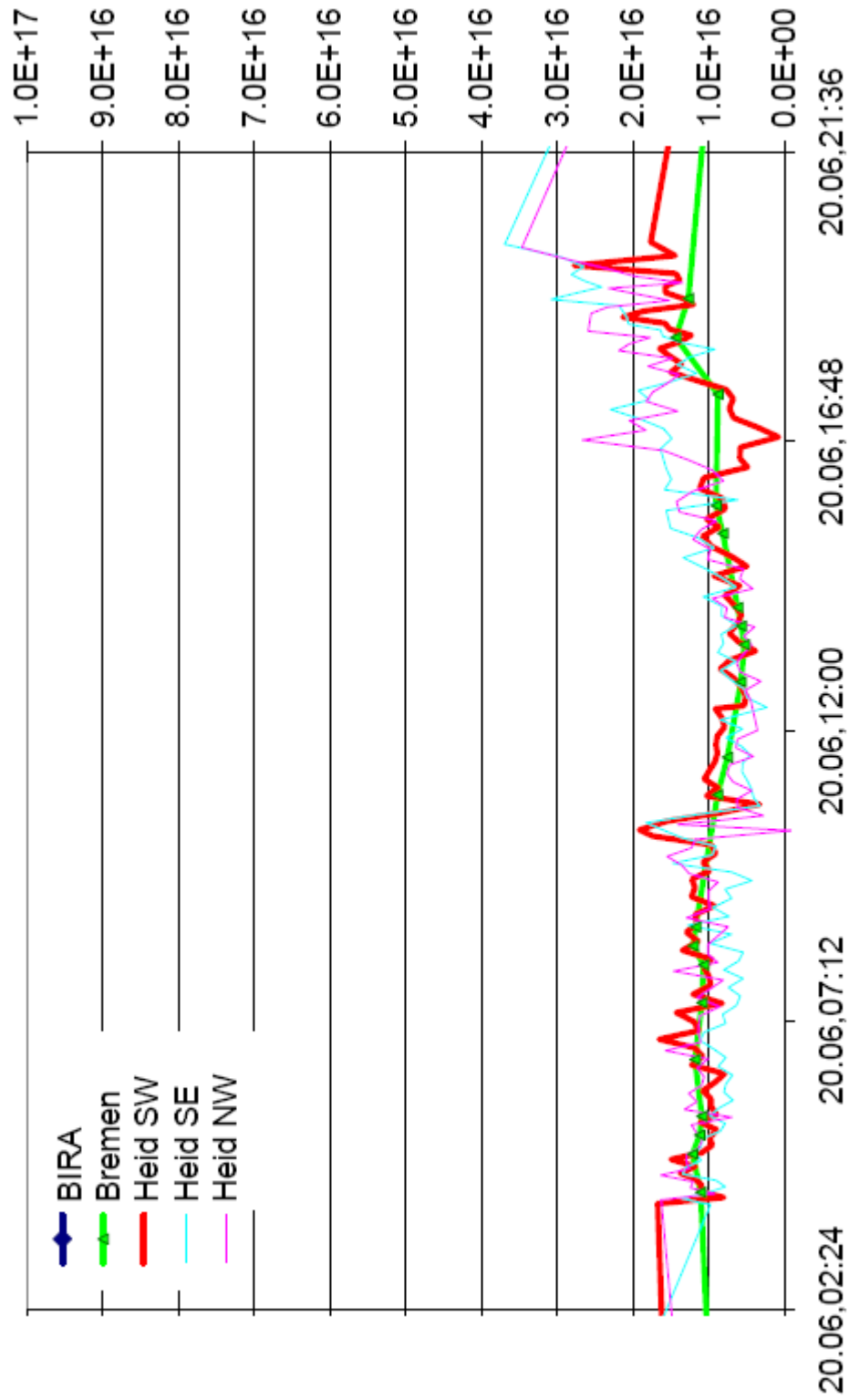


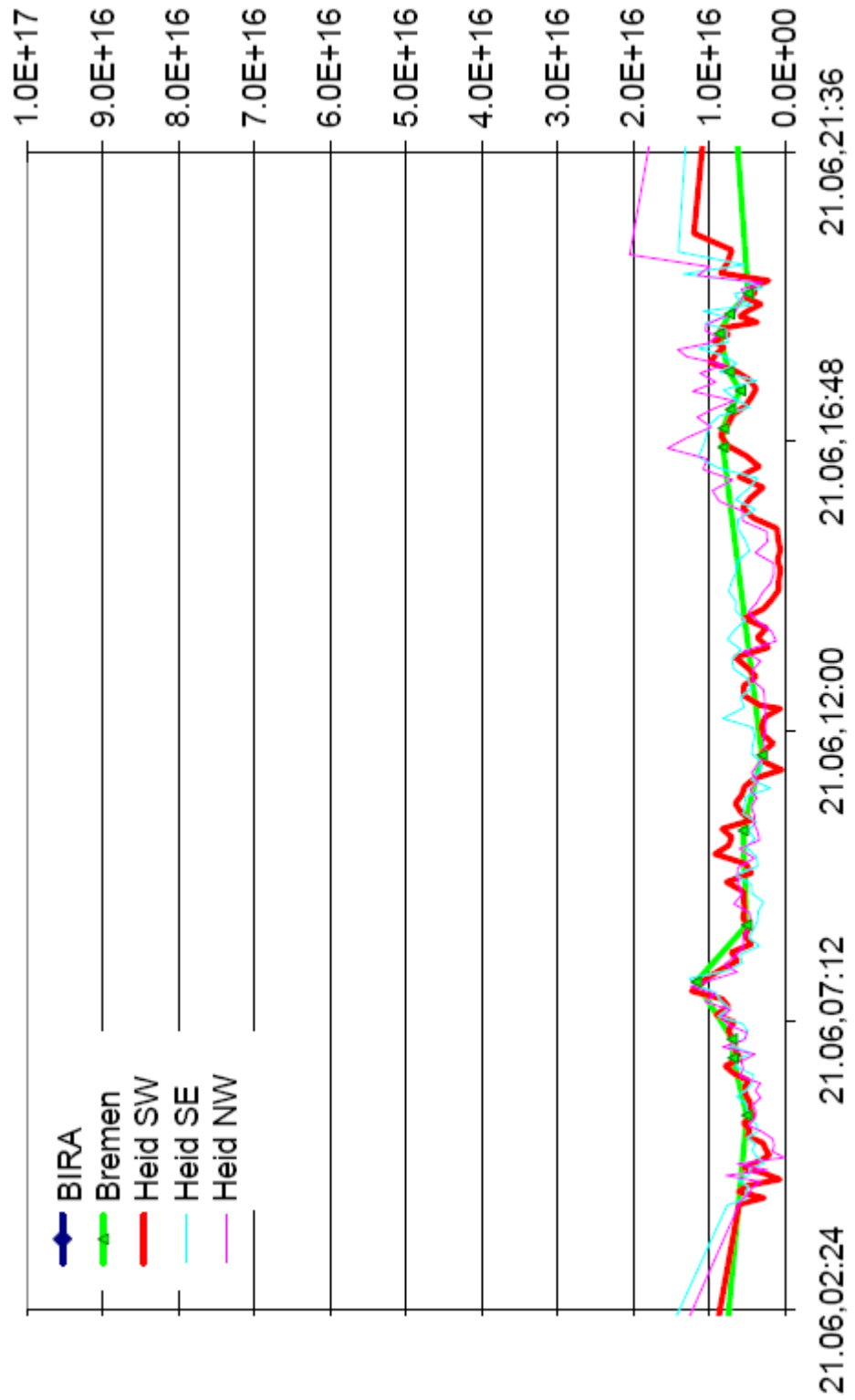


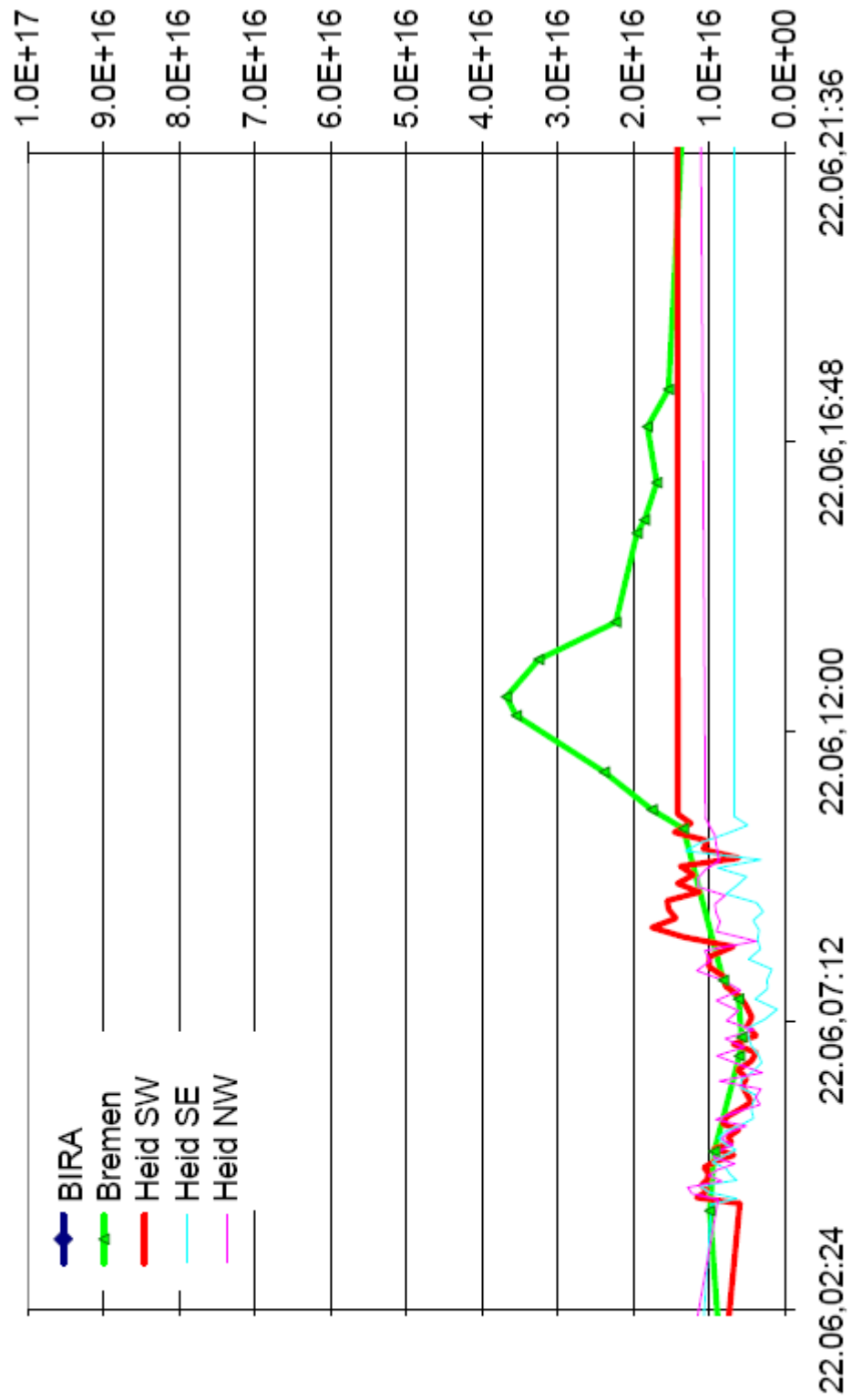


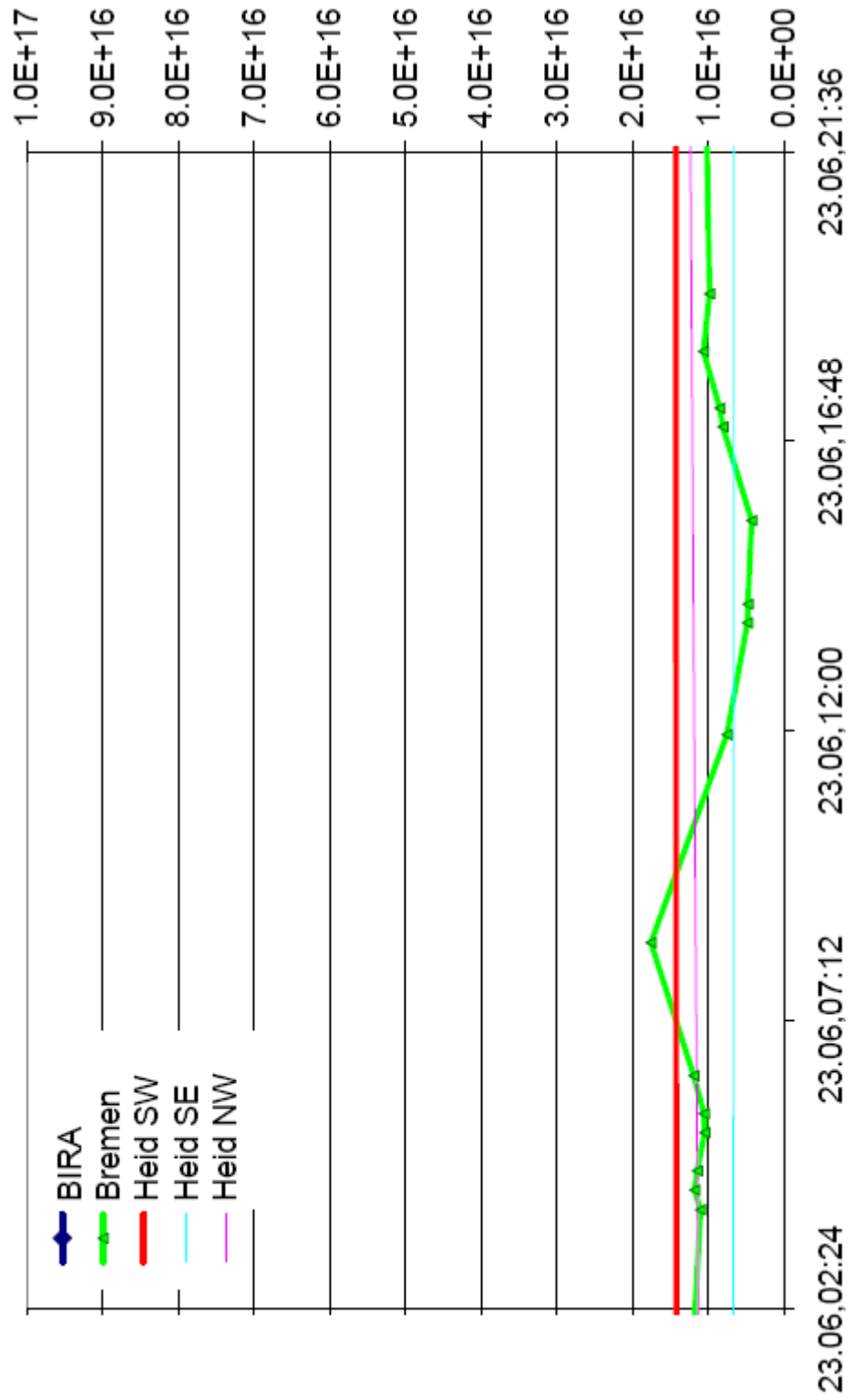


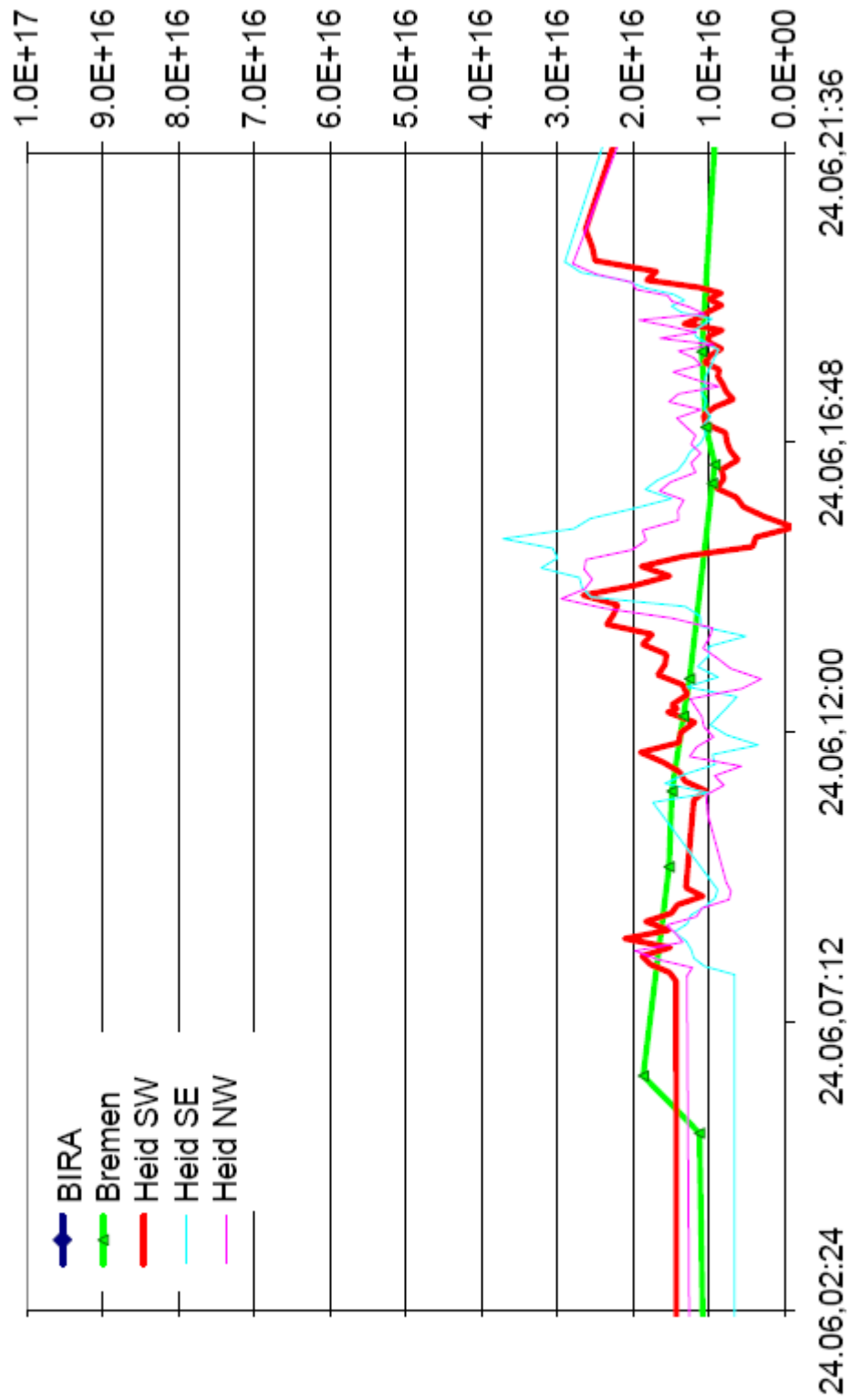


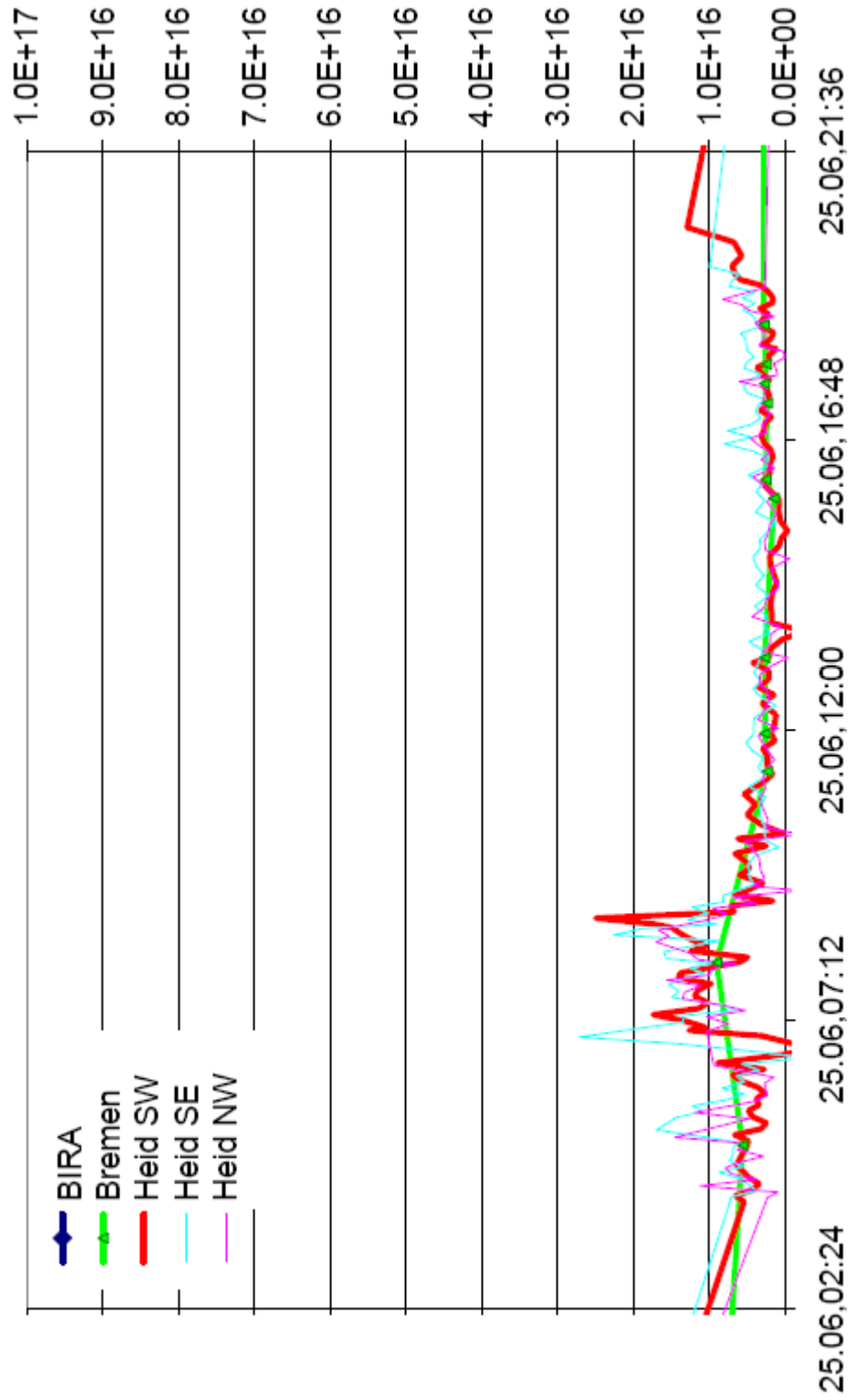


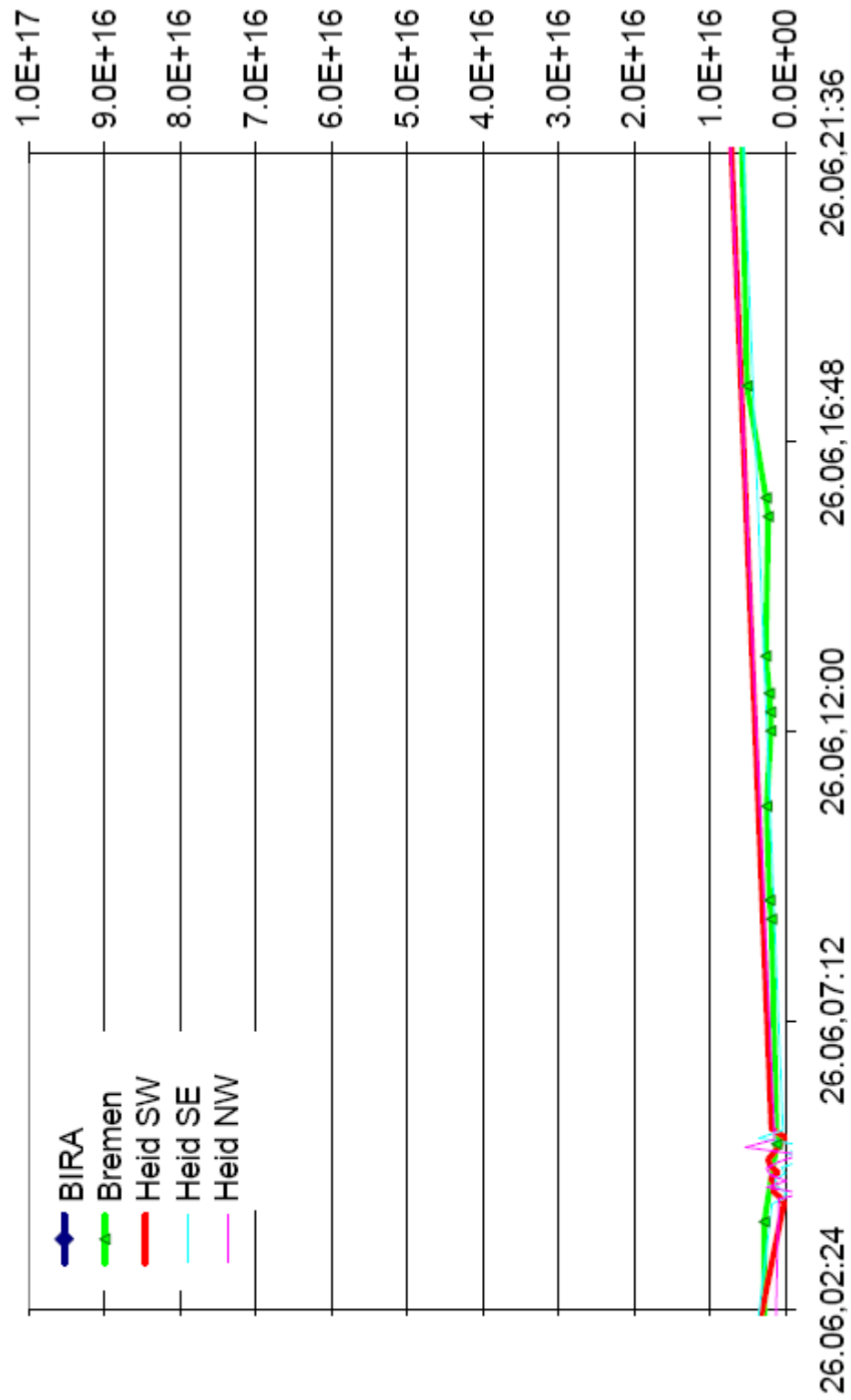


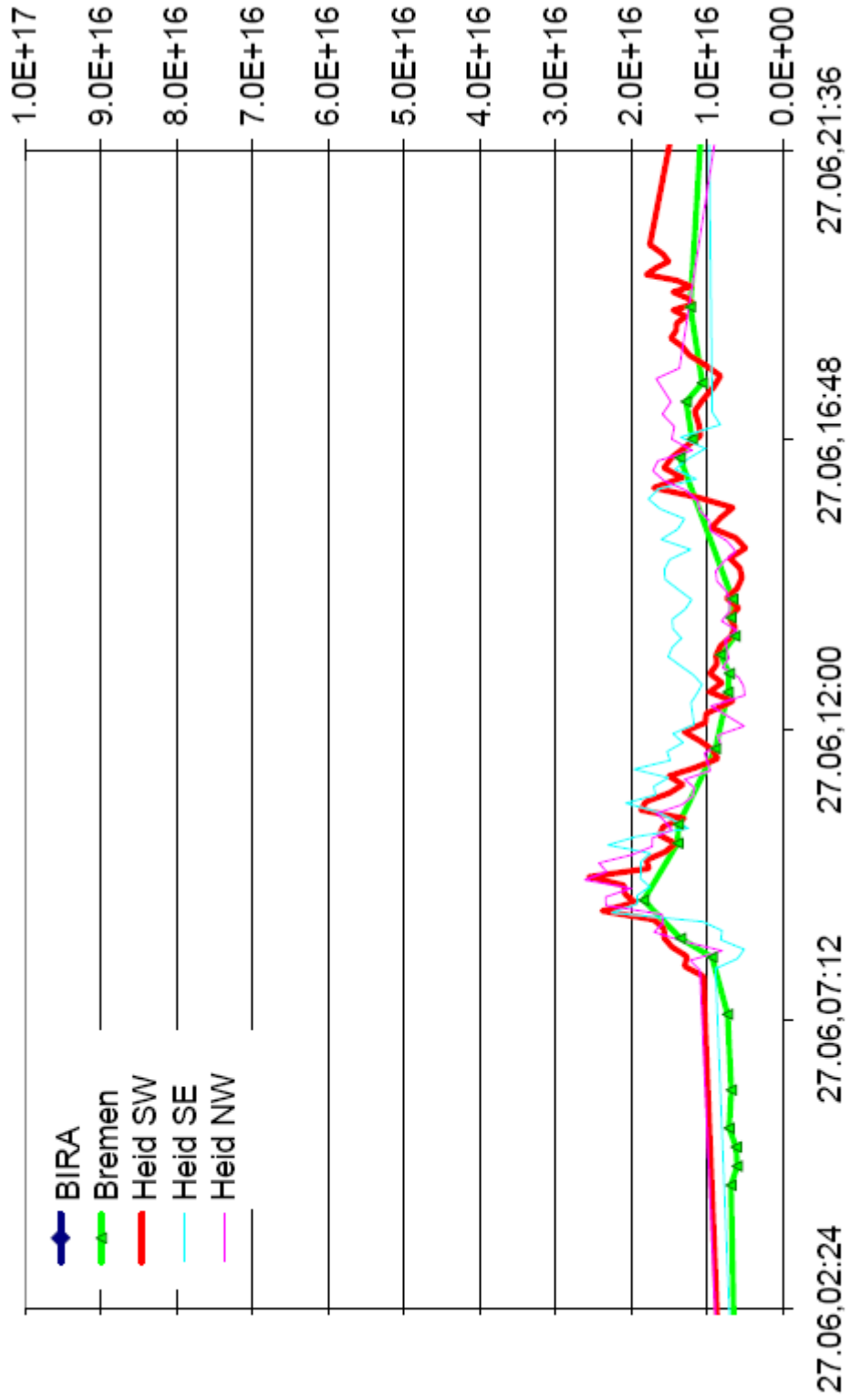


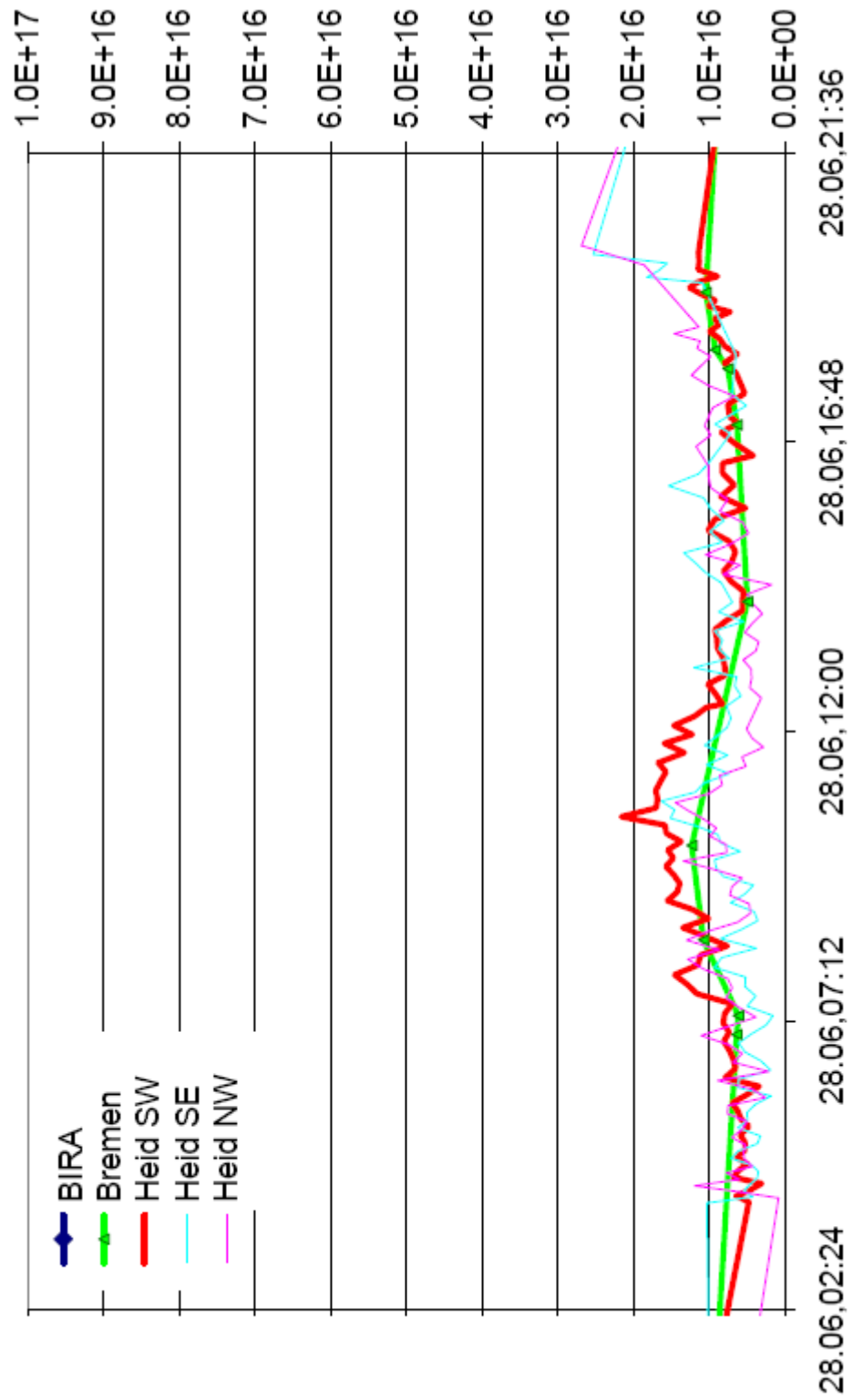


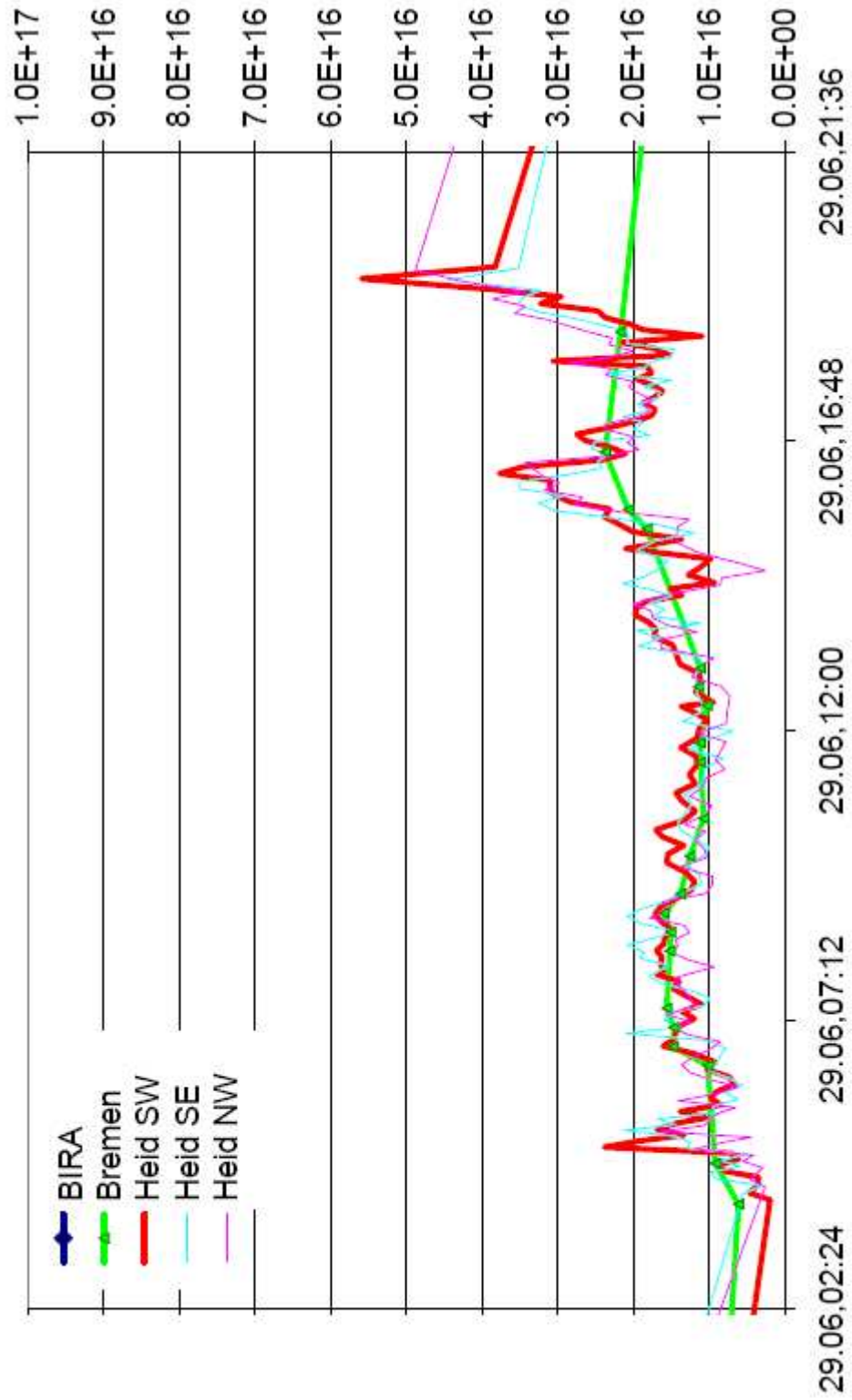


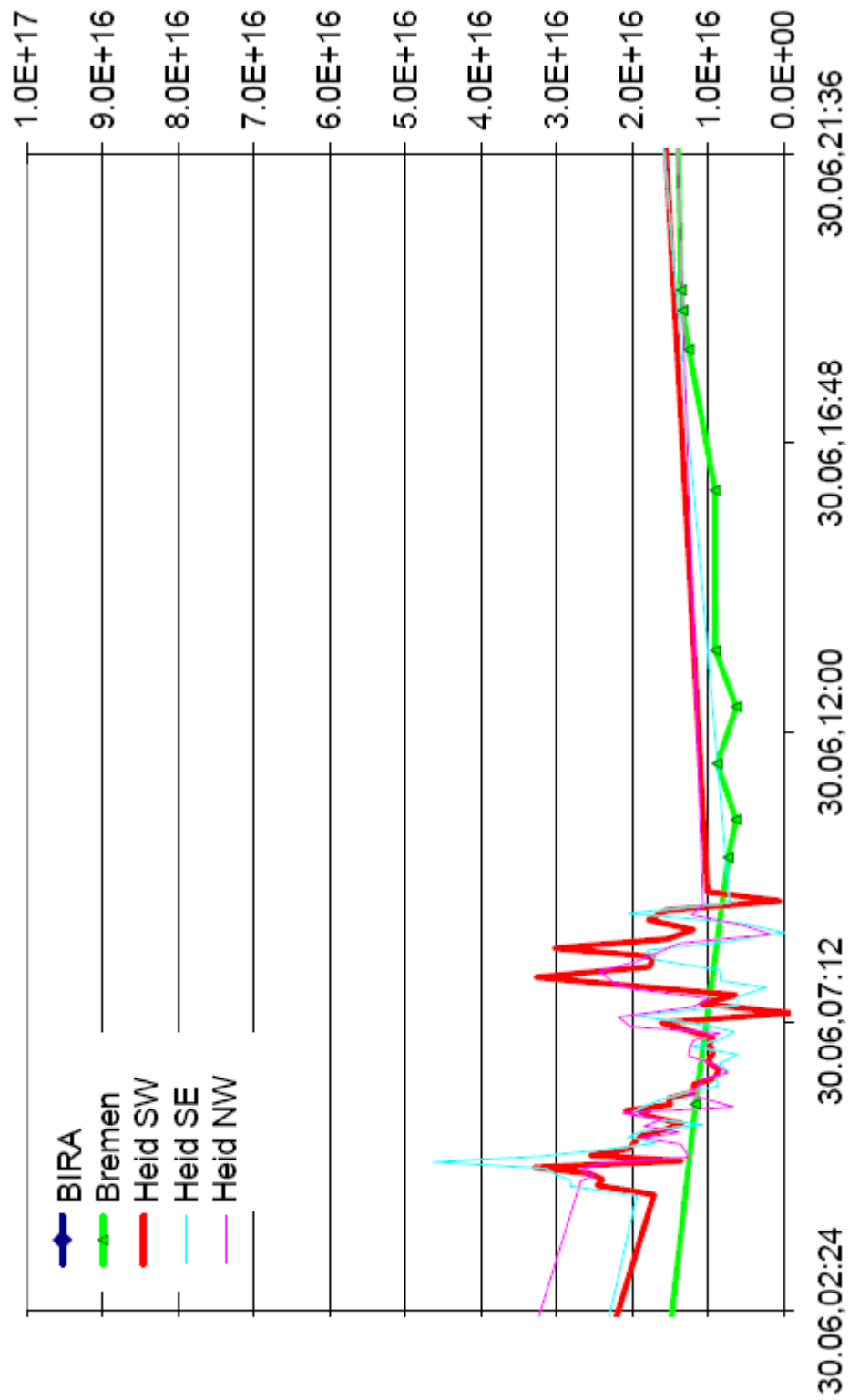


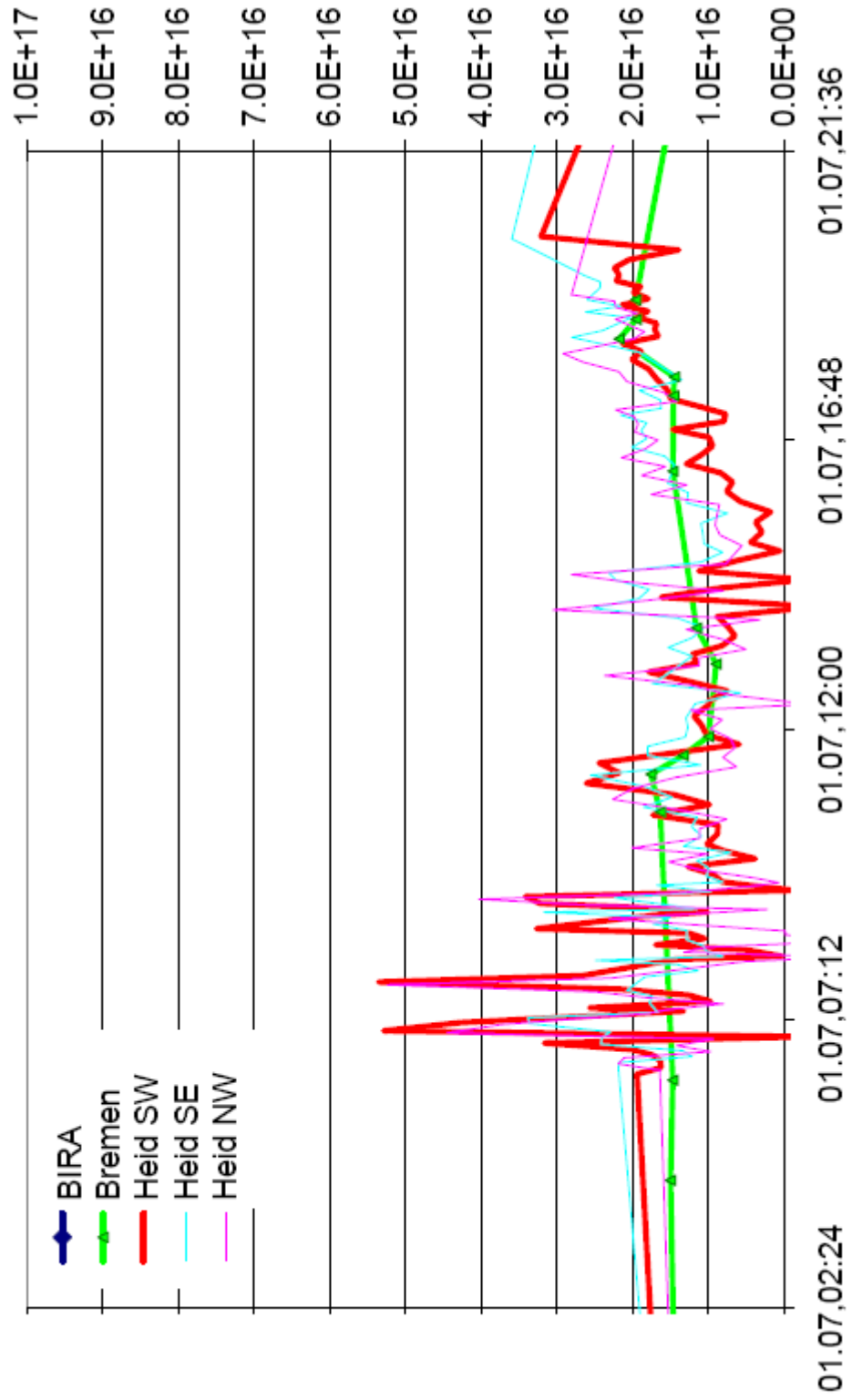


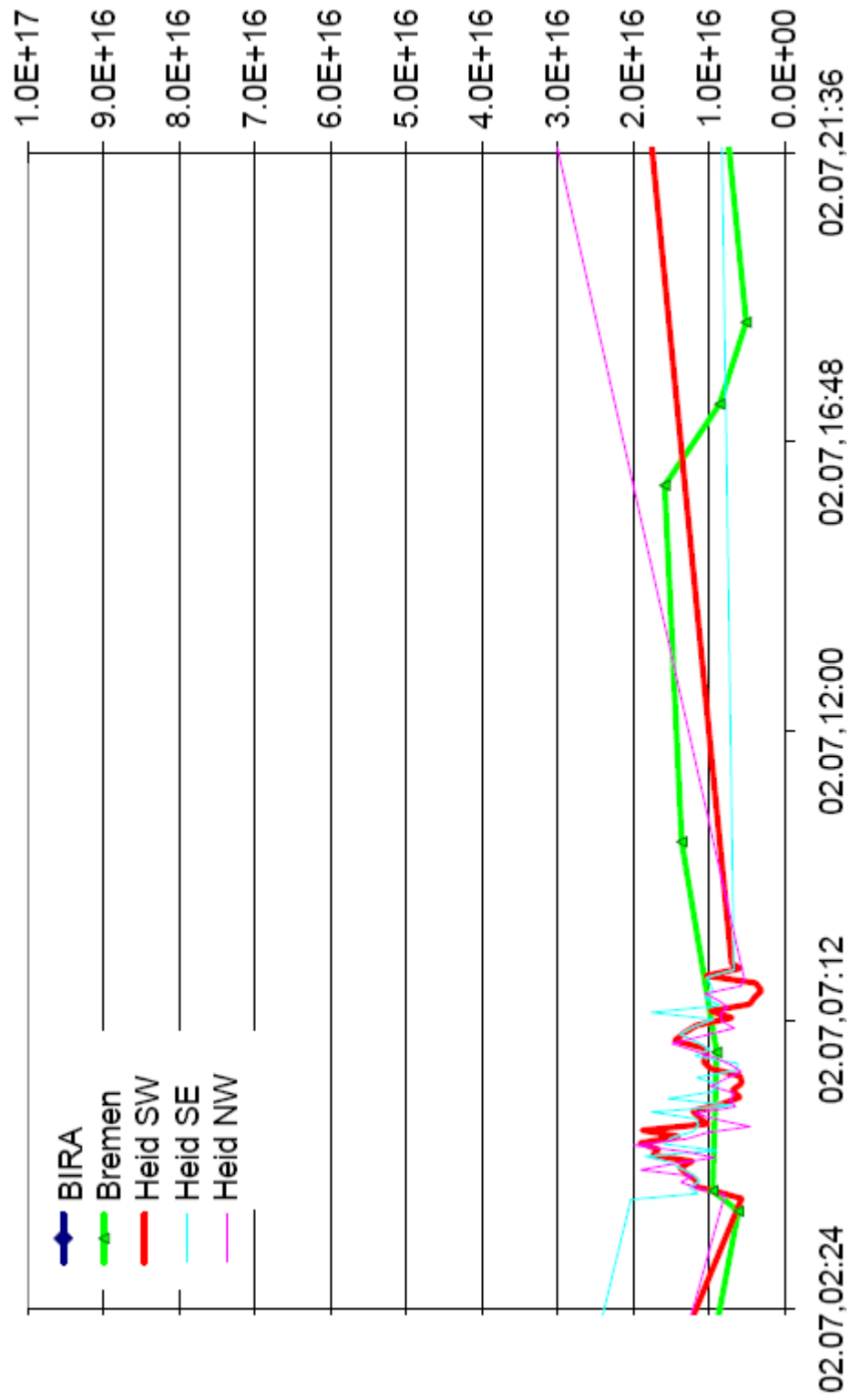


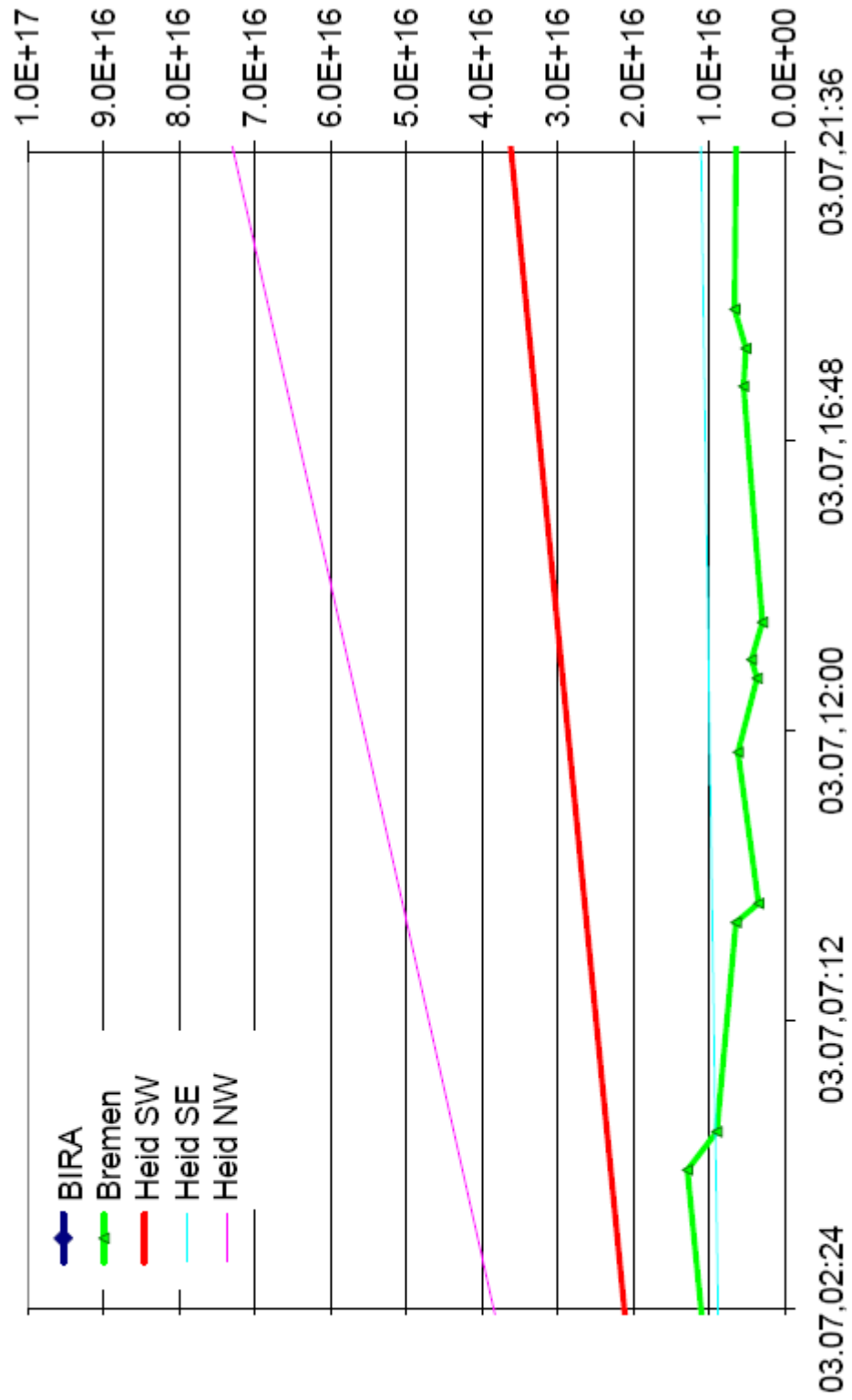


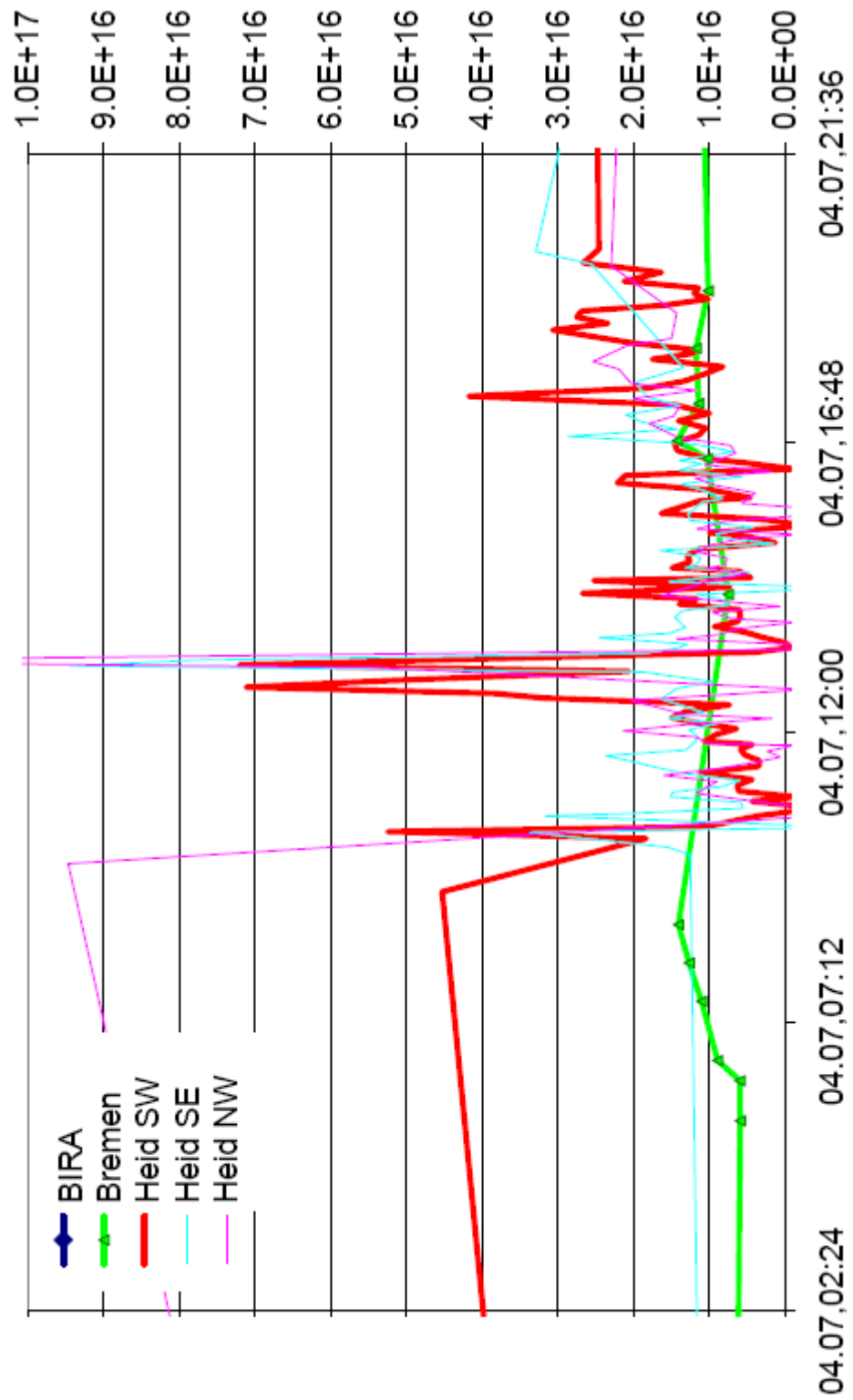


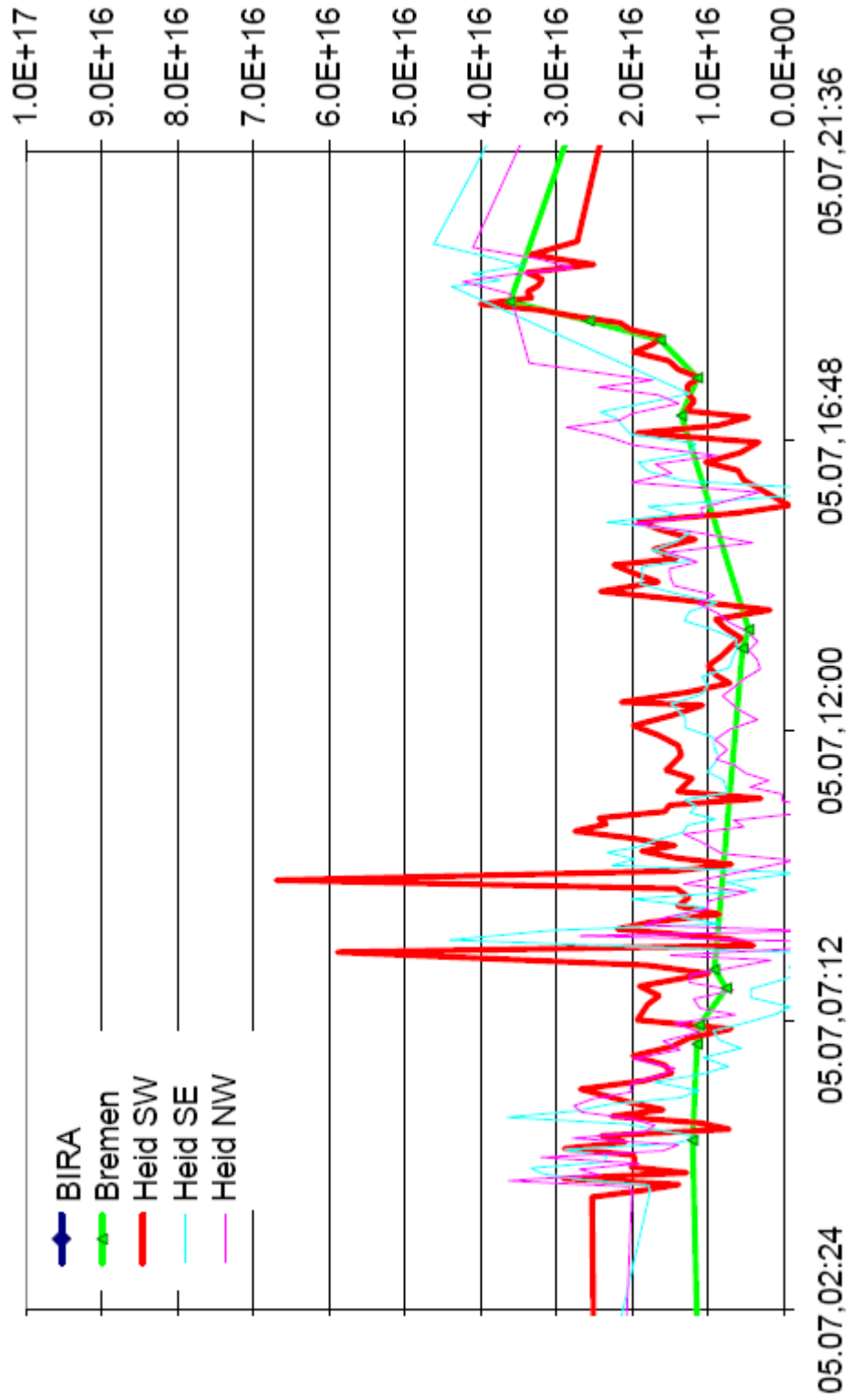


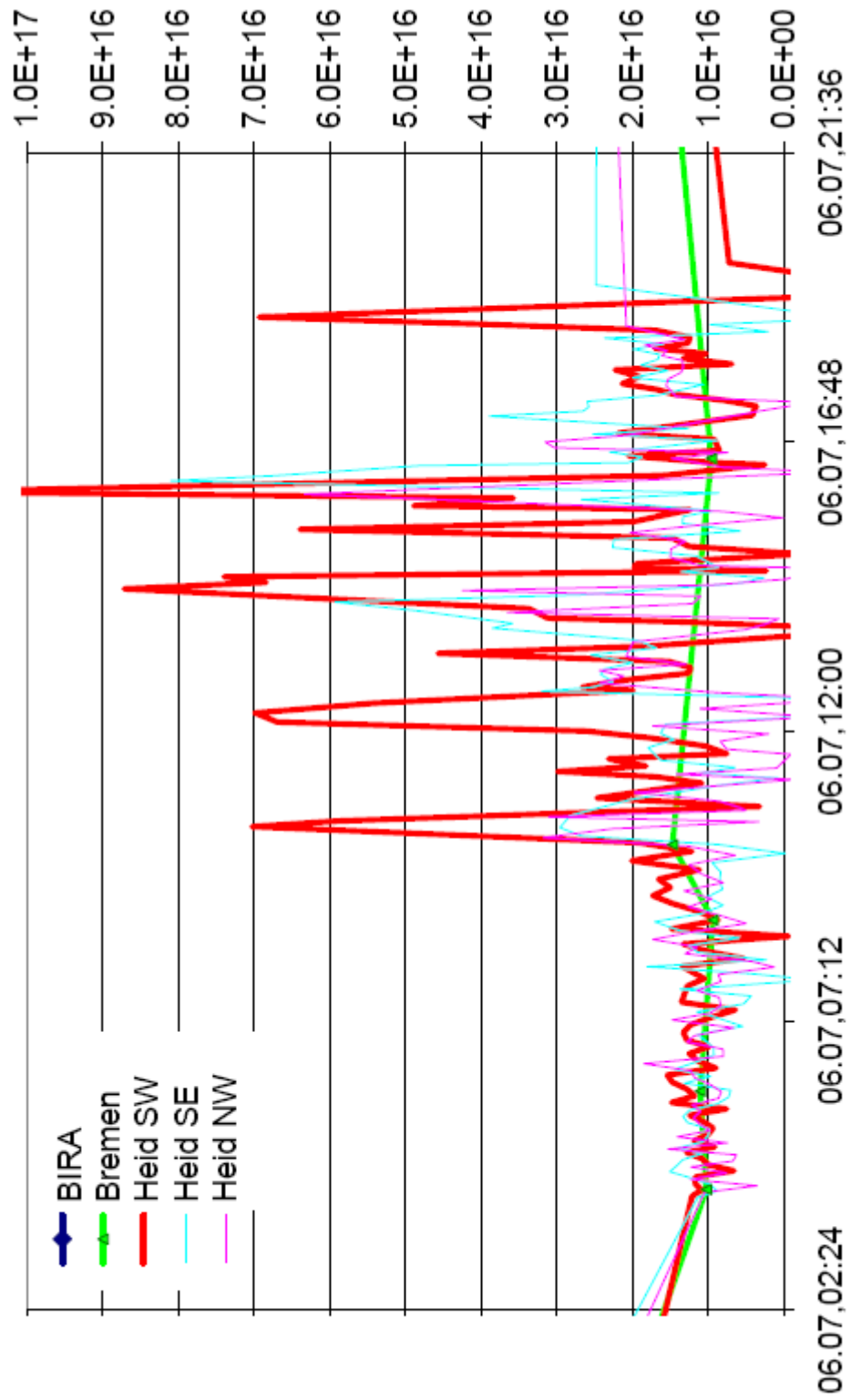


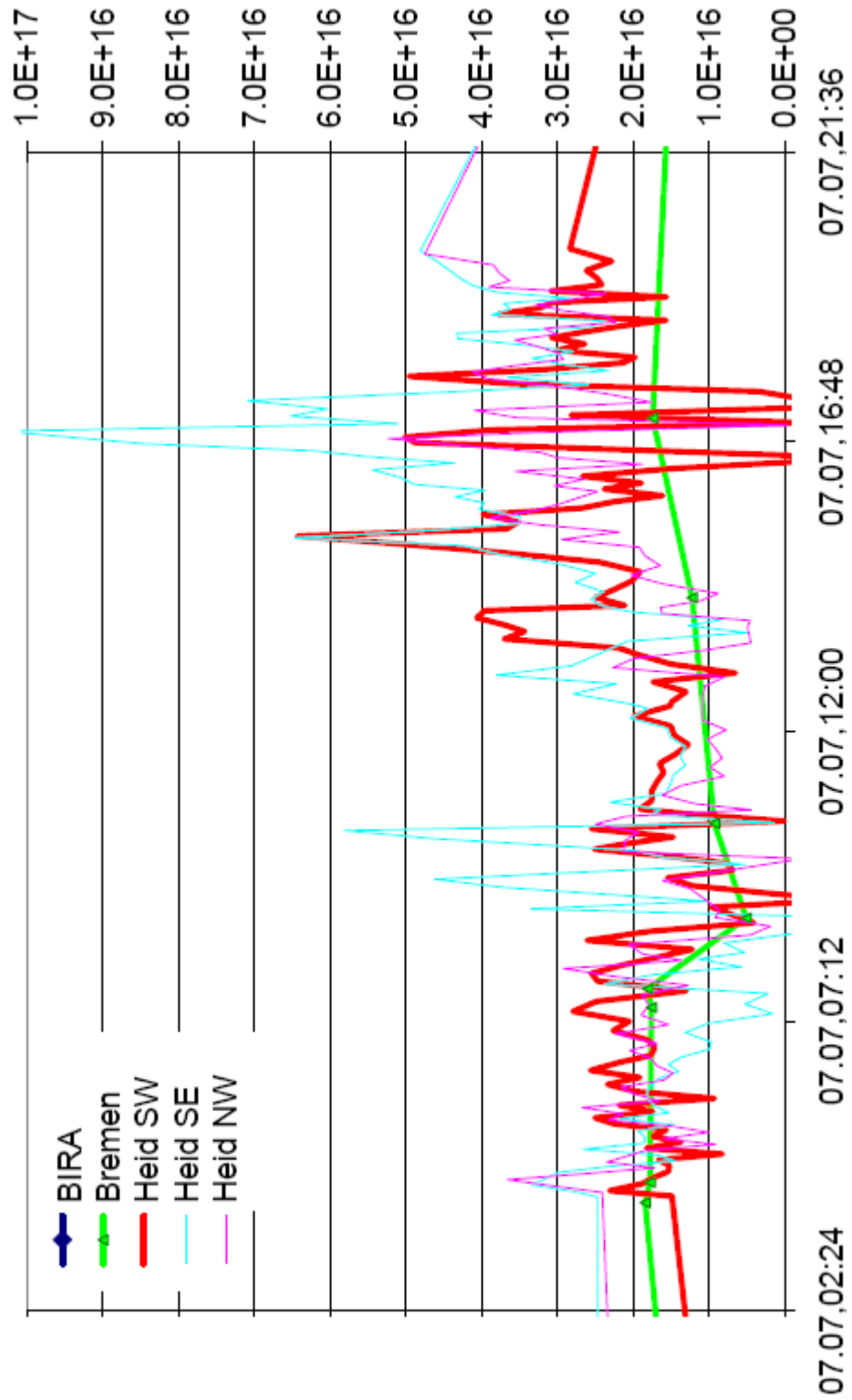


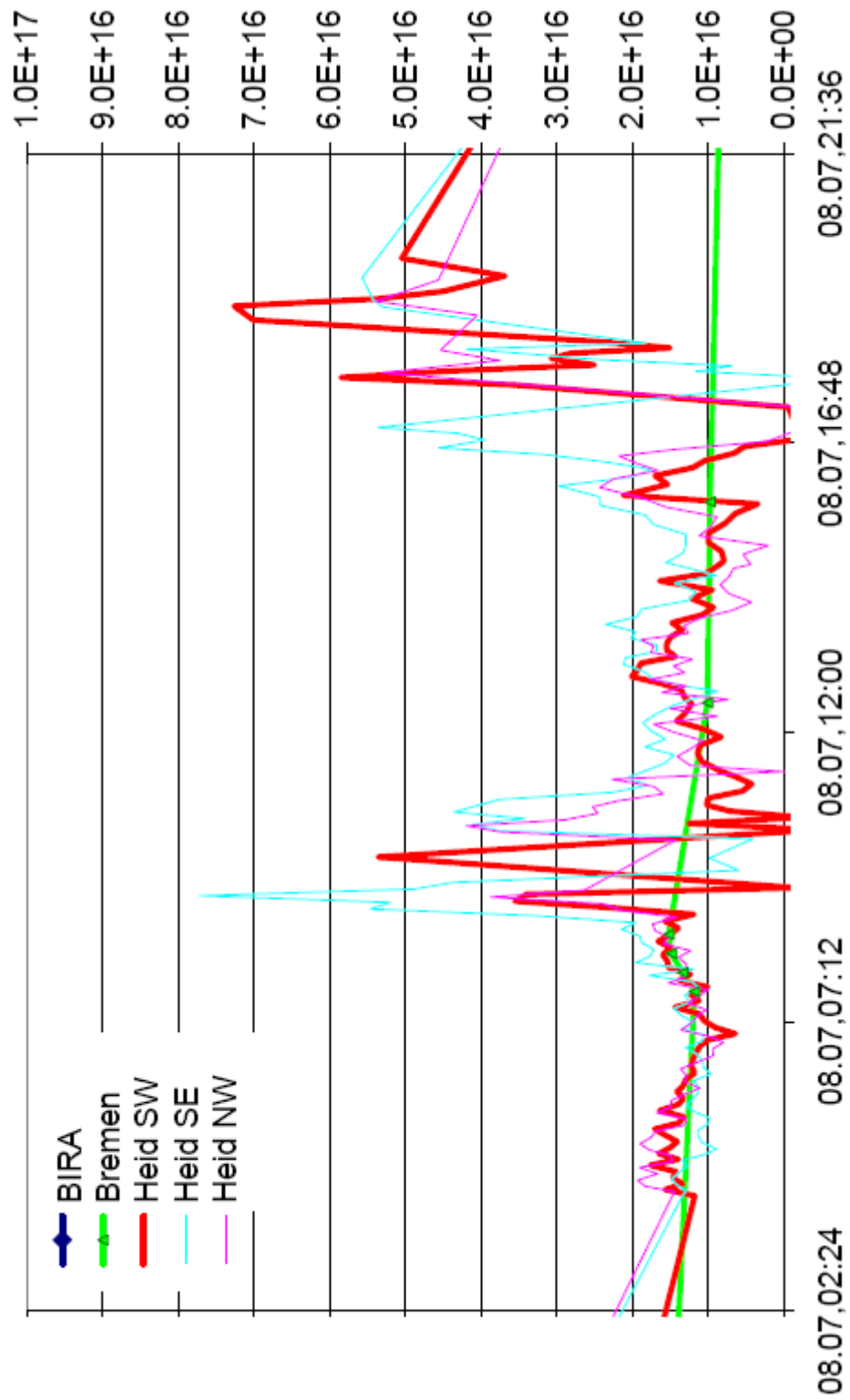


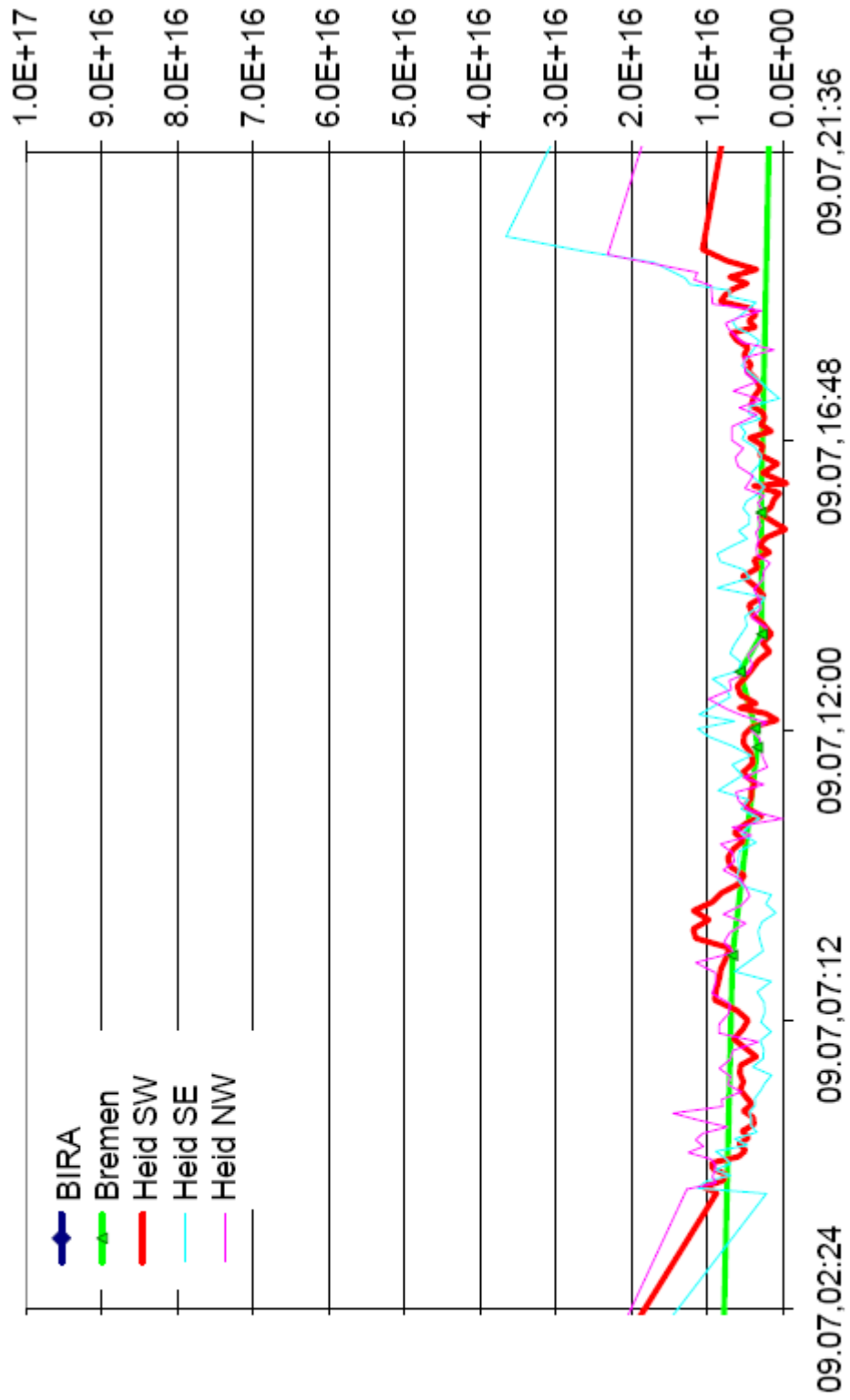


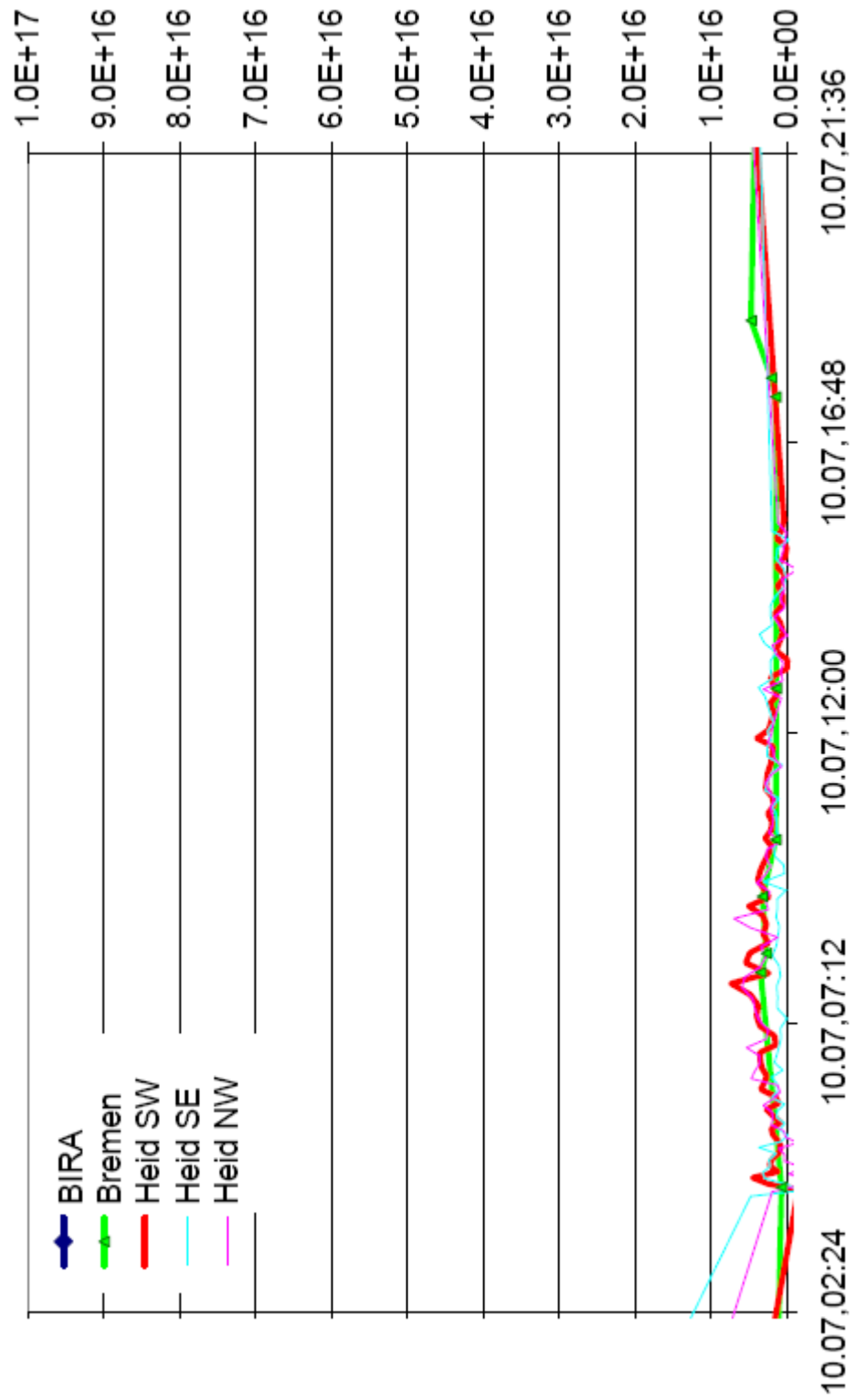


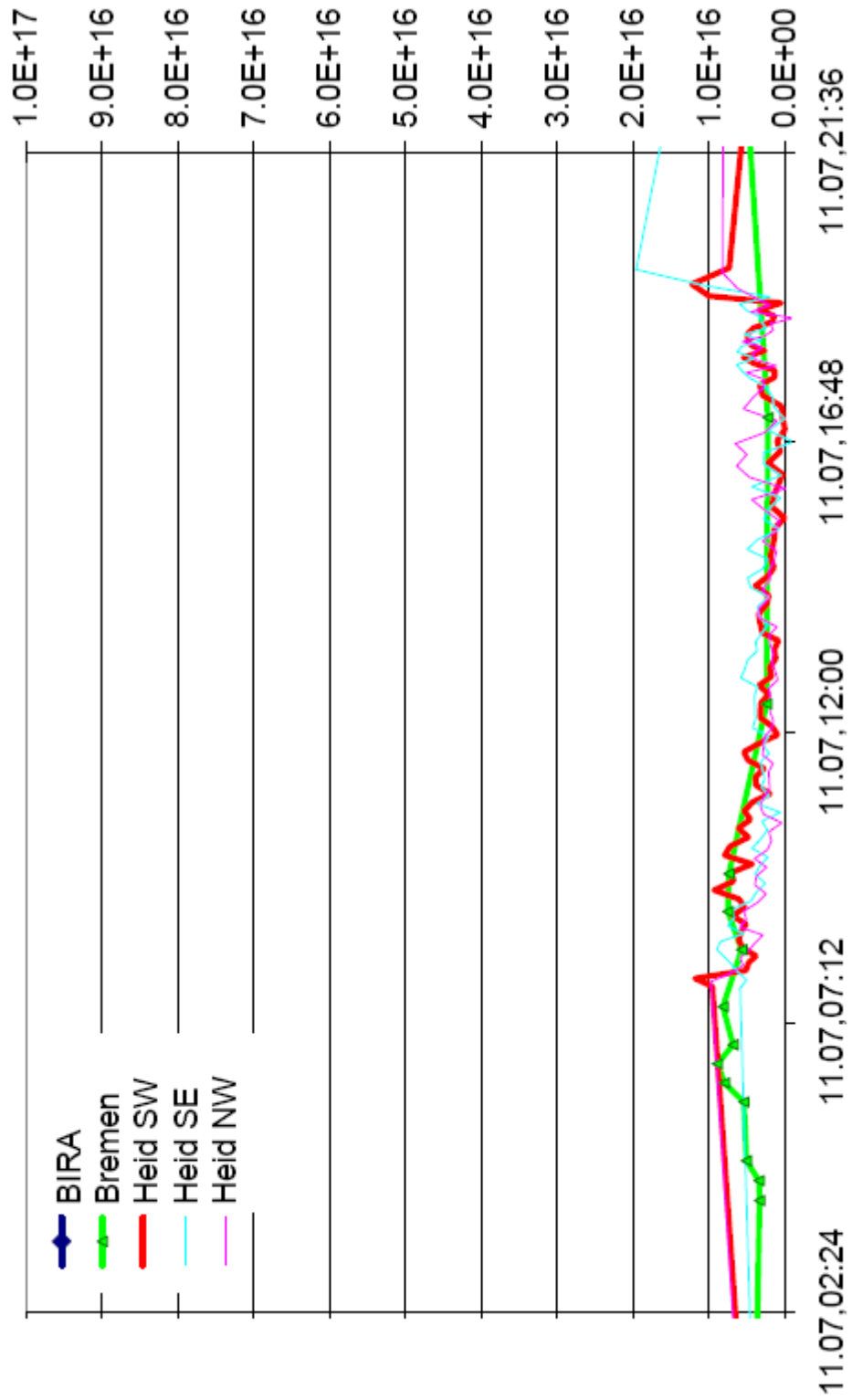


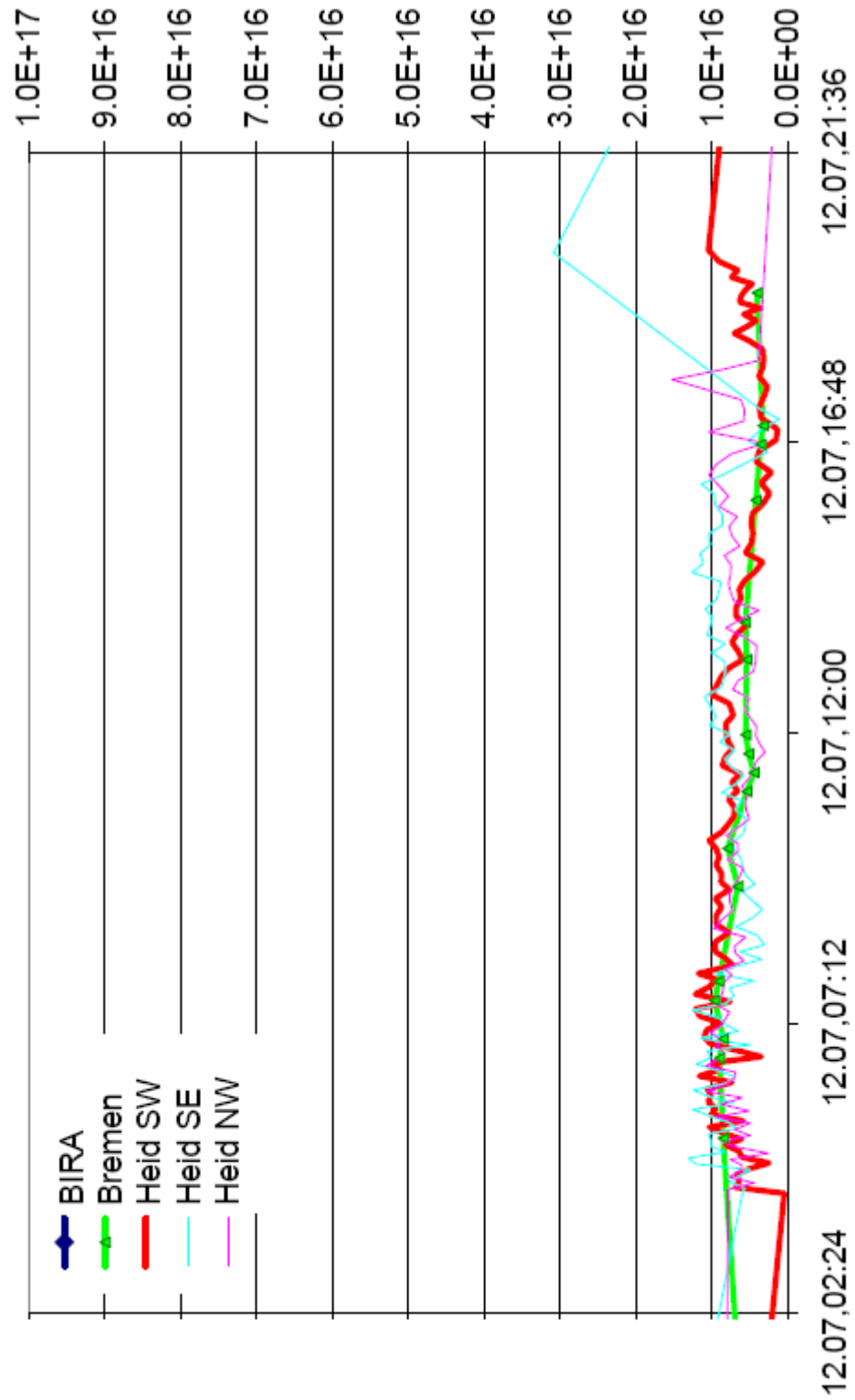


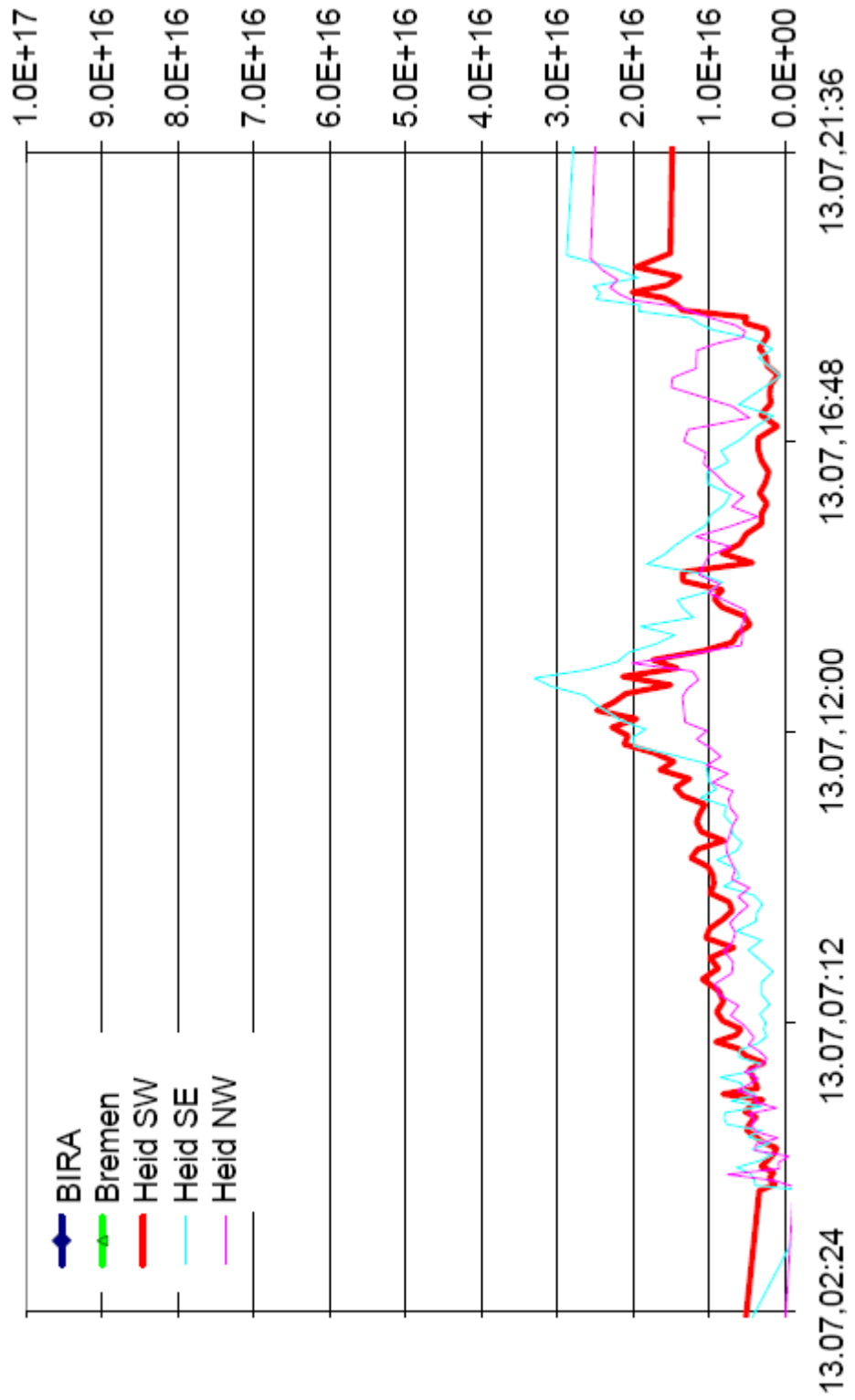












# List of Figures

2.1	Mean repartition of tropospheric $\text{NO}_2$ . . . . .	7
2.2	Ozone mixing ratio isopleths . . . . .	8
2.3	The Chapman cycle. Adapted from [Hönninger, 2002]. . . . .	10
2.4	Comparison between observed and modelled stratospheric ozone mixing ratio, if only the Chapman cycle is taken into account and by taking $\text{HOx}$ , $\text{NOx}$ , and $\text{ClOx}$ chemistry into account. The measurements can be explained best, if $\text{HOx}$ , $\text{NOx}$ , and $\text{ClOx}$ chemistry is included in the models. (Adapted from [Röth, 1994]) . . . . .	11
2.5	An overview of tropospheric bromine chemistry during polar sunrise including the bromine explosion and excluding chlorine chemistry (Adapted from [Hönninger, 2002]). . . . .	15
3.1	<i>Absolute cross section <math>\sigma_{\text{abs}}(\lambda)</math> and narrow band (differential) cross section <math>\sigma'(\lambda)</math> of ozone as instance. <math>\sigma'(\lambda)</math> can be extracted by subtracting the broad band part of the cross section from <math>\sigma_{\text{abs}}(\lambda)</math> which is mathematically the application of a high pass filter. . . . .</i>	23
3.2	<i>Above: The differential optical density <math>\tau'</math> which is derived from <math>I'_0</math>. Below: Dispartment of the absolute cross section <math>\sigma_{\text{abs}}</math> into a broad band part <math>\sigma^{\text{B}}</math> and a narrow band part <math>\sigma'</math>. . . . .</i>	24
3.3	<i>The components of a simplified DOAS setup. Light traverses an air mass and is attenuated by an absorber, characteristically for the trace gas in the atmosphere (in this example formaldehyde). (a) shows the respective spectrum with the absorption structure of formaldehyde. In (b) the light was convolved by the spectrograph and (c) shows the mapping by the detector. Afterwards the spectrum consisting of discrete pixels is stored in a connected PC [Stutz and Platt, 1996]. . . . .</i>	25
3.4	<i>High resolution cross sections from literature in the wavelength range from 290 to 460 nm. From top to down: <math>\text{O}_3</math> [Bogumil et al., 2003], <math>\text{SO}_2</math> [Vandaele et al., 1994], <math>\text{NO}_2</math> [Vandaele et al., 1998], <math>\text{HONO}</math> [Stutz et al., 2000], <math>\text{CHOCHO}</math> [Volkamer et al., 2005], <math>\text{HCHO}</math> [Meller and Moortgat, 2000] as well as <math>\text{BrO}</math> [Wilmouth et al., 1999] in <math>10^{-19} \text{ cm}^2</math> and <math>\text{O}_4</math> [Greenblatt et al., 1990] in arbitrary units. . . . .</i>	27
3.5	<i>(a): High resolution solar spectrum in the wavelength range from 300 to 460 nm. The continuous spectrum is overlaid by Fraunhofer lines. (b): The same as in (a), but convolved with a Gaussian instrument function with 0.7 nm full width at half maximum, which is a typical resolution for DOAS measurements. (c): Ring spectrum modelled from (b). When the solar spectrum has dips, the Ring spectrum features peaks and vice versa, which illustrates the Filling-in process. . .</i>	33

3.6	<i>Sketch of a MAX-DOAS measurement in the single scattering case. The telescope points to different elevation angles including the zenith in order to collect scattered light. The red points indicate scattering events along the line of sight of the elevation angles.</i> . . . . .	37
4.1	Rayleigh scattering phase function . . . . .	42
4.2	Mie scattering phase functions . . . . .	45
4.3	Sketch of the direct comparison retrieval process . . . . .	56
4.4	Calculated O <sub>4</sub> air mass factors for 70° solar zenith angle . . . . .	58
4.5	Ratio of calculated O <sub>4</sub> air mass factors . . . . .	59
4.6	Ratios of the modelled NO <sub>2</sub> ΔAMFs and the measured NO <sub>2</sub> ΔSCD . . . . .	60
4.7	MAX-DOAS measurements under clear sky and cloudy conditions . . . . .	61
5.1	Mini-MAX-DOAS instrument. . . . .	64
5.2	Ocean Optics USB2000 sketch . . . . .	65
5.3	UG5 filter transmittance . . . . .	66
5.4	Auto-MAX-DOAS overview . . . . .	68
5.5	The outdoor part of the Polarstern instrument . . . . .	72
5.6	Cables connecting the outdoors set-up with the indoors set-up . . . . .	72
5.7	The Polarstern indoors set-up . . . . .	73
5.8	Illustration of the spectrograph of the Polarstern instrument . . . . .	73
5.9	Example of an image of the two-dimensional CCD chip . . . . .	74
5.10	Spectrograph stray light areas on the CCD chip . . . . .	76
6.1	Research Vessel Polarstern . . . . .	79
6.2	The route of the first leg of the cruise ANT-XXI/1. . . . .	84
6.3	Temperature vertical profiles during the first week . . . . .	85
6.4	Temperature vertical profiles during the second week . . . . .	85
6.5	Example (1) of elevated tropospheric BrO dSCDs. . . . .	87
6.6	Example (2) of elevated tropospheric BrO dSCDs. . . . .	88
6.7	Indication of tropospheric DSCDs calculation method. . . . .	89
6.8	The exact positions of the RV Polarstern during measurements. . . . .	91
6.9	Tropospheric BrO DSCDs during the 1st leg of the cruise ANT-XXI/1 . . . . .	92
6.10	Ratios from Radiative Transfer Calculations . . . . .	94
6.11	(DAMFs) for the different BrO layer height scenarios . . . . .	97
6.12	The weekly average chlorophyll concentrations. . . . .	99
6.13	The correlation between the BrO (DSCDs) (in molec. /cm <sup>2</sup> ) and the local chlorophyll concentrations (in mg/m <sup>3</sup> ) . . . . .	101
6.14	Two examples of calculated back trajectories. . . . .	102
6.15	Back trajectories were in contact with sea surface . . . . .	102
6.16	The correlation of BrO with the average chlorophyll concentrations upwind. . . . .	103
6.17	The correlation of the BrO (DSCDs) with the maximum chlorophyll concentrations. . . . .	104
6.18	The correlation plots of the BrO the water surface contact time. . . . .	104
6.19	the correlation of BrO (DSCDs) with Product 1 . . . . .	105
6.20	The correlation of the BrO (DSCDs) with Product 2. . . . .	105
6.21	Correlation coefficients of different parameters with BrO. . . . .	107
6.22	Correlations coefficients of BrO with chlorophyll parameters calculated from the first one and two days back in time. . . . .	108

6.23	The route of the cruise and daily positions of the RV Poseidon. . . . .	109
6.24	BrO tropospheric (DSCDs) along the route of the cruise of RV Poseidon between 08.02.2007 and 24.02.2007. . . . .	110
6.25	Two examples of calculated back trajectories with HYSPLIT model for the days 14.02.2007 and 18.02.2007. . . . .	111
6.26	Time series of duration of back trajectories contact with water surface.	111
6.27	The weekly average chlorophyll concentrations at the RV Poseidon measurements area. . . . .	112
6.28	The correlation of the BrO (DSCDs) with the local chlorophyll concentrations (M.Martin). . . . .	113
6.29	<i>The correlation plots of the BrO (DSCDs) at 6<math>\sigma</math> elevation angle (M.Martin 2007) with the water surface contact time. . . . .</i>	114
6.30	<i>The correlation of BrO (DSCDs) (molec./cm<sup>2</sup>) at 6<math>\sigma</math> elevation angle (M.Martin 2007) with the average and maximum chlorophyll concentrations (mg/m<sup>3</sup>) along the tracks of back trajectories. . . . .</i>	114
6.31	Correlations coefficients of different chlorophyll parameters with BrO (DSCDs)(M.Martin 2007). . . . .	115
6.32	The correlation coefficients of BrO with various chlorophyll parameters.	116
6.33	<i>Correlation of BrO (DSCDs) at elevation angle 3<math>\sigma</math> and 10<math>\sigma</math> with aerosol (pH) number measured during day time. [aerosol data adapted from W.Keene et al., 2004] . . . . .</i>	119
6.34	<i>Correlation of BrO (DSCDs) at elevation angle 3<math>\sigma</math> and 10<math>\sigma</math> with aerosol pH number measured during night time.[aerosol data adapted from W.Keene et al., 2004] . . . . .</i>	119
6.35	<i>The correlation of BrO (DSCDs) at elevation angles 3<math>\sigma</math> and 10<math>\sigma</math> with percentage deficit in particulate (Br<sup>-</sup>) marine aerosols relative to sea salt (during day time). [aerosol data adapted from W.Keene et al., 2004] . . . . .</i>	120
6.36	<i>The correlation of BrO (DSCDs) at elevation angles 3<math>\sigma</math> and 10<math>\sigma</math> with the percentage deficit in particulate (Br<sup>-</sup>) marine aerosols relative to sea salt (during the night time).[aerosol data adapted from W.Keene et al., 2004] . . . . .</i>	120
6.37	<i>The correlation of BrO (DSCDs) at elevation angles 3<math>\sigma</math> and 10<math>\sigma</math> with absolute particulate Br<sup>-</sup> deficit relative to sea salt during day time. [aerosol data adapted from W.Keene et al., 2004] . . . . .</i>	122
6.38	<i>The correlation of BrO (DSCDs) at elevation angles 3<math>\sigma</math> and 10<math>\sigma</math> with absolute particulate Br<sup>-</sup> deficit relative to sea salt during night time. [aerosol data adapted from W.Keene et al., 2004]. . . . .</i>	122
6.39	<i>The correlation of BrO (DSCDs) at elevation angles 3<math>\sigma</math> and 10<math>\sigma</math> with absolute particulate Br<sup>-</sup> deficit relative to sea salt during night time.</i>	123
6.40	<i>Left panels show the positions of the RV Polarstern during the three weeks of measurement. Right panels show the weekly average of (AOD 865nm) during the three weeks(23.10.2003 - 01.11.2003)(01.11.2003 - 08.11.2003)(09.11.2003 - 16.11.2003). Please notice that the measurements ended on 13.11.2003. . . . .</i>	124
6.41	<i>The correlation of BrO (DSCDs) at elevation angles 3<math>\sigma</math> and 10<math>\sigma</math> with the dust Aerosol Optical Depth (AOD 865nm) from SeaWifs satellite maps. . . . .</i>	125

6.42	<i>Correlation coefficients of BrO ( DSCDs) with the different aerosol parameters.</i>	125
6.43	<i>Satellite maps of (AOD 865 nm) from SeaWifs for the three weeks (2-9 Feb., 10-17 Feb. and 17-25 Feb.) and also the daily positions of the RV Poseidon during measurements.</i>	126
6.44	<i>The correlation of BrO ( DSCDs) with dust Aerosol Optical Depth (AOD 865 nm) (M. Martin 2007).</i>	127
7.1	The road between Brussels and Heidelberg	131
7.2	The NO <sub>2</sub> dSCDs from measurements along the road between Brussels (Belgium) and Heidelberg (Germany).	132
7.3	The location of Weisweiler power plant.	132
7.4	The term ( $S_{ref.} - S_{strat.}$ ) as a function of time.	136
7.5	The different polynomial fits of the term ( $S_{ref.} - S_{strat.}$ ).	136
7.6	The consistency of the VCD values from different elevation angles.	137
7.7	The route from Brussels to Heidelberg with the NO <sub>2</sub> VCDs color coded.	138
7.8	The route from Brussels to Heidelberg with the NO <sub>2</sub> VCDs.	139
7.9	Tropospheric NO <sub>2</sub> VCDs from cloud free pixels of SCIAMACHY.	139
7.10	Cloud-free NO <sub>2</sub> TVCDs from OMI satellite data.	140
7.11	Buncefield Oil Depot Map.	142
7.12	Buncefield Oil Depot fire pictures.	143
7.13	Buncefield Oil Depot plume intensity.	143
7.14	Buncefield Oil Depot fire plume extent.	144
7.15	A Satellite image of Buncefield Oil Depot plume (NOAA).	144
7.16	A satellite image of the Buncefield Oil Depot fire plume (NASA).	145
7.17	The driving route on 14.12.2005 from Heidelberg to Le Havre via Calais.	147
7.18	The driving route on 14.12.2005 from Calais to Le Havre via Calais.	147
7.19		150
7.20	NO <sub>2</sub> dSCDs on the road between Calais and Le Havre	151
7.21	NO <sub>2</sub> VCDs on the road between Calais and Le havre	151
7.22	NO <sub>2</sub> VCDs as a function of Geo-location along the route on 14.12.2005.	152
7.23	The route of driving on 15.12.2005.	153
7.24	NO <sub>2</sub> dSCDs from the measurements on 15.12.2005	154
7.25	NO <sub>2</sub> VCDs from the measurements on 15.12.2005	154
7.26	The NO <sub>2</sub> VCDs as a function of Geo-location on 15.12.2005	155
7.27	The back trajectories of air on 14.12.2005 (A)	156
7.28	The back trajectories of air on 14.12.2005 (B)	157
7.29	The back trajectories of air on 14.12.2005 (C)	158
7.30	The back trajectories of air on 14.12.2005 (D)	159
7.31	The back trajectories of air on 15.12.2005 (A)	160
7.32	The back trajectories of air on 15.12.2005 (B)	161
7.33	The route around Mannheim-Ludwegshaven area	163
7.34	Location example (1) of Auto-MAX-DOAS during driving	164
7.35	Overview of meteorological stations around Mannheim	164
7.36	Wind direction around Mannheim on 23.08.06	166
7.37	Wind direction around Mannheim on 24.08.06	167
7.38	Wind speed around Mannheim on 23.08.06	168
7.39	Wind speed around Mannheim on 24.08.06	169
7.40	The NO <sub>2</sub> dSCDs on 23.08.2006	170

---

7.41	The NO <sub>2</sub> dSCDs on 24.08.2006 . . . . .	170
7.42	wind . . . . .	171
7.43	wind . . . . .	171
7.44	wind . . . . .	172
7.45	wind . . . . .	172
7.46	Wind . . . . .	173
7.47	Wind . . . . .	173
8.1	Cabauw site on the map . . . . .	179
8.2	The three Heidelberg telescopes at Cabauw site . . . . .	180
8.3	Cabauw VCDs . . . . .	181
8.4	Cabauw VCDs . . . . .	182
8.5	May15 homogeneous morning heterogeneous afternoon . . . . .	183
8.6	Ratios between max. and min. NO <sub>2</sub> DSCDs at Cabauw . . . . .	184
8.7	Scatterplots of the tropospheric NO <sub>2</sub> columns retrieved during DAN- DELIONS campaign . . . . .	185
8.8	MAX-DOAS results comparison with Satellite data . . . . .	186



# List of Tables

2.1	NO <sub>x</sub> emissions . . . . .	6
4.1	Aerosol scenarios . . . . .	57
6.1	Polarstern Technical data . . . . .	80
6.2	Time periods and destinations of the five legs of ANT-XXI . . . . .	82
6.3	Latitudes reached by the RV Polarstern . . . . .	83
8.1	Participating instruments . . . . .	178



# Bibliography

- Aben, I., D. M. Stam, and F. Helderma (2001). The Ring effect in skylight polarisation. *Geophys. Res. Lett.* 28, 519–522.
- Albritton, D. L., A. L. Schmeltekopf, and R. N. Zare (1976). An introduction to the least-squares fitting of spectroscopic data. In R. K. Narahari and M. W. Weldon (Eds.), *Molecular Spectroscopy: Modern Research*. Orlando, Florida, USA: Academic Press.
- Alicke, B., K. Hebestreit, J. Stutz, and U. Platt (1999). Iodine oxide in the marine boundary layer. *Nature* 397, 572 – 573.
- Atkinson, R., D. L. Baulch, R. A. Cox, J. N. Crowley, R. F. Hampson, R. G. Hynes, M. E. Jenkin, M. J. Rossi, and J. Troe (2004). Evaluated kinetic and photochemical data for atmospheric chemistry: Volume I - gas phase reactions of O<sub>x</sub>, HO<sub>x</sub>, NO<sub>x</sub> and SO<sub>x</sub> species. *Atm. Chem. and Phys.* 4, 1461–1738.
- Barrie, L., J. Bottenheim, R. Schnell, P. Crutzen, and R. Rasmussen (1988). Ozone destruction and photochemical reactions at polar sunrise in the lower arctic atmosphere. *Nature* 334, 138–141.
- Bates, D. R. and M. Nicolet (1950). Atmospheric hydrogen. *Publ. Astron. Soc. Pac.* 62, 106–110.
- Beirle, S., U. Platt, M. Wenig, and T. Wagner (2003). Weekly cycle of NO<sub>2</sub> by GOME measurements: a signature of anthropogenic sources. *Atm. Chem. and Phys.* 3, 2225–2232.
- Beirle, S., U. P. and T. Wagner (2004). Monitoring nitrogen oxides with satellite instruments: High resolution maps from gome narrow swath mode and sciamachy. In *Proceedings of the ENVISAT & ERS Symposium, /6-10 September 2004, Salzburg, Austria, ESA publication SP-572, (CD-ROM), /2004c*.
- Bevington, P. (1969). *Data Reduction and Error Analysis for the Physical Sciences*. New York: McGraw-Hill.
- Bobrowski, N., G. Hönninger, B. Galle, and U. Platt (2003). Detection of bromine monoxide in a volcanic plume. *Nature* 423(6937), 273–276.
- Bogumil, K., J. O., T. Homann, S. Voigt, P. Spietz, O. Fleischmann, A. Vogel, M. Hartmann, H. Bovensmann, J. Frerik, and J. Burrows (2003). Measurements of Molecular Absorption Spectra with the SCIAMACHY Pre-Flight Model: Instrument Characterization and Reference Data for Atmospheric Remote-Sensing in the 230-2380 nm Region. *J. Photochem. Photobiol. A: Chem.* 157, 167–184.
- Brinkmann, R. T. (1968). Rotational Raman scattering in planetary atmospheres. *Astrophys. J.* 154, 1087–1093.

- Burrows, J., U. Platt, K. Chance, M. Vountas, V. Rozanov, A. Richter, H. Haug, and L. Marquard (1996). *Study of the Ring Effect*. Noordivijk, The Netherlands: European Space Agency.
- Bussemer, M. (1993). Der Ring-Effekt: Ursachen und Einfluß auf die spektroskopische Messung stratosphärischer Spurenstoffe. Diploma thesis, University of Heidelberg.
- Chance, K. and R. J. D. Spurr (1997). Ring effect studies; Rayleigh scattering, including molecular parameters for rotational Raman scattering and the Fraunhofer spectrum. *Appl. Opt.* *36*, 5224–5230.
- Chapman, S. (1930). On ozone and atomic oxygen in the upper atmosphere. *Philos. Mag.* *10*, 369–383.
- Crutzen, P. J. (1970). The influence of nitrogen oxide on the atmospheric ozone content. *Q.J.R. Meteorol. Soc.* *96*, 320–327.
- Crutzen, P. J. and P. H. Zimmermann (1991). The changing photochemistry of the troposphere. *Tellus* *43AB*, 136–151.
- Deutschmann, T. and T. Wagner (2006). *TRACY-II Users manual*. University of Heidelberg.
- Diebel, D., J. Burrows, R. de Beek, R. Munro, B. Kerridge, L. Marquard, U. Platt, and H. Frank (1995). Detailed analysis of the retrieval algorithms selected for the level 1-2 processing of GOME data (Tracegas study). Technical report, ESA contract 10728/94/NL/CM, prepared by SERCO Europe Ltd., Southall, U.K.
- Eskes, H. J. and K. F. Boersma (2003). Averaging kernels for DOAS total-column satellite retrievals. *Atm. Chem. and Phys.* *3*, 1285–1291.
- Fan, S. and D. Jacob (1992). Surface ozone depletion in arctic spring sustained by bromine reactions on aerosols. *Nature* *359*, 522–524.
- Farman, J. C., B. G. Gardiner, and J. D. Shanklin (1985). Large losses of total ozone in Antarctica reveal seasonal ClO<sub>x</sub>/NO<sub>x</sub> interaction. *Nature* *315*, 207–210.
- Fickert, S., J. W. Adams, and J. N. Crowley (1999). Activation of Br<sub>2</sub> and BrCl via uptake of HOBr onto aqueous salt solutions. *J. Geophys. Res.* *104*, 23719–23727.
- Finlayson-Pitts, B. J. and J. N. Pitts jr. (2000). *Chemistry of the upper and lower atmosphere: Theory, experiments and applications*. Academic Press, San Diego.
- Fish, D. J. and R. L. Jones (1995). Rotational Raman scattering and the Ring effect in zenith-sky spectra. *Geophys. Res. Lett.* *22*, 811–814.
- Fishman, J. and P. Crutzen (1978). The origin of ozone in the troposphere. *Nature* *274*, 855–858.
- Frankenberg, C., J. F. Meirik, M. van Weele, U. Platt, and T. Wagner (2005). Assessing methane emissions from global space-borne observations. *Science* *308*, 1010 – 1014.

- Frankenberg, C., U. Platt, and T. Wagner (2005). Iterative maximum a posteriori (imap)-doas for retrieval of strongly absorbing trace gases: Model studies for CH<sub>4</sub> and CO<sub>2</sub> retrieval from near infrared spectra of SCIAMACHY onboard ENVISAT. *Atm. Chem. and Phys.* 5, 9–22.
- Frieß, U. (2001). *Spectroscopic Measurements of Atmospheric Trace Gases at Neumayer-Station, Antarctica*. Ph. D. thesis, University of Heidelberg.
- Frieß, U., P. S. Monks, J. J. Remedios, A. Rozanov, R. Sinreich, T. Wagner, and U. Platt (2006). MAX-DOAS O<sub>4</sub> measurements: A new technique to derive information on atmospheric aerosols: 2. Modeling studies. *J. Geophys. Res.* 111, D14203.
- Gomer, T., T. Brauers, F. Heintz, J. Stutz, and U. Platt (1993). *MFC User Manual, Vers. 1.98*. Institut für Umweltphysik, Universität Heidelberg.
- Gomer, T., T. Brauers, F. Heintz, J. Stutz, and U. Platt (1995). MFC version 1.98 user manual. Technical report, University of Heidelberg.
- Grainger, J. and J. Ring (1962). Anomalous Fraunhofer line profiles. *Nature* 193, 762.
- Greenblatt, G. D., J. J. Orlando, J. B. Burkholder, and A. R. Ravishankara (1990). Absorption Measurements of Oxygen between 330 and 1140 nm. *J. Geophys. Res.* 95, 18577–18582.
- Hartley, W. N. (1881). On the absorption of solar rays by atmospheric ozone. *J. Chem. Soc.* 39, 111.
- Haug, H. (1996). Raman-Streuung von Sonnenlicht in der Erdatmosphäre. Diploma thesis, University of Heidelberg.
- Hausmann, M., U. Brandenburger, T. Brauers, and H.-P. Dorn (1997). Detection of tropospheric OH radicals by long-path differential-optical-absorption spectroscopy: Experimental setup, accuracy, and precision. *J. Geophys. Res.* 102, 16011–16022.
- Hausmann, M., U. Brandenburger, T. Brauers, and H.-P. Dorn (1999). Simple Monte Carlo methods to estimate the spectra evaluation error in differential-optical-absorption spectroscopy. *Appl. Opt.* 38(3), 462–475.
- Hausmann, M. and U. Platt (1994a). Spectroscopic measurement of bromine oxide and ozone in the high Arctic during Polar Sunrise Experiment 1992. *J. Geophys. Res.* 99 (D12), 25399–25413, 10.1029/94JD01314.
- Hausmann, M. and U. Platt (1994b). Spectroscopic measurement of bromine oxide and ozone in the high arctic during polar sunrise experiments 1992. *J. Geophys. Res.* 99, 25399–25413.
- Hebestreit, K., J. Stutz, D. Rosen, V. Matveiv, M. Peleg, M. Luria, and U. Platt (1999). Doas measurements of tropospheric bromine oxide in mid-latitudes. *Science* 283, 55–57.

- Heckel, A., A. Richter, T. Tarsu, F. Wittrock, C. Hak, I. Pundt, W. Junkermann, and J. Burrows (2005). MAX-DOAS measurements of formaldehyde in the Po-Valley, atmos. chem. phys. 5, 909-918, 2005. *Atm. Chem. and Phys.* 5, 909–918.
- Heneyey, L. and J. Greenstein (1941). Diffuse radiation in the Galaxy. *Astrophys. J. Vol. 93*, 70–83.
- Hönninger, G. (2002). *Halogen Oxide Studies in the Boundary Layer by Multi Axis Differential Optical Absorption Spectroscopy and Active Longpath-DOAS*. Ph. D. thesis, University of Heidelberg.
- Hönninger, G., N. Bobrowski, E. Palenque, R. Torrez, and U. Platt (2004). Reactive bromine and sulfur emissions at salar de uyuni, bolivia. *Geophys. Res. Lett.* 31(4).
- Hönninger, G. and U. Platt (2002). Observations of BrO and its vertical distribution during surface ozone depletion at Alert. *Atmos. Environ.* 36, 2481–2489.
- Hönninger, G., C. von Friedeburg, and U. Platt (2004). Multi axis differential optical absorption spectroscopy (MAX-DOAS). *Atm. Chem. and Phys.* 4, 231–254.
- Houzeau, A. (1858). Preuve de la présence dans l’atmosphère d’un nouveau principe gazeux, l’oxygène naissant. *C. R. Acad. Sci. Paris* 46, 89.
- Johnston, H. S. (1971). Reduction of stratospheric ozone by nitrogen oxide catalysts from supersonic transport exhaust. *Science* 173, 517–522.
- Johnston, P. (1996). Making uv/vis cross sections, reference fraunhofer and synthetic spectra. unpublished manuscript.
- Kern, C., S. Trick, B. Rippel, and U. Platt (2006). Applicability of light-emitting diodes as light sources for active DOAS measurements. *Appl. Opt.* 45, 2077–2088.
- Kraus, S. (2004). Doasis: Doas intelligent system. Software, copyright 2004 stefan kraus, Institute of Environmental Physics, University of Heidelberg, Heidelberg. In cooperation with Hoffmann Messtechnik GmbH.
- Kurucz, R. L., I. Furenlid, J. Brault, and L. Testerman (1984). *Solar Flux Atlas from 296 to 1300 nm*. Sunspot, New Mexico, U.S.A.: National Solar Observatry.
- Lee, D., I. Köhler, E. Grobler, F. Rohrer, R. Sausen, L. Gallardo-Klenner, J. Olivier, F. Dentener, and A. Bouwman (1997). Estimates of global NO<sub>x</sub> emissions and their uncertainties. *Atmos. Environ.* 31 (12), 1735–1749.
- Lehrer, E., G. Hönninger, and U. Platt (2004). A one dimensional model study of the mechanism of halogen liberation and vertical transport in the polar troposphere. *Atm. Chem. and Phys.* 4, 2427–2440.
- Leighton, P. A. (1961). Photochemistry of air pollution. Academic Press, New York.
- Leser, H., G. Hönninger, and U. Platt (2003). Max-doas measurements of bro and no<sub>2</sub> in the marine boundary layer. *Geophys. Res. Lett.* 30(10).
- Leue, C., W. Wenig, T. Wagner, O. Klimm, U. Platt, and B. Jähne (2001, March). Quantitative analysis of NO<sub>x</sub> emissions from Global Ozone Monitoring Experiment satellite image sequences. *J. Geophys. Res.* 106(D6), 5493–5505.

- Levenberg, K. (1944). A method for the solution of certain non-linear problems in least squares. *Quart. Appl. Math.* 2, 164–168.
- Marchuk, G., G. Mikhailov, M. Nazaraliev, R. Darbinjan, B. Kargin, and B. Elepov (1980). *The Monte Carlo Methods in Atmospheric Optics*. Berlin, New York: Springer.
- Marquard, L., T. Wagner, and U. Platt (2000). Improved Air Mass Factor Concepts for Scattered Radiation Differential Optical Absorption Spectroscopy of Atmospheric Species. *J. Geophys. Res.* 105, 1315–1327.
- Marquardt, D. W. (1963). An algorithm for least squares estimation of non-linear parameters. *Soc. Indust. Appl. Math* 11, 431–441.
- McElroy, M. B., R. J. Salawitch, C. S. Wofsy, and J. A. Logan (1986). Reductions of Antarctic ozone due to synergistic interactions of chlorine and bromine. *Nature* 321, 759–762.
- Meller, R. and G. K. Moortgat (2000). Temperature dependence of the absorption cross sections of formaldehyde between 223 and 323 K in the wavelength range 225–375 nm. *J. Geophys. Res.* 105, 7089–7101.
- Mentel, T. F., D. Bleilebens, and A. Wahner (1996). A study of nighttime nitrogen oxide oxidation in a large reaction chamber — The fate of NO<sub>2</sub>, N<sub>2</sub>O<sub>5</sub>, HNO<sub>3</sub>, and O<sub>3</sub> at different humidities. *Atmos. Environ.* 30, 4007–4020.
- Molina, L. and F. Rowland (1974). Stratospheric sink for chlorofluoromethanes: chlorine atom catalyzed destruction of ozone. *Nature* 249, 820–822.
- Noxon, J. F., E. C. Whipple, and R. S. Hyde (1979). Stratospheric NO<sub>2</sub>. 1. Observational Method and Behavior at Midlatitudes. *J. Geophys. Res.* 84, 5047–5076.
- Penndorf, R. (1957). Tables of the refractive index for standard air and the rayleigh scattering coefficient for the spectral region between 0.2 and 200  $\mu$  and their application to atmospheric optics. *J. Opt. Soc. Am.* 47(2), 176–182.
- Perliski, L. M. and S. Solomon (1993). On the evaluation of air mass factors for atmospheric near-ultraviolet and visible absorption spectroscopy. *J. Geophys. Res.* 98, 10,363–10,374.
- Perner, D., D. H. Ehhalt, H. W. Paetz, U. Platt, E. P. Roeth, and A. Volz (1976). OH radicals in the lower troposphere. *Geophys. Res. Lett.* Vol. 3, 466–468.
- Perner, D. and U. Platt (1979). Detection of nitrous acid in the atmosphere by differential optical absorption. *Geophys. Res. Lett.* Vol. 6, 917–920.
- Platt, U., J. S. (2008). *Differential Optical Absorption Spectroscopy Principles and Applications*. Springer-Verlag GmbH.
- Platt, U. (1994). Differential Optical Absorption Spectroscopy (DOAS). In M. W. Sigrist (Ed.), *Air Monitoring by Spectroscopic Techniques*, Volume 127 of *Chemical Analysis*, New York. Wiley-Interscience.

- Platt, U., L. Marquard, T. Wagner, and D. Perner (1997a). Corrections for zenith scattered light doas. *Geophys. Res. Letters* 24(14), 1759–1762.
- Platt, U., L. Marquard, T. Wagner, and D. Perner (1997b). Corrections for Zenith Scattered Light DOAS. *Geophys. Res. Lett.* 24(14), 1759–1762.
- Platt, U. and D. Perner (1980). Direct Measurements of Atmospheric CH<sub>2</sub>O, HNO<sub>2</sub>, O<sub>3</sub>, NO<sub>2</sub> and SO<sub>2</sub> by Differential Optical Absorption in the Near UV. *J. Geophys. Res.* 85, 7453–7458.
- Platt, U., D. Perner, G. W. Harris, A. M. Winer, and J. N. Pitts, Jr. (1980). Detection of NO<sub>3</sub> in the Polluted Troposphere by Differential Optical Absorption. *Geophys. Res. Lett.* 7, 89–92.
- Platt, U., D. Perner, and H. W. Pätz (1979). Simultaneous measurements of atmospheric CH<sub>2</sub>O, O<sub>3</sub> and NO<sub>2</sub> by differential optical absorption. *J. Geophys. Res.* 84, 6329–6335.
- Richter, A. (1997). *Absorptionsspektroskopische Messungen stratosphärischer Spurengase über Bremen. 53* N. Ph. D. thesis, University of Bremen, Bremen, Germany.
- Rodgers, C. D. (1976). Retrieval of atmospheric temperature and composition from remote measurements of thermal radiation. *Rev. Geophys.* 14(4), 609–624.
- Rodgers, C. D. (2000). *Inverse Methods for Atmospheric Sounding*. London: World Scientific.
- Roedel, W. (2000). *Physik unserer Umwelt - Die Atmosphäre*. Springer-Verlag, Berlin.
- Röth, E.-P. (1994). *Ozonloch – Ozonsmog: Grundlagen der Ozonchemie*. Mannheim: Bibliographisches Institut.
- Sanders, R. W., S. Solomon, M. A. Carroll, and A. L. Schmeltekopf (1988). Ground based measurements of O<sub>3</sub>, NO<sub>2</sub>, OClO and BrO during the Antarctic Ozone Depletion Event. In R. D. Bjokov and P. Fabian (Eds.), *Ozone in the Atmosphere, Quadrennial Ozone Symposium 1988*, pp. 65–70. Hampton, Va.: Deepak Publishing.
- Sanghavi, S. (2003). An efficient Mie theory implementation to investigate the influence of aerosols on radiative transfer. Diploma thesis, University of Heidelberg.
- Schönbein, C. (1840). Recherches sur la nature de l'odeur qui se manifeste dans certaines actions chimiques. *C. R. Acad. Sci. Paris* 10, 706.
- Sihler, H. (2007). Light-Emitting Diodes as Light Sources in Spectroscopic Measurements of Atmospheric Trace Gases. Diploma thesis, University of Jena.
- Sillman, S., J. Logan, and S. Wofsy (1990). The sensitivity of ozone to nitrogen oxides and hydrocarbons in regional ozone episodes. *J. Geophys. Res.* 95, 1837–1852.

- Sinreich, R., U. Frieß, T. Wagner, and U. Platt (2005). Multi axis differential optical absorption spectroscopy (MAX-DOAS) of gas and aerosol distributions. *Faraday Discuss.* 130, 153–164.
- Sinreich, R., R. Volkamer, F. Filsinger, U. Frieß, C. Kern, U. Platt, O. Sebastián, and T. Wagner (2007). MAX-DOAS detection of glyoxal during ICARTT 2004. *Atm. Chem. and Phys.* 7, 1293–1303.
- Sioris, C. E. and W. F. J. Evans (1999). Filling in of Fraunhofer and gas-absorption lines in sky spectra as caused by rotational Raman scattering. *Appl. Opt.* 38(12), 2706–2713.
- Solomon, S., R. R. Garcia, F. S. Rowland, and D. J. Wuebbles (1986). On the depletion of Antarctic ozone. *Nature* 321, 755–758.
- Solomon, S., A. L. Schmeltekopf, and R. W. Sanders (1987). On the interpretation of zenith sky absorption measurements. *J. Geophys. Res.* 92, 8311–8319.
- Stutz, J. (1991). Charakterisierung von Photodiodenzeilen zur Messung stratosphärischer Spurenstoffe. Diploma thesis, University of Heidelberg.
- Stutz, J., E. Kim, U. Platt, P. Bruno, C. Perrino, and A. Febo (2000). UV-visible absorption cross section of nitrous acid. *J. Geophys. Res.* 105 (D11), 14858–14592.
- Stutz, J. and U. Platt (1996). Numerical analysis and estimation of the statistical error of Differential Optical Absorption Spectroscopy measurements with least-squares methods. *Appl. Opt.* 35(30), 6041–6053.
- Tuckermann, M., R. Ackermann, C. Gözl, H. Lorenzen-Schmidt, T. Senne, J. Stutz, B. Trost, W. Unold, and U. Platt (1997). DOAS-observation of halogen radical-catalysed Arctic boundary layer ozone destruction during the ARCTOC campaign 1995 and 1996 in Ny-Alesund, Spitsbergen. *Tellus* 49b, 533–555.
- Van de Hulst, H. (1981). *Light scattering by small particles*. New York: Dover publication.
- Van Roozendael, M., S. R. Alliwel, P. V. Johnston, A. Richter, M. V. Roozendael, T. Wagner, D. W. Arlander, J. P. Burrows, D. J. Fish, R. L. Jones, K. K. Tørnkvist, J. C. Lambert, K. Pfeilsticker, and I. Pundt (1999). Analysis for BrO in zenith-sky spectra - an intercomparison exercise for analysis improvement. *J. Geophys. Res.* in preparation.
- van Roozendael, M., C. Fayt, P. Post, C. Hermans, and J.-C. Lambert (2003). Retrieval of BrO and NO<sub>2</sub> from UV-Visible Observations. In P. Borell, P. Borell, J. Burrows, and U. Platt (Eds.), *Sounding the troposphere from space: a new era for atmospheric chemistry*. Springer-Verlag, ISBN 3-540-40873-8.
- Vandaele, A., P. Simon, M. Guilmot, M. Carleer, and R. Colin (1994). SO<sub>2</sub> absorption cross section measurement in the UV using a Fourier transform spectrometer. *J. Geophys. Res.* 99, 25599–25605.

- Vandaele, A. C., C. Hermans, P. C. Simon, M. Carleer, R. Colin, S. Fally, M.-F. Mérienne, A. Jenouvrier, and B. Coquart (1998). Measurements of the NO<sub>2</sub> Absorption Cross-section from 42000 cm<sup>-1</sup> to 10000 cm<sup>-1</sup> (238-1000 nm) at 220 k and 294 k. *J. Quant. Spectrosc. Radiat. Transfer* 59(D18), 171–184.
- Vogt, R., P. J. Crutzen, and R. Sander (1996). A mechanism for halogen release from sea-salt aerosol in the remote marine boundary layer. *Nature* 383, 327–330.
- Volkamer, R., L. T. Molina, M. J. Molina, T. Shirley, and W. H. Brune (2005). DOAS measurement of glyoxal as an indicator for fast VOC chemistry in urban air. *Geophys. Res. Lett.* 32, L08806.
- Volkamer, R., P. Spietz, J. P. Burrows, and U. Platt (2005). High-resolution absorption cross-sections of glyoxal in the UV-vis and IR spectral ranges. *J. Photochem. Photobiol. A: Chem.* 172, 35–36.
- von Friedeburg, C. (2003). *Derivation of Trace Gas Information combining Differential Optical Absorption Spectroscopy with Radiative Transfer Modelling*. Ph.D. thesis, Combined Faculties for the Natural Sciences and for Mathematics, Universität Heidelberg.
- von Friedeburg, C., I. Pundt, K.-U. Mettendorf, T. Wagner, and U. Platt (2005). Multi-Axis-(MAX) DOAS Measurements of NO<sub>2</sub> during the BAB II Motorway Emission Campaign, (BAB II special issue). *Atmos. Environ.* 39, 5, 977-985 5, 977–985.
- von Glasow, R., R. von Kuhlmann, M. G. Lawrence, U. Platt, and P. J. Crutzen (2004). Impact of reactive bromine chemistry in the troposphere. *Atm. Chem. and Phys.* 4, 2481–2497.
- Wagner, T. (1999). *Satellite observations of atmospheric halogen oxides*. Ph. D. thesis, University of Heidelberg, Heidelberg, Germany.
- Wagner, T., J. P. Burrows, T. Deutschmann, B. Dix, C. von Friedeburg, U. Frieß, F. Hendrick, K.-P. Heue, H. Irie, H. Iwabuchi, Y. Kanaya, J. Keller, C. A. McLinden, H. Oetjen, E. Palazzi, A. Petritoli, U. Platt, O. Postylyakov, J. Pukite, A. Richter, M. van Roozendaal, A. Rozanov, V. Rozanov, R. Sinreich, S. Sanghavi, and F. Wittrock (2007). Comparison of box-air-mass-factors and radiances for Multiple-Axis Differential Optical Absorption Spectroscopy (MAX-DOAS) geometries calculated from different UV/visible radiative transfer models. *Atm. Chem. and Phys.* 7, 1809–1833.
- Wagner, T., B. Dix, C. v. Friedeburg, U. Frieß, S. Sanghavi, R. Sinreich, and U. Platt (2004). MAX-DOAS O<sub>4</sub> measurements: A new technique to derive information on atmospheric aerosols - Principles and information content. *J. Geophys. Res.* 109, D22205.
- Wilmouth, D. M., T. F. Hanisco, N. M. Donahue, and J. G. Anderson (1999). Fourier transform ultraviolet spectroscopy of the  $A^2\Pi_{3/2} \leftarrow X^2\Pi_{3/2}$  transition of BrO. *J. Phys. Chem.* 103, 8935–8945.
- Wiscombe, W. J. (1980). Improved Mie scattering algorithms. *Appl. Opt.* 19, 1505–1509.

- Wittrock, F., H. Oetjen, A. Richter, S. Fietkau, T. Medeke, A. Rozanov, and J. P. Burrows (2004). MAX-DOAS measurements of atmospheric trace gases in Ny-Alesund - Radiative transfer studies and their application. *Atm. Chem. and Phys.* 4, 955-966.
- Woyde, M. (2007). Erprobung einer InGaAs-Photodiodenzeile zur Detektion von Methan im NIR-Bereich. Diploma thesis, University of Heidelberg.



## Acknowledgments

I would like to thank all the people who continuously supported me and helped me during the course of this thesis:

Prof. Dr. U. Platt: For the opportunity to study in Germany within his research group. Also I want to thank him for his continuous support and very useful discussions about my research, for the several opportunities he gave me to participate in various international scientific meetings where I could present and discuss my research work.

Prof. Dr. Thomas Wagner: For his very valuable support and continuous help on all levels, for his guidance during all the phases of my thesis work, for his patience and understanding during the hard phases of my thesis too and for his great ability to always give me some of his time whenever I needed in despite of his very busy schedule. With his priceless help, this thesis became a reality.

Many thanks to the International Max Planck Research School (IMPRS) for offering me the stipend which enabled me financially to study in Germany and also enabled me to participate in a rich variety of lecture courses, summer schools and scientific meetings. I would like to thank personally Prof. Dr. Jos Lelieveld for his continuous support and his all efforts to keep the school at its best efficiency through the several meetings with all the IMPRS students.

Also many thanks to Dr. Tineke Lelieveld, the coordinator of the IMPRS, for her great help and caring about all the IMPRS students including me. She did a great job organizing everything, solving our problems and helping us to achieve the best scientific performance.

For all my fellow PhD students at the IMPRS, thank you all for the nice activities and the great times we had together during conferences, summer schools, lecture courses and also during the IMPRS days.

The Air Chemistry Group at the Institute of Environmental Physics in Heidelberg: Thank you all for the nice and cooperative atmosphere and the nice discussions, for the friendly spirit which made it easier for me to adapt in Heidelberg. I want to thank every member of the group in his name.

Special thanks to Dr. Roman Sinreich and Dr. Nicole Bobrowski for introducing me to the WinDOAS software and getting me acquainted to data analysis, for their very nice and friendly support on all levels.

The Satellite Group of Max Planck Institute for Chemistry in Mainz: Thanks a lot for the nice time I spent working with you in Mainz during the last year of my thesis, the friendly atmosphere and the support you all gave me.

Thanks for Miss Ellen Eigemeir, Dr. Roman Sinreich, Mr. Thomas Lehmann and Dr. Barbara Dix for proof reading parts of my thesis.

Thanks also to my diploma student, Torsten Stein, for his nice help and driving for long hours during the Auto-Max-DOAS measurements. Also for driving all-night to enable us to measure at the northern coast of France at the correct time.

The RV Polarstern Captain Udo Domke and his crew for all the great efforts helping and supporting me during the installation and measurements of the MAX-DOAS on board the Polarstern.

Many thanks to Dr. Ellen Brinkma (Royal Netherlands Meteorological Institute KNMI) for her organizational efforts during the DANDELIONS measurement Cam-

paign in Cabauw, the Netherlands. Also thanks to Mr. Warmer (from KNMI) for taking care about power supply problems at Cabauw site to keep the instruments running all the time without interruptions.

Special thanks to Dr. Udo Friess for his very interesting discussions and support during the first year of my thesis.

Thanks to Dr. Klaus-Peter Heue for his help about providing me creative solutions for handling data problems. Also for providing me his routine for color coding measurements paths on google earth maps, which I used in chapter 7.

Many thanks to Dr. Andreas Richter (Institute of Environmental Physics, University of Bremen) for providing us satellite data of SCIAMACHY for comparison with our MAX-DOAS Cabauw results and also for the interesting discussions during the campaign preparation.

Thank you very much all the team of the mechanical and electronic workshop of the IUP Heidelberg for their great efforts preparing and maintaining instruments for campaigns. They always finished the job in time and with a great precision and quality.

Finally I would like to thank my parents for their support, encouragement, understanding and patience during the course of my study in Germany and also during all the long way of my graduate studies.